Synthesis and Characterization of New Compounds Structurally Related to Superconducting Iron-Pnictides

In the System *Ae*–*T*–*E* (*Ae* = Ca, Sr, Ba; *T* = Fe Co, Ni, Rh; *E* = Si, Ge, P, As)

M. Sc. Andrea Viola Hoffmann

Dissertation

Technische Universität München

Fakultät für Chemie

Lehrstuhl für Anorganische Chemie

mit Schwerpunkt Neue Materialien

Technische Universität München

Lehrstuhl für Anorganische Chemie mit Schwerpunkt Neue Materialien

Synthesis and Characterization of New Compounds Structurally Related to Superconducting Iron-Pnictides

In the System *Ae*–*T*–*E* (*Ae* = Ca, Sr, Ba; *T* = Fe Co, Ni, Rh; *E* = Si, Ge, P, As)

Andrea Viola Hoffmann

Vollständiger Abdruck der von der Fakultät für Chemie der Technischen Universität München zur Erlangung des akademischen Grades eines

Doktors der Naturwissenschaften (Dr. rer. nat.)

genehmigten Dissertation.

Vorsitzende:		Univ.-Prof. Dr. Corinna Hess
Prüfer der Dissertation:		
	1.	Univ.-Prof. Dr. Thomas F. Fässler
	2.	Univ.-Prof. Dr. Tom Nilges

Die Dissertation wurde am 22.09.2015 bei der Technischen Universität München eingereicht und durch die Fakultät für Chemie am 26.11.2015 angenommen.

Der experimentelle Teil dieser Arbeit wurde in der Zeit von November 2010 bis Februar 2015 am Lehrstuhl für Anorganische Chemie mit Schwerpunkt Neue Materialien der Technischen Universität München unter wissenschaftlicher Leitung von Herrn Prof. Dr. Thomas F. Fässler durchgeführt.

Ich erkläre hiermit an Eides statt, dass ich die vorliegende Arbeit ohne unzulässige Hilfe Dritter und ohne Benutzung anderer als der angegebenen Hilfsmittel angefertigt habe. Die aus anderen Quellen direkt oder indirekt übernommenen Daten und Konzepte sind unter Angabe des Literaturzitats gekennzeichnet.

Garching, den 22.09.2015

Experiencing the world through endless

second-hand information isn’t enough.

If we want authenticity we have to initiate it.

That’s it, that’s all.

T. Rice

For my Family and Hardl

Acknowledgment

I would like to thank the people who helped me to achieve this thesis with guidance, practical advices, finding solutions for problems and necessary measurements:

First of all would I like to express my gratitude to **Prof. Dr. Thomas F. Fässler** for offering me a position in his department, for the interesting topic, the guidance in the years at the university and the helpful discussions. I also thank him for the opportunity to work with the SQUID Magnetometer giving me the chance to expand my knowledge in this method.

I like to thank my supervisor **Dr. Viktor Hlukhyy** for his help when I encountered problems with the syntheses and helping me to solve structural and computational challenges. He introduced me into the waste topic of intermetallic phases and solid state chemistry and I highly appreciate his patience in teaching me.

I would like to thank the **Deutsche Forschungsgemeinschaft** for the funding of the project SPP1458.

Dr. Lisa Siggelkow for introducing me into the equipment and into the computational program.

Dr. Bele Boeddinghaus for the numerous hours teaching me the SQUID Magnetometer and the interpretation of the data.

Dr. Markus Waibel for the help with computer problems, his advices and helpful discussions, for proofreading my manuscripts as well as for the lunch breaks.

Dr. Michael Zeilinger for giving me advice in synthesis methods, for proofreading my manuscripts and for making the many weekends at the university enjoyable.

Dr. Bernhard Wahl and **Dr. Wilhelm Klein** for the help with crystallographic matters.

Iryna Kurylyshyn for advices with the computational methods and always being there for me.

Volodymyr Baran for the measurements at the IPSD-2T.

Ingrid Werner for the help to maintain the SQUID Magnetometer.

Special thanks to **Manuela Donaubauer** for all the help with the organizational aspects and being the good soul of the department.

Lorenzo Toffoletti for a cup of coffee when necessary. In addition many others have made big contributions by discussions, help in the laboratories and by creating a friendly and collegial environment. I would like to extend my thanks to all my co-workers during my time at the university: **Dr. Christian Benda**, **Manuel Bentlohner**, **Dr. Daniel Bräunling**, **Carina Dressel, Dr. Haiyan He**, **Thomas Henneberger**, **Alexander Henze**, **Dr. Florian Kiefer**, **Dr. Prashant W. Menezes**, **Dr. Sandra Scharfe**, **Lavinia Scherf**, **Dr. Annette Schier**, **Dr. Saskia Stegmaier**, **Herta Slavik**, all our Post-Docs, **Ursula Madan-Singh**, **Prof. Dr. Florian Kraus** and his group; **Prof. Dr. Tom Nilges** and his group: **Lucia Weissenborn**, **Dr. Oliver Osters**, **Dr. Magnus Greiwe**, **Dr. Malte Giller** and the rest as well as **Franz Haseidl** and the group of **Prof. Dr. Dirk Johrendt** at the LMU**.**

Most of all would I like to thank **my family** for their endless love and support during all my stages in life, the encouragement to further my horizon and being always there for me. My special thanks to my fiancé **Leonhard Hörth** for staying at my side in good and bad times, for all the adventures we have together as well as his help, encouragement and advices in all aspects of life. And to all **my friends** for an open ear and encouragement throughout the years.

Abstract

This thesis focuses on the extension of chemical compounds in the system *Ae*–*T*–*E* (*Ae* = Ca, Sr, Ba; *T* = Fe, Co, Ni, Rh; *E* = Si, Ge, P, As) with $ThCr_2Si_2$ structure type, analogous to the superconducting iron-pnictides, and related structures including the investigation of their structural and physical properties. In this context new ternary and pseudo-ternary as well as new binary compounds were synthesized by solid state syntheses.

The new phases were investigated with powder and single crystal X-ray diffraction analyses, Energy Dispersive X-ray spectroscopy (EDX) and magnetic and conductivity measurements to test for superconductivity. The electronic structure calculations were performed with the TB-LMTO-ASA program. The Density of States (DOS) curves, the band structures including fat bands, the Crystal Orbital Hamilton Population (COHP) and the topological analyses of the Electron Localization Function (ELF) were used to explain the chemical bonding situation of new compounds.

In the first part of this thesis the effects of charge doping were studied in respect to the electronic structure and superconducting behavior. The new solid solution series $SrNi_2(P_{1-x}Ge_x)_2$ as well as the compounds $BaFe_2(P_{0.930(6)}Ge_{0.070(6)})_2$ and $Ca(Fe_{1-x}Rh_x)_2Si_2$ (x = 0, 0.66(3), 1), all crystallizing in the $ThCr_2Si_2$ structure type, were synthesized and analyzed. The variations in the structural parameters with focus on the tunable *E*–*E* distance along [001] and the effect of partial substitution on the superconducting temperature T_c are discussed. Electronic structure calculations are presented to complete the investigation.

The second part of the thesis discusses in detail the electronic structure and chemical bonding situation of the compound CaCoSi which is isostructural to the superconducting phases NaFeAs, LiFeAs and LiFeP.

In addition three new compounds in the Ca–Fe–As phase system, $Ca_{14}FeAs_{11}$, Ca_4As_3 and $Ca_{11}As_{9.68(2)}$, were found as side products in samples made from the elements Ca, Fe, As, Rh and Si. The compounds were reproduced from the elements and the structures of the compounds are reported in detail in the third part of the thesis. The ternary compound $Ca_{14}FeAs_{11}$ crystallizes in the $Ca_{14}AlSb_{11}$ structure type, it is the first member of this family containing Fe and the first compound that contains isolated $FeAs_4$ tetrahedra. Electronic structure calculations were performed for the compound using two different atom models. A description of the binary compound Ca_4As_3, which is isostructural to the Ba_4P_3 compound, in analogy to the Zintl-Klemm concept is presented. The second binary compound $Ca_{11}As_{9.68(2)}$ crystallizes in a distorted version of the $Ho_{11}Ge_{10}$ structure type. Single crystal refinement showed a deficiency for one atomic As position resulting in the composition $Ca_{11}As_{9.68(2)}$, the compound cannot be described in analogy to the Zintl-Klemm concept. A detailed description of the structure and a comparison to other members of the family is discussed.

Zusammenfassung

Im Rahmen dieser Arbeit wurde das Phasensystem *Ae*–*T*–*E* (*Ae* = Ca, Sr, Ba; *T* = Fe, Co, Ni, Rh; *E* = Si, Ge, P, As) auf neue Verbindungen untersucht und deren strukturelle und physikalische Eigenschaften bestimmt. Der Fokus lag dabei auf dem $ThCr_2Si_2$ Strukturtyp, in welchem auch bekannte Eisen-Pniktid Supraleiter kristallisieren, und verwandten Strukturtypen. Es wurden neue ternäre und pseudoternäre sowie neue binäre Verbindungen mittels Festkörpersynthese hergestellt und charakterisiert.

Die Struktur der neuen Verbindungen wurde anhand von Pulver- und Einkristall-Röntgenbeugung geklärt. Es erfolgte eine Analyse der Kristalle mithilfe der energiedispersiven Röntgenspektroskopie und Untersuchung der Verbindungen hinsichtlich Supraleitfähigkeit mittels magnetischer und Leitfähigkeits-Messungen. Darüber hinaus wurde die elektronische Struktur der Verbindungen betrachtet, dazu wurden die Zustandsdichte (DOS) und die Bandstruktur inklusive der Fatbands mit dem TB-LMTO-ASA Programm berechnet. Zusätzlich wurde die chemische Bindung der Verbindungen anhand von Crystal Orbital Hamilton Population (COHP) erläutert und die topologische Analyse der Elektrondichte (ELF) beschrieben.

Im ersten Teil dieser Arbeit werden die neuen Verbindungen mit $ThCr_2Si_2$ Strukturtyp besprochen. Der Fokus der Untersuchungen lag dabei darauf, den Einfluss der Gesamtladung der Verbindung auf die strukturellen sowie elektronischen und supraleitenden Eigenschaften zu analysieren. Dazu wurden mittels Teilsubstitution die feste Lösung $SrNi_2(P_{1-x}Ge_x)_2$ sowie die Verbindungen $BaFe_2(P_{0.930(6)}Ge_{0.070(6)})_2$ und $Ca(Fe_{1-x}Rh_x)_2Si_2$ (x = 0, 0.66(3), 1) hergestellt und untersucht. Die Variationen der Strukturparameter mit Blick auf den flexiblen *E*–*E* Abstand entlang [001] und der Einfluss der Teilsubstitution auf die supraleitenden Eigenschaften und die Sprungtemperatur werden betrachtet. Die Beschreibung der elektronischen Struktur und der chemischen Bindungssituation komplettiert die Diskussion.

Im zweiten Teil der Arbeit werden die elektronischen Eigenschaften und die chemischen Bindungsverhältnisse von CaCoSi detailliert besprochen. Diese

Verbindung ist isostrukturell zu den supraleitenden Phase NaFeAs, LiFeAs und LiFeP.

Die drei neuen Verbindungen $Ca_{14}FeAs_{11}$, Ca_4As_3 und $Ca_{11}As_{9.68(2)}$ im Phasensystem Ca–Fe–As wurden zuerst als Nebenprodukte bei Ansätzen aus Ca, Fe, As, Rh und Si entdeckt und konnten aus den Elementen reproduziert werden. Die Strukturen der Verbindungen werden im dritten Teil dieser Arbeit detailliert beschrieben. Die ternäre Verbindung $Ca_{14}FeAs_{11}$ ist die erste Phase mit Eisen, welche im $Ca_{14}AlSb_{11}$ Strukturtyp kristallisiert und die erste Verbindung mit isolierten $FeAs_4$ Tetraedern. Die elektronische Struktur der Verbindung wurde anhand von verschiedenen Modellen berechnet. Die Struktur der binären Verbindung Ca_4As_3 wird in Analogie zum Zintl-Klemm Konzept beschrieben, sie kristallisiert im Ba_4P_3 Strukturtyp. Die zweite binäre Verbindung $Ca_{11}As_{9.68(2)}$ kristallisiert in einer verzerrten Version des $Ho_{11}Ge_{10}$ Strukturtyps. Eine Unterbesetzung einer der As-Lagen in der Verbindung konnte anhand der Einkristallmessung bestimmt werden. Eine detaillierte Beschreibung der Struktur, welche nicht analog dem Zintl-Klemm Konzept beschrieben werden kann, und der Vergleich mit anderen Verbindungen des Strukturtyps werden diskutiert.

Content

1. Introduction 1
- 1.1. Motivation 1
- 1.2. Intermetallic Compounds 2
  - 1.2.1. Superconductors 3
  - 1.2.1.1. Cuprate superconductors 3
  - 1.2.1.2. Iron-pnictide and related superconductors 4
- 1.3. Scope and outline of this work 10
- 1.4. References 13

2. Experimental Section 17
- 2.1. General Experimental Methods 17
  - 2.1.1. Elements used for Synthesis 17
  - 2.1.2. Reaction Container 18
  - 2.1.3. Arc melting Furnace 19
  - 2.1.4. Resistance Furnace 20
  - 2.1.5. Induction Furnace 22
  - 2.1.6. Planetary ball mill 22
- 2.2. Analytical Methods 23
  - 2.2.1. Powder X-ray diffraction 23
  - 2.2.2. Single Crystal X-ray diffraction 25
  - 2.2.3. Scanning Electron Microscopy (SEM) and Energy Dispersive X-ray Spectroscopy (EDX) 26
  - 2.2.4. Magnetic Measurements 26
  - 2.2.5. Conductivity Measurements 28
- 2.3. Computational Methods 29
- 2.4. References 31

3. New Intermetallic Compounds with $ThCr_2Si_2$ Type Structure 33
- 3.1. Introduction 33
- 3.2. $SrNi_2(E_{1-x}Ge_x)_2$ with E = P, As 36
  - 3.2.1. Syntheses of the compounds and alloys used as precursors 36
  - 3.2.2. Results and discussion 41
  - 3.2.2.1. Crystal Structure of $SrNi_2(P_{1-x}Ge_x)_2$ solid solution 41
  - 3.2.2.2. Magnetic Properties 56
  - 3.2.2.3. Conductivity measurements 59
  - 3.2.2.4. Electronic structure and chemical bonding 61
  - 3.2.3. Investigation of $SrNi_2(As_{1-x}Ge_x)_2$ solid solution 66

3.3. Investigation of $BaFe_2(P_{1-x}Ge_x)_2$ solid solution 68
3.3.1. Synthesis of the binary precursors and the pseudo-ternary samples 68
3.3.2. Crystal Structure 70
3.4. Investigation of $Ca(Fe_{1-x}Rh_x)_2Si_2$ solid solution 73
3.4.1. Synthesis of the ternary and pseudo-ternary compounds 73
3.4.2. Results and Discussion 75
3.4.2.1. Crystal structure 75
3.4.2.2. Chemical Bonding 80
3.5. References 90
4. Intermetallic CaCoSi phase 93
4.1. Introduction 93
4.2. Results and discussion 94
4.3. References 102
5. New compounds in the Ca–Fe–As phase system 103
5.1. Introduction 103
5.2. Intermetallic $Ca_{14}FeAs_{11}$ phase 106
5.2.1. Synthesis of $Ca_{14}FeAs_{11}$ 107
5.2.2. Results and discussion 108
5.2.2.1. Crystal Structure 109
5.2.2.2. Differential Scanning Calorimetry 118
5.2.2.3. Electronic structure of $Ca_{14}FeAs_{11}$ 118
5.3. New binary Ca–As phases 123
5.3.1. Syntheses of the binary phases 123
5.3.1.1. Ca_4As_3 123
5.3.1.2. $Ca_{11}As_{9.68(2)}$ 125
5.3.2. Results and discussion 126
5.3.2.1. Crystal structure of Ca_4As_3 126
5.3.2.2. $Ca_{11}As_{9.68(2)}$ crystal structure 132
5.4. Comparison of the new compounds within the Ca–As–Fe system 140
5.5. References 142
6. Summary and Outlook 145
Appendix 151
List of Figures 183
List of Tables 192

Nomenclature

Abbreviations

111 compounds	compounds of PbClF (alternatively CeFeSi) structure type
1111 compounds	compounds of ZrCuSiAs structure type
122 compounds	compounds of ThCr$_2$Si$_2$ structure type
A	alkaline metals
ADP	anisotropic displacement parameters
Ae	alkaline earth metal
ASA	atomic-sphere approximation
CCD	charge coupled device
Cif	crystallographic information file
COHP	Crystal Orbital Hamilton Population
cT	collapsed ThCr$_2$Si$_2$ type structure
DC	direct current
DOS	Density of States
EDX	energy dispersive X-ray spectroscopy
ELF	electron localization function
ES	empty spheres
GOF	*goodness of fit*
HT	high-temperature phase
iCOHP	integrated Crystal Orbital Hamilton Population
ICSD	Inorganic Crystal Structure Databank
iDOS	integrated Density of States
IPDS	imaging plate diffraction system
IP-PSD	imaging plate position sensitive detector
LDA	local density approximation
LMTO	linear muffin-tin orbital

L-PSD	linear position sensitive detector
LT	low-temperature phase
MPMS	magnetic property measurement system (*Quantum Design*)
pDOS	partial Density of States
PPMS	physical property measurement system (*Quantum Design*)
RE	rare earth metals
RSO	reciprocating sample option
SEM	scanning electron microscopy
SQUID	superconducting quantum interference device
T	transition metal
TB	tight binding
ucT	uncollapsed $ThCr_2Si_2$ type structure
E	element of group 14 or 15
Z	number of empirical formula units per unit cell
zfc-fc	zero-field cooled-field cooled

Units and Symbols

⌀	diameter
a.u.	atomic units
Å	angström
cm	centimeter
d	interatomic distance
E_F	Fermi energy
emu	electro-magnetic units, magnetic moment
g	gram/mass
h	hours
H	magnetic field
H_c	critical field for superconductors
K	Kelvin
kV	kilovolt
M	magnetization
m	long moment
mA	milliampere
mg	milligram
M_g	mass magnetization
mm	millimeter
M_m	molar magnetization
mol	molar
MPa	megapascal
M_v	volume magnetization
Oe	Oersted
Pa	Pascal
R	residual factor

$\mathrm{T_c}$	critical temperature for superconductors
T_C	Curie temperature
T_ev	evaporation temperature
U	thermal displacement parameter
V	volume
2θ	diffraction angle
α	tetrahedral angle
λ	wavelength
σ	standard deviation
χ	susceptibility
χ_g	mass susceptibility
χ_m	molar susceptibility
χ_v	volume susceptibility
η	isosurface value

1. Introduction

1.1. Motivation

The ever rising demand for energy around the globe, the difficulties to generate energy in an environmentally friendly manner and the diminishing reservoirs of natural gas, oil and coal all are aspects that drive researchers to find new and better energy sources. The power problem that is currently faced can be separated into two parts, the energy sources and the transport of the energy to the end-user. Superconducting materials could be used in the field of the energy transport and storage to decrease the losses of energy taking place throughout the networks of power lines build with normal conductors.

Application of superconductors for energy transportation is one of the main goals that researchers in this field work on. The efficiency of electric generators can be increased if the wires are made of superconducting materials instead of normal conducting materials. Another idea is to employ superconductors to improve energy storage and to use superconducting wires in transformers. The methods are commercially available on small scales due to the high costs of these systems. As a prerequisite compounds with bulk superconductivity and high critical temperatures are needed. Ideally the T_c should be close to room-temperature so no expensive cooling is needed. So far the highest T_c is reported for $HgBa_2Ca_2Cu_3O_{8+y}$ which becomes superconducting at 135 K.[1]

Energy companies like Rheinisch-Westfälisches Elektrizitätswerk (RWE) in Germany and American Superconductor (AMSC) in America operate test areas where the power is transmitted through superconducting wires. However, the transmission distances are short due to the expensive cooling needed. This makes the search for new materials with high T_c values a focus in academic and industrial research. In addition, the materials should also be easily manufactured in large quantities at low cost, the handling and formation of the materials should be possible to fit the needs of application and health & environmental risks should be low. So far no material fulfilling these requirements is known.

The newly discovered family of iron-pnictides gained popularity immediately and many scientists focused on the syntheses and characterization of compounds belonging to this family. The new group of high-temperature superconductors (HTS's) provides researchers with the opportunity to get more insight into the origin of superconductivity. Within a few years more and more new compounds were reported and new iron-pnictide families with superconducting behavior were discovered.[2-5] The search for new compounds with superconducting behavior is vital to help getting a better idea what drives superconductivity in these compounds.

1.2. Intermetallic Compounds

Intermetallic compounds contain by definition two or more metallic elements.[6] They have regular crystal structures with a defined composition. This definition includes also the post-transition metals like Al, Ga, In, Tl, Sn and Pb as well as the elements like Si and Ge which are at the border between metals and non-metals. In contrast the definition does not include alloys of homogenous solid solutions of metals or interstitial compounds. The periodic system contains over 80 elements that are metals, which gives rise to a huge variety of possible intermetallic compounds and alloys. The crystal structures and the properties of intermetallics are therefore diverse. They can be classified for example as Hume-Rothery phases and as Laves phases with intermetallic bonding in the structures, as polar intermetallic and as Zintl phases which are at the border between intermetallic and ionic materials.[7-9]

Application of intermetallic compounds can be found in many different areas, for example in the field of construction, in battery and thermoelectric materials and in magnetic materials for recording and data storage. Commonly known intermetallics are industrial steel, stainless steel and brass which find application in all areas of life. Intermetallic materials are also found as electrodes in commercially available batteries.[10, 11] Thermoelectric materials are employed in different fields, for example in power generation and thermocouples.[12, 13] The application of thermoelectric generators in cars is a field of great interest to scientists. Intermetallic materials like FePt are considered for application in the area of data storage due to the magnetic coercive properties of nanoparticles.[14]

Other magnetic properties found in intermetallic compounds are superconductivity and giant magnetoresistance (GMR). Superconducting magnets can be used in Magnetic Resonance Imaging (MRI) devices and particle accelerators while GMR materials are used as magnetic field sensors for data reading.

1.2.1. Superconductors

Superconductivity was first observed in 1911 by H. Kamerlingh Onnes when he worked on cooling experiments with Hg.[15-17] He discovered that the resistivity of Hg drops to zero below 4 K. Superconducting materials have the ability to totally exclude magnetic fields which reduces the resistivity to zero. As a result electricity can flow through superconducting materials without energy losses. This effect makes superconductors interesting for application in the field of power supply and transportation.

The high-temperature superconductors (HTS), also called type 2 superconductors, have attracted the interest of scientists for decades. Many compounds have been synthesized and their properties were investigated. Type 2 superconductors cannot satisfactorily be described with the BCS-Theory (Bardeen-Cooper-Schrieffer) which explains the phenomenon of superconductivity in type 1 superconductors.[18] Even though thousands of publications dealing with type 2 superconductors can be found, an explanation for the origin of superconductivity with high T_c values is still missing.

1.2.1.1. Cuprate superconductors

The cuprates were for many years believed to be the only compounds that exhibit high-temperature superconducting behavior. The compounds are not intermetallic phases but ceramics which adopt perovskite like structures.[19] Since the important units in the structures are the 2D CuO_2 layers in which superconductivity takes place these materials are viewed as 2D superconductors. It has been observed that the number of CuO_2 layers in the unit cell of the compound relates to T_c. The lowest T_c values are observed for compounds with one CuO_2 layer in the unit cell and T_c increases when the unit cell contains two or three CuO_2 layers.

Examples are the Hg compounds $HgBa_2CuO_4$ (one layer) with $T_c = 94$ K,[20] $HgBa_2CaCu_2O_6$ (two layers) with $T_c = 128$ K and $HgBa_2Ca_2Cu_3O_8$ (three layers) with $T_c = 134$ K.[21]

The CuO_2 layers are sensitive to substitution in respect to the superconducting behavior of the materials. The undoped cuprate materials, so-called parent compounds, are antiferromagnetic insulators and superconductivity is only observed upon charge doping.[22]

The high T_c values for cuprate superconductors, which are in multiple cases higher than the boiling point of liquid N_2 (77 K), make the materials attractive in regards to possible industrial applications. However, the ceramic cuprate materials are brittle which makes the handling and forming of the materials difficult in practice. Cuprate materials are used in the superconducting wires for the Holbrook Superconductor Project on Long Island, USA.[23]

1.2.1.2. Iron-pnictide and related superconductors

Superconductivity in iron-pnictide compounds was first discovered in 2006 by the group of Hosono. They observed superconducting behavior below 4 K for LaFePO.[24] The isostructural LaNiPO was also reported as a superconductor with a T_c of 3 K.[25] However, LaFeAsO does not show superconducting behavior. Since the T_c values of the compounds were rather low scientists did not take much notice. With the discovery in 2008 that a partial substitutions of O with F in LaFeAsO could induce superconductivity at temperatures at 26 K[26] the topic caught world-wide attention. In the same year the group of Johrendt reported superconductivity in $Ba_{1-x}K_xFe_2As_2$ with a maximum T_c value of 38 K for $x = 0.4$.[27] These discoveries lead to the new family of iron-pnictide high-temperature superconductors and immediately researchers around the world focused on the topic. Similar to the cuprates the iron-arsenides have so-called parent compounds (*Ae*/*RE*)FeAsO and (*Ae*/*RE*)Fe_2As_2 (*Ae* = alkaline earth metals, *RE* = rare earth metals) which are not superconducting but charge doping or pressure can induce superconductivity. Within a few years more members of the iron-pnictide superconductor family could be identified. Superconductivity is also observed in iron-chalcogenide compounds with similar structures to the iron-pnictides.

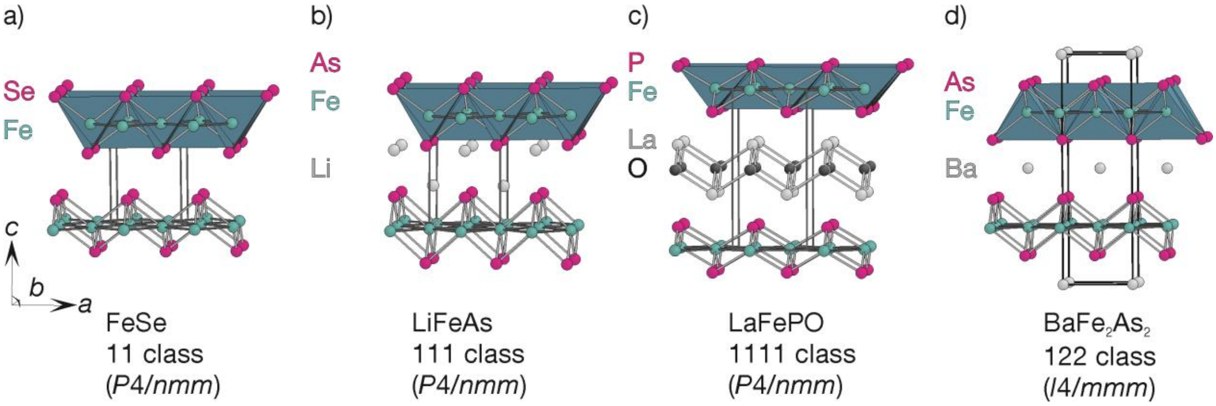

Figure 1.1 Classes of the iron-pnictide superconductor family presented as models: a) 11 class, example FeSe superconductor; b) 111 class, example LiFeAs superconductor; c) 1111 class, example LaFePO superconductor; d) 122 class, example $BaFe_2As_2$ parent compound.

The iron-based superconductors reported so far can be divided in multiple classes based on structure types. All iron-pnictide superconductor classes contain the structure motif of tetrahedral layers in the form of anti-PbO[28] type layers stacked along the *c*-axis. The tetrahedral layers have the Fe atoms (or other transition metals) surrounded by 4 pnictide or chalcogenide atoms forming $FeAs_4$ tetrahedra with shared edges in the *ab*-plane. The layers are separated by different units which define the individual classes. The classes are commonly referred to by the abbreviation of the stoichiometry coefficient for the structure types. Four of the most prominent iron-pnictide/chalcogenide superconductor classes are presented in Figure 1.1.

The so-called 11 class crystallizes in the anti-PbO structure type in the tetragonal space group *P*4/*nmm*.[29] The structure contains only the tetrahedral layers which are stacked without a separating unit between them (Figure 1.1a). Superconductors in this class are for example FeSe[29] and $FeTe_{1-x}Se_x$[30] with T_c values of 8 K and 14 K (respectively). The stoichiometry in the superconducting materials are not exactly 1:1 (iron:chalcogenide) but a small excess of Fe (or alternatively a small deficiency of chalcogenide) is observed.[3]

The superconductors NaFeAs and LiFeAs belong to the 111 compounds which crystallize in the CeFeSi (alternatively anti-PbFCl) structure type (Figure 1.1b).[31] The tetrahedral layers are separated by two layers of cations and can be described as a filled version of the 11 structure type. Within this class LiFeAs has the highest T_c at approximately 18 K.[32]

The compounds isostructural to LaFePO, the first iron-pnictide superconductor reported,[24] with ZrCuSiAs type structure[33] contain polyanionic FeAs tetrahedral layers which are separated alternatingly by polycationic (*RE*/*Ae*)O tetrahedral layers (Figure 1.1c). The structure can be viewed as a filled version of the 111 compounds. Iron-pnictide superconductors with critical temperatures above 50 K, like $SmFeAsO_{0.85}F_{0.15}$[34] and $Sr_{1-x}Sm_xFeAsF$,[35] belong to this class.

The superconducting iron-pnictides and chalcogenides with $ThCr_2Si_2$ structure type are labelled as 122 compounds (Figure 1.1d). In this structure type the polyanionic tetrahedral layers are separated by one layer of cations. Special about this structure type is the shift of the adjacent layers in the *a,b*-direction which makes it possible that covalent bonding interactions occur between the tetrahedral layers. Two tetragonal modifications exist for this structure type: the so-called uncollapsed modification (ucT) without covalent bond along [001] and the collapsed modification (cT) with covalent bonds along [001] resulting in 3D $FeAs_4$ tetrahedra networks. This structural variable plays an important role for the appearance of superconductivity within the class. The most famous compound in this class is $Ba_{0.6}K_{0.4}Fe_2As_2$ which was the first reported superconducting member of the class with a T_c of 38 K.[27, 36]

Superconductivity is also found in compounds like Sr_2VO_3FeAs[37] with a T_c of approximately 37 K and $Ca_3Al_2O_{5-x}Fe_2As_2$ with a T_c of 30.2 K.[38] These superconductors are referred to as 21311 and 32522 phases with polyanionic tetrahedral layers separated by cationic, perovskite-like oxid layers. The newest iron-pnictide superconductors are compounds like $Ca_{10}(Fe_{2-x}Pt_xAs_2)_5(Pt_nAs_8)$ referred to as 10-3-8 and 10-4-8 superconducting compounds (depending on *n*).[39, 40]

The discovery of superconductivity in iron-pnictides also led to the reinvestigation of known compounds with similar structures in respect to their magnetic behavior. It was soon found that superconductivity exists in numerous $AeNi_2E_2$ (*Ae* = Sr, Ba; *E* = Ge, P, As)[41-45] compounds in their stoichiometric composition. Like the first reported iron-pnictide superconductors LaFePO and LaNiPO,[24, 25] their T_c values are below 5 K. It is also noteworthy that the $RENi_2B_2C$ (*RE* = La, Y, Tm, Er, Ho, Lu)[46-48] superconducting compounds reported in the 1990s are structural similar to the 122 compounds. In these compounds the Ni_2B_2

tetrahedral layers are connected along the *c*-direction by the C atoms with covalent B–C–B bonds (see Figure 1.2).

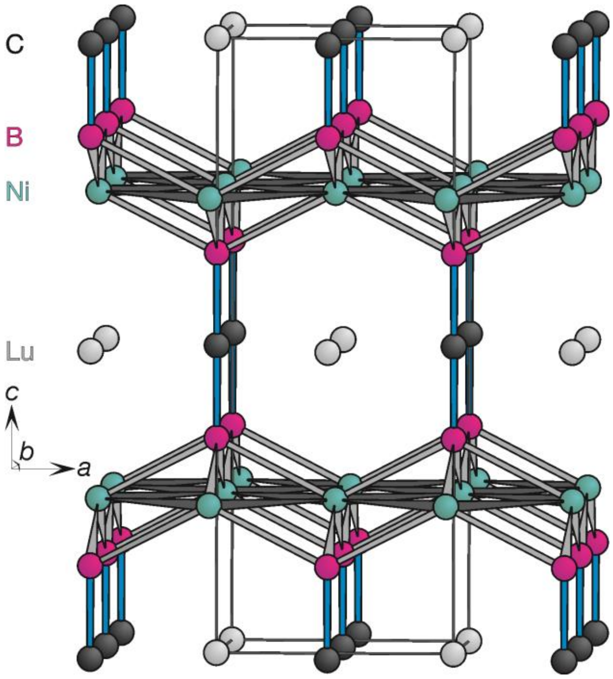

Figure 1.2 Structure of $LuNi_2B_2C$ superconductor (T_c = 16.6 K) Lu = gray, Ni teal, B = magenta and represented as C = black spheres; bonds between Ni–Ni (dark gray), Ni–B (light gray lines) and B–C (blue lines) are included.

Most iron-arsenide/chalcogenide compounds do not display superconductivity when the composition is stoichiometric (parent compounds like $BaFe_2As_2$ in Figure 1.1d). Often a structural and/or magnetic phase transition takes place and an antiferromagnetic spin-density–wave (SDW) at low temperatures is observed.[26, 27, 49, 50] The high-temperature tetragonal modification exhibits paramagnetism. Upon cooling the compounds undergo a structural and magnetic transition to an orthorhombic modification with an stripe type antiferromagnetic order (see Figure 1.3).[51]

The structural and magnetic phase transition is sensitive to manipulations by charge doping or chemical/physical pressure which is needed to induce superconductivity into the parent compounds.[27, 29, 30, 34, 35, 52-55] Partial substitution on either crystallographic site within the structures is possible to suppress the transition.

The partial substitution influences the structural parameters which in turn results in small but important changes in the electronic structure of the compounds.[5] The superconductivity in iron-pnictides/chalcogenides and related compounds takes place in the tetrahedral Fe$E_{4/4}$ layers (E = P, As, Se, Te). The distance separating the layers and the structural parameters within the layers are therefore most important to the magnetic properties of the compounds.

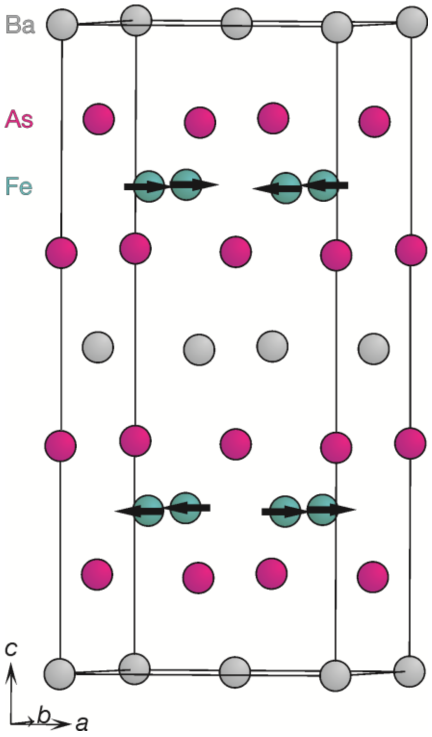

Figure 1.3 $BaFe_2As_2$ model in the low-temperature modification with space group *Fmmm*; Ba shown in gray, Fe in turquois and As in magenta. The orientations of the magnetic moments of Fe are presented as black arrows.[51]

The bonding strength within the tetrahedral layers and the coordination of the pnictide/chalcogenide atoms around the central iron-atom are said to be crucial. In the beginning the transition temperature of superconducting iron-pnictides/chalcogenides was discussed in relation to the tetrahedral angle within the tetrahedra, claiming that the highest T_c values are achieved when the angle is closest to the ideal value of 109.47 °.[56] In recent years the height of the pnictogen/chalcogen atoms above/below the planar iron layers are discussed in relation to the T_c values of superconductors.[57, 58]

In iron-pnictide/chalcogenide compounds superconductivity is favored when the SDW anomaly gets suppressed, they can coexist when the charge-doping is in the under-doped range of the phase diagram.[36, 59-61] The highest T_c values are observed when the magnetic phase transition is fully suppressed and the ideal doping concentration is achieved, for example in the solid solution $Ba_{1-x}K_xFe_2As_2$.[36]

The tetrahedral layers, which play a crucial role for iron-pnictide/chalcogenide and related superconductors, are expected to play the important role in the electronic structure of the compounds. The electronic properties near the Fermi level are dominated by the Fe-d states for the parent and superconducting compounds.[49] The compounds exhibit metallic behavior and a pseudo-gap is observed above the Fermi level. Iron-pnictide/chalcogenide superconductors are reported to have quasi-two dimensional Fe-d conduction bands. In addition small contributions of the pnictogen/chalcogen-p states are observed at the Fermi level. For the superconducting compounds electron- and hole-pockets are observed at the Fermi level. The interactions between the pockets are vital for the magnetic properties of the compounds.[62] The manipulations by partial substitution or applied physical pressure influence the nesting between the pockets at the Fermi surface. Not only does the nesting determine the appearance of superconductivity but is has been reported that the properties of the superconducting gaps in compounds can vary.[58]

The structure motif of TE_4 tetrahedra is also found in other iron-chalcogenides like Na_5FeS_4,[63] $A_3Fe_2E_4$ (A = K, Na, Rb, Cs, Tl; E = S, Se)[64-68] and A_3FeE_3 (A = K, Na, Cs; E = S, Se) compounds.[69-72] In the A_3FeE_3 compounds the tetrahedra share common edges and form 1D chains. In $A_3Fe_2E_4$ compounds, only two tetrahedra are connected via an edge forming $[Fe_2E_6]$ units. The covalent FeE_4 bonds in the tetrahedra are not all equidistant like it is in the compounds with 2- or 3-dimensional layers; the distances and the tetrahedral angles vary. In Na_3FeS_3 the distances in the $[Fe_2S_6]^{4-}$ unit vary between 2.25 Å and 2.30 Å,[71] in K_3FeSe_3 the variation is between 2.36 Å and 2.42 Å.[64] In the compounds with 1D FeE_4 chains the covalent bonds are longer (2.28 Å - 2.34 Å and 2.40 Å - 2.47 Å for $Na_3Fe_2S_4$ and $K_3Fe_2Se_4$, respectively).[64, 65] The tetrahedra are slightly distorted in the compounds.

Isolated FeS_4 tetrahedra are found in the structure of Na_5FeS_4.[63] The covalent Fe–S bonds are reported to vary between 2.27 Å - 2.90 Å and the tetrahedra show a distortion with tetrahedral angles between 106 ° and 113 °.

In order to investigate the relations between structural and electronic properties of superconductors and related compounds, detailed and accurate information about the structural parameters and the compositions are needed; in addition the search for new compounds is ongoing. This is the part that solid state chemists focus on.

1.3. Scope and outline of this work

Important for the understanding of the properties of HT iron-pnictide superconductors and related compounds is a detailed knowledge of structural parameters and the compositions for partial substituted compounds with superconducting behavior. The electronic structure and physical properties of the materials can be tuned by charge doping with various elements on different atomic positions in the compounds. In this work the research for new compounds belonging to the 111 and 122 families, which was started in the Master-Thesis,[73] is continued. The focus was put on the system *Ae*–*T*–*E* (*Ae* = Ca, Sr, Ba; *T* = Fe, Co, Ni, Rh and *E* = Si, Ge, P, As) searching for new ternary compounds isostructural to 111 and 122 superconductors. The effect of the valence electron number on the properties of a compound was investigated by trying out elements from different groups for the *T* and *E* position.

As part of the project the effects of partial substitution on the *T* or *E* position in ternary compounds by an element with a different valence electron number were studied. Different attempts to synthesize pseudo-ternary compounds were made to study the effect of charge doping on the magnetic behavior of ternary compounds. The main focus was put on substitution of Fe with Co, Ni or Rh (more valence electrons) and of P or As with Si or Ge (less valence electrons).

The structures and compositions of new compounds as well as the bonding situation within the structures were investigated in order to obtain better understanding of the properties.

In the next chapter the general syntheses and analytical methods used are described. Detailed information for each result is given in the corresponding chapter.

The third chapter of this thesis deals with ternary and pseudo-ternary phases which are isostructural to the 122 family of iron-pnictide superconductors. The aim of the investigation was to expand the 122 family and to find new superconducting compounds. Three different aspects where significant for the choice of the investigated compound: 1) finding compounds that could be possible new parent compounds for superconductors, 2) possible induction of superconductivity in non-superconducting ternary compounds by partial substitution and 3) the influence of charge doping by partial substitution on the T_c for ternary superconducting Ni-compounds.

The ternary compounds CaT_2Si_2 (T = Fe, Rh) were investigated in order to determine if they can be used as arsenic-free parent compounds just like the undoped iron-pnictides. Partial substitution of Fe with Co, Ni and Rh was tried leading to the discovery of the $Ca(Fe_{1-x}Rh_x)_2Si_2$ solid solution.

The compound $BaFe_2P_2$ is isoelectronic to the superconductor parent compound $BaFe_2As_2$. The focus of this investigation was to see if partial substitution of P with Ge could induce superconductivity similar to the reported successes in the solid solutions $BaFe_2(As_{1-x}P_x)_2$ and $BaNi_2(P_{1-x}Ge_x)_2$.[74, 75]

The solid solutions $SrNi_2(E_{1-x}Ge_x)_2$ (E = P, As) were chosen to investigate the effect of charge doping on the T_c value of the $SrNi_2E_2$ (E = Ge, P, As) superconducting compounds, similar to the effects observed for T_c in the $BaNi_2(P_{1-x}Ge_x)_2$ solid solution.[74]

New compounds are presented; their crystal structure and the individual bonding situation are explained. The compounds are discussed in relation to other 122 family members and in addition magnetic, conductive and electronic properties are given for certain phases.

The fourth chapter compares the electronic structure of CaCoSi with isostructural compounds and structurally related 122 compounds. CaCoSi does not show superconducting behavior but is closely related to superconducting compounds, therefore the variations in the electronic structure were investigated to help understand the pre-requests for the appearance of superconductivity in this structure type.

New compounds within the ternary phase system of Ca–Fe–As are discussed in the fifth chapter. Ternary Ca–Fe–As compounds all contain tetrahedral [$FeAs_4$] layers; $CaFe_2As_2$[76] with 2D layers is parent compounds for iron-pnictide based superconductors with $ThCr_2Si_2$ structure type and to the class of related $(CaFe_{1-x}Pt_xAs)_{10}Pt_{4-y}As_8$ superconducting compounds.[39, 40, 77, 78] Investigation of the Ca–Fe–As system resulted in the discovery of two new binary Ca–As and one ternary Ca–Fe–As compound. The first ternary compound with isolated $FeAs_4$ tetrahedra is presented. The crystal structures of three new phases are explained and compared in regards to known isostructural phases and previously reported compounds in the ternary Ca–Fe–As system.

1.4. References

[1] L. Gao, Z. J. Huang, R. L. Meng, J. G. Lin, F. Chen, L. Beauvais, Y. Y. Sun, Y. Y. Xue, C. W. Chu, *Physica C* **1993**, *213*, 261-265.
[2] X. Chen, P. Dai, D. Feng, T. Xiang, F.-C. Zhang, *Nat. Sci. Rev.* **2014**, *1*, 371-395.
[3] Y. Mizuguchi, Y. Takano, *J. Phys. Soc. Jpn* **2010**, *79*, 102001.
[4] D. C. Johnston, *Advances in Physics* **2010**, *59*, 803-1061.
[5] D. Johrendt, *J. Mater. Chem.* **2011**, *21*, 13726-13736.
[6] G. E. R. Schulze, *Metallphysik*, Akademie-Verlag, Berlin, **1967**.
[7] W. Klemm, *Proc. Chem. Soc., London* **1958**, *329*.
[8] U. Müller, *Anorganische Strukturchemie, Vol. 5. Auflage*, B.G. Teubner Verlag/ GWV Fachverlage GmbH, Wiesbaden, **2006**.
[9] E. Zintl, *Angew. Chem.* **1939**, *52*, 1-6.
[10] C. Daniel, J. O. Besenhard, *Handbook of Battery Materials*, 2 ed., Wiley-VCH Verlag, **2011**.
[11] M. Winter, R. J. Brodd, *Chem. Rev.* **2004**, *104*, 4245-4270.
[12] T. P. Hogan, J. Yang, R. Funahashi, T. M. Tritt, *Thermoelectric Power Generation, Vol. 1044 MRS Proceedings*, Cambridge University Press, **2014**.
[13] D. D. Pollock, *Thermocouples: Theory and Properties*, CRC Press, **1971**.
[14] Z. Li, W. Gao, I. S. Golovin, V. P. Zlomanov, Y. Imai, A. M. Russel, M. Rennhofer, M. Stoica, *Intermetallics Research Progress*, Nova Science Publishers, **2008**.
[15] H. Kamerlingh Onnes, *Comm. Phys. Lab. Univ. Leiden* **1911**, *120b*.
[16] H. Kamerlingh Onnes, *Comm. Phys. Lab. Univ. Leiden* **1911**, *122b*.
[17] H. Kamerlingh Onnes, *Comm. Phys. Lab. Univ. Leiden* **1911**, *124c*.
[18] J. Bardeen, L. N. Cooper, J. R. Schrieffer, *Phys. Rev.* **1957**, *108*, 1175-1204.
[19] J. G. Bednorz, K. A. Müller, *J. Phys.: Condens. Matter* **1986**, *64*, 189-193.
[20] S. N. Putilin, E. V. Antipov, O. Chmaissem, M. Marezio, *Nature* **1993**, *326*, 226-228.
[21] A. Schilling, M. Cantoni, J. D. Guo, H. R. Ott, *Nature* **1993**, *363*, 56-58.
[22] K. M. Shen, J. C. S. Davis, *Materials Today* **2008**, *11*.
[23] J. F. Maguire, J. Yuan, *Physica C* **2009**, *469*, 874-880.
[24] Y. Kamihara, H. Hiramatsu, M. Hirano, R. Kawamura, H. Yanagi, T. Kamiya, H. Hosono, *J. Am. Chem. Soc.* **2006**, *128*, 10012.
[25] T. Watanabe, H. Yanagi, T. Kamiya, Y. Kamihara, H. Hiramatsu, M. Hirano, H. Hosono, *Inorg. Chem.* **2007**, *46*, 7719-7721.
[26] Y. Kamihara, T. Watanabe, M. Hirano, H. Hosono, *J. Am. Chem. Soc* **2008**, *130*, 3296-3297.
[27] M. Rotter, M. Tegel, D. Johrendt, *Phys. Rev. Lett.* **2008**, *101*, 107006.
[28] R. G. Dickinson, J. B. Friauf, *J. Am. Chem. Soc.* **1924**, *46*, 2457-2463.
[29] F.-C. Hsu, J.-Y. Luo, K.-W. Yeh, T.-K. Chen, T.-W. Huang, P. M. Wu, Y.-C. Lee, Y.-L. Huang, Y.-Y. Chu, D.-C. Yan, M.-K. Wu, *Proc. Natl. Acad. Sci. U S A* **2008**, *105*, 14262-14264.
[30] B. C. Sales, A. S. Sefat, M. A. McGuire, R. Y. Jin, D. Mandrus, Y. Mozharivskyj, *Phys. Rev. B* **2009**, *79*, 094521.
[31] O. I. Bodak, E. I. Gladyshevskii, P. I. Kripyakevich, *J. Struct. Chem.* **1970**, *11*, 283-288.
[32] J. H. Tapp, Z. Tang, B. Lv, K. Sasmal, B. Lorenz, P. C. W. Chu, A. M. Guloy, *Phys. Rev. B* **2008**, *78*, 060505.
[33] V. Johnson, W. Jeitschko, *J. Solid State Chem.* **1974**, *11*, 161-166.
[34] R. Zhi-An, L. Wei, Y. Jie, Y. Wei, S. X. Li, Z. Cai, C. G. Can, D. X. Li, S. L. Ling, Z. Fang, Z. Z. Xian, *Chinese Phys. Lett.* **2008**, *25*, 2215.
[35] G. Wu, Y. L. Xie, H. Chen, M. Zhong, R. H. Liu, B. C. Shi, Q. J. Li, X. F. Wang, T. Wu, Y. J. Yan, J. J. Ying, X. H. Chen, *J. Phys.: Condens. Matter* **2009**, *21*, 142203.
[36] M. Rotter, M. Pangerl, M. Tegel, D. Johrendt, *Angew. Chem. Int. Ed.* **2008**, *47*, 7949-7952.
[37] X. Zhu, F. Han, G. Mu, B. Zeng, P. Cheng, B. Shen, H.-H. Wen, *Phys. Rev. B* **2009**, *79*, 220512.
[38] P. M. Shirage, K. Kihou, C.-H. Lee, H. Kito, H. Eisaki, A. Iyo, *J. Am. Chem. Soc* **2011**, *133*, 9630-9633.
[39] C. Löhnert, T. Strürzer, M. Tegel, R. Frankovsky, G. Friederichs, D. Johrendt, *Angew. Chem. Int. Ed.* **2011**, *50*, 9195 –9199.
[40] M. Nohara, S. Kakiya, K. Kudo, Y. Nishikubo, K. Oku, E. Nishibori, H. Sawa, T. Yamamoto, T. Nozaka, *J. Phys. Soc. Jpn* **2011**, *80*, 093704.
[41] F. Ronning, T. Klimczuk, E. D. Bauer, H. Volz, J. D. Thompson, *J. Phys.: Cond. Matt* **2008**, *20*, 322201.

[42] T. Mine, H. Yanagi, T. Kamiya, Y. Kamihara, M. Hirano, H. Hosono, *Solid State Commn.* **2008**, *147*, 111.
[43] F. Ronning, E. D. Bauer, T. Park, S.-H. Baek, H. Sakai, J. D. Thompson, *Phys. Rev. B.* **2009**, *79*, 134507.
[44] F. Ronning, N. Kurita, E. D. Bauer, B. L. Scott, T. Park, T. Klimczuk, R. Movshovich, J. D. Thompson, *J.Phys.: Condens. Matter* **2008**, *20*, 342202.
[45] C. D. Yang, H. C. Hsu, W. Y. Tseng, H. C. Chen, H. C. Ku, M. N. Ou, Y. Y. Chen, Y. Y. Hsu, *J. Phys.: Conf. Ser.* **2011**, *273*, 012089.
[46] R. J. Cava, H. Takagi, H. W. Zandbergen, J. J. Krajewski, W. F. Peck Jr, T. Siegrist, B. Batlogg, R. B. van Dover, R. J. Felder, K. Mizuhashi, J. O. Lee, H. Eisaki, S. Uchida, *Nature* **1994**, *367*, 252-253.
[47] R. J. Cava, H. W. Zandbergen, B. Batlogg, H. Eisaki, H. Takagi, J. J. Krajewski, W. F. Peck Jr, E. M. Gyorgy, S. Uchida, *Nature* **1994**, *327*, 245-247.
[48] T. Siegrist, H. W. Zandbergen, R. J. Cava, J. J. Krajewski, W. F. Peck Jr, *Nature* **1994**, *367*, 254-256.
[49] D. Kasinathan, A. Ormeci, K. Koch, U. Burkhardt, W. Schnelle, A. Leithe-Jasper, H. Rosner, *New Journal of Physics* **2009**, *11*, 025023.
[50] **G. F. Chen**, **W. Z. Hu**, **J. L. Luo**, **N. L. Wang**, *Phys. Rev. Lett.* **2009**, *102*, 227004.
[51] Y. Su, P. Link, A. Schneidewind, T. Wolf, P. Adelmann, Y. Xiao, M. Meven, R. Mittal, M. Rotter, D. Johrendt, T. Brückel, M. Löwenhaupt, *Phys. Rev. B.* **2009**, *79*, 064504.
[52] K. Cho, M. A. Tanatar, N. Spyrison, H. Kim, Y. Song, P. Dai, C. L. Zhang, R. Prozorov, *Phys. Rev. B* **2012**, *86*, 020508(R).
[53] S. R. Saha, N. P. Butch, T. Drye, J. Magill, S. Ziemak, K. Kirshenbaum, P. Y. Zavalij, J. W. Lynn, J. Paglione, *Phys. Rev. B* **2012**, *85*, 024525.
[54] H. D. Wang, C. H. Dong, Z. J. Li, Q. H. Mao, S. S. Zhu, C. M. Feng, H. Q. Yuan, M. H. Fang, *EPL* **2011**, *93*, 47004.
[55] T. P. Ying, X. L. Chen, S. F. Jin, T. T. Zhou, X. F. Lai, H. Zhang, W. Y. Wang, *Sci. Rep.* **2012**, *2*, 426.
[56] C.-H. Lee, A. Iyo, H. Eisaki, H. Kito, M. T. Fernandez-Diaz, T. Ito, K. Kihou, H. Matsuhata, M. Braden, K. Yamada, *J. Phys. Soc. Jpn.* **2008**, *77*, 083704.
[57] Y. Mizuguchi, Y. Hara, K. Deguchi, S. Tsuda, T. Yamaguchi, K. Takeda, H. Kotegawa, H. Tou, Y. Takano, *Supercond. Sci. Technol.* **2010**, *23*, 054013.
[58] K. Kuroki, H. Usui, S. Onari, R. Arita, H. Aoki, *Phys. Rev. B* **2009**, *79*, 224511.
[59] S. Nandi, M. G. Kim, A. Kreyssig, R. M. Fernandes, D. K. Pratt, A. Thaler, N. Ni, S. L. Bud'ko, P. C. Canfield, J. Schmalian, R. J. McQueeney, A. I. Goldman, *Phys. Rev. Lett.* **2010**, *104*, 057006.
[60] S. A. J. Kimber, A. Kreyssig, Y. Z. Zhang, H. O. Jeschke, R. Valenti, F. Yokaichiya, E. Colombier, J.-Q. Yan, T. C. Hansen, T. Chatterji, R. J. McQueeney, P. C. Canfield, A. I. Goldman, D. N. Argyriou, *NATURE MATERIALS* **2009**, *8*, 471-475.
[61] S. Jiang, H. Xing, G. Xuan, C. Wang, Z. Ren, C. Feng, J. Dai, Z. Xu, G. Cao, *J. Phys.: Condens. Matter* **2009**, *21*, 382203.
[62] H. Ding, P. Richard, K. Nakayama, K. Sugawara, T. Arankane, Y. Sekiba, A. Takayama, S. Souma, T. Sato, T. Takahashi, Z. Wang, X. Dai, Z. Fang, G. F. Chen, J. L. Luo, N. L. Wang, *EPL* **2008**, *83*, 47001.
[63] K. O. Klepp, W. Bronger, *Z. Anorg. Allg. Chem.* **1986**, *532*, 23-30.
[64] W. Bronger, H. S. Genin, P. Müller, *Z. Anorg. Allg. Chem.* **1999**, *625*, 274-278.
[65] K. Klepp, H. Boller, *Monatsh. Chem.* **1981**, *112*, 83-89.
[66] K. O. Klepp, W. Sparlinek, *Z. Kristallogr.* **1996**, *211*, 626.
[67] D. Welz, P. Deppe, W. Schaefer, H. Sabrowsky, M. Rosenberg, *J. Phys. Chem. Solids* **1989**, *50*, 297-308.
[68] W. Bronger, U. Ruschewitz, P. Müller, *J. Alloys Compds.* **1995**, *218*, 22-27.
[69] W. Bronger, U. Ruschewitz, *J. Alloys Compds.* **1993**, *198*, 177-179.
[70] W. Bronger, U. Ruschewitz, P. Müller, *J. Alloys Compds.* **1992**, *187*, 95-103.
[71] P. Müller, W. Bronger, *Z. Naturforsch.* **1979**, *34 b*, 1264-1266.
[72] P. Müller, B. W., *Z. Naturforsch.* **1981**, *36 b*, 646-648.
[73] A. V. Hoffmann, *Masterthesis*, Uppsala University **2010**.
[74] D. Hirai, F. von Rohr, R. J. Cava, *Phys. Rev. B* **2012**, *86*, 100505(R).
[75] M. Rotter, C. Hieke, D. Johrendt, *Phys. Rev. B* **2010**, *82*, 014513.

[76] N. Ni, S. Nandi, A. Kreyssig, A. I. Goldman, E. D. Mun, S. L. Bud'ko, P. C. Canfield, *Phys. Rev. B* **2008**, *78*, 014523.
[77] N. Ni, J. M. Allred, B. C. Chan, R. J. Cava, *Proc Natl Acad Sci U S A* **2011**, *108*, E1019.
[78] M. Nohara, S. Kakiya, K. Kudo, Y. Oshiro, S. Araki, C. Kobayashi, K. Oku, E. Nishibori, H. Sawa, *Solid State Comm* **2012**, *152*, 635.

2. Experimental Section

2.1. General Experimental Methods

All manipulations were performed in an argon filled glove box (MBraun, MB20 G, H_2O and O_2 levels < 0.1 ppm) to prevent oxidation of the alkaline earth elements. Different thermal treatment methods were used for classical solid-state reactions. Heating processes were performed either in an arc melting system, a resistance-, an induction- or a muffle- furnace. Starting sample mass was 0.4 g - 0.6 g. Pellets were made inside the glove box with a hydraulic press (Specac® Atlas 15 tons manual press) using steel press matrices ($\varnothing_{in} = 6, 13$ mm). Pellets were pressed for 5 - 10 minutes at 5 tons.

2.1.1. Elements used for Synthesis

The compounds investigated in this work were either synthesized using pure elements or pre-melted alloys. The elements used are listed in Table 2.1 including the manufactures and the degree of purity.

Table 2.1 Starting chemicals, source, shape and purity (atomic %).

Element	**Manufacture**	**Shape**	**Purity* / %**
Calcium	Alfa Aesar	ingots	99.5
Strontium	Alfa Aesar	pieces	99.5
Iron	Alfa Aesar	granules	99.98
	ChemPur	powder	99.9
Rhodium	Alfa Aesar	shots	99.9+
Cobalt	Alfa Aesar	ingots	99.9
Nickel	Alfa Aesar	wire	99.9+
	Alfa Aesar	powder	99.9+
Silicon	Alfa Aesar	pieces	99.999
Germanium	Alfa Aesar	pieces	99.999
Phosphorous$_{red}$	Alfa Aesar	powder	99.98
Arsenic	ChemPur	pieces	99.999

* Manufacture Specification

2.1.2. Reaction Container

The solid state reactions in this work were performed in different reaction containers depending on the elements and heat sources that were used.

Transition metal containers of niobium or tantalum were used for high temperature syntheses in induction and resistance furnaces. Nb and Ta have high melting temperatures (T_m = 2750 K and 3290 K, respectively) and therefore reactions between the sample material and the reaction containers are not expected. The ampoules were prepared in the laboratory from Nb/Ta tubes ($\varnothing_{ext}$ = 10 mm, $width_{wall}$ = 0.5 mm) and sheets (width = 0.5 mm). The tubes were cut into 3 - 5 cm long pieces, from the sheets caps were stamped out. The prepared ampoules and caps were cleaned prior to use by placing them in a beaker with diluted HCl in the ultrasonic bath for 20 minutes, the procedure was repeated with deionized water twice. The ampoules and caps were then dried in a drying oven (Binder Series ED) at 393 K. Figure 2.1a shows two ampoules, one is closed with a cap on both sides for use in an induction furnace (bottom); the other is closed by squeezing the top together and then welded for use in the resistance furnace (top). The welding processes were performed with an arc furnace inside a glove box.

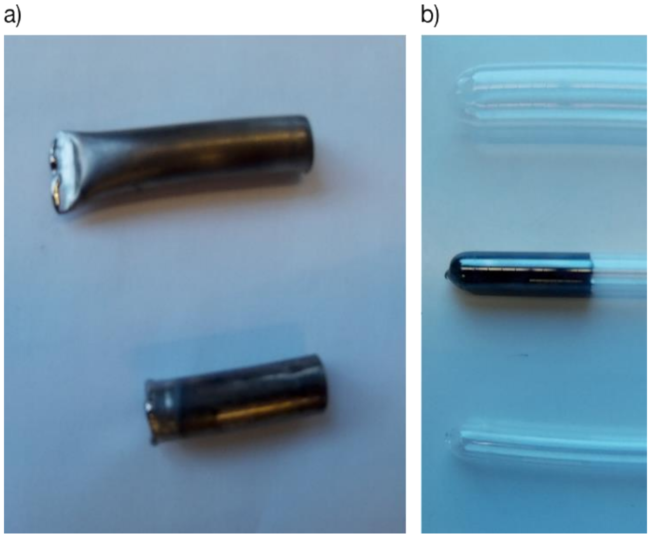

Figure 2.1 Photographs of the different reaction containers used in this work: a) Nb/Ta ampoules closed by caps on one side (top) or on both sides (bottom); b) silica glass tubes of different diameter (top, bottom) and a graphitized example (middle).

Silica glass tubes were used for reactions in muffle furnaces. The tubes ($\varnothing_{in}$ = 10, 18 mm) were closed on one side using a H_2/O_2 burner for the molding process and cleaned in a KOH bath, afterwards they were washed with deionized water and dried at 393 K. A photograph of different silica glass tubes is shown in Figure 2.1b.

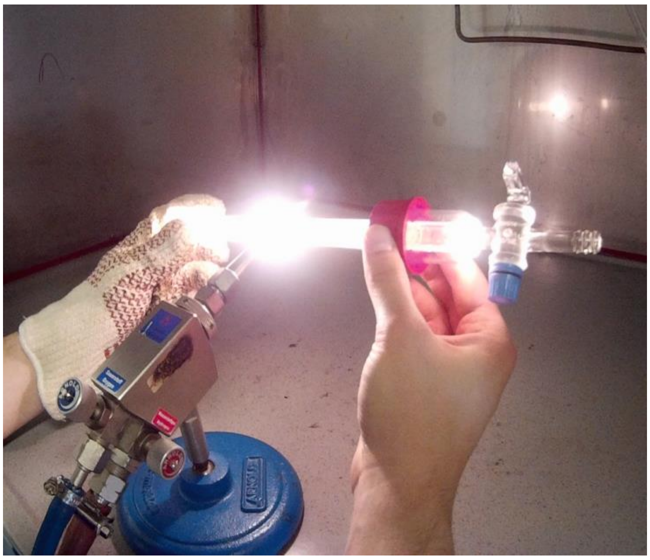

Figure 2.2 Photograph of a silica glass tube attached to a quick fit molded inside a H_2/O_2 burner flame.

In some cases the silica glass tubes were graphitized to prevent reactions of the elements with the tube (Figure 2.1b, middle). The graphitization process was performed by filling 2 - 3 drops of acetone into cleaned tubes and heating them outside at low temperature in the flame of a H_2/O_2 burner while rotating them. To ensure a thick enough layer of graphite the step was repeated 2 - 3 times. Afterwards the tubes were washed carefully with deionized water to prevent damage to the graphite layer and then dried again at 393 K overnight. The filled ampoules were attached to a quick fit inside of a glove box keeping the argon atmosphere, the closing process was performed outside of the glove box (see Figure 2.2). The silica glass tubes were first evacuated - flushed with argon three times, the tubes were finally closed under partial vacuum. In case of extra precaution a smaller silica glass tube or Nb/Ta tube was placed in a larger silica glass tube filled with some rock wool at the bottom.

2.1.3. Arc melting Furnace

The arc melting system (Mini Arc Melting System, MAM-1, Johanna Otto GmbH), used for the preparation of Nb/Ta ampoules and for ternary intermetallic compounds, has a water cooled copper sample holder as anode and a tungsten rod as cathode. The whole system is placed inside a glove box to ensure a closed system under inert conditions. The setup is shown in Figure 2.3. The arc melting furnace is connected to a current generator placed outside of the glove box.

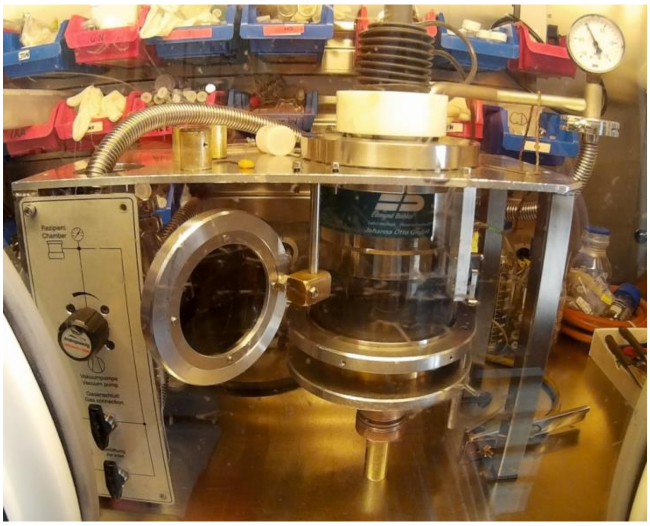

Figure 2.3 Mini Arc Melting Furnace installed inside a glove box.

In a first step the transition metal and the tetrel element were melted with a 1:1 stoichiometry to pre-react. The reguli were either used as binary precursor or for ternary intermetallic compounds the alkaline earth metals were added after the first melting step. In case of the binary mixtures evaporation losses were unlikely due to the high evaporation temperatures of the used elements (T_{ev} = 3023 K, 3200 K, 3968 K, 3003 K, 2628 K, 3103 K for Fe, Co, Rh, Ni, Si and Ge). To counteract the evaporation losses of the lower evaporating alkaline earth metals (T_{ev} = 1757 K, 1655 K for Ca and Sr) they were provided in excess. The reguli were turned over and melted multiple times with increasing current (corresponding to higher temperatures) to ensure homogeneity.

2.1.4. Resistance Furnace

Two types of resistance furnaces were employed. One type was a tubular furnace (Model LOBA, HTM REETZ GmbH with a EUROTHERM Deutschland GmbH 2416 regulator) used in combination with a large silica glass *Schlenk* tube closed with a removable cap. The *Schlenk* tubes were filled with the fully prepared Nb/Ta ampoules in the first step (max. 5 ampoules) and evacuated/flushed with argon multiple times at a *Schlenk*-line. Afterwards the *Schlenk* tubes were set under partial vacuum and placed in the furnace. The temperature is controlled by a type S or type K thermocouple placed in the middle of the furnace. A metal cage is placed above the furnace to ensure safety in case of an explosion of the *Schlenk* tube (see Figure 2.4a). A temperature program was chosen for the individual samples which will be further described later in the chapters.

The second type of resistance furnace is a muffle furnace (Nabertherm, Controller P330/ B180) where the silica glass tubes were thermally treated. The muffle furnaces are positioned inside an extractor hood for security reasons (Figure 2.4b). The heating coils and thermocouples are positioned at the side of the furnace, but since multiple samples were placed in the furnace simultaneously the temperatures may have varied slightly due to the position of the individual reaction containers inside the furnace. The tubes were either placed in a vertical position for loose powder samples or in a lying position if powders were pressed into a pellet. For long–term thermal treatment and annealing the resistance furnace is the best choice.

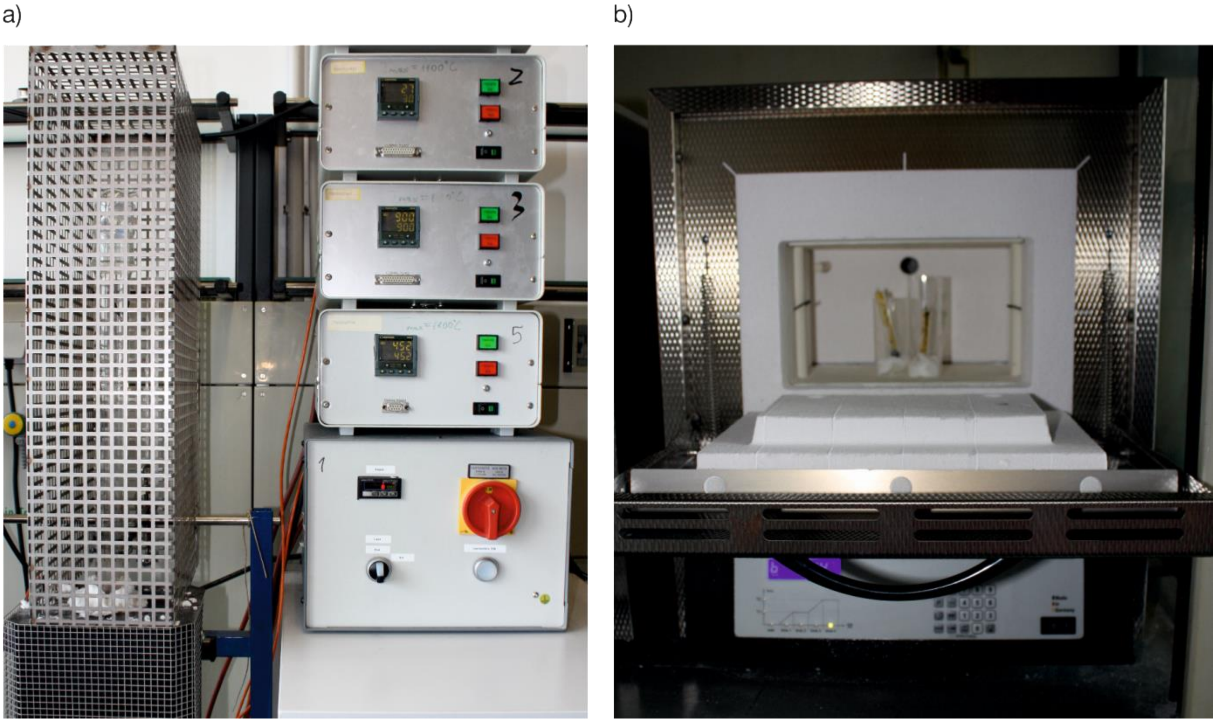

Figure 2.4 Photograph of the resistance furnace: a) tubular furnace with the tubes protected by a metal cage; b) muffle furnace in extractor hood.

2.1.5. Induction Furnace

The induction furnace (self-assembly) contains a sample chamber cooled by water flow (Figure 2.5a) and is partially surrounded by an inductor copper coil connected to the generator (Hüttinger Elektronik, Freiburg, Type TIG 2.5/300; Figure 2.5b) as heating source. The cylindrical Nb/Ta ampoules (Figure 2.1a, bottom) were placed within the chamber and kept under argon flow during thermal treatment. The temperature could be defined using a pyrometer (SENSOR THERM GmbH, measurement range ~ 1173 - 2773 K); measurement is based upon thermal reaction within the ampoules. The technique was used to either do high-temperature syntheses above 1273 K or to anneal compounds at high temperatures to increase the purity and crystallinity of samples prepared with the arc furnace.

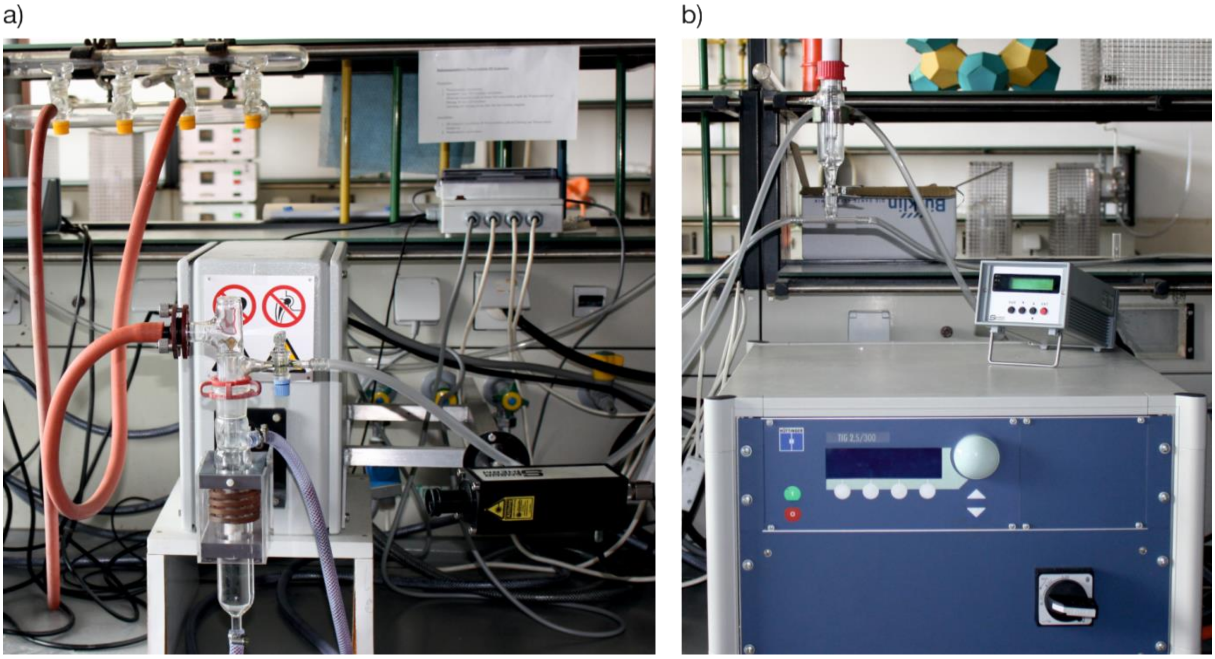

Figure 2.5 Photograph of the induction furnace with the sample chamber and pyrometer a) connected to the generator b) with the pyrometer control unit on top.

2.1.6. Planetary ball mill

A planetary ball mill (FRITSCH Pulverisette6 classic line) was used to ground products, mainly the alloys used as precursors, to fine powders to increase the reactivity. Milling took place in a WC (wolfram carbide) holder ⌀ = 12 mm with 6 WC balls ⌀ = 10 mm. The standard program for the milling was 200 rpm in reverse mode for 1 h.

2.2. Analytical Methods

2.2.1. Powder X-ray diffraction

All precursors and samples were checked for purity and compositions via powder X-ray diffraction analysis. Three different types of diffractometer were used depending on sample composition and measurement temperature. A Stoe *Stadi P* diffractometer (Fa. Stoe, Darmstadt) with a Ge(111) monochromatized Cu-$K_{\alpha 1}$ radiation ($\lambda = 1.54056$ Å) coupled to an imaging plate position sensitive detector (IP-PSD) and later coupled to a Mythen 1K detector for short measurement times (shorter than 1 hour) or a linear position sensitive detector (L-PSD), later coupled to a Mythen 1K detector, for long measurement times. A Stoe *Stadi P* diffractometer (Fa. Stoe, Darmstadt) with a Ge(111) monochromatized Mo-$K_{\alpha 1}$ radiation ($\lambda = 0.7093$ Å) coupled to a Mythen 1K detector was used to measure samples containing high amount of Fe. The wavelength of $K_{\alpha 1}$ radiation for Cu and Fe is close (1.54056 Å and 1.93597 Å, respectively).[1] Fe absorbs therefore some of the Cu-radiation and the noise-to-signal ratio for Fe phases is poor. Mo-radiation gives better signal-to-noise ratios for Fe phases.

Samples were either measured in transmission geometry using a flatbed sample holder or in Debye-Scherrer geometry for capillaries. The samples were ground prior to the measurements to ensure homogeneous distribution and even sizes of the crystallites of the phases. The powders were fixed between two pieces of Scotch® Magic Tape™ (810, 3M) which was placed in the flat bed sample holder or filled into a Mark capillary (Fa. Hilgenberg, $\varnothing_{in} = 0.3$ mm, wall thickness = 0.01 mm) which was sealed with wax. Precise measurements used for Rietveld refinement were performed for 4 - 30 h and corrected for zero shift and angle deviations of the equipment using an external Si standard. Short measurements were performed between 5 - 90° 2θ angles while long measurements for compounds with partial elemental substitution had a range of 5 - 110° 2θ. The effects of substitutions are often more noticeable at higher angles leading to splitting or merging of reflections. The *Stoe* software package WinXPOW[2] was used to evaluate the powder patterns. First all patterns were checked for known phases with data from Powder Diffraction File (PDF-2, included in WinXPOW),[3] from Inorganic

Crystal Structure Databank (ICSD)[4] and Pearson's Crystal Data.[5] The measured reflections belonging to new compounds were indexed with WinXPOW[2] and the lattice parameters where calculated from least-square fits. The reflection patterns were also compared to reflection profiles calculated from crystal structure parameters obtained by single crystal X-ray diffraction measurements.

Phase pure samples or samples that contained only one additional known phase were measured for long times (4 - 30 h) with the L-PSD or Mythen 1K detector to obtain good signal-to-noise ratios for Rietveld refinement. Si standard was measured for 15 minutes before or after the measurement to correct the data for instrument based errors using WinXPOW.[2] The step size for the measurements was below 0.1° 2θ and an exposure time of at least 5 seconds per step was used. Rietveld refinement of the structures was done with FullProf Suite.[6] The observed reflections are fitted with a least-square method and variables for a free refinement are the cell parameters, the atomic positions, thermal displacement and occupation parameters for atoms as well as background and profile fitting parameters. Quality of the refinement is demonstrated in low R_p-, R_{wp}-, R_{exp}-, Goodness-of-fit and R_{Bragg}-values. The thermal displacement parameters for powder Rietveld refinement have been isotropically refined.

A *Huber G670* with Co-$K_{\alpha1}$ radiation (λ = 1.788965 Å, Ge(111) monochromator, Si as external standard) with an Imaging-Plate-Guinier diffractometer was used to measure samples in a temperature range of 10 - 300 K. The samples were placed between two layers of tape and measured on an oscillating flat sample. The measurements were performed in 10 K intervals. Each measurement had a total run-time of 30 minutes, a step size of 0.05 ° in a 2θ range of 5 - 100 °. The measurements and refinements were provided by M.Sc F. Hummels of the Johrendt-Group at the LMU München.

The data was pre-processed with HConvertor[7] and Rietveld refinements were done using the TOPAS package[8] employing the March-Dollase[9] function and the Le-Bail[10] approach.

2.2.2. Single Crystal X-ray diffraction

Single crystal X-ray diffraction measurements were performed on two types of diffractometers. An *Xcalibur3* (Oxford diffractions) diffractometer with graphite monochromatized Mo-K_α (λ = 0.71071 Å, power: 40 mA ; 50 kV) radiation, coupled to a charge coupled device (CCD) area detector and equipped with a N_2 flow cooling unit (Cryostat Cryojet controller, Oxford Cryosystems) was used for air sensitive crystals and measurements at temperatures below 300 K. Air stable crystals could also be measured on a Stoe *IPDS*-2T diffractometer with graphite monochromatized Mo-K_α (λ = 0.71071 Å power: 40 mA / 50 kV) radiation and an image plate detector in some cases.

The crystals were picked under a microscope either inside a glove box in case of air sensitive compounds or outside. The crystals were fixed on top of a glass filament with nail polish. The glass filaments were attached to a brass rod with wax. Crystals were tested for quality and cell parameters with a standardized measuring program of 5 minutes (Oxford diffractometer) or 30 minutes (Stoe *IPDS*-2T diffractometer). Measurements were performed for 20 - 30 h depending on the scattering ability of the crystals. Commonly measurement parameters on the Oxford diffractometer were 4 ω runs and 1 φ run with a detector distance of 50 mm and measure times of 30 - 50 seconds per frame, parameters on the Stoe diffractometer were 2 Ω runs with a detector distance of 100 mm and 60 - 120 seconds per frame. In some cases the detector distance was decreased to 80 mm when measurements were done on the Stoe diffractometer.

The unit cell determination and data reduction were performed with the provided manufacture programs *CrysAlis Red* (Oxford diffractions)[11] and *X-Area* (Stoe),[12] the raw data were corrected for background, polarization and Lorentz factor. For crystal data collected on the Oxford device an empirical absorption correction was applied,[11] for crystal data collected on the Stoe device and in some cases on the Oxford device a numerical absorption correction was employed.[12-14] The determination of the crystal structures was done with the *SHELXTL*[15] package for all compounds. The space group was first determined using the *XPREP*[16] subroutine, then the starting atomic positions of the structure were solved with direct methods (*SHELXS-97*)[17] and subsequently refined with the full matrix least-square on F_O^2 method (*SHELXL-97*).[18] The atomic positions were all refined with anisotropic displacement parameters and the occupancy parameters for each atomic position was checked in separate least-square cycles to check the correct composition of the compounds. For the final description of the crystal structure the coordinates of the atomic positions were chosen according to the suggestion by the program *Structure Tidy*[19] to obtain standardized crystal descriptions.

The obtained crystallographic information files (CIF) were loaded into the *Diamond*[20] program to generate graphical presentations, pictures were finalized with *CorelDRAW*.[21]

2.2.3. Scanning Electron Microscopy (SEM) and Energy Dispersive X-ray Spectroscopy (EDX)

Single crystals were tested for elemental composition using a *JEOL SEM 5900 LV* Scanning Electron Microscope equipped with an Oxford Instruments *INCA* energy dispersive X-ray microanalysis system and a Si(Li) detector. SEM method is used to get a topological presentation of the crystals while the EDX unit measures the energy of the X-ray emitted from the sample which is characteristic for each element.

The operation voltage was set to 20 kV for all measurements (120 seconds collection time). After the X-ray diffraction analysis the crystals where transferred onto a carbon pad which was glued on top of an aluminum sample holder. Crystals were tested qualitatively to verify the absence of elements heavier than sodium in addition to the starting elements, the composition of each crystal was determined by semi-quantitatively analysis (without the use of an internal standard).

2.2.4. Magnetic Measurements

Magnetic measurements were performed with a *MPMS XL 5* (Quantum Design) superconducting quantum interference device (SQUID) magnetometer with liquid Helium cooling. A temperature range of 1.8 - 400 K and magnetic fields up to 50000 Oe (5 Tesla) are measurable. All measurements were performed in the reciprocal sample option (RSO).

Samples were filled in gelatin capsules, the capsule weight and the sample weight were determined for each sample. Commonly the capsules had a mass of 36 - 40 mg and sample mass was at least 20 mg. The closed capsules were fixed in the center of a plastic straw (Quantum Design) which was then attached to the transportation device of the SQUID. The sample position in the SQUID was adjusted with the automatic DC center scan technique. All samples were tested as default for superconductivity in the range of 1.8 - 30 K using the zero-field cooled/field cooled (zfc-fc) method with an applied field (H) of 15 Oe and a step size of 2 K in sweep mode. Magnetization data between 0 - 50000 Oe were collected at room-temperature with a step size of 1000 Oe (in the range of 0 - 10000 Oe) and 10000 Oe (in the range of 10000 - 50000 Oe) were measured to determine the magnetic behavior of the sample.

Phase pure samples that showed no ferromagnetic impurity were investigated more throughout. Susceptibility between 1.8 K and 300 K was measured with a step size of 2 - 4 K for different fields (H). Samples that displayed superconducting behavior were measured with a more precise zfc-fc program using settle mode and a step size of 0.1 K.

Relevant raw data parameters were temperature, field (H), long moment (emu) and long scan standard deviation collected using the *MultiVu*[22] program (Quantum Design), raw data handling was done in *Origin*.[23] The long moment measured is defined as

$$m_{\text{measured}} = m_{\text{sample}} + m_{\text{capsule}} \qquad \text{(Equation 2.1).}$$

To correct the measured moment for the capsule moment a selection of capsules from the batch have been measured and a mean value of $3.927 * 10^{-7}$ emu/g*Oe was determined. The magnetization (M) for a sample is calculated from field dependent measurements (constant temperature) using following equation:

$$M = m_{\text{sample}} / p \qquad \text{(Equation 2.2)}$$

where the variable p can either be the sample mass (g), the sample volume V or the sample molar mass (m). The chosen parameter defines the magnetization in respect to the sample mass (M_g), the sample volume (M_V) or the sample molarity (M_m). Susceptibility values are calculated from measurements spanning a temperature range at a constant field. To get the susceptibility values (χ) the magnetization *M* is divided by the field

$$\chi = M/\mathrm{H} \qquad \text{(Equation 2.3).}$$

The susceptibility is either defined as mass, volume or molar susceptibility (χ_g, χ_V, χ_m) depending which magnetization was chosen. Normally the volume or molar magnetization and susceptibility are given for samples. χ_m is corrected for the diamagnetic susceptibility of the atoms using the *Pascal*'s constants.[24] However if the sample is not phase pure and the content of impurity cannot be established, results are given in relation to the sample mass (M_g, χ_g).

Zero field cooled-field cooled (zfc-fc) measurements are a specific test for superconductivity where the sample is cooled to the lowest possible temperature without an applied field. A small field is given to ensure critical field (H_c) presence and a temperature dependent measurement is performed up to a certain temperature (zfc) and then down again (fc). With this method it is possible to detect T_c's above 1.8 K and the splitting of the magnetic moment into the Shielding and the *Meissner* contribution. To determine the volume of superconducting phase in a sample the susceptibility is given as

$$\chi_V = \left(M_p/\mathrm{H}\right)^* 4\pi \qquad \text{(Equation 2.4).}$$

Ideal diamagnetism has a $4\pi\chi_V$ value of −1. The Shielding fraction (zfc branch) should be close to the ideal diamagnetic value for a superconducting compound, the *Meissner* fraction (fc branch) is dependent on the applied field. The difference between the two fractions gives an estimation of the volume of superconductivity. The critical fields (H_c) for a superconducting phase are determined by performing isothermal magnetization measurements at low temperatures and plotting the volume magnetization M_V.

2.2.5. Conductivity Measurements

Heat capacity and resistivity measurements were done with a *PPMS* (Quantum Design). The powder (400 mg) was hot-pressed (640 MPa at 953 K for 10 minutes and at 973 K for 2 hours) into a pellet before the measurements. The press used was a uniaxial hot-press (Weber-Pressen), the press matrix (INCOLEL-Ni-based superalloy covered with boron nitride) had an inner diameter of 10 mm. The press matrix was filled under air, then evacuated and subsequently flooded with Ar (500 mbar). The hot-pressing was done by inductive heating the powder while applying uniaxial pressure.

The temperature dependence of the electrical resistivity was measurement by the standard four contact method. The magnetic field was applied perpendicular to the current direction, measurements at 1 mA and 10 mA were performed. The specific heat data were obtained by a relaxation technique, measurement at zero field and at H = 30000 Oe were performed.

The measurements were provided by Dr. V. Grinenko of the Hühne group at the IFW Dresden.

2.3. Computational Methods

The linear muffin-tin orbital (LMTO) method with an atomic sphere approximation (ASA) using the tight-binding (TB) program TB-LMTO-ASA[25] was used to calculate the electronic structure of compounds. The radii of the muffin-tin spheres were determined after *Jepsen* and *Andersen*.[26] The ASA radii of the spheres are changed to model the full potential; the volume of the resulting spheres is equal to the unit cell volume to achieve space filling. In some cases empty spheres (ES) are inserted to minimize overlapping (< 16 %) and to achieve space filling. The exchange-correlation terms are calculated within the local density approximation (LDA) and are parameterized according to *von Barth* and *Hedin*.[27]

The valence functions used for the basis set for the short-ranged atom-centered TB-LMTOs were: s-d valence functions for *Ae* atoms (*Ae* = Ca, Sr), s-d valence functions for *T* atoms (*T* = Co, Fe, Rh, Ni) and s,p valence functions for *E* atoms (*E* = Si, P, As). The *Ae*-p orbitals and empty spheres were treated by the down-folding technique.[28] All *k*-space integrations are performed by the tetrahedron method.[29] The Fermi level was set at zero eV.

Analyses of the chemical bonding between atoms are based on the total and partial Density of States (DOS, pDOS) representations including the integrated

Density of States (iDOS). The energy contribution of all electronic states for selected bonds are calculated by the Crystal Orbital Hamiltonian Population (COHP),[30] the integrated COHP (iCOHP) gives information about the contribution of the covalent part of a particular interaction to the total energy of the crystal. Band structures including fat bands for band character analyses were plotted for the individual atomic orbitals. The atomic orbital character is represented as a function of band width in the fat band analyses. The *Gnuplot*[31] program was used for the graphical representation of DOS, COHP and band plots.

Topological analyses of the electron density distribution were done by calculating the Electron Localization Function (ELF)[32-35] of the compounds. The ELF representations, in the range of 0 - 1, show a slice of the crystal structure which allows for the location of bonds and lone pairs. The isosurfaces with a certain ELF value (η) are included in the pictures of the ELF representation. Graphical representations were done using the *XCrySDen*[36] and *VESTA*[37] programs.

2.4. References

[1] F. Raaz, *Röntgenkristallographie: Einführung in die Grundlagen*, De Gruyter, Berlin, **1975**.
[2] Stoe, *WinXPOW*, 2.08ed., Stoe & Cie GmbH, Darmstadt, **2003**.
[3] Stoe, *PDF-2 Powder Diffraction File*, Stoe & Cie GmBH, Darmstadt, **2010**.
[4] *FindIt ICSD Database*, 1.7.0ed., FIZ Karlsruhe, Germany, **2010**.
[5] P. Villars, K. Cenzual, *Pearson's Crystal Data: Crystal Structure Database for Inorganic Compounds (on CD-ROM)*, 1.0ed., ASM International, Materials Park, Ohio, Usa, **2007/8**.
[6] J. Rodriguez-Carvajal, *FullProf. 2k*, 5.4ed., Laboratoire Leon Brillouin (CEA-CNRS), France, **2014**.
[7] M. Tegel, *HConvert*, 0.8ed., Ludwig Maximilians Universität, München, **2011**.
[8] A. Coelho, *TOPAS-Academic*, 4.1ed., Coelho Software, Brisbane, **2007**.
[9] W. A. Dollase, *J. Appl. Cryst.* **1986**, *19*, 267-272.
[10] A. Le Bail, A. Jouanneaux, *J. Appl. Cryst.* **1997**, *30*, 265-271.
[11] Scale3, *ABSPACK CrysAlis RED*, Version 1.171.33.34ded., Oxford Diffraction Ltd., Poland Sp. z o.o., **2009**.
[12] *X-Area*, 1.56ed., Stoe & Cie GmbH, Darmstadt, **2011**.
[13] *X-RED32*, Version 1.48ed., Stoe & Cie GmbH, Darmstadt, **2008**.
[14] *X-SHAPE*, 2.11ed., STOE & Cie GmbH, Darmstadt (Germany), **2008**.
[15] G. M. Sheldrick, *Acta Cryst.* **2008**, *A 64*, 112.
[16] *XPREP*, Bruker Analytical X-ray Instruments Inc., University of Goettingen, **2000**.
[17] G. M. Sheldrick, *SCHELXS-97*, University of Goettingen, **1997**.
[18] G. M. Sheldrick, *SCHELXL-97*, University of Goettingen, **1997**.
[19] L. M. Gelato, E. Parthe, *J. Appl. Crystallogr.* **1987**, *20*, 139-143.
[20] K. Brandenburg, *Diamond Version 3.2g,*, Crystal Impact GbR, Bonn, Germany, **2011**.
[21] *CorelDRAW Essentials*, 4ed., Corel Coporation, Ottawa, Canada, **2009**.
[22] *MPMS MultiVu*, 1.56ed., Quantum Design Inc., San Diego, USA, **2007**.
[23] *Origin*, 8ed., OriginLab Corporation, Northampton, Massachusetts, **2007/10**.
[24] G. A. Bain, J. F. Berry, *Journal of Chemical Education* **2008**, *85*, 532-536.
[25] M. v. Schilfgaarde, O. Jepsen, O. K. Andersen, A. Burkhardt, T. A. Paxton, G. Krier, *The Stuttgart Tight-Binding LMTO-ASA program*, 4.7ed., Max Planck Institut für Festkörperforschung, Stuttgart, **1997**.
[26] O. Jepsen, O. K. Andersen, *Z. Phys. B.* **1995**, *97*, 35.
[27] U. v. Barth, L. Hedin, *J. Phys. Chem. C* **1972**, *5*, 1629-1642.
[28] O. K. Andersen, O. Jepsen, *Phys. Rev. Lett.* **1984**, *53*, 2571-2574.
[29] P. E. Blöchl, O. Jepsen, O. K. Andersen, *Phys. Rev. B* **1994**, *49*, 16223-16233.
[30] R. Dronskowski, P. E. Blochl, *J. Phys. Chem.* **1993**, *97*, 8617-8624.
[31] T. Williams, C. Kelley, *Gnuplot*, 4.4ed., **2011**.
[32] A. D. Becke, K. E. Edgecombe, *J. Chem. Phys.* **1990**, *92*, 5397.
[33] T. F. Fässler, *Chem. Soc. Rev.* **2003**, *32*, 80-86.
[34] T. F. Fässler, A. Savin, *Chem. Unserer Zeit* **1997**, *31*, 110-120.
[35] A. Savin, R. Nesper, S. Wengert, T. F. Fässler, *Angew. Chem. Int. Ed. Engl.* **1997**, *36*, 1808-1832.
[36] A. Kokalj, *Comp. Mater. Sci* **2003**, *28*, 155-168.
[37] K. Momma, F. Izumi, *VESTA: a three-dimensional visualization system for electronic and structural analysis*, J. Appl. Cryst., 41, 653-658, **2008**.

3. New Intermetallic Compounds with ThCr$_2$Si$_2$ Type Structure

3.1. Introduction

One of the most common structures for intermetallic compounds is the tetragonal ThCr$_2$Si$_2$ structure type (Figure 3.1).[1] They often have the composition (RE/A/Ae)T_2E_2 (RE = rare earth elements, A = alkaline metals, Ae = alkaline earth metals; T = transition metals and E = elements of the 13th - 15th group).[2, 3]

The structure type contains layers of edge-sharing tetrahedra stacked along the *c*-axis with one layer of cations in between. The centers of the TE_4 tetrahedra are occupied by transition metals forming a square net in the *ab*-plane which is alternatingly capped by the E elements. The tetrahedral substructure is described as polyanionic [$TE_{4/4}$] layers. The three adjustable parameters in this structure type are the lattice parameters *a, c* and the only free atomic coordinate *z* for the E atom.

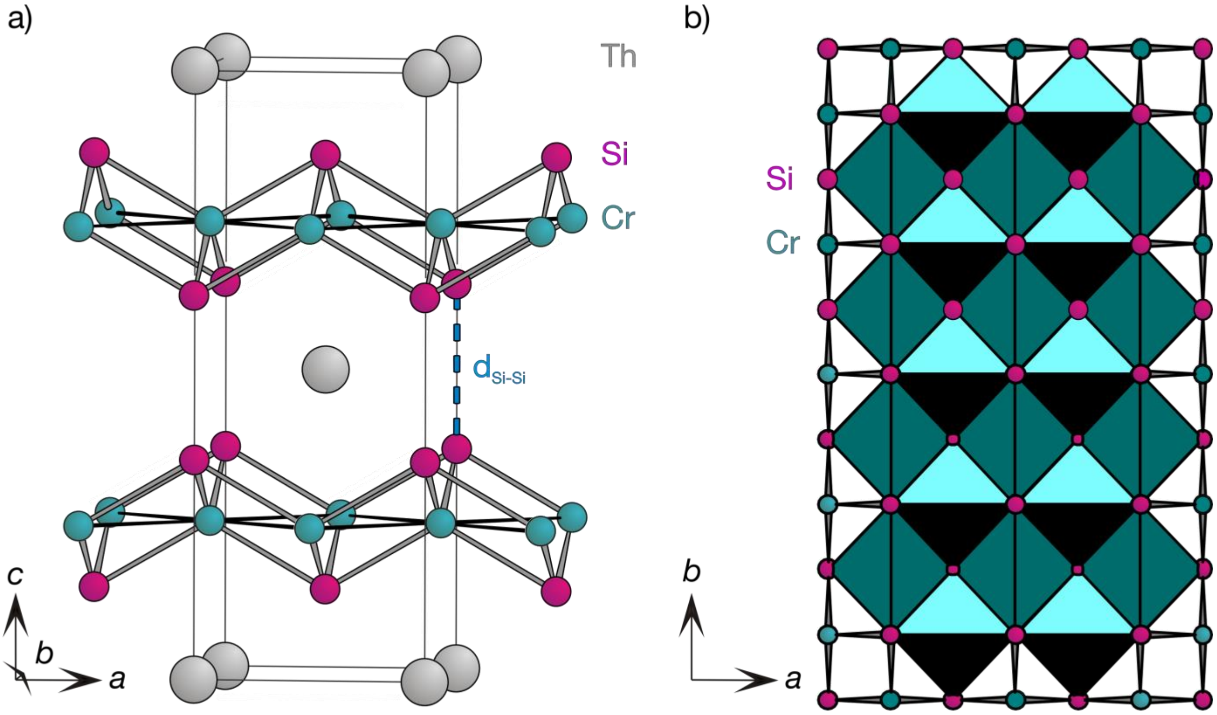

Figure 3.1 Model of the ThCr$_2$Si$_2$ structure type: Th as light gray, Cr as turquois and Si as magenta spheres. a) unit cell including the bonds, the interlayer distance $d_{E\text{–}E}$ (blue dashed line) is marked; b) polyanionic [$TE_{4/4}$] layer along [001] including tetrahedra.

The structure type shows a high degree of structural freedom depending on the elemental composition of the compounds. A collapsed (cT) and an uncollapsed (ucT) modification is possible, multiple members for each have been reported.[4, 5]

The collapsed modification, alternatively also described as $CeAl_2Ga_2$ structure type,[6] is mainly observed for compounds with short *c*-axes and large z_E atomic parameters. The distance between the polyanionic layers ($d_{E–E}$) is short with a covalent *E*–*E* bonding interaction. This modification therefore has a three-dimensional $[TE_{4/4}]$ network. The stronger interlayer interaction influence the structural parameters and the electronic structure as is discussed for $BaMn_2P_2$ as an example and for RET_2Ge_2 (*RE* = rare earth metals, *T* = transition metals).[4, 5] The tetrahedral layers are described as 3D $[T_2E_2]^{2-}$ polyanions with Ae^{2+} as counter cations. Some examples related to the systems investigated in this work are $AeCo_2Si_2$ (*Ae* = Ca, Sr), $CaCo_2P_2$, $CaNi_2E_2$ (*E* = P, As) and $LiCu_2P_2$.[7-12]

The uncollapsed modification, on the contrary, usually has a longer *c*-axis, it is also described as the $BaZn_2P_2$ structure type.[13] This results in a large distance between the polyanionic two-dimensional $[TE_{4/4}]$ layers. The interactions within the layers are strengthened compared to the cT modification resulting in comparably shorter $d_{T–T}$ and $d_{T–E}$ values. The tetrahedral layers are described as 2D $[T_2E_2]^{2-}$ polyanions with Ae^{2+} as counter cations. The trend observed is that the compounds with cations of larger size tend to crystallize in the uncollapsed modification. Examples are most of AeT_2P_2 and AeT_2As_2 compounds (*Ae* = Sr, Ba; *T* = Mn - Ni).[9]

The physical and magnetic properties within the family are versatile and rich. In 1994 superconductivity in RET_2B_2C (*RE* = Y, Ho - Lu; *T* = Pd, Ni) compounds was reported by the group of Cava.[14-17] It was the next family of high-temperature superconductors after the cuprates. The compounds crystallize also in the *I*4/*mmm* space group like the iron-pnictide superconductors. They contain the same tetrahedral layers, only that they are connected by C atoms along the *c*-direction in RET_2B_2C compounds.

Many ternary compounds with $ThCr_2Si_2$ structure type do not exhibit superconductivity but superconducting behavior can be induced upon partial substitution. The iron-pnictides, for example, often show a structural transition from a tetragonal modification (*I*4/*mmm*) at high temperatures to an orthorhombic modification (*Fmmm*) at low temperatures. The structural transition is accompanied by a magnetic transition from a paramagnetic state to an antiferromagnetic state with spin-density-wave in the orthorhombic modification.[18] The transitions can be suppressed with charge doping, chemical pressure and physical pressure.

In 2008 superconductivity in iron-pnictide compounds was reported in the system $Ba_{1-x}K_xFe_2As_2$ with a maximum critical temperature (T_c) of 38 K ($x = 0.4$).[19, 20] The superconducting iron-pnictide and related compounds with $ThCr_2Si_2$ structure type are often referred to as 122 compounds nowadays; the class is called the 122 family.

The search for new parent compounds and new superconducting members of the 122 family led to the reinvestigation of known compounds with this structure type. Magnetic and conductivity measurements were made and the possible induction of superconductivity by partial substitution was investigated. It was found that a number of ternary $AeNi_2E_2$ (Ae = Sr, Ba; E = Ge, P, As) compounds exhibit superconductivity at low temperatures even without substitution.[21-25] The ternary compounds $SrNi_2P_2$[26] and $BaNi_2As_2$[21] are special cases within the group because they show a phase transition to distorted modifications below 320 K and 130 K, respectively. $SrNi_2P_2$ transforms from the tetragonal structure (*I*4/*mmm*) at high temperatures (HT-phase) to an orthorhombic *Immm* modification at low temperatures (LT-phase).[26] The phase transition is not accompanied by a magnetic transition but the LT-phase accommodates superconductivity at 1.4 K.[25] $BaNi_2As_2$ is the only $AeNi_2E_2$ (Ae = Ca, Sr, Ba; E = Ge, P, As) compound for which a magnetic phase transition has been reported.[21] The transformation from paramagnetic to antiferromagnetic behavior co-commits with the structure transformation from the tetragonal *I*4/*mmm* modification at high temperatures (HT-phase) to a triclinic $P\bar{1}$ modification (LT-phase) with distortion in the planar Ni–Ni network.[27] Superconductivity below 0.7 K is reported for the compound.[21, 28] The critical temperature (T_c) of Ni-based superconductors can be enhanced with partial substitution forming solid solutions.[29] Even though T_c is small compared to the iron-pnictide superconductors they give vital information to the question of origin for superconductivity in type 2 superconductors.

In recent years more focus has been put on the parameter $h_{T\text{–}E}$ of 122 superconductors which describes the height of the E atoms above/below the square T plane within the $[TE_{4/4}]$ layers. It can be calculated by multiplying the difference between the atomic coordinated z for the E and T atoms by the length of the c-axis:

$$h_{T\text{–}E} = (z_E - z_T) * c_{\text{lattice}} \qquad \text{(Equation 3.1).}$$

The atomic coordinate for the T element z_T has a fixed value of ¼ in the *I*4/*mmm* space group. Comparison of the critical temperature (onset) of different superconductors has shown that $h_{T\text{–}E}$ values close to 1.38 Å are favorable for high T_c.[30]

The ternary and pseudo-ternary compounds described in this chapter all crystallize in the $ThCr_2Si_2$ structure type (space group *I*4/*mmm* No.139, with $Z = 2$).

3.2. $SrNi_2(E_{1-x}Ge_x)_2$ with E = P, As

The ternary compounds $SrNi_2P_2$, $SrNi_2As_2$ and $SrNi_2Ge_2$ all crystallize in the uncollapsed $ThCr_2Si_2$ type structure and exhibit superconducting behavior below 1.4 K. The idea for the investigation of the solid solutions was to analyze the structural and physical variations upon partial substitution.

3.2.1. Syntheses of the compounds and alloys used as precursors

Different synthesis methods were tried for the quaternary samples $SrNi_2(P_{1-x}Ge_x)_2$. Preparing samples from the pure elements in different x-ratios lead to products containing ternary or pseudo-ternary phases and multiple binary side-phases. To prevent the formation of binary side-products the syntheses of the quaternary $SrNi_2(E_{1-x}Ge_x)_2$ samples were subsequently tried by using the ternary parent compounds as starting materials.

The pseudo-ternary compounds were prepared in a multi-step synthesis. First the ternary compounds $SrNi_2E_2$ (E = Ge, P and As) were synthesized. The syntheses methods were first tried according to the literature, where phase-pure products for $SrNi_2P_2$ and $SrNi_2As_2$ were obtained, while impurities were found in the product of

$SrNi_2Ge_2$.[10, 26, 31] First, the methods described in the literature were tried and modifications were made if necessary in order to obtain phase-pure products.

$SrNi_2P_2$

In the literature synthesis of phase pure $SrNi_2P_2$ is reported by using the starting composition 1Sr: 2Ni: 2P (elements placed in a corundum crucible sealed in a silica glass ampoule), heat-treated at 1173 K (15 h), annealed at 1373 K (20 h) and washing the product with diluted acetic acid.[26]

For $SrNi_2P_2$ Sr pieces, Ni powder and P_{red} powder were used as starting elements. Samples prepared from the stoichiometric composition 1:2:2 (0.131 g Sr: 0.176 g Ni: 0.095 g P) always contained the ternary phases $SrNi_5P_3$ in addition to $SrNi_2P_2$. Therefore, based on numerous experiments, a nominal starting composition of 1.05:2:2 (0.134 g Sr: 0.171 g Ni: 0.095 g P) with a total weight of 0.4 g was chosen. A small excess of Sr was provided, since some losses of Sr during the synthesis were observed in previous samples. The mixture was pelletized and sealed in a silica glass tube. Thermal treatment took place in a muffle furnace. For the first heating cycle a slow ramping program was chosen (see Figure 3.2a). The tubes were opened in a glove box, the sample was ground, additional amount of P_{red} powder (0.04 g) was added and a pellet was made. The extra P was added to counteract the formation of $SrNi_5P_3$. Annealing was done in silica glass tubes in a muffle furnace (Figure 3.2b).

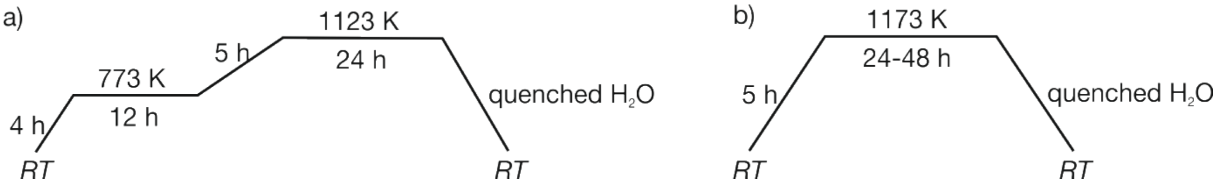

Figure 3.2 Temperature program for $SrNi_2P_2$ precursor: a) first heating cycle; b) second heating cycle.

Powder X-ray analyses revealed that the precursors synthesized with added P contained $SrNi_2P_2$, no $SrNi_5P_3$ was observed (see Figure A1, Appendix). In addition reflections with low intensity were observed in the powder pattern which could not be assigned to any known phase. It was possible to obtain phase pure $SrNi_2P_2$ by washing the reaction product with diluted HCl. However, washed powders did not react with the $SrNi_2Ge_2$ precursor in the subsequent reactions to form quaternary products, in contrast to precursors containing some impurities.

$SrNi_2Ge_2$

In the literature the nominal starting composition was chosen as 1Sr: 2Ni: 2Ge and the elements were melted in an arc furnace, the resulting powder pattern did not show phase purity.[31]

Synthesis of the ternary precursor was done from the elements melted in an arc furnace. Starting composition was chosen as 1.05:2:2 (Sr:Ni:Ge). First Ni (0.116 g, wire) and Ge (0.143 g, pieces) were pre-melted, then Sr (0.092 g) was added in small excess. The reguli were melted three consecutive times to ensure homogeneity. The products were ground and checked for purity with powder X-ray diffraction analyses. The powder patterns showed reflections belonging to $SrNi_2Ge_2$ and in addition reflections of $SrNi_3Ge_2$ was observed. In order to prevent the formation of $SrNi_3Ge_2$ excess of Sr (7 at. %) and Ge (3 at. %) had to be added. The total mass of the sample was 0.414 g (0.113 g Sr, 0.128 g Ni and 0.173 g Ge). The resulting product was checked for phase purity, the powder pattern contained only reflections belonging to $SrNi_2Ge_2$ (see Figure A2, Appendix).

The precursor was ground to fine powder using a planetary ball mill to increase reactivity. The compound is air and moisture stable.

$SrNi_2As_2$

In the literature the nominal starting composition 1.1Sr: 2Ni: 2As was chosen (elements placed in a corundum crucible), heat-treated at 1273 K (12 h), annealed at 1373 K (48 h) and the product was washed in hot diluted HCl.[10]

The ternary precursor was synthesized from Sr pieces, Ni powder and As pieces, the starting composition was chosen as 1:2:2 (0.172 g Sr: 0.229 g Ni: 0.292 g As) with a total mass of 0.693 g. Thermal treatment took place in graphitized silica glass tubes heated in a muffle furnace (temperature program given in Figure 3.4a). The product was checked for purity with powder X-ray diffraction analysis, the reflections in the powder pattern belong to $SrNi_2As_2$ (see Figure A3, Appendix).

Pseudo-ternary $SrNi_2(P_{1-x}Ge_x)_2$ compounds

The solid solution $SrNi_2(P_{1-x}Ge_x)_2$ can be synthesized in different ways, the final products however, show different results depending on the method chosen. Using the binary precursor NiP and NiGe and adding Sr leads to the formation of $SrNi_2(P_{1-x}Ge_x)_2$. In addition $SrNi_5P_3$ and/or binary $Ni_{2.74}Ge_2$ could be identified in the powder patterns (example see Figure A4, Appendix). By using ternary precursors products with less impurities and better sized crystals could be synthesized.

The ternary alloys were mixed with the nominal ratio of $x = 0.15$, 0.25, 0.40, 0.55, 0.70, 0.85 and the powders were pelletized, the masses used for the different compositions are listed Table 3.1.

Table 3.1 Masses of the $SrNi_2E_2$ (E = P, Ge) precursors used for the $SrNi_2(P_{1-x}Ge_x)_2$ samples described in this chapter.

Nominal composition, x	**$SrNi_2P_2$ precursor / g**	**$SrNi_2P_2$ prec. / mol × 10^3**	**$SrNi_2Ge_2$ precursor / g**	**$SrNi_2Ge_2$ prec. / mol × 10^3**
0.15	0.325	1.22	0.075	0.21
0.25	0.300	1.12	0.131	0.37
0.40	0.286	1.07	0.250	0.71
0.55	0.219	0.82	0.350	1.00
0.70	0.130	0.49	0.400	1.14
0.85	0.063	0.24	0.500	1.43

The pellets (⌀ = 6 mm) were sealed in silica glass tubes and thermally treated in a muffle furnace. After heating the ampoules were opened in a glove box, the pellets were ground and re-pelletized. Annealing took place in silica glass tubes and a muffle furnace (temperature program for all cycles given in Figure 3.3).

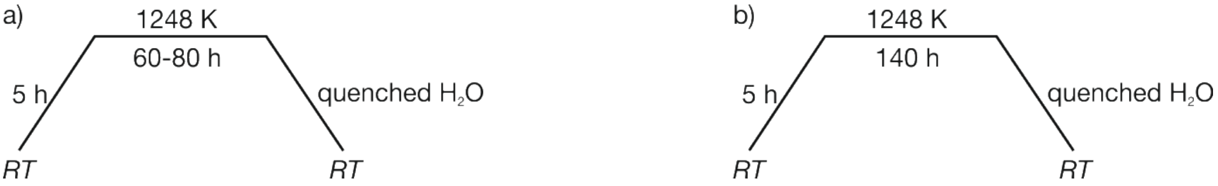

Figure 3.3 Temperature program for $SrNi_2(P_{1-x}Ge_x)_2$ samples: a) first heating cycle; b) second heating cycle.

The products were ground and powder X-ray diffractograms were recorded. Measurements were done at room-temperature using a rotating flat sample holder and Si as external standard in the 2θ range of 5 - 110 °.

Phase pure products of $SrNi_2(P_{1-x}Ge_x)_2$ solid solutions could be synthesized by using the $SrNi_2P_2$ precursors that contained no $SrNi_5P_3$ as secondary phase. 4 - 6 h measurements were done to get powder data for Rietveld refinement for all compositions. Single crystals of good quality were measured at room-temperature on a *Xcalibur3* (Oxford) diffractometer or a *Stoe IPDS*-2T diffractometer. Single crystal measurements at 130 K were also performed for several crystals. Refinement parameters for the powder and single crystal measurements are given in Table 3.3 - Table 3.6. The compounds are stable against air and moisture. The crystals are plate-shaped and have metallic luster.

Results of EDX measurements on the single crystals are given in Table A1 (Appendix). The semi-quantitative EDX analysis reveals the elemental compositions (values given in at. %) which, within standard deviations, correspond to the compositions determined from single crystal data refinement.

Pseudo-ternary $SrNi_2(As_{1-x}Ge_x)_2$ *compounds*

The ternary precursors were mixed with the nominal ratio of $x = 0.1$, 0.3, 0.5, 0.7, 0.9 (different masses used listed in Table 3.2) and the powders were pelletized.

Table 3.2 Masses of the $SrNi_2E_2$ (E = As, Ge) precursors used for the $SrNi_2(As_{1-x}Ge_x)_2$ samples described in this chapter.

Nominal composition, x	**$SrNi_2As_2$ precursor / g**	**$SrNi_2As_2$ prec. / mol × 10^3**	**$SrNi_2Ge_2$ precursor / g**	**$SrNi_2Ge_2$ prec. / mol × 10^3**
0.1	0.406	1.14	0.044	0.13
0.3	0.281	0.79	0.119	0.34
0.5	0.151	0.43	0.149	0.43
0.7	0.091	0.26	0.209	0.60
0.9	0.031	0.09	0.269	0.77

The pellets were sealed in silica glass tubes (graphitized) and thermally treated in a muffle furnace. After heating the tubes were opened in a glove box, the pellets were ground and re-pelletized. Annealing took place in silica glass tubes which were placed and heated in a muffle furnace (temperature program given in Figure 3.4b).

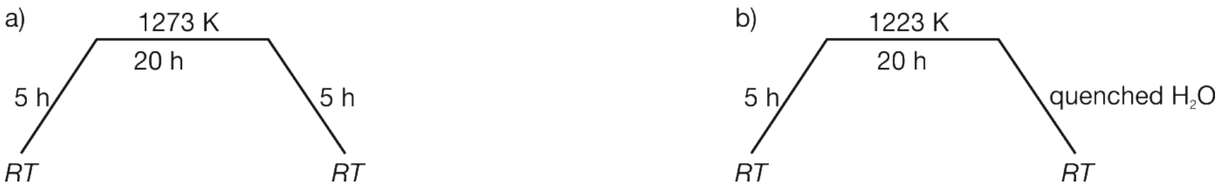

Figure 3.4 Temperature program for: a) SrNi$_2$As$_2$ precursor; b) SrNi$_2$(As$_{1-x}$Ge$_x$)$_2$ samples.

The products were ground and powder X-ray diffraction patterns were collected. The reflections could all be indexed with the theoretical patterns of known ternary and binary phases, suggesting no formation of mixed SrNi$_2$(As$_{1-x}$Ge$_x$)$_2$ solid solution. Single crystals were tested on a *Xcalibur3* (Oxford) diffractometer. The cell parameters of the tested crystals were determined and compared to those of SrNi$_2$As$_2$ and SrNi$_2$Ge$_2$. The differences between cell parameters of the measured crystals and that of the ternary compounds were all within the standard deviation. EDX measurements on crystals also showed no sign of partial substitution, the crystals contained either As or Ge.

3.2.2. Results and discussion

In this subchapter the results obtained from the samples SrNi$_2$(E_{1-x}Ge$_x$)$_2$ (E = P, As) will be presented. First the solid solution SrNi$_2$(P$_{1-x}$Ge$_x$)$_2$ is described and discussed. The topic of the next subchapter (3.2.3) are the information gathered from samples with the nominal compositions SrNi$_2$(As$_{1-x}$Ge$_x$)$_2$.

3.2.2.1. Crystal Structure of SrNi$_2$(P$_{1-x}$Ge$_x$)$_2$ solid solution

The ternary superconducting compounds SrNi$_2$P$_2$ (T_c = 1.4 K, *Immm* space group)[25] and SrNi$_2$Ge$_2$ (T_c = 0.87 K, *I*4/*mmm space group*)[24] are the ternary side phase of the solid solution. SrNi$_2$P$_2$ exists in two modifications: below 320 K it has orthorhombic structure (LT modification in *Immm* space group),[26] the high temperature (HT) modification crystallizes in *I*4/*mmm* space group. In the LT modification SrNi$_2$P$_2$ has covalent P–P bonds ($d_{P1–P1}$ = 2.45 Å) between every third P atom in the *ab*-plane while the distance is elongated to 3.28 Å ($d_{P2–P2}$) for non-bonding P atoms. As a result the [NiP] layers show buckling in the *ab*-plane. The lattice parameter for the orthorhombic “partially collapsed” SrNi$_2$P$_2$ phase are

$a = 3.95$ Å, $b = 11.85$ Å and $c = 10.43$ Å.[26] It has been determined that the LT orthorhombic modification is responsible for superconductivity below 1.4 K.[25]

The HT modification crystallizes in the uncollapsed version with $a = b = 3.95$ Å, $c = 10.68$ Å and $d_{P–P} = 3.12$ Å ($T_{measurement} = 373$ K). The separation of the [NiP] layers at high temperatures (> 320 K) leads to an expansion of the unit cell and the *c*-parameter jumps up to 10.68 Å. $SrNi_2Ge_2$ crystallizes in the tetragonal *I*4/*mmm* space group in the uncollapsed modification. The tetrahedral [NiGe] layers are separated along [001] and no covalent Ge–Ge bonds are present ($d_{Ge–Ge} = 3.12$ Å). Structure models for the HT (*I*4/*mmm*) and LT (*Immm*) modifications of $SrNi_2P_2$ are presented in Figure 3.5 (HT = a, LT = b).

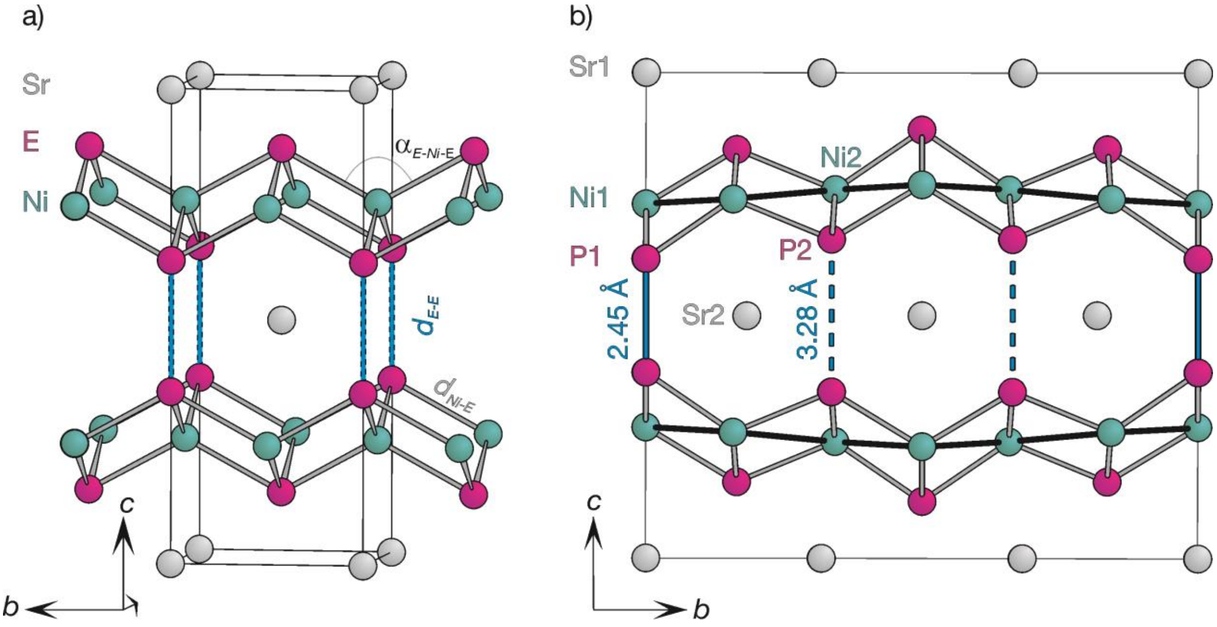

Figure 3.5 Structure model of a) $SrNi_2E_2$ (*E* = Ge, P and As)[23, 26, 31] in ucT *I*4/*mmm* modification (HT $SrNi_2P_2$ above 320 K); b) $SrNi_2P_2$ in “partially collapsed” orthorhombic *Immm* modification (LT). The distance $d_{E–E}$ is 2.83 Å for *E* = Ge, As and 3.12 Å for *E* = P.

Successful substitution of P with Ge could be proven from refinements of powder and single crystal data. Structure details were obtained via single crystal X-ray diffraction measurements for $SrNi_2(P_{1-x}Ge_x)_2$ with $x_{nom} < 0.85$ (no measureable crystals for $x_{nom} = 0.85$ could be isolated) and from Rietveld refinement of powder X-ray diffraction data for all samples. Refinement details are provided in Table 3.3 - Table 3.6 and Table A2 - Table A9 (Appendix) (single crystal and powder refinements). Rietveld refinement plots for the powder patter of all $SrNi_2(P_{1-x}Ge_x)_2$ solid solution are given in Figure A5 - Figure A10 (Appendix).

The solid solution $SrNi_2(P_{1-x}Ge_x)_2$ crystallize in the tetragonal space group *I*4/*mmm* ($Z = 2$) with $ThCr_2Si_2$ type structure at room-temperature. The tetragonal lattice parameters and the structural parameter $z_{P/Ge}$ (atomic *z* coordinate of the P/Ge atoms) as well as the exact composition obtained from single crystal measurements and powder measurements are given in Table 3.7. The experimentally determined composition x_{exp} from powder data and single crystal data deviate slightly for the samples with low Ge-content but are in good agreement for the samples with x_{nom} = 0.4 - 0.70. The nominal composition and the experimentally determined values are in good agreement, a plot of x_{nom} vs x_{exp} obtained from the powder data is shown in Figure 3.6a. Slight variations in the cell parameters can be observed between the powder and single crystal data but are within acceptable range for the different methods (see Table 3.7). The following structural description is mainly based on results of the powder data refinement unless it is explicitly stated otherwise. The refinements for the two P-richest compounds x_{exp} = 0.110(3) and 0.212(3) were done with the TOPAS program,[32, 33] the refinements for the other compositions with the FullProf Suite.[34]

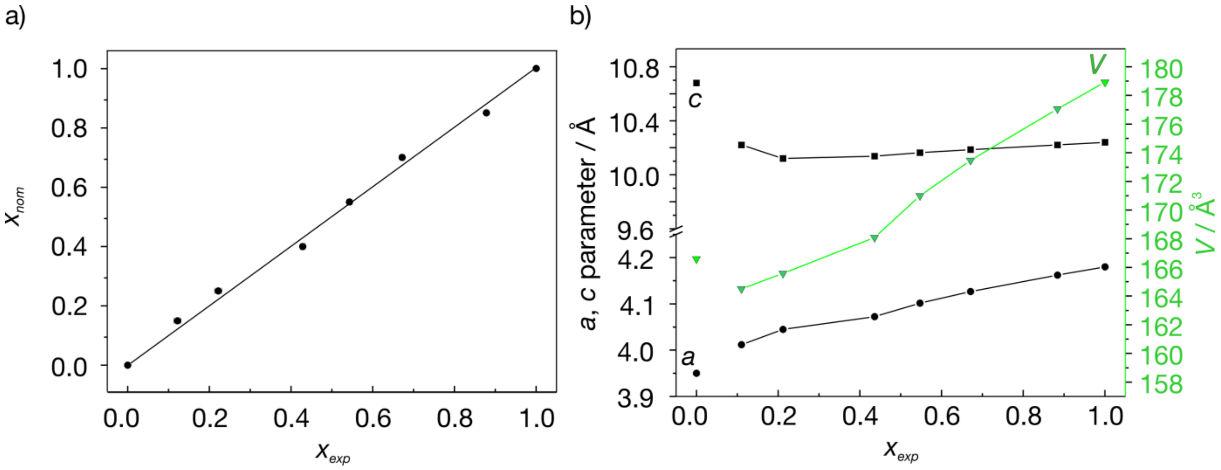

Figure 3.6 Dependence of composition (a) and lattice parameters (b) of mixed $SrNi_2(P_{1-x}Ge_x)_2$ and the ternary compounds (x = 0, 1 taken from literature; lattice parameters for HT $SrNi_2P_2$ *I*4/*mmm*, 373 K measurement).[26, 31] Lines within the diagrams are for visible help. The standard deviation is within the size of the symbols used.

The lattice parameters show clear variation for each $SrNi_2(P_{1-x}Ge_x)_2$ sample (*I*4/*mmm* space group). The lattice parameter *a* increases linearly from 4.0119(1) Å (x_{exp} = 0.110(3)) to 4.1622(2) Å (x_{exp} = 0.884(1)) with increasing amount of Ge-substitution (Figure 3.6b). The c lattice parameter deviates from a Vegard-like linear behavior, it decreases first from 10.220(1) Å (x_{exp} = 0.110(3)) to 10.121(1) Å (x_{exp} = 0.212(3)) and then increases linear up to 10.24 Å ($SrNi_2Ge_2$) with further Ge-substitution. The lattice parameter for the ternary parent phase $SrNi_2P_2$ are for the HT modification ($T_{measurement}$ = 373 K) in the *I*4/*mmm* space group.

The structural phase transition for $SrNi_2P_2$ from HT *I*4/*mmm* to LT *Immm* (at 320 K) is already suppressed with ~11 at. % Ge-substitution (exp. data) at room-temperature and the tetragonal structure is stabilized.

Table 3.3 Crystal data and measurement details for single crystal refinement of $SrNi_2(P_{1-x}Ge_x)_2$ with x_{nom} < 0.4, collected at room-temperature (white column) and at 130 K (gray column).

Empirical formula		**$SrNi_2(P_{0.86(1)}Ge_{0.14(1)})_2$**	
Diffractometer		*Oxford Xcalibur3*	
Space group, *Z*		*I*4/*mmm*	
Formula weight	/ g·mol^{-1}	278.84	
Measurement temperature	/ K	293	130
Unit cell dimensions	/ Å	*a* = 4.012(1) *c* = 10.227(1)	*a* = 4.024(1) *c* = 9.927(1)
	/ Å^3	*V* = 164.6(1)	*V* = 160.7(1)
Absorption coefficient	/ mm^{-1}	30.342	31.288
Crystal size	/ mm	0.09 × 0.05 × 0.01	0.09 × 0.05 × 0.01
Absorption correction		semi-empirical	semi-empirical
Calculated density	/ g·cm^{-3}	5.605	5.761
F(000)		257	258
θ range	/ °	3.99 to 32.68	4.11 to 32.57
Range in *hkl*		± 6,± 6, $-13 \leq l \leq 15$	± 6, ± 6, $-14 \leq l \leq 12$
Reflections collected		1494	1470
Independent reflections		114 (R_{int} = 0.0370)	109 (R_{int} = 0.0348)
Reflections with $I \geq 2\sigma(I)$		95 (R_σ = 0.0157)	102 (R_σ = 0.0143)
Data/Parameters		114/10	109/10
GOF on F^2		1.195	1.138
Final *R* indices [$I \geq 2\sigma(I)$]		R_1 = 0.0246 wR_2 = 0.0603	R_1 = 0.0221 wR_2 = 0.0519
R indices (all data)		R_1 = 0.0352 wR_2 = 0.0660	R_1 = 0.0246 wR_2 = 0.0532
Largest diff. peak and hole	/ e Å^{-3}	2.529 and −1.340	2.309 and −1.132

Table 3.4 Crystal data and measurement details for single crystal refinement of $SrNi_2(P_{1-x}Ge_x)_2$ with $x_{nom} < 0.4$, collected at room-temperature (white column) and at 130 K (gray column).

Empirical formula		**$SrNi_2(P_{0.76(1)}Ge_{0.24(1)})_2$**	
Diffractometer		*Oxford Xcalibur3*	
Space group, *Z*		*I4/mmm*	
Formula weight	/ g·mol^{-1}	287.37	
Measurement temperature	/ K	293	130
Unit cell dimensions	/ Å	*a* = 4.038(1)	*a* = 4.034(1)
		c = 10.109(1)	*c* = 10.026(1)
	/ Å^3	*V* = 164.8(1)	*V* = 163.1(1)
Absorption coefficient	/ mm^{-1}	32.250	32.538
Crystal size	/ mm	0.06 × 0.04 × 0.01	0.06 × 0.04 × 0.01
Absorption correction		semi-empirical	semi-empirical
Calculated density	/ g·cm^{-3}	5.791	5.846
F(000)		265	264
θ range	/ °	4.03 to 32.45	4.07 to 32.48
Range in *hkl*		$-5\leq h \leq 6$, ± 6, $-15\leq l \leq 12$	± 6, ± 6, $-14\leq l \leq 12$
Reflections collected		1514	1492
Independent reflections		113 (R_{int} = 0.0959)	114 (R_{int} = 0.0444)
Reflections with $I \geq 2\sigma(I)$		89 (R_σ = 0.0325)	90 (R_σ = 0.0297)
Data/Parameters		113/10	114/10
GOF on F^2		1.236	1.251
Final *R* indices [$I \geq 2\sigma(I)$]		R_1 = 0.0235	R_1 = 0.0289
		wR_2 = 0.0499	wR_2 = 0.0650
R indices (all data)		R_1 = 0.0378	R_1 = 0.0503
		wR_2 = 0.0548	wR_2 = 0.0717
Largest diff. peak and hole	/ e Å^{-3}	1.841 and −1.359	3.767 and −1.903

Table 3.5 Crystallographic data of the Rietveld refinements for $SrNi_2(P_{1-x}Ge_x)_2$ solid solution (powder X-ray diffraction measurements at room-temperature).

Empirical formula		**$SrNi_2(P_{0.880(3)}Ge_{0.110(3)})_2$**	**$SrNi_2(P_{0.788(3)}Ge_{0.212(3)})_2$**	**$SrNi_2(P_{0.564(2)}Ge_{0.436(2)})_2$**
Diffractometer		Huber G670	Huber G670	STOE Stadi P
Program		TOPAS	TOPAS	FullProf
Unit cell dimensions		*a* = 4.0119(1)	*a* = 4.0448(1)	*a* = 4.0722(1)
	/ Å	*c* = 10.220(1)	*c* = 10.121(1)	*c* = 10.137(1)
	/ Å^3	*V* = 164.50(1)	*V* = 165.58(1)	*V* = 168.09(1)
ρ_{calc}	/ g·cm^{-3}	5.501	5.708	5.992
GOF on F^2		0.815	0.493	1.1
$R_{p,pattern}$		0.014	0.002	0.138
$R_{wp,pattern}$		0.021	0.014	0.113
$R_{exp,pattern}$		0.026	0.028	0.096
R_{Bragg}		1.41	0.76	1.99
Empirical formula		**$SrNi_2(P_{0.453(2)}Ge_{0.547(2)})_2$**	**$SrNi_2(P_{0.329(2)}Ge_{0.671(2)})_2$**	**$SrNi_2(P_{0.116(1)}Ge_{0.884(1)})_2$**
Diffractometer		STOE Stadi P	STOE Stadi P	STOE Stadi P
Program		FullProf	FullProf	FullProf
Unit cell dimensions		*a* = 4.1017(2)	*a* = 4.1267(1)	*a* = 4.1622(2)
	/ Å	*c* = 10.164(1)	*c* = 10.186(1)	*c* = 10.220(1)
	/ Å^3	*V* = 171.00(1)	*V* = 173.46(1)	*V* = 177.06(2)
ρ_{calc}	/ g·cm^{-3}	6.069	6.181	6.378
GOF on F^2		1.8	1.4	1.4
$R_{p,pattern}$		0.205	0.158	0.133
$R_{wp,pattern}$		0.181	0.125	0.119
$R_{exp,pattern}$		0.099	0.091	0.082
R_{Bragg}		3.86	4.34	1.89

Table 3.6 Crystal data and measurement details for single crystal refinement of $SrNi_2(P_{1-x}Ge_x)_2$ with $x_{nom} > 0.4$, collected at room-temperature.

Empirical formula	$\mathbf{SrNi_2(P_{0.56(2)}Ge_{0.44(2)})_2}$	$\mathbf{SrNi_2(P_{0.45(1)}Ge_{0.55(1)})_2}$	$\mathbf{SrNi_2(P_{0.35(1)}Ge_{0.65(1)})_2}$
Diffractometer	*Stoe IPDS*-2T	*Stoe IPDS*-2T	*Stoe IPDS*-2T
Detector distance / mm	80	100	80
Formula weight / g·mol^{-1}	303.23	312.76	321.09
Space group, *Z*	*I4/mmm*, 2	*I4/mmm*, 2	*I4/mmm*, 2
Unit cell dimensions / Å	a = 4.0747(6)	a = 4.0957(6)	a = 4.1183(6)
/ Å	c = 10.145(2)	c = 10.149(2)	c = 10.182(2)
/ Å^3	V = 168.44(5)	V = 170.25(5)	V = 172.69(5)
Absorption coefficient / mm^{-1}	34.708	36.214	37.317
Crystal size / mm	0.05 × 0.04 × 0.01	0.08 × 0.06 × 0.06	0.08 × 0.07 × 0.04
Absorption correction	numerical	numerical	numerical
Calculated density / g·cm^{-3}	5.979	6.101	6.175
F(000)	278	285	292
θ range / °	4.02 to 29.89	4.02 to 29.12	4.0 to 31.74
Range in *hkl*	± 5, ± 5, ± 14	± 5, ± 5, ± 13	± 6, ± 6, ± 14
Reflections collected	1738	1559	1582
Independent reflections	95 (R_{int} = 0.0858)	86 (R_{int} = 0.0405)	114 (R_{int} = 0.0372)
Reflections with $I \geq 2\sigma(I)$	94 (R_σ = 0.0191)	86 (R_σ = 0.0126)	108 (R_σ = 0.0131)
Data/Parameters	95/9	86/9	114/10
GOF on F^2	1.464	1.236	1.150
Final *R* indices [$I \geq 2\sigma(I)$]	R_1 = 0.0378	R_1 = 0.0123	R_1 = 0.0166
	wR_2 = 0.0991	wR_2 = 0.0298	wR_2 = 0.0295
R indices (all data)	R_1 = 0.0383	R_1 = 0.0123	R_1 = 0.0182
	wR_2 = 0.0993	wR_2 = 0.0298	wR_2 = 0.0298
Largest diff. peak and hole / e Å^{-3}	2.594 and −0.905	0.640 and −0.750	0.708 and −1.278

The highest deviation from linearity for the *c* and *V* lattice parameters is observed for the value *c* (10.220(1) Å) in the ~11 at. % Ge-substituted compound. With increasing Ge-content the *c/a* value decreases, due to a faster increase of *a* lattice parameter compared to *c* lattice parameter (see Figure 3.7). The decrease is not linear; a jump between the c/a value for HT $SrNi_2P_2$ ($x = 0$, at 373 K) and that of the compound value $x_{exp} = 0.110(3)$ happens, similar to the trend of the c-values.

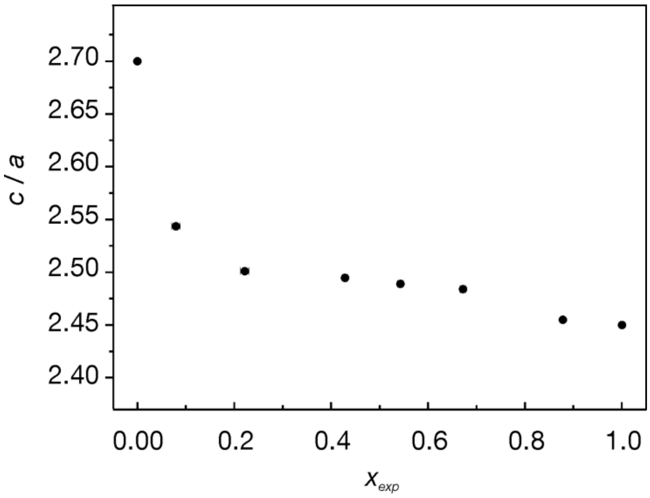

Figure 3.7 c/a ratio vs x_{exp} obtained from powder data refinement (room-temperature data, Table 3.7).

Table 3.7 Cell parameters, atomic coordinate $z_{P/Ge}$ and x values for $SrNi_2(P_{1-x}Ge_x)_2$ (space group $I4/mmm$, $Z = 2$) obtained from powder data (-p) and single crystal data (-sc) at room-temperature. Parameters for the ternary compounds (*) are taken from literature[26, 31] (parameters for the high-temperature $I4/mmm$ modification of $SrNi_2P_2$ measured at 373 K).

x_{nom}	x_{exp}	a / Å	c / Å	V / Å^3	c/a	$z_{P/Ge}$
0.00*	0	3.95	10.68	166.6	2.70	0.354
0.15-p	0.110(3)	4.0119(1)	10.220(1)	164.50(1)	2.547	0.3608(2)
0.15-sc	0.14(1)	4.0119(1)	10.227 (1)	164.61(2)	2.549	0.3596(2)
0.25-p	0.212(3)	4.0448(1)	10.121(1)	165.58(1)	2.502	0.3574(2)
0.25-sc	0.24(1)	4.0377(1)	10.109(2)	164.81(2)	2.504	0.3604(2)
0.40-p	0.436(2)	4.0722(2)	10.137(1)	168.09(1)	2.489	0.3590(2)
0.40-sc	0.44(2)	4.0747(6)	10.145(2)	168.44(5)	2.490	0.3599(3)
0.55-p	0.547(2)	4.1017(2)	10.164(1)	171.00(1)	2.478	0.3592(3)
0.55-sc	0.55(1)	4.0957(6)	10.149(2)	170.25(5)	2.478	0.3597(1)
0.70-p	0.671(2)	4.1267(1)	10.186(1)	173.46(1)	2.468	0.3599(2)
0.70-sc	0.65(1)	4.1183(6)	10.182(2)	172.69(5)	2.472	0.3600(1)
0.85-p	0.884(1)	4.1622(2)	10.220(1)	177.06(2)	2.455	0.3608(2)
1.00*	1	4.18	10.24	178.92	2.45	0.362

In correspondence with the lattice parameter variations due to the substitution, a merging of reflections at high 2θ angles (45 - 110 °) in the powder X-ray patterns is observed (see Figure 3.8).

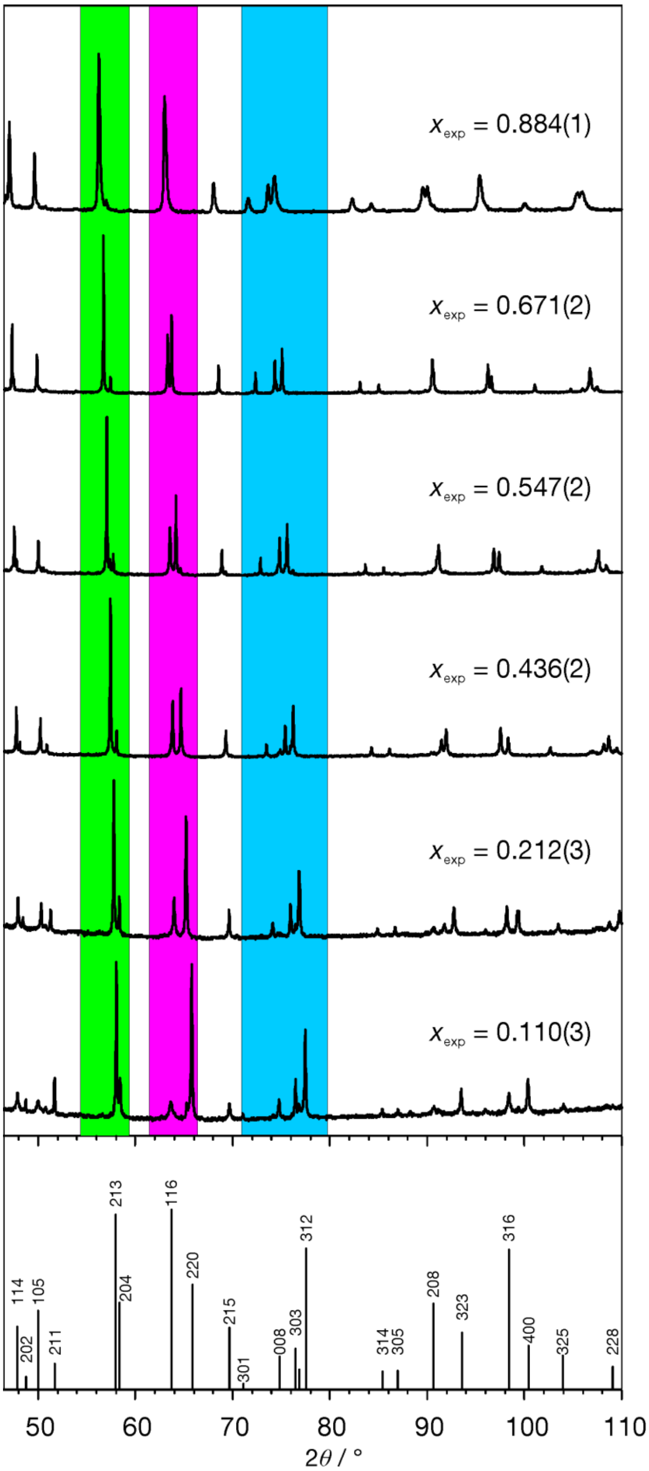

Figure 3.8 Powder X-ray patterns of phase pure samples of SrNi$_2$(P$_{1-x}$Ge$_x$)$_2$ between 45 - 110 ° 2θ, composition x_{exp} determined via Rietveld refinement. The theoretical reflection positions for the compound with x_{exp} = 0.110(3) including their corresponding *hkl* values are shown in the bottom. The highlighted areas show examples of merging reflections.

The green highlighted 2θ range (54 - 59 °, Figure 3.8) shows the reflections for *hkl* [312] and [204]. The reflection corresponding to [213] moves to lower 2θ values with increasing Ge-content. The reflection corresponding to [204] is almost merged with the [213] reflection for x_{exp} = 0.110(3) and x_{exp} = 0.884(1) while it is further separated for x_{exp} = 0.212(3) - 0.671(2). The range of 62 - 66 ° 2θ (highlighted magenta) shows the reflections [116] and [220] *hkl*. The reflections are clearly separated in x_{exp} = 0.110(3) and move closer together with increasing Ge content. For x_{exp} = 0.884(1) the two reflections are merged. The 2 reflections for *hkl* [303] and [312] (highlighted blue) move towards lower 2θ values and move closer together upon Ge-substitution in the solid solution. The observed shifts of the individual reflections result from the variations in the lattice parameters, the different shifting direction (towards higher or lower 2θ value) is due to the anisotropic changes of the *a* and *c* parameter for the different compositions.

The change in atomic coordinate *z* for the P/Ge position ($z_{P/Ge}$), the interatomic distances $d_{Ni–Ni}$, $d_{Ni–P/Ge}$ and $d_{P/Ge–P/Ge}$ as well as the height of the P/Ge atoms (above, below) the square Ni plane ($h_{Ni–P/Ge}$) and the tetrahedral angle α all affects the cell parameters (for a visual representation of the individual parameters within the structure type see Figure 3.9). The dependency of these parameters from x_{exp} is given in Table 3.8 for both single crystal (gray highlighted values) and powder X-ray diffraction measurements. The trends of these parameters obtained from the powder X-ray refinements are visualized in Figure 3.10a (interatomic distances) and Figure 3.10b ($z_{P/Ge}$, $h_{P/Ge}$ and α) for $SrNi_2(P_{1-x}Ge_x)_2$ solid solution. The parameters of the ternary side phase (*I*4/*mmm*, HT modification for $SrNi_2P_2$) are included.

The *z* atomic coordinates for P/Ge in the $SrNi_2(P_{1-x}Ge_x)_2$ compounds (powder data) are very similar for the whole solid solution, fluctuating around 0.360. z_P for $SrNi_2P_2$ is the smallest with 0.354 and z_{Ge} for $SrNi_2Ge_2$ is the largest with 0.362 (see Figure 3.10b). The increase in $z_{P/Ge}$ is almost linear for the solid solution. The only $z_{P/Ge}$ value of 0.3608(2) that deviates from linearity is that for x_{exp} = 0.110(3) and has the same value as the compound with x_{exp} = 0.884(1). The same is observed for the *c* lattice parameters of the two compounds, both having the value 10.220(1) Å.

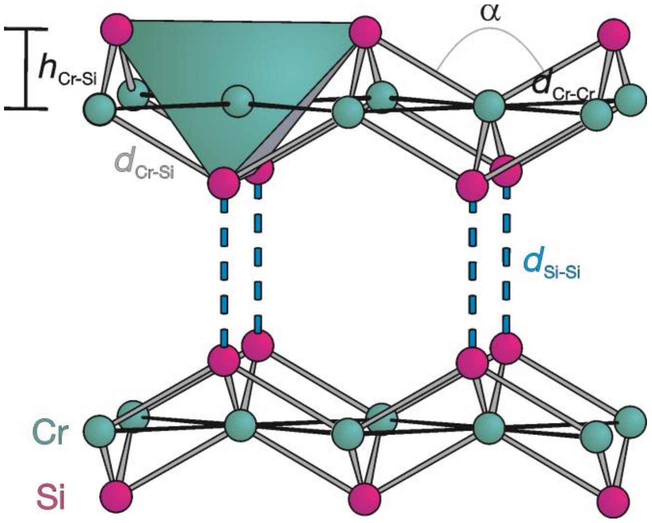

Figure 3.9 Polyanionic substructure model of ThCr$_2$Si$_2$ including all the relevant structural parameters for the phase.

The interatomic distances $d_{Ni–Ni}$ and $d_{Ni–P/Ge}$ show an almost linear increase with higher Ge-substitution (Figure 3.10a). The distance between the Ni atoms in the square *ab*-plane, which are directly coupled to the *a* lattice parameter ($d_{Ni-Ni} = {}^{a}/_{\sqrt{2}}$), increase from 2.837(1) Å to 2.943(1) Å and show Vegard-like behavior upon Ge-substitution. The elongation of $d_{Ni–Ni}$ results in weaker interactions within the Ni plane.

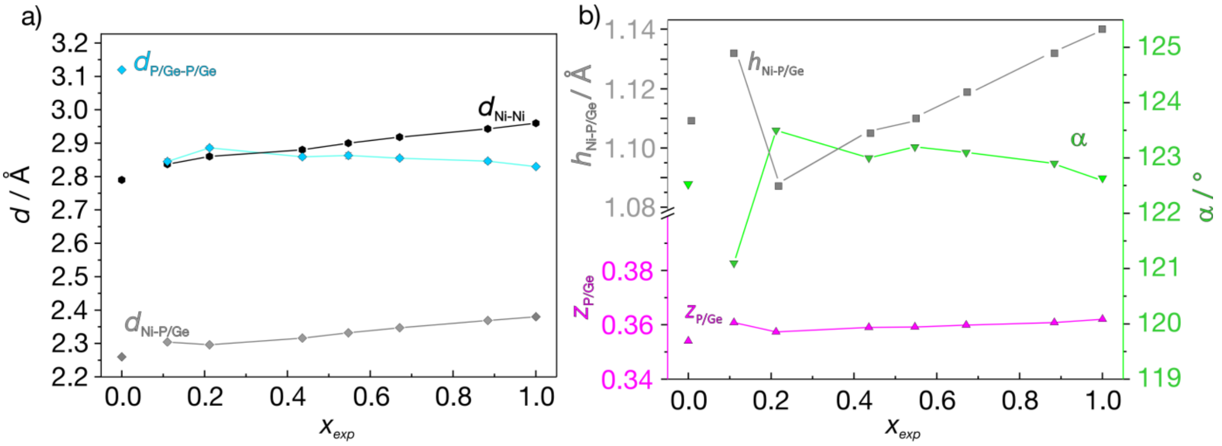

Figure 3.10 Trend of important structural parameter for SrNi$_2$(P$_{1-x}$Ge$_x$)$_2$ and ternary compounds (x = 0, 1 taken from literature).[26, 31] Dependency of a) interatomic distances $d_{Ni–Ni}$ (black symbols) and $d_{Ni–P/Ge}$ (gray symbols) within the tetrahedral layers and $d_{P/Ge–P/Ge}$ (blue symbols) between the layers; b) atomic coordinate $z_{P/Ge}$ (magenta symbols); the height of the P/Ge atoms above the plane of Ni atoms, $h_{Ni-P/Ge}$ (gray symbols), and the tetrahedral angle α (green symbols) from the experimental x values. Lines within the diagrams are for visible help. Standard deviation is smaller than the size of the symbols.

Compared to the covalent Ni–Ni distances in Ni-metal, which have a single bond value of 2.49 Å, $d_{\text{Ni–Ni}}$ in the $SrNi_2(P_{1-x}Ge_x)_2$ solid solution are approximately 0.4 - 0.5 Å longer.[35] Similar values for $d_{\text{Ni–Ni}}$ have been observed for ternary $AeNi_2P_2$[9, 22, 26] and $AeNi_2Ge_2$[29, 36, 37] (*Ae* = Ca, Sr, Ba) compounds. The interatomic distance $d_{\text{Ni–P/Ge}}$ within the $[Ni(P/Ge)_{4/4}]$ layers shows deviation from linearity, like it is observed for all parameters connected to the *c* lattice value. $d_{\text{Ni–P/Ge}}$ ranges from 2.296(1) Å to 2.369(1) Å in the $SrNi_2(P_{1-x}Ge_x)_2$ solid solution. The value of $d_{\text{Ni–P/Ge}}$ for $SrNi_2(P_{1-x}Ge_x)_2$ with $x_{\text{exp}} = 0.110(3)$ is slightly higher (2.304(1) Å) than that of $x = 0$ and $x_{\text{exp}} = 0.212(3)$ (2.27 Å and 2.296(1) Å, respectively) leading to the deviation from linearity. As with $d_{\text{Ni–Ni}}$, the values for the mixed compounds are larger than for the pure P-compound and smaller than that of the pure Ge-compound.

Table 3.8 Selected atomic distances, height ($h_{\text{Ni–P/Ge}}$), angle (α) within the tetrahedral layer (parameters shown in Figure 3.9) and the temperature at which the data was collected for $SrNi_2(P_{1-x}Ge_x)_2$ solid solution. The gray highlighted values correspond to single crystal data while the non-highlighted values correspond to data from powder Rietveld refinement.

x_{nom}	x_{exp}	T_{meas} / K	$d_{\text{P/Ge–P/Ge}}$ / Å	$d_{\text{Ni–P/Ge}}$ / Å	$d_{\text{Ni–Ni}}$ / Å	α / °	$h_{\text{Ni–P/Ge}}$ / Å
0.15	0.14(1)	300	2.874(5)	2.298(2); ×4	2.837(1); ×4	121.6(2)	1.120
	0.14(1)	130	2.720(3)	2.303(2); ×4	2.845(1); ×4	121.7(2)	1.122
	0.110(3)	300	2.845(3)	2.304(1); ×4	2.837(1); ×4	121.1(1)	1.132
0.25	0.24(1)	300	2.844(3)	2.307(2); ×4	2.855(1); ×4	122.2(2)	1.115
	0.24(1)	130	2.774(5)	2.307(2); ×4	2.852(1); ×4	122.0(2)	1.119
	0.212(3)	300	2.886(2)	2.296(1); ×4	2.860(1); ×4	123.5(2)	1.087
0.40	0.44(2)	300	2.859(2)	2.316(1); ×4	2.880(1); ×4	123.0(1)	1.105
	0.436(2)	300	2.843(5)	2.323(2); ×4	2.881(1); ×4	122.6(6)	1.115
0.55	0.55(1)	300	2.847(2)	2.331(1); ×4	2.896(1); ×4	122.9(1)	1.113
	0.547(2)	300	2.863(3)	2.332(1); ×4	2.900(1); ×4	123.2(4)	1.110
0.70	0.65(1)	300	2.851(2)	2.344(1); ×4	2.912(1); ×4	122.9(1)	1.120
	0.671(2)	300	2.855(2)	2.347(1); ×4	2.918(1); ×4	123.1(1)	1.119
0.85	0.884(1)	300	2.846(2)	2.369(1); ×4	2.943(1); ×4	122.9(1)	1.132

In contrast, the distance between the Ni–P layers along the *c*-axis, $d_{\text{P/Ge–P/Ge}}$, decreases with increasing Ge-content. Since this distance is mainly affected by the *c* lattice parameter and $z_{\text{P/Ge}}$, a non-linear decrease is observed.

$d_{P/Ge–P/Ge}$ has a value of 2.845(3) Å for x_{exp} = 0.110(3), jumps to 2.886(2) Å for x_{exp} = 0.212(3) and then slowly decreases to 2.83 for $x = 1$. The $d_{P/Ge–P/Ge}$ values of the $SrNi_2(P_{1-x}Ge_x)_2$ compounds indicate a clear separation of the layers along the c-axis. Values for covalent single bonds are approximately 2.20 Å for P and 2.45 Å for Ge.[38] The solid solution $SrNi_2(P_{1-x}Ge_x)_2$ belongs to the compounds with uncollapsed $ThCr_2Si_2$ type structure (at room-temperature).

The height of the E atoms to the adjacent square T plane ($h_{T–E}$) shows deviation from Vegard-like behavior within the $SrNi_2(P_{1-x}Ge_x)_2$ solid solution since it dependents on the c and $z_{P/Ge}$ parameters. $h_{Ni–P/Ge}$ decreases first from 1.132 Å to 1.087 Å (x_{exp} = 0.110(3) and 0.212(3), respectively) and then increases almost linear upon further Ge-substitution up to 1.14 Å for $SrNi_2Ge_2$.

The tetrahedral angle α shows a very irregular curve progression. $SrNi_2(P_{1-x}Ge_x)_2$ with x_{exp} = 0.110(3) has the lowest value of all compounds with 121.1(1) °. The other Ge-substituted compounds have values close to 123 ° which is rather far away from the ideal tetrahedral angle of 109.4 °. As was mentioned before, $h_{T–E}$ and, in correspondence α, seem to play an important role for the value of the critical temperature in superconducting 122 compounds.[30, 39] The values $h_{Ni–P}$ and α for the HT modification of $SrNi_2P_2$ were determined at 373 K. $h_{Ni–P}$ for ucT $SrNi_2P_2$ (1.11 Å) is the same as for $SrNi_2(P_{1-x}Ge_x)_2$ solid solution with x_{exp} = 0.547(2) while the tetrahedral angle α (121.1 °) is similar to that of x_{exp} = 0.110(3) (121.1(1) °).

To investigate the behavior of the P-rich pseudo-ternary samples with respect to a possible phase transition at low temperatures X-ray measurements of single crystals have been performed at room-temperature and at 130 K temperature. The single crystal measurements of $SrNi_2(P_{1-x}Ge_x)_2$ with x_{exp} = 0.14(1) and 0.24(1) (composition determined from singe crystal refinements, see Table 3.3 and Table 3.4) at 300 K and 130 K show anisotropy in the lattice parameters and the important structural parameters. The deviations are more pronounced for x_{exp} = 0.14(1); the a lattice parameter is slightly elongated upon cooling (4.012(1) Å to 4.024(1) Å) while the c lattice parameter decreases noticeably from 10.227(1) Å to 9.927(1) Å.

$z_{P/Ge}$ increases from 0.3608(2) to 0.3830(3) upon cooling. In response the distance between the $[Ni(P/Ge)_{4/4}]$ layers, $d_{P/Ge–P/Ge}$, decreases about 0.15 Å from 2.875(5) Å to 2.720(3) Å, which is still in the range of non-covalent bonds. The a

lattice parameters is almost identical for $x_{\mathrm{exp}} = 0.24(1)$ with 4.038(1) Å and 4.034(1) Å (300 K and 130 K, respectively). The *c*-axis decreases from 10.109(1) Å to 10.026(1) Å upon cooling. The $z_{\mathrm{P/Ge}}$ atomic coordinate changes from 0.3603(2) to 0.3617(2) at lower temperatures. $d_{\mathrm{P/Ge–P/Ge}}$ decreases about 0.07 Å from 2.844(3)Å to 2.774(5) Å in accordance to the smaller *c*-axis and the higher $z_{\mathrm{P/Ge}}$ value. A phase transition from the uncollapsed structure type (ucT) to the collapsed structure type (cT) or the orthorhombic structure type, as is found in pure $SrNi_2P_2$ and for P-rich compounds of the $SrNi_2(P_{1-x}As_x)_2$ solid solution, is not observed upon cooling (to 130 K) the single crystals of P-rich $SrNi_2(P_{1-x}Ge_x)_2$ compounds. The phase transitions in P-rich compounds of the $SrNi_2(P_{1-x}As_x)_2$ solid solution (ucT to orthorhombic structure for $x = 0$ - 0.075 and from ucT to cT for $x = 0.1$ and 0.25) all are observed at temperatures above 170 K.[40] The P-rich single crystals of the $SrNi_2(P_{1-x}Ge_x)_2$ solid solution were measured at 130 K which should be low enough to see a possible transition.

To be certain, in-situ powder X-ray measurements at temperatures between 300 K and 10 K (10 K intervals) were performed in cooperation with F. Hummels (Prof. Johrendt, LMU München) for the P-rich $SrNi_2(P_{1-x}Ge_x)_2$ solid solution with $x_{\mathrm{exp}} = 0.110(3)$ and 0.212(3) to check for a possible phase transition. The occupation factors for the atomic positions and the P/Ge ratio on the mixed atomic position were refined only for the powder diffraction data measured at 300 K and fixed for the refinements of the same sample at lower temperatures.

The changes in lattice parameters in the range of 10 - 300 K (given in Table A10 and Table A11, Appendix) are shown in Figure 3.11. The cell parameters from the single crystal measurements at 130 K are included in the figure (red symbols). The cell parameters for $x_{\mathrm{exp}} = 0.110(3)$ (Figure 3.11a) display a s-like curve upon cooling with an increase of *a* parameter from 4.0119(1) Å to 4.0214(1) Å and a decrease of *c* parameter from 10.220(1) Å to 9.849(1) Å, the volume changes accordingly from 164.50(1) Å^3 to 159.27(1) Å^3. The biggest deviation from linearity happens between 200 - 250 K. The changes for the Ge-richer compound ($x_{\mathrm{exp}} = 0.212(3)$, Figure 3.11b) are less pronounced in this temperature range. The *a* lattice and the *c* lattice decreases monotonically upon cooling from 4.0448 Å to 4.0376(1) Å and 10.212(1) Å to 9.984(1) Å (*a* and *c*, respectively). The volume decreases from 165.58(1) Å^3 to 162.76(1) Å^3. It was not possible to reliably calculate $z_{P/Ge}$ from powder data and, in correspondence, the Ni–P/Ge and Ni–Ni interatomic distances from the low temperature measurements. The lattice parameters at 10 K are only slightly smaller and no abrupt changes between 130 K and 10 K are observed. A phase transition to collapsed type structure is therefore unlikely. The lattice parameters obtained at 130 K from powder measurements (red symbols in Figure 3.11) deviate slightly from those obtained from single crystal measurements at that temperature.

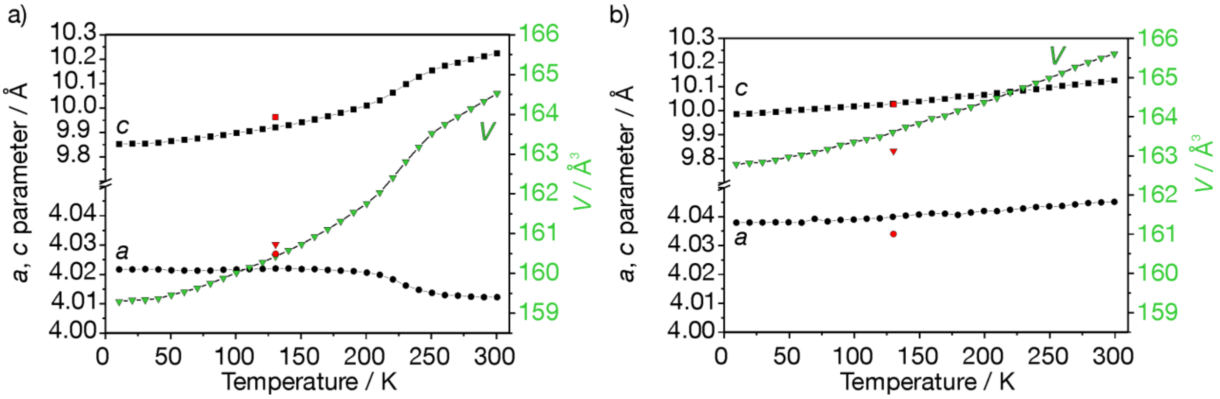

Figure 3.11 Lattice parameters at different temperature between 10 - 300 K (10 K steps) for $SrNi_2(P_{1-x}Ge_x)_2$: a) x_{exp} = 0.110(3) and b) x_{exp} = 0.212(3).

The structural parameters of the $SrNi_2(P_{1-x}Ge_x)_2$ solid solution are within the range of ternary $AeNi_2E_2$ compounds (listed in Table 3.9). Covalent bonds between the $[TP_{4/4}]$ for other 122 phosphides have values of 2.30 - 2.45 Å ($CaNi_2P_2$ and $SrNi_2P_2$, respectively).[9, 26] $CaNi_2E_2$ (E = P, As) crystallizes in the collapsed tetragonal (cT) modification, the P-compound has the smallest a and c parameters, $d_{P–P}$ value (2.30 Å) and the highest z_P value. The $LaNi_2E_2$ (E = Ge, P) compounds also crystallize in the cT structure and therefore show rather short c-axes and higher z_E values than the other compounds. The c/a values for the collapsed compounds lie between 2.36 and 2.44. The c/a ratio for the uncollapsed compounds $AeNi_2P_2$ (Ae = Sr, Ba) is higher (2.70 and 2.99 for Sr and Ba, respectively).

$SrNi_2As_2$ shows values close to that of $SrNi_2Ge_2$, the slight variations are due to the size effect of the E atom. Even though both compounds have ucT structure the c/a ratio is closer to that of the collapsed compounds (2.44 and 2.47 for Ge and As, respectively). Here the large values for the a-axis reduced the c/a ratio.

Table 3.9 Structural parameters of selected $AeNi_2E_2$ (Ae = Ca, Sr, Ba, La; E = P, As, Ge) compounds with $ThCr_2Si_2$ type structure. cT stands for collapsed, ucT for uncollapsed tetragonal modification.

Compounds	***a* / Å**	***c* / Å**	***V* / Å³**	z_E	$d_{E\text{–}E}$ / Å	$d_{Ni\text{–}E}$ / Å	$d_{Ni\text{–}Ni}$ / Å	α / °	$h_{Ni\text{–}E}$ / Å	**Ref**
$CaNi_2P_2$-cT	3.92	9.36	143.8	0.377	2.30	2.29	2.77	117.3	1.19	[9]
$SrNi_2P_2$-ucT	3.95	10.68	166.6	0.354	2.79	2.26	3.12	121.3	1.11	[26]
$BaNi_2P_2$-ucT	3.95	11.82	184.4	0.343	2.79	2.26	3.71	121.7	1.10	[26]
$LaNi_2P_2$-cT	4.01	9.60	154.5	0.370	2.50	2.31	2.84	120.2	1.15	[41]
$CaNi_2As_2$-cT	4.07	9.95	164.8	0.370	2.59	2.36	2.87	119.2	1.19	[10]
$SrNi_2As_2$-ucT	4.15	10.29	177.2	0.362	2.83	2.38	2.93	121.8	1.15	[10]
$SrNi_2Ge_2$ucT	4.18	10.24	178.9	0.362	2.83	2.38	2.96	122.6	1.14	[31]
$LaNi_2Ge_2$-cT	4.19	9.90	173.5	0.368	2.61	2.40	2.96	121.7	1.17	[42]

The solid solution $LaNi_2(P_{1-x}Ge_x)_2$ within the whole substitution range have been reported to show slight deviations from Vegard's law.[42] Just like the ternary side phases the solid solution all crystallize in the cT structure. Superconductivity above 1.8 K was not reported for any of these compounds.

The group of Cava investigated the structural and magnetic effects for the $BaNi_2(P_{1-x}Ge_x)_2$ solid solution.[29] The ternary side phase $BaNi_2P_2$ displays superconducting behavior while $BaNi_2Ge_2$ crystallizes in a distorted version of the $ThCr_2Si_2$ type structure.[29, 37] The distortion is not the same as observed in $SrNi_2P_2$ however, it is more pronounced in the Ni_2Ge_2 layers.[37] The substitution of P with Ge leads to an increase of T_c with a maximum at 20 at. % Ge-substitution and superconductivity disappears for Ge-substitution above 50 at. %. The structural instability of $BaNi_2Ge_2$ can be totally suppressed when at least 70 at. % P is present. The changes in structure parameters is non-linear like observed for the $SrNi_2(P_{1-x}Ge_x)_2$ solid solution.

The comparison of the structural changes observed in $SrNi_2(P_{1-x}Ge_x)_2$ solid solution with other $SrNi_2P_2$ based solid solutions show similar behavior. Keimes *et al.*[40] have reported multiple solid solutions based on $SrNi_2P_2$, namely the previously mentioned $SrNi_2(P_{1-x}As_x)_2$ solid solution, as well as the $Sr(Ni_{1-x}T_x)_2P_2$ solid solutions (T = Co and Cu) and $Sr_{1-x}Ca_xNi_2P_2$ solid solution. They have observed that in all four cases the structural phase transition observed in pure $SrNi_2P_2$ can be suppressed by low amounts ($x > 0.1$) of substitution on any atomic site. However a phase transition from uncollapsed to collapsed $ThCr_2Si_2$ modification is always observed for P-rich compositions. No investigations on superconductivity were reported for these systems. The compound with the highest amount of P in the $SrNi_2(P_{1-x}Ge_x)_2$ solid solution has a Ge-content of ~11 at. %, which might already be enough to suppress the phase transition (ucT-cT) to very low temperatures or even totally. Single crystal measurements or high-resolution powder data down to temperatures of 1 K would be needed to give reliable conclusion if a transition from the ucT tetragonal phase to the collapsed one takes place or not.

3.2.2.2. Magnetic Properties

Zfc-fc magnetic measurements (H = 15 Oe, temperature range 1.8 - 15 K) for all samples are presented in Figure 3.12 and Figure A11 (Appendix). Superconductivity is observed for the two P-richest $SrNi_2(P_{1-x}Ge_x)_2$ samples with $x_{exp} = 0.110(3)$ (red curve) and $x_{exp} = 0.212(3)$ (green curve). The curve for $x_{exp} = 0.110(3)$ shows two drops of susceptibility, one at approximately 9 K ($T_{c2,onset}$) which is rather small and a more pronounced drop at approximately 3 K ($T_{c1,onset}$). Due to the small changes in susceptibility for $T_{c2,onset}$ it can be assumed that there is an impurity in the sample that has also superconducting behavior. The source of this impurity could not be determined. The drop in susceptibility at 3 K arises from the main phase, unfortunately $T_{c1,onset}$ is close to the temperature limit of the magnetometer and the split of the zfc curve (Shielding part) and the fc curve (Meissner part) is not observed. Therefore the volume of the superconducting phase could not be determined with this method. The compound with ~21 at. % Ge also shows superconductivity below 2.4 K. Again the split of the Shielding and Meissner part could not be determined.

The second drop in susceptibility at approximately 9 K can also be seen in this sample (upon closer inspection) but is even less pronounced so that it is not visible on this scale. The samples with higher x values (> 0.4) show no superconducting behavior above 1.8 K. The curve for $x_{exp} = 0.436(2)$ lies at higher susceptibility values than all other curves, the deviation is most likely because of ferromagnetic impurities (see Figure A11, Appendix).

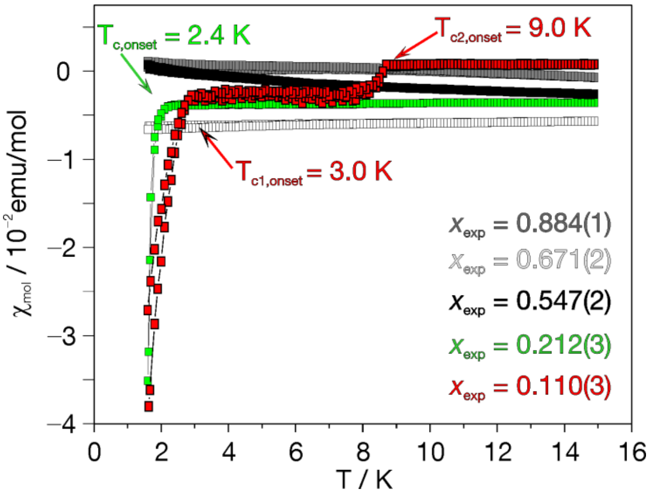

Figure 3.12 Zero field cooled-field cooled (zfc-fc) measurements for the samples of $SrNi_2(P_{1-x}Ge_x)_2$ solid solution with an applied field of 15 Oe. The compounds with x_{exp} = 0.110(3) (red curve) and 0.212(3) (green curve) show superconducting behavior ($T_{c,onset}$ marked with arrows).

$SrNi_2(P_{1-x}Ge_x)_2$ solid solution are expected to be superconducting at low temperatures in the full range since both ternary side phases $SrNi_2P_2$ and $SrNi_2Ge_2$ exhibit superconductivity (T_c = 1.4 K and 0.87 K, respectively).[24, 25] Magnetic measurements were only possible down to 1.8 K however, therefore no prove for this assumption can be given in case of the compounds with $x_{exp} > 0.212(3)$. The partial substitution of P with Ge increases the observed T_c to a maximum of 3 K ($T_{c,onset}$) for ~11 at. % Ge and then a reduction in $T_{c,onset}$ takes place for further substitution. The same observations were reported for the $BaNi_2(P_{1-x}Ge_x)_2$ solid solution that display a dome like shape of T_c (x = 0.5 - 1) with a maximum of 2.9 K at ~20 at. % Ge substitution.[29] For the solid solution $SrNi_2(P_{1-x}As_x)_2$, $Sr(Ni_{1-x}T_x)_2P_2$ (T = Co and Cu) and $Sr_{1-x}Ca_xNi_2P_2$[40] no investigation for possible superconducting behavior were reported until now and could be interesting taking into account their close structural features to the investigated $SrNi_2(P_{1-x}Ge_x)_2$.

For the determination of the critical fields H_{c1} and H_{c2}, field dependent measurements at 1.8 K were carried out for the superconducting samples $SrNi_2(P_{1-x}Ge_x)_2$ with x_{exp} = 0.110(3) and 0.212(3). Figure 3.13a and Figure 3.13b show the molar magnetization vs the applied fields H for both compounds.

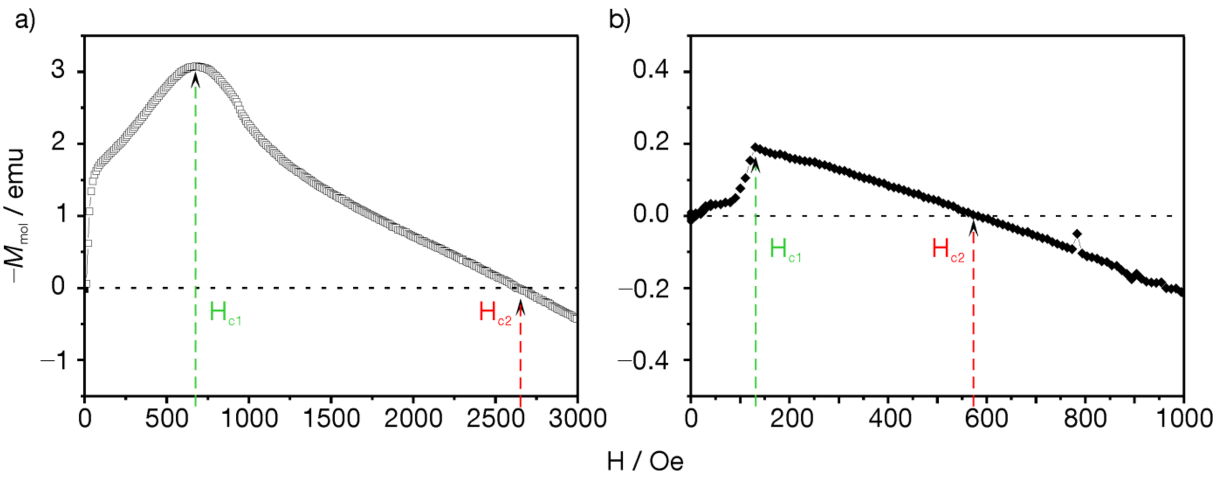

Figure 3.13 Field dependent magnetic measurements at 1.8 K for superconducting $SrNi_2(P_{1-x}Ge_x)_2$ solid solution (magnetization plotted): a) x_{exp} = 0.110(3), H range 0 - 3000 Oe in 10 Oe steps; b) x_{exp} = 0.212(3) H range 0 - 1000 Oe in 10 Oe steps. The upper critical field H_{c2} is shown in red and the lower critical field H_{c1} is shown in green, the zero line (black dashed) is shown as visual help.

The curves show the trend typically observed for type 2 superconductors. A type 1 superconductor would show an abrupt drop from the maximum that cuts through zero upon the onset of superconductivity and has only one transition temperature (see Figure 3.14).[43] The P-richer compound (Figure 3.13a) has an upper critical field (H_{c2}) of approximately 2626 Oe and a lower critical field (H_{c1}) of approximately 683 Oe (at 1.8 K).

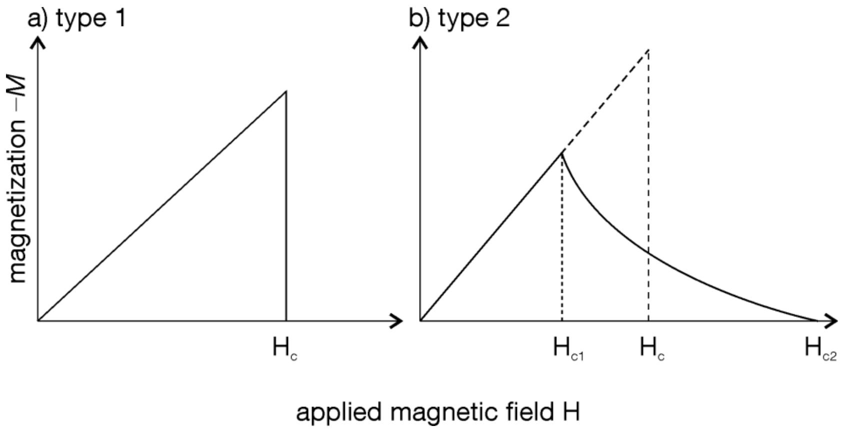

Figure 3.14 Schematic representation for the magnetization curve in dependence of the field for a) type 1 and b) type 2 superconductors.

The compound with ~21 at. % Ge-substitution has a lower H_{c2} value of ~575 Oe and a H_{c1} value of approximately 130 Oe. H_c therefore shows also a decrease with increasing Ge-substitution similar to the decrease observed for T_c.

Compared to the reported critical field values of $SrNi_2P_2$ (H_{c2} = 390 Oe; H_{c1} = 88 Oe calculated for zero temperature)[25] both compounds show an increase for H_c in accordance to the higher T_c values. Reference H_c values for $SrNi_2Ge_2$ were not reported.

3.2.2.3. Conductivity measurements

The electric resistivity and heat capacity of the P-richest sample of the mixed $SrNi_2(P_{1-x}Ge_x)_2$ solid solution ($x_{nom} = 0.15$, x_{exp} 0 0.110(3)) was measured in cooperation with Dr. V. Grinenko (Prof. Hühne group, IFW Dresden). Part of the sample (powder) was hot-pressed (973 K for 2 hours) into a pellet and cut to a rectangular shaped piece prior to the measurements.

The hot-pressed pellet was further used for resistivity and heat capacity measurements. The results from the measurements are shown in Figure 3.15. Resistivity data (Figure 3.15a) shows an almost linear decline between 300 - 10 K, between 9 K and 8 K a small drop is observed (T_{c2}, Figure 3.15a, upper inset) as previous mentioned from the zfc-fc measurements. The drop is assigned to a superconducting phase of approximately 2 at. %. The resistivity exhibits a sharp drop to zero at around 3 K assigned to the $SrNi_2(P_{1-x}Ge_x)_2$ phase ($x_{nom} = 0.15$). The plot in the lower inset of Figure 3.15a shows the data collected at H = 0 Oe with electrical currents of I = 1 mA and 10 mA. Increasing the electrical current from 1 mA to 10 mA does not decrease T_c significantly.

Heat capacity data at low temperature are shown in Figure 3.15b. The data was collected at zero field (zf) and at 30000 Oe applied field to suppress superconductivity. Sommerfeld coefficient γ_n of 11.3 mJ/mol K^2 is defined using a standard expression $C/T = \gamma_n + \beta_3 T^2 + \beta_5 T^4$, where β_3 and β_5 are the lattice contribution of the specific heat. The β_3 value of 0.29 mJ/mol K^4 corresponds to the *Debye* temperature $\theta_D = (12\pi^4 RZ/5\beta)^{1/3} = 320$ K, where R is the molar gas constant and $Z = 5$ is the number of atoms per formula unit. From the zf data T_c is determined to be 2.9 K at the midpoint of the ΔC jump (Figure 3.15b inset, green line).

The superconducting specific-heat jump $\Delta C/T_c$ at T_c has a very small value of 2.2 mJ/mol K^2 resulting in a normalized value $\Delta C/T_c\gamma \approx 0.2$.

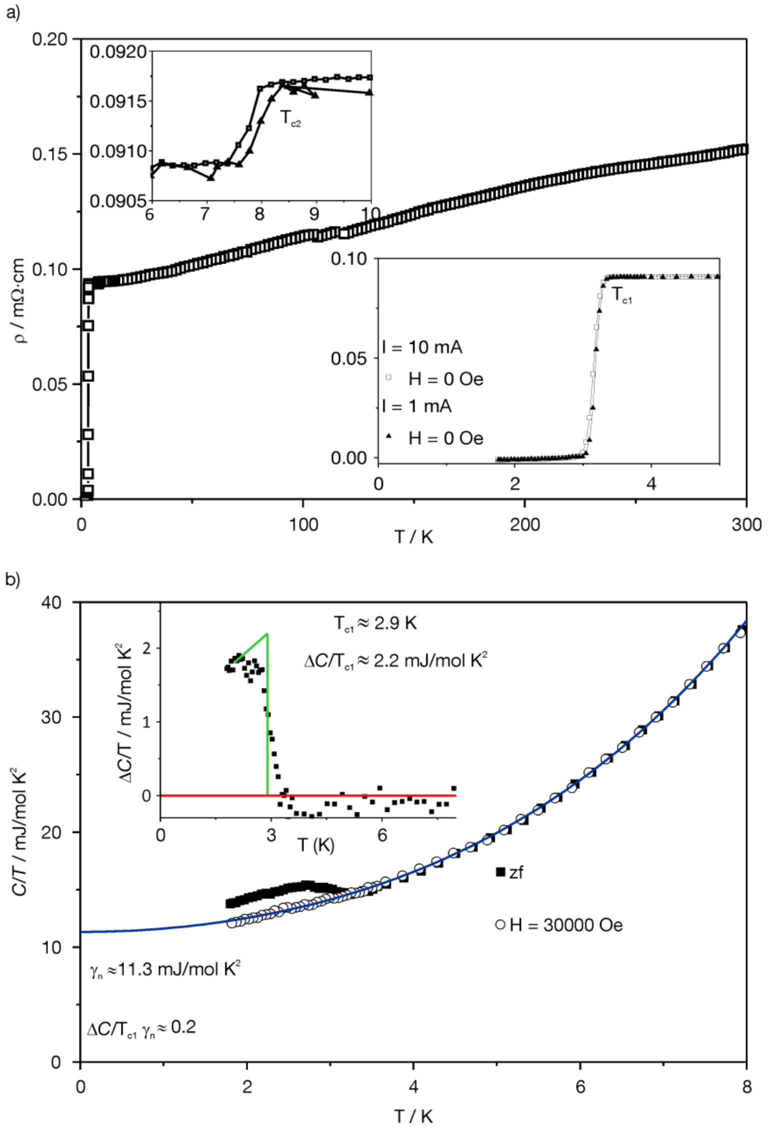

Figure 3.15 a) Electrical resistivity measurements of the $SrNi_2(P_{1-x}Ge_x)_2$ solid solution (x_{nom} = 0.15); upper insert shows a close up of the data between 6 - 10 K and bottom insert shows measurements at different applied currents I. b) Heat capacity measurements performed without an applied field (zf) and an applied field H = 30000 Oe, the fitted curve (blue) is used as reference; in the top the difference heat capacity is plotted including the entropy construction plot.

For the pure compounds $\Delta C/T_c\gamma$ values reported are 1.27[25] or 1.2[44] for single crystals of $SrNi_2P_2$ and 0.88 - 1.05 (polycrystalline samples)[45] for $SrNi_2Ge_2$. A possible reason for the low $\Delta C/T_c\gamma$ value could be poor crystallinity of the sample and consequently a small amount of superconducting fraction. On the other hand the $\Delta C/T_c\gamma$ values reported for $SrPd_2Ge_2$ show a significant difference for measurements using a single crystal ($\Delta C/T_c\gamma = 2.1$)[46] or a polycrystalline samples

($\Delta C/T_c\gamma = 0.7$).[45] The reason why the superconducting volume fraction is very low could not be determined.

Powder X-ray diffraction pattern for the two hot-pressed sample is shown in Figure A12 (Appendix) including the powder pattern for the sample before hot-pressure treatment (bottom curve, theoretical *Bragg* positions green lines) as reference. The quality of the sample is reduced after hot-pressure treatment deducible from the signal to noise ratio and the half-width of the reflections. The sharp reflections of the powder before the treatment are broadened for the hot-pressed samples indicating that crystallinity is poorer. In addition impurity reflexes between $2\theta = 30 - 50$ ° become visible (marked with * for curve b). The origin of these reflections could not be determined.

The lattice parameters for the $SrNi_2(P_{1-x}Ge_x)_2$ phase ($x_{exp} = 0.110(3)$) show a s-like curve upon cooling (see Figure 3.11a in Chapter 3.2.2.1), the deviation from linearity occurs in the range of 200 – 250 K. The normal state resistivity in that region (Figure 3.15a) also shows a deviation from linearity. The origin for the structural effects that influence the deviation for both the lattice parameters and the resistivity could not be determined.

Zfc-fc magnetic measurements on the hot-pressed pellet showed a superconducting jump at approximately 3 K as was observed for the powder measurements discussed in Chapter 3.2.2.2.

3.2.2.4. Electronic structure and chemical bonding

The electronic structures of the pure $SrNi_2P_2$ and the $SrNi_2(P_{1-x}Ge_x)_2$ solid solution with ~14 at. % Ge have been calculated. It is not possible to calculated mixed occupations on atomic sites with the TB-LMTO-ASA program; therefore a model calculated with full occupation of P was used. Input parameter were taken from refinement of $SrNi_2(P_{1-x}Ge_x)_2$ ($x_{exp} = 0.14(1)$) single crystal measurement at 130 K, the phase will be referred to “$SrNi_2(P_{0.86}Ge_{0.14})_2$” in the following discussion. The Fermi level for “$SrNi_2(P_{0.86}Ge_{0.14})_2$” was adjusted to −0.1 eV. The value was determined from the iDOS value for a theoretical composition of 14 at. % Ge with an electron count of 31.72 states/cell. The input parameters for Ge-free $SrNi_2P_2$ (*Immm*) were taken from literature.[26] $SrNi_2P_2$ has two crystallographic positions for each atom sort due to the previously described distortion. The total DOS and the partial DOS for both compounds are shown in Figure 3.16.

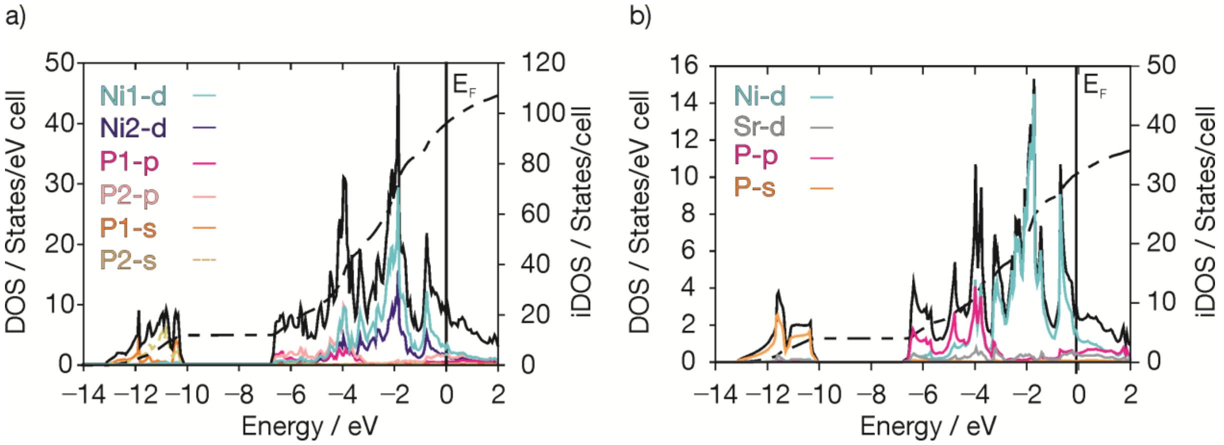

Figure 3.16 DOS and partial DOS of $SrNi_2P_2$: a) *Immm* and b) ucT *I4/mmm*; the Fermi level for the pseudo-ternary compound is set at −0.1 eV corresponding to the composition $SrNi_2(P_{0.86}Ge_{0.14})_2$ according to a rigid band model. Total DOS (black) including pDOS of Ni-d (turquois, blue), P-p (magenta, brown) and P-s (orange, gray).

The DOS is split into two blocks clearly divided by a band gap of 3 eV in both cases. The first block is located at energies between −13.2 eV and −10 eV. Main contributions in these blocks come from the P-s orbitals for both models with slight P-p contributions. Comparing the DOS curve in the low energy block of both compounds shows certain differences. Above the band gap (−10 eV to −7 eV) the second DOS block is located. The pDOS of Ni-d and P-p show similar shapes in the region between −7 eV and −3 eV for both models. This indicates strong hybridization of the Ni-d and P-p orbitals. These orbitals correspond to the covalent Ni–P bonds in the [NiP] layers. The DOS region between −3 eV and 1 eV is almost exclusively formed by Ni-d orbitals.

Both models show no band gap at the Fermi level indicating metallic character for the compounds. Main contributions come from the Ni-d orbitals with an admixture of P-p. The contributions of P-s and Sr-d (only shown for "$SrNi_2(P_{0.86}Ge_{0.14})_2$") are small but non-zero at the Fermi level. At the Fermi level a local maximum peak is observed for $SrNi_2P_2$. The main contribution at the Fermi level comes from Ni1-d pDOS. The adjusted Fermi level (−0.1 eV) for the "$SrNi_2(P_{0.86}Ge_{0.14})_2$" model cuts through the shoulder of the peak. A local maximum at the Fermi level is correlated to a degree of structural or magnetic instability, which is often stated to be important for the appearance of superconductivity in the 122 family.

Comparing the DOS of "$SrNi_2(P_{0.86}Ge_{0.14})_2$" with those of ternary $AeNi_2P_2$ and $AeNi_2As_2$ (Ae = Sr, Ba) superconductors (in *I*4/*mmm* type structure) show that the overall shape of the DOS and the contributions of the pDOS are similar.[47] One difference observed for the $BaNi_2E_2$ (E = P, As) is that Ba-p orbital contributions are found at energies lower than the *E*-s pDOS peaks which lie between −12 eV and −10 eV.[47] For the isostructural iron-pnictides the valence electron count is reduced by 4 electrons. As a result the Fermi level for the iron-pnictides is shifted towards lower energies to the DOS part which is located at approximately −1.5 eV for the "$SrNi_2(P_{0.86}Ge_{0.14})_2$" model.[48-50] At the lower energy region (–3 eV to −1 eV) the contributions from the P-p orbitals is reduced.

The individual contributions of the orbitals to the DOS are obtained via band structure calculations including fat bands (shown in Figure 3.17). The *k*-paths parallel to the *c*-direction are $\mathrm{Z} \rightarrow \Gamma$ and $\mathrm{X} \rightarrow \mathrm{P}$; the paths parallel to the *ab*-plane are $\Gamma \rightarrow \mathrm{X}$ and $\mathrm{P} \rightarrow \mathrm{N}$ (Brillouin zone[51] for space group *I*4/*mmm* shown in Figure A13, Appendix). The Fermi level is crossed by multiple bands in the $\Gamma \rightarrow \mathrm{X}$ and $\mathrm{P} \rightarrow \mathrm{N}$ paths. All Ni-d orbitals show crossing, the main contributions come from Ni-d_{xy} and Ni-$d_{xz,yz}$ (Figure 3.17c, d), some contributions from the "P/Ge"-$p_{x,y}$ are observed as well (Figure 3.17g). The Fermi level is not crossed by any bands along the $\mathrm{Z} \rightarrow \Gamma$ path. Along the $\mathrm{X} \rightarrow \mathrm{P}$ path one band touches the Fermi level (–0.1 eV). Main contributions to this band come from Ni-$d_{xz,yz}$ and "P/Ge"-p_z fat bands with some contribution of the "P/Ge"-s fat band. A similar situation is found in $BaNi_2P_2$.[47]

In iron-based superconductors multiple pockets (hole-like pockets and electron-like pockets) are observed, located at the Z and Γ *k*-points, $\mathrm{Z} \rightarrow \Gamma$ and $\mathrm{X} \rightarrow \mathrm{P}$ *k*-paths are both oriented along the *c*-direction in real space.[52] Due to the shift of the Fermi level towards the conduction band in Ni-compounds no pockets at these *k*-points are observed in $SrNi_2P_2$, "$SrNi_2(P_{0.86}Ge_{0.14})_2$" and $BaNi_2P_2$ (tetragonal structure type), but a valence band touches the Fermi level at the P *k*-point. The different situation at the Fermi level for iron-pnictides influences the superconducting properties and supports higher T_c values.

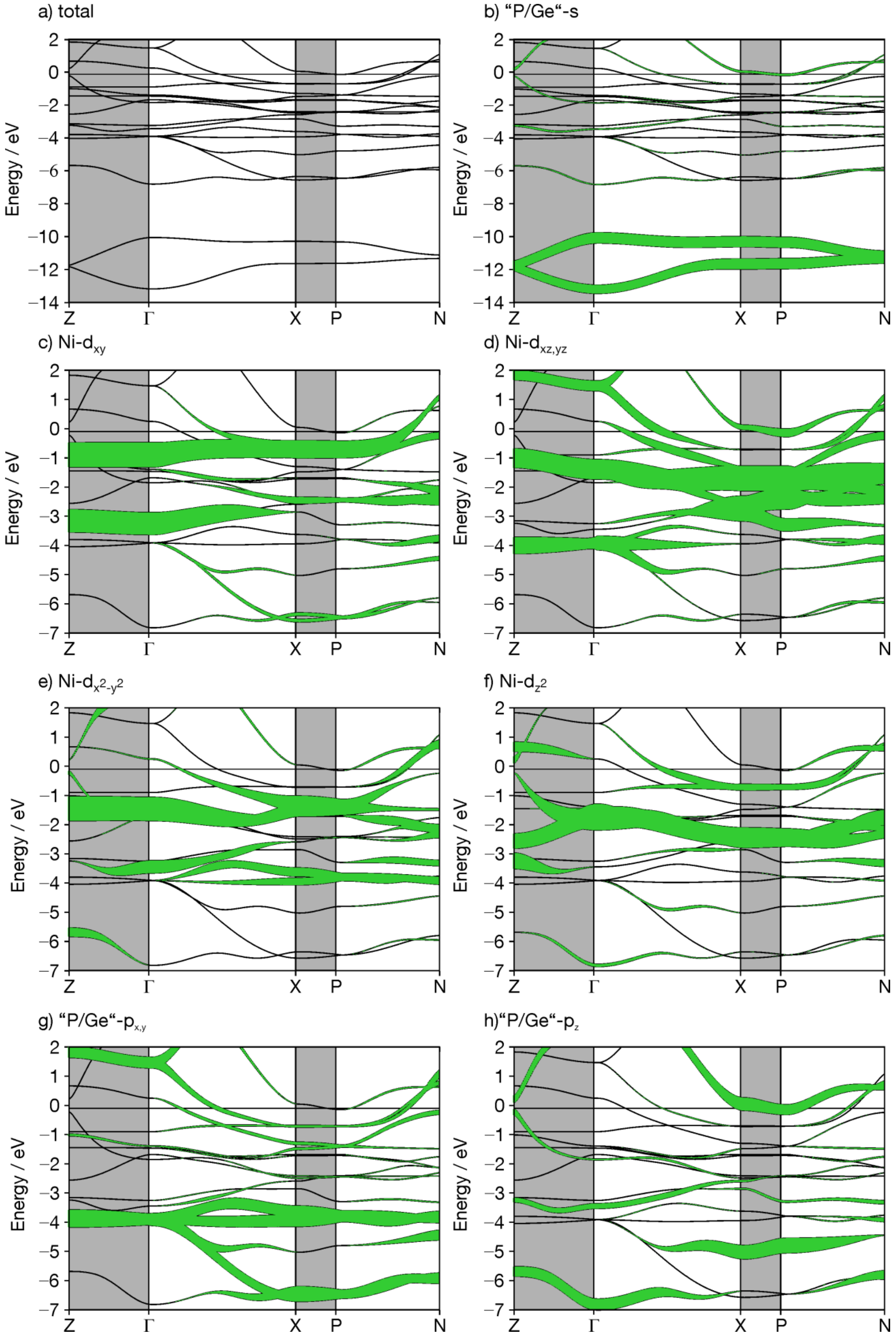

Figure 3.17 Band structure (a) and fat band representations (b-h) of "SrNi$_2$(P$_{0.86}$Ge$_{0.14}$)$_2$": a) all bands, b) "P/Ge"-s, c) Ni-d_{xy}, d) Ni-$d_{xz,yz}$, e) Ni-d_{x2-y2}, f) Ni-d_{z2}, g) "P/Ge"-$p_{x,y}$ and h) "P/Ge"- p_z; *k*-paths parallel to the *c*-direction are highlighted gray, paths parallel to *ab*-plane are white.

Hybridization between the Ni-$d_{xz,yz}$ fat bands and the "P/Ge"-$p_{x,y}$ fat bands is observed along $\mathrm{Z} \rightarrow \Gamma$ *k*-path (*c*-direction in real space) corresponding to the Ni–P/Ge bonds in the $[Ni(P/Ge)_{4/4}]$ layers.

Information about the interactions between the tetrahedral layers for $SrNi_2P_2$ (*Immm*) and "$SrNi_2(P_{0.86}Ge_{0.14})_2$" can be obtained from Electron Localization Function (ELF) analyses (Figure 3.18). In $SrNi_2P_2$ a bisynaptic valence basin ($\eta > 0.71$) is observed that corresponds to the covalent interlayer bond between the P1 atoms (denoted ①). Between the non-bonding P2 atoms monotactic ELF domains oriented along the *c*-direction are observed (②). Monotactic (non-bonding) ELF domains are also found between the "P/Ge" atoms in "$SrNi_2(P_{0.86}Ge_{0.14})_2$". The domains are closer to each other than in $SrNi_2P_2$ (P2–P2) which is in correspondence with the observed distances (3.28 Å for $SrNi_2P_2$ vs 2.720(3) Å for "$SrNi_2(P_{0.86}Ge_{0.14})_2$").

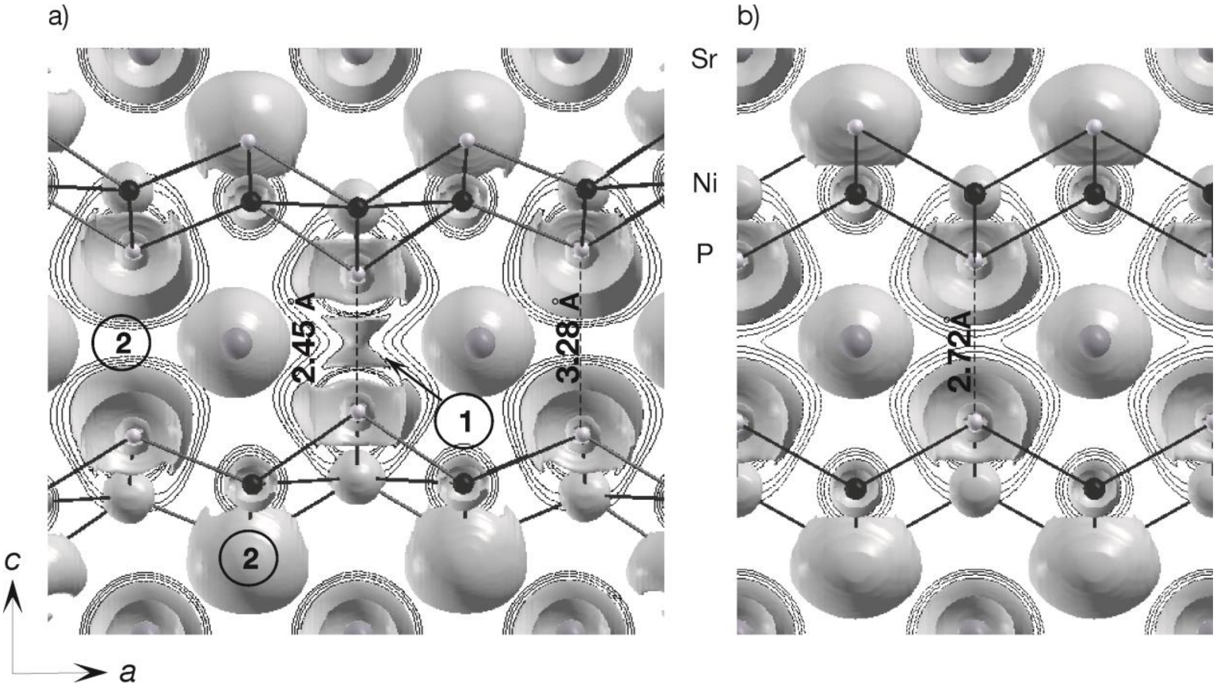

Figure 3.18 ELF representation of a) $SrNi_2P_2$ (*Immm*) and b) "$SrNi_2(P_{0.86}Ge_{0.14})_2$" (*I*4/*mmm*) calculated from the all electron density. 2D contour line diagram of the ELF ranging from $\eta = 0.4$ to $\eta = 0.7$ is included. 3D plot with bisynaptic ELF domains located between the P1 atoms of $SrNi_2P_2$ are denoted with ①, monotactic ELF domains located at the P2 atoms denoted with ②.

3.2.3. Investigation of SrNi$_2$(As$_{1-x}$Ge$_x$)$_2$ solid solution

As part of this work the system SrNi$_2$(As$_{1-x}$Ge$_x$)$_2$ was investigated. The isostructural compounds SrNi$_2$As$_2$ and SrNi$_2$Ge$_2$ (ucT-*I*4/*mmm* structure type) both are superconducting compounds with T$_c$ values of 0.67 K and 0.87 K (respectively).[23, 24] The aim was to synthesize the solid solution analogue to the previous described SrNi$_2$(P$_{1-x}$Ge$_x$)$_2$ compounds, since a possible substitution of As with Ge was expected. The diffraction patterns for $x_{\text{nom}} = 0.1$, 0.3, 0.7, 0.9 are presented in Figure 3.19.

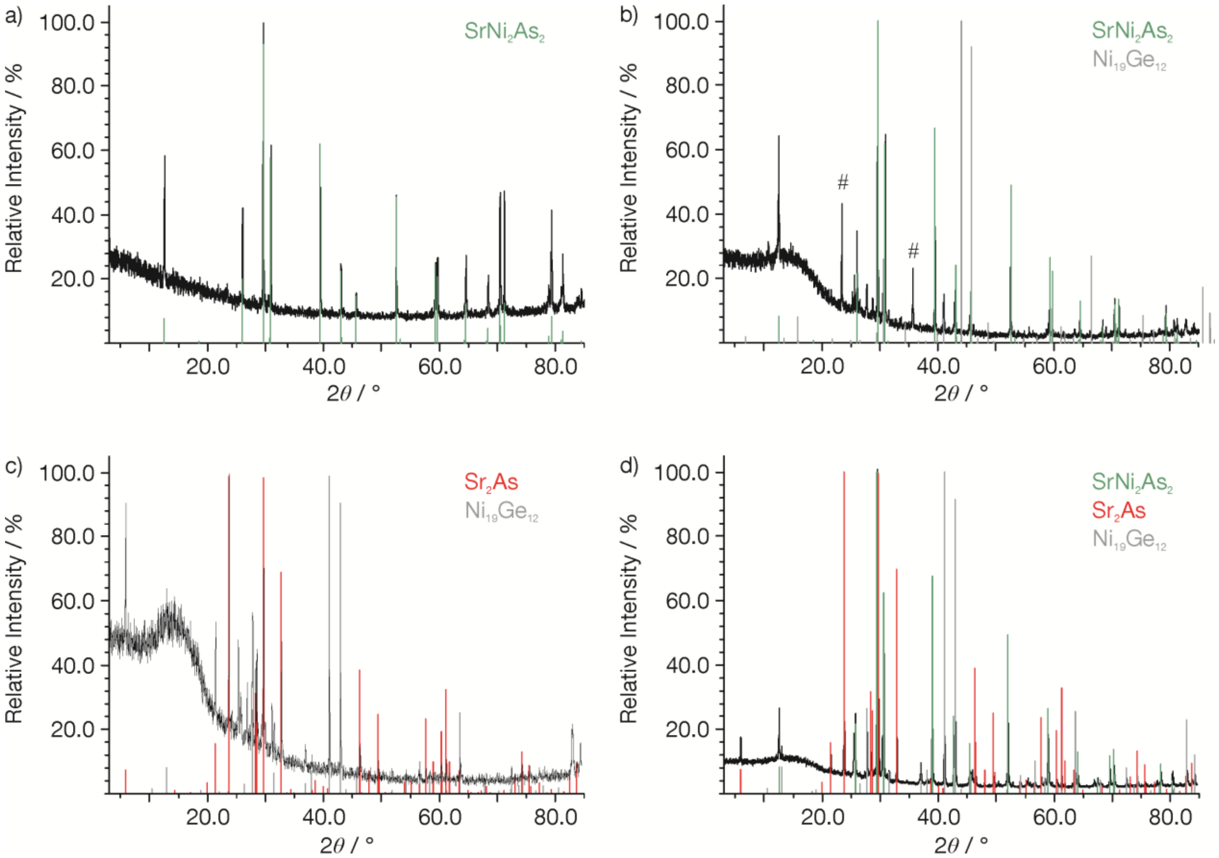

Figure 3.19 Powder X-Ray diffraction pattern for SrNi$_2$(As$_{1-x}$Ge$_x$)$_2$ samples: a) $x_{\text{nom}} = 0.1$, b) $x_{\text{nom}} = 0.3$, c) $x_{\text{nom}} = 0.7$ and d) $x_{\text{nom}} = 0.9$. Theoretical pattern from 122 phase (green), Ni$_{19}$Ge$_{12}$ phase (gray) and Sr$_2$As (red) included. Measurements performed on a Stoe Stadi P (Cu-K$_{\alpha 1}$, measurement range 5 - 85 ° 2θ, 0.1 ° step size, Si as external standard), reflections marked with # are of unknown origin.

The powder X-ray pattern of the sample made with $x_{\text{nom}} = 0.1$ (Figure 3.19a) showed almost exclusively reflections that belong to the 122 phase. The cell parameters calculated were $a = 4.153(1)$ Å and $c = 10.251(2)$ Å with a volume of 177(1) Å^3. The reported cell parameters for SrNi$_2$As$_2$ are $a = 4.154$ Å and $c = 10.290$ Å, $V = 177.2$ Å^3.[10] The variations are minor so possible substitution cannot conclusively be proven. It is not possible to determine Ge-substitution with X-ray diffraction measurements of single crystals because As and Ge have only one electron difference. A distinction between Ge and As is possible with EDX analyses. The $K_{\alpha 1}$ line for Ge lies at 9.887 keV, for As $K_{\alpha 1}$ = 10.544 keV.[53] EDX measurements on isolated crystal showed no indication of Ge.

The samples that were made with higher amounts of $SrNi_2Ge_2$ precursor (x_{nom} > 0.1) showed unexpected results. The increase of Ge content lead to the appearance of binary phases instead to a shift of the 122 reflections indicating unsuccessful substitution of Ge on the As position. For the sample with x_{nom} = 0.3, the reflections for $SrNi_2As_2$ phase and $Ni_{19}Ge_{12}$ are observed (Figure 3.19b). In addition, some reflections are observed (~23 ° and 40 ° 2θ) that could not be indexed with any reported ternary or binary phase.

The sample with nominal 70 at. % $SrNi_2Ge_2$ precursor shows the most intriguing powder pattern. No reflections of a 122 phase are observed (Figure 3.19c); only binary Sr_2As and $Ni_{19}Ge_{12}$ phases could be identified. In addition numerous reflections of unknown origin (24 - 28 ° and ~32 ° 2θ) are present. In the sample with the highest tried mixture ($x_{nom} = 0.9$) reflections for the 122 phase ($SrNi_2Ge_2$) are again observed in addition to Sr_2As and $Ni_{19}Ge_{12}$ phase (Figure 3.19d).

A possible explanation for the observed decomposition of the ternary phases during the reaction could be that a formation of the binary phases is favored rather than a substitution of As with Ge in the ternary phase. Based on the results obtained for the sample ($x_{nom} = 0.7$) with an approximate composition of 1:3 ($SrNi_2As_2$:$SrNi_2Ge_2$), a possible reaction could be:

$$1SrNi_2As_2 + 3SrNi_2Ge_2 \rightarrow 2Sr_2As + \text{“}Ni_xGe_y\text{”}$$

The observed phase $Ni_{19}Ge_{12}$ has a composition of 61 at. % Ni and 29 at. % Ge. The additionally observed, unknown reflections could belong to an unknown binary or ternary phase.

No prove of Ge-substitution in $SrNi_2As_2$ could be obtained. Wherever the solution range is very small or does not exist in $SrNi_2(As_{1-x}Ge_x)_2$ is an open question.

3.3. Investigation of $BaFe_2(P_{1-x}Ge_x)_2$ solid solution

Trials to synthesize $BaFe_2(P_{1-x}Ge_x)_2$ solid solution, similar to the previous described $SrNi_2(P_{1-x}Ge_x)_2$ one (Chapter 3.2) and the reported $BaNi_2(P_{1-x}Ge_x)_2$[29] have been made.

3.3.1. Synthesis of the binary precursors and the pseudo-ternary samples

Samples with the nominal composition of $BaFe_2(P_{1-x}Ge_x)_2$ were prepared in multi-step synthesize. The samples were made with binary FeP and FeGe alloys as precursors, since the compound $BaFe_2Ge_2$, in contrast to $BaFe_2P_2$, is not known and could not be synthesized in the course of this work. The nominal compositions for samples made in course of this work were $x = 0.05$, 0.07, 0.1, 0.15, 0.2, 0.25 and 0.3.

FeP and FeGe alloys as precursors

FeP was prepared by mixing the elements in a stoichiometric ratio of 1:1 (0.643 g Fe, 0.357 g P_{red}) and making a pellet. Powder X-ray diffraction analysis showed small amounts of Fe_2P as side phase. The sample was ground, an addition of P_{red} powder (0.050 g) was given to ensure phase purity and the powder was pelletized. The pellet was sealed in a silica glass tube and thermally treated in a muffle furnace (see Figure 3.20). Powder X-ray diffraction analysis showed phase purity of the precursor (Figure A14, Appendix).

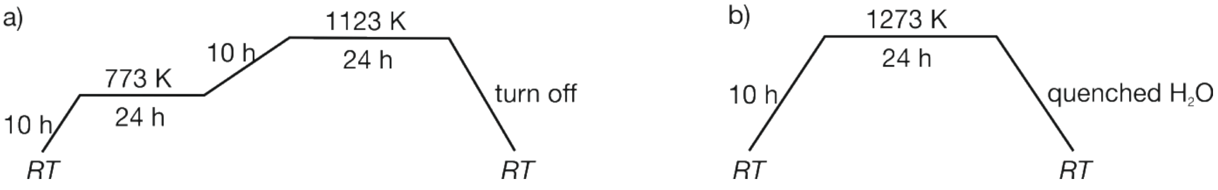

Figure 3.20 Temperature program for FeP precursor: a) first heating cycle; b) second heating cycle.

FeGe was prepared from elements in a ratio 1:1 (0.174 g Fe and 0.226 g Ge) with a total weight of 0.4 g by melting in an arc furnace. Phase purity was confirmed via powder X-ray diffraction measurement (Figure A15, Appendix).

Pseudo-ternary $BaFe(P_{1-x}Ge_x)_2$

Samples were prepared by mixing Ba, FeP alloy and FeGe alloy in different ratios:

$$1Ba+2-2x FeP+2x FeGe \rightarrow BaFe_2P_{2-2x}Ge_{2x} \rightarrow BaFe_2(P_{1-x}Ge_x)_2$$

The ratio of FeP:FeGe was varied to result in nominal compositions of $x = 0.05$, 0.07, 0.1, 0.15, 0.2, 0.25 and 0.3 (see Table 3.10). Excess of Ba (approximately 3 at. %) was given in each case to counteract losses due to reaction with the silica tubes (temperature program given in Figure 3.21).

Powder X-ray analyses for samples with nominal $x < 0.3$ showed the presence of ternary $BaFe_2P_2$[9] phase and binary Fe–Ge phases, no noticeable shifts in the reflections of the ternary phase could be observed.

For the sample with $x_{\mathrm{nom}} = 0.3$ a slight shift of the reflections, belonging to the ternary 122 phase, could be distinguished via powder X-ray diffraction (see Figure A16, Appendix).

Table 3.10 Masses of Ba, FeP and FeGe used for the different nominal compositions of the samples for $BaFe_2(P_{1-x}Ge_x)_2$ solid solution.

Nominal Composition, x	**Ba / g**	**Ba / mol × 10^3**	**FeP / g**	**FeP / mol × 10^3**	**FeGe / g**	**FeGe / mol × 10^3**
0.05	0.269	1.96	0.311	3.58	0.024	0.19
0.07	0.265	1.93	0.303	3.49	0.034	0.26
0.10	0.103	0.75	0.110	1.27	0.018	0.14
0.15	0.173	1.26	0.185	2.14	0.048	0.37
0.20	0.113	0.82	0.110	1.27	0.041	0.32
0.25	0.173	1.26	0.164	1.89	0.080	0.62
0.30	0.128	0.93	0.110	1.27	0.070	0.54

The reflections were indexed and the cell parameters were determined to be $a = 3.857(2)$ Å, $c = 12.464(5)$ Å and $V = 185.4(2)$ Å^3 in comparison to $a = 3.840$ Å, $c = 12.442$ Å and $V = 183.5$ Å^3 for $BaFe_2P_2$.[9] Single crystals were isolated from that sample and measured at room-temperature on a *Stoe IPDS*-2T diffractometer. Most measured single crystals had the composition $BaFe_2P_2$, one measured single crystal showed partial substitution of P with Ge. The compound is stable against air and moisture. Plate shape crystals with metallic luster are found.

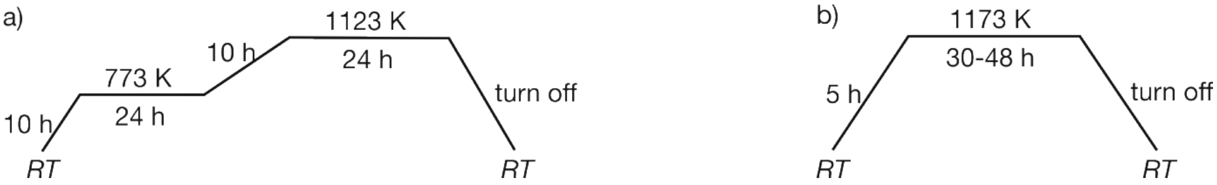

Figure 3.21 Temperature program for $BaFe(P_{1-x}Ge_x)_2$ single crystals: a) first heating cycle; b) second heating cycle.

Semi-quantitative EDX analysis of the single crystal confirmed the inclusion of Ge in the crystal, the elemental composition (Table A12, Appendix; values given in at. %), within standard deviation, corresponds to that determined from single crystal data refinement.

3.3.2. Crystal Structure

The measured single crystal could be refined in the tetragonal *I*4/*mmm* space group, refinement results and structure parameters are given in Table 3.11 - Table 3.13 and Table A13 (Appendix).

Partial substitution of Ge ($x_{exp} = 0.070(6)$) on the P atomic position in $BaFe_2(P_{1-x}Ge_x)_2$ does almost not influence the lattice parameters compared to pure $BaFe_2P_2$.[9] The *a*-axis is only approximately 0.01 Å longer ($a = 3.851(1)$ and 3.84 Å for $BaFe_2(P_{0.930(6)}Ge_{0.070(6)})_2$ and $BaFe_2P_2$, respectively) and the *c*-axis approximately 0.02 Å longer ($c = 12.464(3)$ Å compared to 12.44 Å). The volume increases from $V = 183.5$ Å^3 ($BaFe_2P_2$) to 184.8(1) Å^3 in the substituted compound. The increase of lattice parameters is in correspondence with the larger covalent radius of Ge (1.20 Å compared to 1.07 Å for P).[54] The *c*/*a* ratio for both compounds is identical and has a value of 3.24.

$BaFe_2P_2$ belongs to the so-called uncollapsed type (ucT) with non-bonding interactions of the P atoms along the *c*-direction. The distance between the 2D [FeP] layers ($d_{P–P}$) is 3.84 Å. The small amount of Ge-substitution does affect the interlayer distance only slightly. $d_{P/Ge–P/Ge}$ is found to be 3.819(3) Å long and clearly non-bonding (see Table 3.13). Covalent bonds between P–P occur in the range of 2.2 - 2.5 Å.[26, 38, 55] Even though the *c* lattice parameter increases, $d_{P/Ge–P/Ge}$ decreases for the substituted compound.

The weak interactions between the [FeP/Ge] layers along the *c*-axis strengthens the bonds within the layers as has been reported for members of this family in the past.[4] The distance between Fe atoms in the square network in the *ab*-plane emphasizes weak coupling interactions. $d_{\text{Fe–Fe}}$ is not affected by the Ge-substitution with values of 2.72 Å ($BaFe_2P_2$) and 2.723(1) Å ($BaFe_2(P_{0.930(6)}Ge_{0.070(6)})_2$).

Table 3.11 Crystal data, measurement details and structure parameter for single crystal refinement of $BaFe_2(P_{0.930(6)}Ge_{0.070(6)})_2$, collected at room-temperature. Standard deviations are given in brackets.

Empirical formula		$\mathbf{BaFe_2(P_{0.930(6)}Ge_{0.070(6)})_2}$
Diffractometer		*Stoe IPDS*-2T
Detector distance	/ mm	90
Formula weight	/ g·mol^{-1}	316.81
Space group, *Z*		*I*4/*mmm*, 2
Unit cell dimensions	/ Å	$a = 3.851(1)$
		$c = 12.464(3)$
	/ Å^3	$V = 184.8(1)$
Absorption coefficient	/ mm^{-1}	19.939
Crystal size	/ mm	0.04 × 0.04 × 0.01
Absorption correction		numerical
Calculated density	/ g·cm^{-3}	5.693
F(000)		281
θ range	/ °	3.245 to 30.47
Range in *hkl*		$-4 < h < 5$, ± 5, ± 17
Reflections collected		2040
Independent reflections		112 ($R_{\text{int}} = 0.0793$)
Reflections with $I \geq 2\sigma(I)$		106 ($R_\sigma = 0.0276$)
Data/Parameters		106/9
GOF on F^2		1.117
Final *R* indices [$I \geq 2\sigma(I)$]		$R_1 = 0.0203$
		$wR_2 = 0.0246$
R indices (all data)		$R_1 = 0.0251$
		$wR_2 = 0.0253$
Largest diff. peak and hole	/ e Å^{-3}	0.987, −1.159

The distances between the Fe atoms and the adjacent P atoms in the tetrahedral layer show slight increase upon substitution. $d_{\text{Fe–P}}$ is reported as 2.26 Å for $BaFe_2P_2$ and 2.272(1) Å for $BaFe_2(P_{0.930(6)}Ge_{0.070(6)})_2$, indicating strong covalent bonding interactions.

The height of the square network formed by the Fe atoms and the capping P atoms ($h_{\text{Fe–}E}$) is an important variable within this structure type. It is directly related to the *c* lattice parameter and the atomic *z* coordinate for the P atom. $h_{\text{Fe–P}}$ is increased by 0.02 Å upon Ge substitution (1.19 Å to 1.21 Å). In connection with the distances and the height within the tetrahedral layers the angle of the tetrahedra (α) is only slightly affected as well. α is 116.1 ° in $BaFe_2P_2$ and 115.9(1) ° in the pseudo-ternary compound. In both cases the α varies significantly from the ideal tetrahedral angle of 109.4 °.

Table 3.12 Wyckoff positions, atomic coordinates and isotropic equivalent displacement parameters / Å^2 × 10^3 for $BaFe_2(P_{0.930(6)}Ge_{0.070(6)})_2$ (space group *I*4/*mmm*, *Z* = 2). Standard deviations are given in brackets.

Atom	**Wyckoff position**	***x***	***y***	***z***	**U_{eq} / Å^2 × 10^3**
Ba	2*a*	0	0	0	11(1)
Fe	4*d*	0	½	¼	10(1)
P/Ge	4*e*	0	0	0.3468(2)	11(1)

Comparing the effects of Ge-substitution on P in this work with that of As-substitution on P in $BaFe_2(P_{1-x}As_x)_2$ solid solution[56] leads to some interesting observations. The lattice parameters increase with increasing As content like in the case of $BaFe_2(P_{1-x}Ge_x)_2$. However, the changes within the tetrahedral layer are different for the two solid solutions. In $BaFe_2(P_{0.930(6)}Ge_{0.070(6)})_2$ $d_{Fe–P}$ and z_P becomes larger upon Ge-substitution while α decreases.

Table 3.13 Interatomic distances (*d*) including their multiplicity (after semi-colon), height ($h_{Fe–P/Ge}$) and tetrahedral angle (α) for $BaFe_2(P_{0.930(6)}Ge_{0.070(6)})_2$ and $BaFe_2P_2$.[9] Standard deviations are given in brackets.

Compound	***c*/*a***	**$d_{Fe–Fe}$ / Å**	**$d_{Fe–P/Ge}$ / Å**	**$d_{P/Ge–P/Ge}$ / Å**	**$h_{Fe–P/Ge}$ / Å**	**α / °**
$BaFe_2(P_{0.930(6)}Ge_{0.070(6)})_2$	3.24	2.723(1)	2.272(1); ×4	3.819(3); ×4	1.21	115.9(1)
$BaFe_2P_2$	3.24	2.72	2.26; ×4	3.84; ×4	1.19	116.1

In $BaFe_2(P_{1-x}As_x)_2$ the same increase of $d_{Fe–P/As}$ is observed, but z_P and α become smaller with higher As content. $h_{Fe–P}$ also decreases with higher As content. $BaFe_2(As_{1-x}P_x)_2$ solid solution exhibit superconducting behavior for $x = 0.3 - 0.6$. The range for substituting P for Ge in $BaFe_2(P_{1-x}Ge_x)_2$ could not be determined in this work since only one set of data from single crystal measurement was obtained. It is expected to be rather small since the ternary compound $BaFe_2Ge_2$ has not been synthesized yet and trials with large x_{nom} values only showed small substitution percentage.

3.4. Investigation of $Ca(Fe_{1-x}Rh_x)_2Si_2$ solid solution

Three new compounds in the $Ca(Fe_{1-x}Rh_x)_2Si_2$ solid solution were synthesized and analyzed, the ternary side phases $CaFe_2Si_2$ and $CaRh_2Si_2$ as well as the quaternary $Ca(Fe_{0.34(3)}Rh_{0.66(3)})_2Si_2$. The investigation included powder and single crystal X-ray diffraction methods, magnetic measurements to test for superconductivity of the products as well as calculations of the electronic structure.

3.4.1. Synthesis of the ternary and pseudo-ternary compounds

The samples from the solid solution of $Ca(Fe_{1-x}Rh_x)_2Si_2$ were prepared using a one- or two step synthesize. The starting nominal compositions were chosen as $x = 0$, 0.5 and 1.

$CaFe_2Si_2$ and $CaRh_2Si_2$

$CaFe_2Si_2$ was synthesized in a two-step method. Fe granules and Si pieces were mixed in a 1:1 ratio (0.4 g Fe and 0.202 g Si) and melted in an arc furnace. The regulus was turned around and heated multiple times to guarantee homogeneity of the alloy. The product FeSi was ground and checked for purity with powder X-ray diffraction. The ternary sample was prepared by placing Ca ingots and the FeSi powder in a nominal ratio of 1:2 Ca:FeSi (0.120 g Ca and 0.500 g FeSi) in an Nb ampoule, and thermally treating it in a resistance furnace (temperature program given in Figure 3.22a). The product contained mainly $CaFe_2Si_2$, whereas FeSi and Ca_5Si_3 were detected as side phases (see Figure A17, Appendix).

Multiple attempts were made to obtain phase pure $CaFe_2Si_2$ samples. One approach was to provide excess of Ca: different nominal Ca:FeSi ratios 1.1:2, 1.2:2 and 2:2 were tested (see Table 3.14).

A second approach was to try different heating methods. Samples with the nominal starting composition of 1.1:2 (Ca:FeSi, 0.106 g Ca and 0.4 g FeSi) were either pressed into pellets and heated in an arc-furnace, or samples were placed in Ta ampoules which were sealed and heated to temperatures at 1473 K for 30 minutes in an induction furnace.

Table 3.14 Masses of Ca and FeSi used for the different nominal compositions of the $CaFe_2Si_2$ samples.

Nominal Composition, Ca:FeSi	Ca / g	Ca / mol × 10^3	FeSi / g	FeSi / mol × 10^3
1.1:2	0.132	3.29	0.500	5.96
1.2:2	0.143	3.57	0.500	5.96
2:2	0.240	5.99	0.500	5.96

The samples contained the ternary $CaFe_2Si_2$ phase and binary FeSi and Ca_5Si_3. In the course of this work no phase pure $CaFe_2Si_2$ products could be synthesized with the different methods tested.

Single crystal of good quality was isolated from the sample with 1:2 (Ca:FeSi) ratio thermally treated in a resistance furnace (Nb ampoule) and measured at room-temperature on a *Stoe IPDS*-2T diffractometer. The single crystals of $CaFe_2Si_2$ are stable against air and moisture.

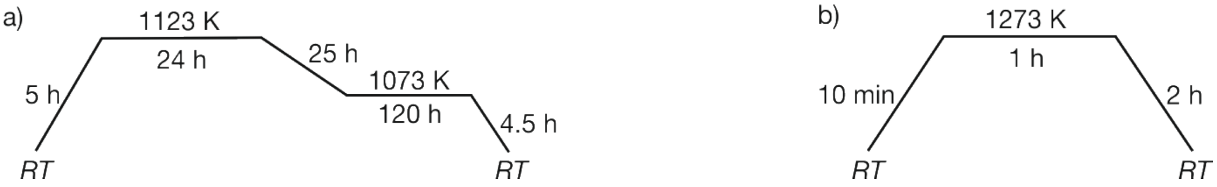

Figure 3.22 Temperature program for: a) $CaFe_2Si_2$; b) second heating cycle of $CaRh_2Si_2$.

$CaRh_2Si_2$ was synthesized in an arc furnace. First, Rh and Si pieces in a ratio of 1:1 (0.201 g Rh, 0.055 g Si) were melted, then Ca ingots (0.048 g) in the ratio 1.23:2 Ca:"RhSi" were added.

Excess of Ca was provided to counteract evaporation losses. After thermal treatment in the arc furnace the sample was ground, pelletized and annealed in a Ta ampoule using an induction furnace (temperature program given in Figure 3.22b). The final product contained $CaRh_2Si_2$ and RhSi as a side phase (see Figure A18, Appendix).

Single crystals (plate shape with metallic luster) were isolated from the product and measured at room-temperature on a *Xcalibur3* (Oxford) diffractometer. The single crystals of $CaRh_2Si_2$ are stable against air and moisture.

$Ca(Fe_{1-x}Rh_x)_2Si_2$

A sample with the nominal composition of $Ca(Fe_{1-x}Rh_x)_2Si_2$ ($x = 0.5$) was prepared from pure elements in a ratio 1:1:1:2 (Ca:Fe:Rh:Si). The elements (0.063 g Ca, 0.088 g Fe, 0.161 g Rh and 0.088 g Si) were placed in a Ta ampoule; the sealed ampoule was thermally treated using a resistance furnace (temperature program given in Figure 3.23).

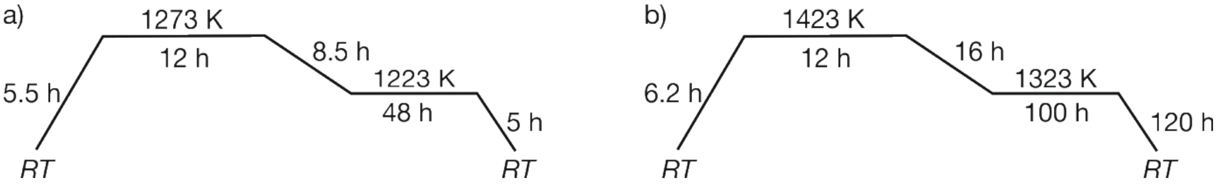

Figure 3.23 Temperature program for the $Ca(Fe_{1-x}Rh_x)_2Si_2$ sample: a) first heating cycle; b) second heating cycle.

The sample was ground, pelletized and annealed to obtain single crystals of good quality. The product contained pseudo-ternary $Ca(Fe_{1-x}Rh_x)_2Si_2$ and FeSi phases determined from powder X-ray diffraction measurement (see Figure A19, Appendix). Air and moisture stable single crystals (plate shape, metallic luster) were isolated and measured at room-temperature on a *Xcalibur3* (Oxford) diffractometer.

Semi-quantitative EDX analyses of the single crystals reveal the elemental compositions (Table A14, Appendix; values given in at. %) which, within the standard deviations, correspond to the composition determined from the single crystal data refinement.

3.4.2. Results and Discussion

3.4.2.1. Crystal structure

Structure details were obtained via single crystal X-ray diffraction measurements for all three compounds. Crystal data refinement details are provided in Table 3.15 and Table A15 - Table A18 (Appendix), the corresponding structural parameters are listed in Table 3.16.

Table 3.15 Crystal data, measurement details and structure parameter for single crystal refinement of $Ca(Fe_{1-x}Rh_x)_2Si_2$ for x_{exp} = 0, 0.66(3), 1; data collected at room-temperature. Standard deviations are given in brackets.

Empirical formula		**$CaFe_2Si_2$**	**$Ca(Fe_{0.34(3)}Rh_{0.66(3)})_2Si_2$**	**$CaRh_2Si_2$**
Diffractometer		*Stoe IPDS*-2T	*Oxford Xcalibur3*	*Oxford Xcalibur3*
Detector distance	/ mm	100	50	50
Formula weight	/ g·mol^{-1}	207.96	264.43	302.08
Space group, *Z*		*I*4/*mmm*, 2	*I*4/*mmm*, 2	*I*4/*mmm*, 2
Unit cell dimensions	/ Å	a = 3.939(1)	a = 4.059(1)	a = 4.070(1)
		c = 10.185(1)	c = 9.939(1)	c = 9.984(1)
	/ Å^3	V = 158.0(1)	V = 163.8(1)	V = 165.3(1)
Absorption coefficient	/ mm^{-1}	11.254	11.591	11.963
Crystal size	/ mm	0.04 × 0.04 × 0.005	0.12 × 0.06 × 0.02	0.05 × 0.04 × 0.01
Absorption correction		numerical	semi-empirical	semi-empirical
Calculated density	/ g·cm^{-3}	4.372	5.363	6.068
F(000)		200	246	276
θ range	/ °	4.00 to 29.15	4.10 to 29.70	4.08 to 32.79
Range in *hkl*		± 5, ± 5, ± 13	$-5 < h < 3$, ± 5, ± 13	± 6, ± 5, $-14 < l < 15$
Reflections collected		1463	1335	1570
Independent reflections		85 (R_{int} = 0.1107)	90 (R_{int} = 0.0368)	114 (R_{int} = 0.0782)
Reflections with $I \geq 2\sigma(I)$		68 (R_σ = 0.0318)	89 (R_σ = 0.0115)	90 (R_σ = 0.0301)
Data/Parameters		68/8	90/10	90/9
GOF on F^2		1.317	1.763	1.093
Final *R* indices [$I \geq 2\sigma(I)$]		R_1 = 0.045	R_1 = 0.030	R_1 = 0.026
		wR_2 = 0.103	wR_2 = 0.062	wR_2 = 0.073
R indices (all data)		R_1 = 0.068	R_1 = 0.030	R_1 = 0.035
		wR_2 = 0.112	wR_2 = 0.063	wR_2 = 0.075
Largest diff. peak and hole	/ e Å^{-3}	0.926, −0.850	1.234, −0.808	3.943, −2.518

The *a* parameter for the three compounds varies about 0.13 Å, increasing linearly from 3.939(1) for $CaFe_2Si_2$ to 4.059(1) Å for the pseudo-ternary compound to 4.070(1) Å for $CaRh_2Si_2$. Substituting Fe with Rh therefore shows a small increase of the *a*-axis. The *c* lattice parameter decreases upon Rh substitution, however a deviation from linearity is observed. It goes from 10.185(1) Å ($CaFe_2Si_2$) to 9.939(1) Å ($Ca(Fe_{0.34(3)}Rh_{0.66(3)})_2Si_2$) and then increases again to 9.984(1) Å for the ternary $CaRh_2Si_2$ compound. The cell volume increases from 158.0(1) Å^3 to 163.8(1) Å^3 and 165.3(1) Å^3 with increasing Rh content.

The atomic position z_{Si} for the compounds also shows a non-linear trend. In $CaFe_2Si_2$ z_{Si} is 0.3746(4), it decreases to 0.3716(4) for $Ca(Fe_{0.34(3)}Rh_{0.66(3)})_2Si_2$ and then increases to 0.3733(4) for $CaRh_2Si_2$. The relation of z_{Si} to c lattice parameter is reflected in the $h_{T\text{–}Si}$ value. The height of the Si atoms above the T square net decreases from 1.27 Å in $CaFe_2Si_2$ to 1.21 Å $Ca(Fe_{0.34(3)}Rh_{0.66(3)})_2Si_2$ and then increases to 1.23 Å in $CaRh_2Si_2$. The observed variations in the structural parameters results in small changes in the interatomic distances. The largest effect is observed for $d_{T\text{–}T}$ within the *ab*-plane. The substitution of Fe with the bigger Rh leads to an elongation of the *T*–*T* distance of almost 0.1 Å: $d_{T\text{–}T}$ goes from 2.785(1) Å to 2.870(1) Å and 2.878(1) Å with increasing Rh content. The distance between the transition metal and Si in the tetrahedra only increases minimally with Rh substitution. $d_{T\text{–}Si}$ changes from 2.343(2) Å to 2.362(2) Å and 2.378(1) Å in $Ca(Fe_{1-x}Rh_x)_2Si_2$ with $x = 0, 0.66(3), 1$; respectively.

As a result of the changes in distances within the [$TSi_{4/4}$] layer the tetrahedral angle becomes noticeable larger for the Rh compounds. α increases from 114.4(2) ° for $CaFe_2Si_2$ to 118.5(8) ° for $Ca(Fe_{0.34(3)}Rh_{0.66(3)})_2Si_2$ and the decreases to 117.6(2) ° for $CaRh_2Si_2$.

Table 3.16 Atomic distances (*d*) including their multiplicity (after semi-colon), height ($h_{T\text{–}Si}$) and angle (α) within the tetrahedral layer for $Ca(Fe_{1-x}Rh_x)_2Si_2$ solid solution. Standard deviations are given in brackets.

Compound	z_{Si}	*c/a*	$d_{T\text{–}T}$ **/ Å**	$d_{T\text{–}Si}$ **/ Å**	$d_{Si\text{–}Si}$ **/ Å**	$h_{T\text{–}Si}$ **/ Å**	α **/ °**
$CaFe_2Si_2$	0.3746(4)	2.59	2.785(1); ×4	2.343(2); ×4	2.555(9); ×1	1.27	114.4(2)
$Ca(Fe_{0.34(3)}Rh_{0.66(3)})_2Si_2$	0.3716(4)	2.45	2.870(1); ×4	2.362(2); ×4	2.552(8); ×1	1.21	118.5(8)
$CaRh_2Si_2$	0.3733(4)	2.45	2.878(1); ×4	2.378(1); ×4	2.529(8); ×1	1.23	117.6(2)

The interlayer distances $d_{Si\text{–}Si}$ are similar for all three compounds, ranging from 2.555(9) Å to 2.552(8) Å and 2.529(8) Å ($Ca(Fe_{1-x}Rh_x)_2Si_2$, $x = 0, 0.66(3), 1$; respectively). The relatively short $d_{Si\text{–}Si}$ values indicate covalent bonding interactions between the [$TSi_{4/4}$] layers along the *c*-direction. Comparison with the interatomic distance of covalent Si–Si bonds in cubic silicon (2.35 Å)[38] and in Si-containing 122 compounds with collapsed $ThCr_2Si_2$ structure type (2.32 - 2.58 Å)[57-60] confirm that observation.

A Vegard-like behavior for the solid solution $Ca(Fe_{1-x}Rh_x)_2Si_2$ ($x = 0$, 0.66(3), 1) is not observed due to the anomalous compression of the structure along the *c*-axis which affects all parameters directly related to the *c* value.

Comparison with $CaCo_2Si_2$[12] leads to interesting observations (important structural parameters given in Table 3.17). The main structural changes are again related to the *c* lattice parameter and z_{Si} parameter. But the changes are mostly in contrast to those observed for full replacement of Fe with the larger Rh in CaT_2Si_2 instead of with the smaller Co. The *c* lattice parameter decreases from 10.185(1) Å to 9.92 Å (Fe and Co, respectively) while the *a* lattice parameter is almost identical (3.939(1) Å to 3.92 Å), *c/a* goes from 2.59 to 2.53 as a result. The volume decreases from 158.0(1) Å^3 to 152 Å^3. The distance between the *T* atoms, which is only affected by the *a* parameter, is therefore also almost identical (d_{T-T} = 2.785(1) Å and 2.77 Å for $CaFe_2Si_2$ and $CaCo_2Si_2$, respectively).

The z_{Si} coordinate is smaller in the Co compound (0.3746(4) vs 0.370). The parameters that are related to the *c*-axis and the z_{Si} coordinate all show noticeable changes. The d_{Si-Si} between the [$TSi_{4/4}$] layers is slightly elongated in $CaCo_2Si_2$ (2.555(9) Å to 2.58 Å) because of the different z_{Si} value while h_{T-Si} decreases (1.27 Å to 1.19 Å in Fe- and Co-compound, respectively). The interlayer interactions are weaker in $CaCo_2Si_2$ therefore the interactions within the [CoSi] layers are strengthened. This can be observed in the shortening of d_{T-Si} from 2.343(2) Å to 2.29 Å (Fe- and Co-compound, respectively). To accommodate the smaller h_{T-Si} and d_{T-Si} values the tetrahedral angle in $CaCo_2Si_2$ has to become wider (117.4 ° compared to 114.4(2) °for $CaFe_2Si_2$).

The substitution of the larger Rh atoms in $CaRh_2Si_2$ with the smaller Co atoms in $CaCo_2Si_2$ (lighter homologue) leads to a decrease in the *a*-axis (4.070(1) Å to 3.92 Å) and *c*-axis (9.984(1) Å to 9.92 Å) while the *c/a* ratio increases (2.45 to 2.53 for Rh- and Co-compound, respectively).

Correspondingly, the volume for $CaCo_2Si_2$ is smaller (152 Å compared to 165.3(1) Å). z_{Si} is slightly decreased from 0.3733(4) to 0.370 upon total Co-substitution. Since the bigger variation is in the *a* parameter, the distances d_{T-T} within the [$TSi_{4/4}$] layers are noticeably smaller in $CaCo_2Si_2$ (2.878(1) Å for $CaRh_2Si_2$

and 2.77 Å for $CaCo_2Si_2$), $d_{T\text{–Si}}$ changes from 2.378(1) Å to 2.29 Å ($CaRh_2Si_2$ and $CaCo_2Si_2$, respectively).

Table 3.17 Important structural parameters for related CaT_2E_2 (T = Fe, Co, Rh; E = Si, As) 122 compounds.

Empirical formula		**$CaCo_2Si_2$[12]**	**$CaFe_2As_2$ ucT[61]**	**$CaRh_2As_2$[62]**
Unit cell:	/ Å	a = 3.92	a = 3.87	a = 4.15
	/ Å	c = 9.92	c = 11.73	c = 10.23
	/ $Å^3$	V = 152	V = 176	V = 176
c/a		2.53	3.03	2.47
z_E		0.370	0.367	0.374
$d_{T\text{–}T}$	/ Å	2.77	2.74	2.93
$d_{T\text{–}E}$	/ Å	2.29	2.37	2.43
$d_{E\text{–}E}$	/ Å	2.58	3.13	2.58
$h_{T\text{–}E}$	/ Å	1.19	1.37	1.27
α	/ °	117.4	109.5	117.2

The tetrahedral angles α, however, are similar for both compounds with 117.6(3) ° and 117.4 °. Due to these observations (shorter intralayer distances and almost identical α values) $h_{T\text{–Si}}$ needs to be smaller in $CaCo_2Si_2$ (1.19 Å) compared to $CaRh_2Si_2$ (1.23 Å). As a result the distance between the tetrahedral layers should be elongated for $CaCo_2Si_2$ which is confirmed from the experimental data ($d_{\text{Si–Si}}$ = 2.529(8) Å and 2.58 Å for $CaRh_2Si_2$ and $CaCo_2Si_2$, respectively). The same observation applies for the comparison of $CaRh_2Si_2$ with $CaCo_2Si_2$ as has been made for the comparison of $CaFe_2Si_2$ with $CaCo_2Si_2$. This is also in correspondence for observations made for other compounds belonging to the 122 family.[4]

The isostructural $Ca(Fe_{1-x}Rh_x)_2As_2$ solid solution has been reported in recent years (x = 0 - 0.6, 1).[61-65] $CaFe_2As_2$ is a parent compound of iron-pnictide superconductors with uncollapsed $ThCr_2Si_2$ type structure (ucT) but can be transformed into the collapsed modification (cT) when hydraulic pressure is applied.[64] The compound does not exhibit superconducting behavior at ambient conductions but it can be induced by physical pressure[64] or by chemical pressure via substitution.[61, 66, 67] $CaRh_2As_2$ on the other hand belongs to the collapsed $ThCr_2Si_2$ type structure (cT).[62] The solid solution shows a structural transformation from ucT to cT above $x \approx 0.024$. The changes in lattice parameters are linear in the range of $0 < x < 0.6$ but do not fulfill Vegard's law when compared with the values for $CaRh_2As_2$. Structural parameters for the ternary CaT_2As_2 (T = Fe, Rh) compounds are listed in Table 3.17.

Comparison of $CaFe_2Si_2$ with its As equivalent (at ambient pressure) shows that the a lattice parameter is slightly smaller in $CaFe_2As_2$ (3.939(1) Å to 3.87 Å) but the c lattice is more than 1.5 Å larger (10.185(1) Å to 11.73 Å). Correspondingly, the c/a ratio is increased from 2.59 to 3.03 due to the longer c-axis in ucT $CaFe_2As_2$. $d_{\text{Fe–Fe}}$ is reduced slightly from 2.785(1) Å to 2.74 Å while $d_{\text{Fe–}E}$ is minimally increased from 2.343(2) Å to 2.37 Å ($CaFe_2Si_2$ and $CaFe_2As_2$, respectively). The biggest changes are observed for the parameters connected to the c-axis: z_E, $d_{E–E}$ and $h_{\text{Fe–}E}$ and α. The changes are a direct result from the non-bonding interactions between the $[FeAs_{4/4}]$ layers in $CaFe_2As_2$. z_{As} is 0.367 ($z_{\text{Si}} = 0.3746(4)$) and slightly smaller, while $d_{\text{As–As}}$ is elongated (3.13 Å compared to $d_{\text{Si–Si}} = 2.555(9)$ Å) and $h_{\text{Fe–As}}$ is larger (1.37 Å compared to $h_{\text{Fe–Si}} = 1.27$ Å). The tetrahedral angle is almost ideal in $CaFe_2As_2$ (109.5 °, compared to 114.4(2) ° in $CaFe_2Si_2$).

Comparing $CaRh_2Si_2$ with its As equivalent shows less significant variations.[62] Both compounds have the collapsed structure and therefore most differences are only due to the size effect of As atoms. The lattice parameters increase when the larger As is present ($a = 4.070(1)$ Å and 4.15 Å; $c = 9.984(1)$ Å and 10.23 Å; $V = 165.3(1)$ Å^3 and 176 Å^3 for Si- and As-compound, respectively). The c/a ratio, z_E and a values are almost identical while all interatomic distances are about 0.05 Å longer in $CaRh_2As_2$. The interactions within and between the $[RhE_{4/4}]$ layers seem to be of similar strength for both compounds.

3.4.2.2. Chemical Bonding

The electronic structure for the two ternary compounds $CaFe_2Si_2$ and $CaRh_2Si_2$ is analyzed using DOS (including the pDOS for T-d, Si-s,p and Ca-d orbitals), the band structure (including fat bands), COHP (including iCOHP) for selected distances and ELF plots.

The total DOS with the contributions of partial DOS of the isostructural compounds are shown in Figure 3.24a,c for $CaFe_2Si_2$ and $CaRh_2Si_2$, respectively. In both cases two blocks which are separated by a band gap of approximately 1 eV are observed.

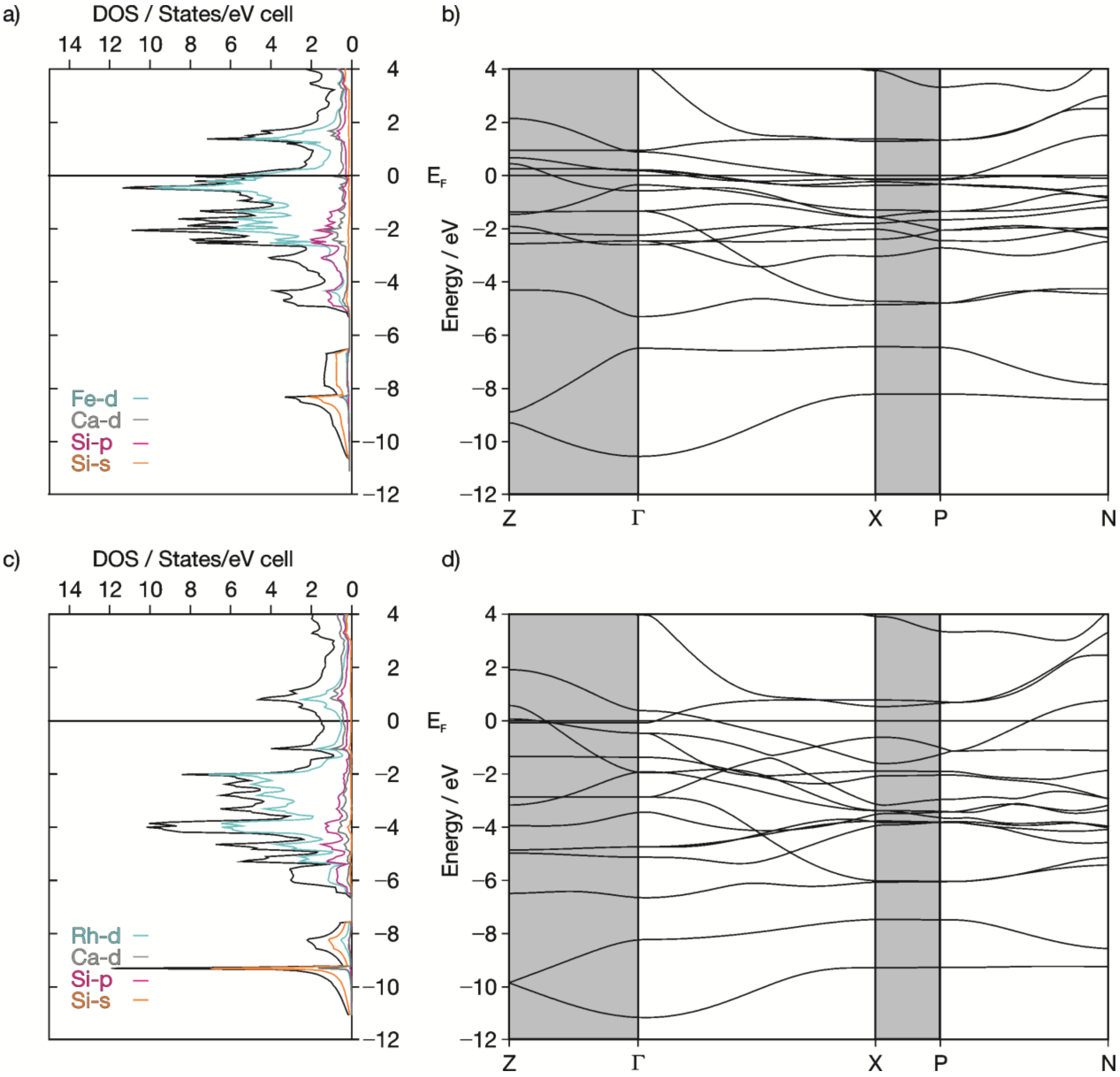

Figure 3.24 DOS and band structure of $CaFe_2Si_2$ (a,b; top) and $CaRh_2Si_2$ (c,d; bottom): a,c) DOS (black) including pDOS of *T*–d (turquois), Ca–d (gray), Si–p (magenta) and Si–s (orange); b,d) total band structure, *k*-paths parallel to the *c*-direction are highlighted gray, path parallel to *ab*-plane are white.

One block is located at lower energies between −10.5 eV and −6.5 eV ($CaFe_2Si_2$) and −11 eV and −7.5 eV ($CaRh_2Si_2$). This block is dominated by the Si-s states with some contributions of the other pDOS. Comparing the shape of the DOS in the block at lower energies certain differences are observed. In $CaFe_2Si_2$ the DOS curve is flatter and the maximum value is approximately 3.5 States/eV cell (at −8.5 eV). In this energy region the DOS of $CaRh_2Si_2$ shows a sharper curve progression with a peak of approximately 12 States/eV cell (at –9.5 eV). The Si-s states lie closer together in $CaRh_2Si_2$ which corresponds with the observed smaller *c*/*a* ratio of that compound.

The block above the band gap for both compounds are at energies higher than –5.5 eV ($CaFe_2Si_2$) and –6.5 eV ($CaRh_2Si_2$). In the first part of that block (–5.5 eV to –1 eV for $CaFe_2Si_2$ and –6.5 eV to –3.5 eV for $CaRh_2Si_2$) the *T*-d and Si-p pDOS are most dominant and show a similar shape. Hybridization of these orbitals corresponds to the covalent *T*–Si bonds within the [$TSi_{4/4}$] layers. The upper half of the second block is mainly made up of *T*-d orbitals (–1 eV T = Fe and –3.5 eV T = Rh).

No band gap is observed at the Fermi level (E_F) for both compounds indicating metallic character. However, E_F is located close to a local maximum formed by the Fe-d for $CaFe_2Si_2$ whereas E_F is located at a local minimum (pseudo-gap) with smaller Rh-d contributions for $CaRh_2Si_2$. The contributions of Ca-d states to the valence bands are negligible since Ca serves as an electron-donor in these compounds (Ca^{2+}). The contribution of Si atoms at the Fermi level is small but non-zero. The observed shift of the Fermi level towards the conduction band for $CaRh_2Si_2$ is due to the higher electron count. The local maximum at E_F in $CaFe_2Si_2$ can be correlated to a degree of possible structural or magnetic instability which has been observed for iron containing 122 superconductors. Full substitution of Rh supplies an increased valence electron count (+2*e*) to the electronic structure which results in the shift of E_F from the local maximum DOS in $CaFe_2Si_2$ to a pseudo-gap located between two local maxima DOS in $CaRh_2Si_2$.

In comparison with the isostructural $CaCo_2Si_2$ compound[12] a similar shift of E_F towards the conduction band is observed. The Fermi level is located close to a pseudo-gap between two local maxima in $CaCo_2Si_2$ similar to $CaRh_2Si_2$. Co also provides two extra valence electrons to the formula like $CaRh_2Si_2$ compared to $CaFe_2Si_2$.

Different observations are made when comparing the DOS of CaT_2Si_2 compounds with that of $SrCo_2Si_2$ (see Figure 3.25). $SrCo_2Si_2$[7] has the same electron count as $CaCo_2Si_2$ and $CaRh_2Si_2$ but the situation at the Fermi level is different. In $SrCo_2Si_2$ E_F is even further shifted towards the conduction band and located next to a local maximum at approximately 0.1 eV. That maximum is located at approximately 1.4 eV in $CaFe_2Si_2$, at approximately 0.9 eV in $CaRh_2Si_2$ and at approximately 0.5 eV in $CaCo_2Si_2$. The difference for $SrCo_2Si_2$ arises due to the different bonding situation between the $[CoSi_{4/4}]$ layers. Unlike the CaT_2Si_2 compounds, which all have covalent bonding interactions between the $[TSi_{4/4}]$ layers, in $SrCo_2Si_2$ the interactions between adjacent Si atoms along the *c*-direction are non-bonding. The formal count of electrons in the CaT_2Si_2 compounds is $Ca^{2+}[T_2Si_2]^{2-}$ with 3D $[T_2Si_2]^{2-}$ while in $SrCo_2Si_2$ the $[Co_2Si_2]^{2-}$ 2D. The 3D $[T_2Si_2]^{2-}$ layers can be regarded as an oxidative coupling product of the 2D $[Co_2Si_2]^{2-}$ layers. Assuming the charge of the cations *Ae* remains the same, this difference affects the electron configuration of the *T* atoms which results in the shift of DOS near the Fermi level.

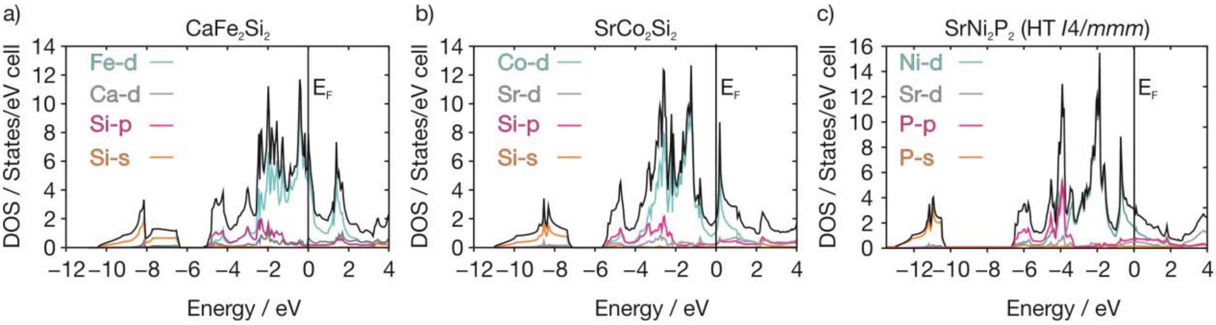

Figure 3.25 DOS including pDOS of $CaFe_2Si_2$ (a), $SrCo_2Si_2$ (b) and $SrNi_2P_2$ (c, HT modification of $SrNi_2P_2$, cell parameters from 373 K measurement)[26]: total DOS shown in black, *T*–d in turquois, *Ae*–d in gray, *E*–p in magenta and *E*–s in orange.

Replacing the Co atoms with Ni shifts the Fermi level even higher towards the conduction band and the local maximum observed at positive energies (1.4 eV in $CaFe_2Si_2$, 0.9 eV in $CaRh_2Si_2$, 0.5 eV in $CaCo_2Si_2$ and 0.1 eV in $SrCo_2Si_2$) is located below the Fermi level for $CaNi_2Ge_2$[68], $SrNi_2Ge_2$[69] and $SrNi_2P_2$ (HT *I4/mmm* modification, lattice parameters obtained at 373 K).[26] $CaNi_2Ge_2$ shows the cT modification with covalent Ge–Ge bonds while $SrNi_2Ge_2$ and $SrNi_2P_2$ (HT) has the ucT modification with isolated layers. In both cases the local peak lies at approximately −0.4 eV. The increase in electron count does not just shift the Fermi level towards the conduction band, the DOS curve above the band gap gets squeezed together. For $CaFe_2Si_2$, $CaCo_2Si_2$, $SrCo_2Si_2$, $BaCo_2Ge_2$, $CaNi_2Ge_2$ and $SrNi_2Ge_2$ the second DOS block above the band gap starts at values larger than

−6 eV regardless of the bonding situation in the compounds. In case of $CaRh_2Si_2$ the band gap ends at −6.5 eV.

Comparison of $CaRh_2Si_2$ (cT) with $AeRh_2As_2$ (*Ae* = Sr, Ba, both ucT)[62, 70] shows that the electron count of the bonded Si-dimer is similar to the electron count of the two non-bond As anions in the uncollapsed structure. The same goes for $CaFe_2Si_2$ (cT) and $CaFe_2As_2$ (ucT).[48] Similar charge distributions are observed in the $CaFe_2E_2$ compounds and are expected for the $AeRh_2E_2$ compounds. The similarities of the charge distribution are also reflected in DOS analyses. The shape of the Fe-d pDOS in both compounds is similar near the Fermi level; a pseudo-gap next to E_F has also been reported for $CaFe_2As_2$.

The observations made in the DOS analyses are reflected by the band structure of the two CaT_2Si_2 compounds (see Figure 3.24b, d). The *k*-paths parallel to the *c*-direction are $\mathrm{Z} \rightarrow \Gamma$ and X → P; the paths parallel to the *ab*-plane are $\Gamma \rightarrow \mathrm{X}$ and P → N (Brillouin zone[51] for space group *I*4/*mmm* is shown in Figure A13, Appendix).

The individual contribution of orbitals is determined by fat band representations for both compounds (Figure 3.26 for $CaFe_2Si_2$ and Figure 3.27 for $CaRh_2Si_2$). As previously described, the bands at low energies (−10.5 eV to −6.5 eV for $CaFe_2Si_2$ and −11 eV to −7.5 eV for $CaRh_2Si_2$) are closer together in $CaRh_2Si_2$. These bands are formed by the Si-s orbitals (see Figure 3.26f and Figure 3.27f). The Fe-d_{xy} fat bands are located mainly at −2 eV contributing to the valence band and at 0.9 eV mainly responsible for the Fe-d states in the conduction band (Figure 3.26a). The largest contribution at the Fermi level comes from Fe-$d_{x^2-y^2}$ fat bands (Figure 3.26b) and from Fe-$d_{xz,yz}$ fat bands (Figure 3.26c). Both orbitals cross the Fermi level in the $\Gamma \rightarrow \mathrm{X}$ and P → N sections (crystallographic *ab*-plane). The Fe-$d_{x^2-y^2}$ orbitals point towards the nearest neighboring Fe atoms within the square Fe-plane while the Fe-$d_{xz,yz}$ orbitals point toward the adjacent Si atoms in the tetrahedral layer. The Fe-$d_{xz,yz}$ fat bands show strong hybridization with the Si-p fat bands (Figure 3.26e) in the region of −3.5 eV and −1 eV which indicate strong covalent Fe–Si bonds. In the section $\mathrm{Z} \rightarrow \Gamma$ (crystallographic *c*-direction) the Fermi level is crossed by Fe-d_{z^2} bands together with Si-p bands.

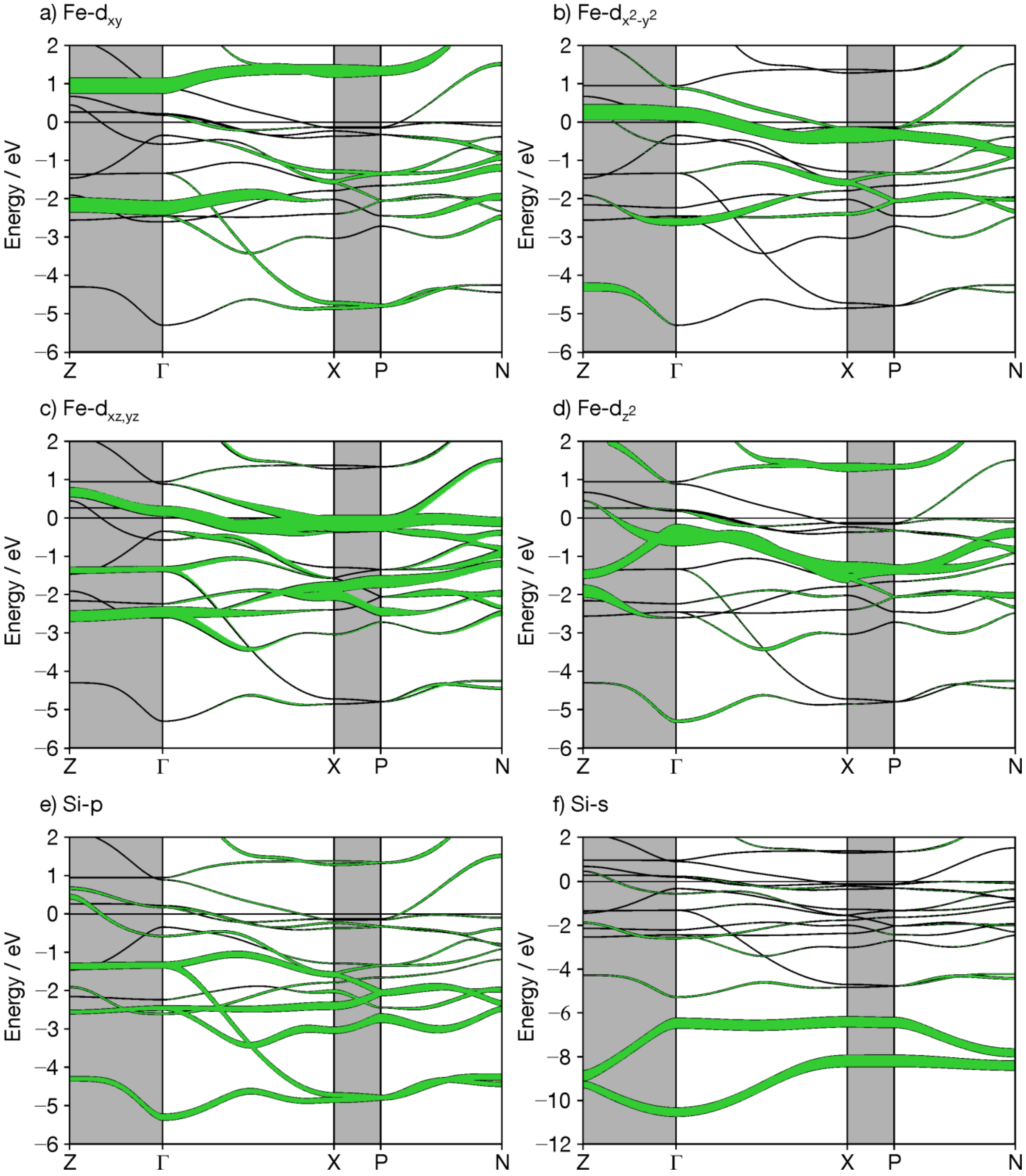

Figure 3.26 Band structure including fat band representation of $CaFe_2Si_2$ orbitals: a) Fe-d_{xy}; b) Fe- $d_{x^2-y^2}$; c) Fe-$d_{xz,yz}$; d) Fe-d_{z^2}; e) Si-p; f) Si-s. *k*-paths parallel to the *c*-direction are highlighted gray, paths parallel to *ab*-plane are white.

The situation for $CaRh_2Si_2$ is slightly different because of the shift of E_F, as previously discussed. The upper Rh-d_{xy} fat bands are now located below the Fermi level (–0.1 eV) and the lower ones are shifted to –5 eV (Figure 3.27a). As a result the Rh-d_{xy} and Rh-$d_{xz,yz}$ fat bands (Figure 3.27c) have now the main contributions close to E_F.

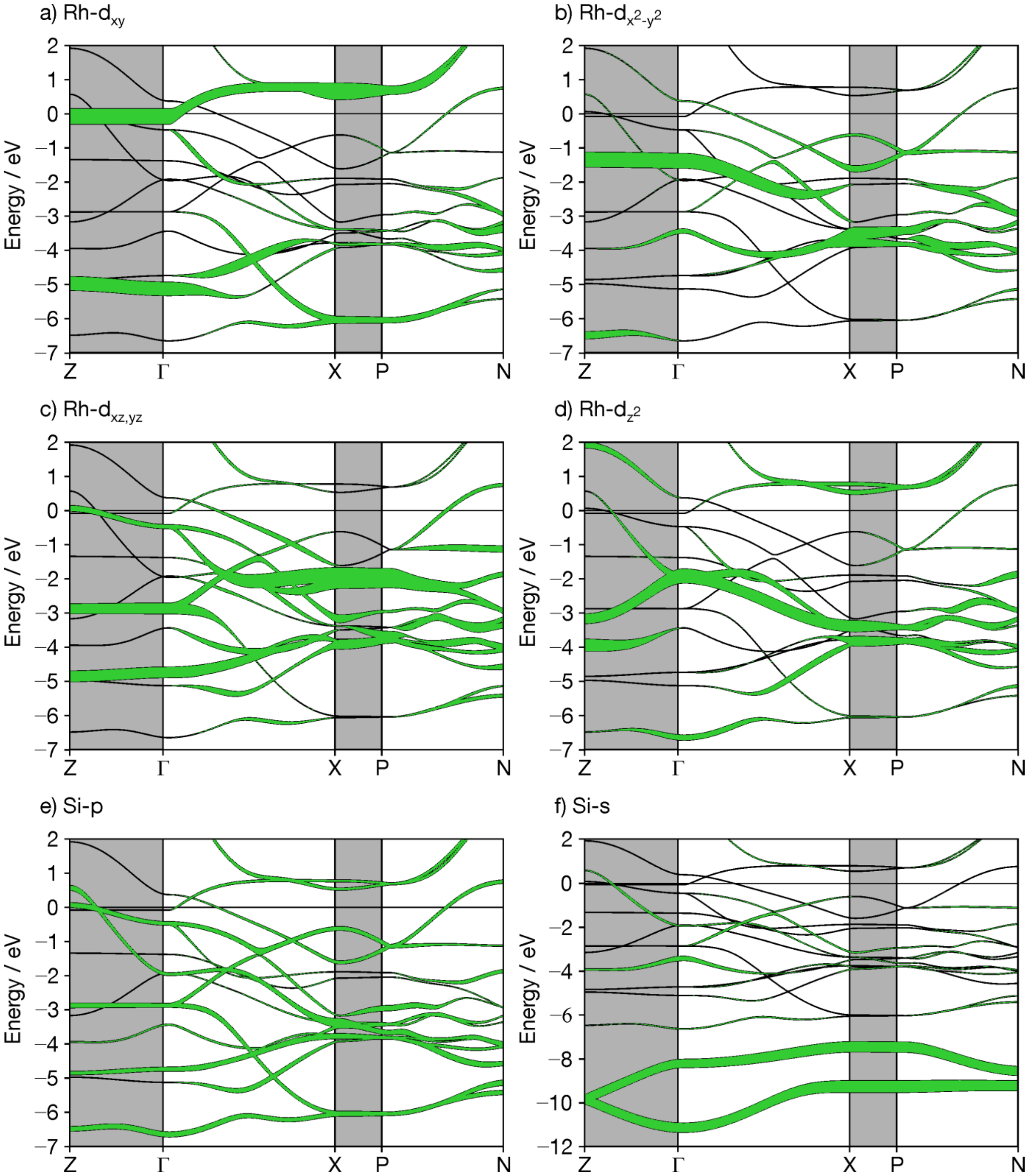

Figure 3.27 Band structure including fat band representation of $CaRh_2Si_2$ orbitals: a) Rh-d_{xy}; b) Rh-$d_{x^2-y^2}$; c) Rh-$d_{xz,yz}$; d) Rh-d_{z^2}; e) Si-p; f) Si-s. *k*-paths parallel to the *c*-direction are highlighted gray, paths parallel to *ab*-plane are white.

The Rh-$d_{xz,yz}$ orbitals that point towards the Si atoms show again strong hybridization with the Si-p fat bands (Figure 3.27e), indicating strong Rh–Si interactions. The Rh-$d_{x^2-y^2}$ orbitals (Figure 3.27b), that point to the adjacent Rh atoms, are shifted to −1.3 eV and the Rh-d_{z^2} fat bands (Figure 3.27d) are shifted approximately 2 eV to lower energies. As a result the Fermi level is mainly crossed by Si-p bands hybridizing with the Rh-$d_{xz,yz}$ ones along $\mathrm{Z} \rightarrow \Gamma$ (*c*-direction). Along

Γ → X and P → N (*ab*-direction) the Si-p orbitals hybridize with the Rh-d_{x2-y2} and Rh-d_{xy} orbitals and cross the Fermi level.

The lower valence electron count in CaFe$_2$Si$_2$ and CaRh$_2$Si$_2$ compared to "SrNi$_2$P$_{0.86}$Ge$_{0.14}$" (described in Chapter 3.2.2.4) results in a shift of the Fermi level towards lower energies. In "SrNi$_2$P$_{0.86}$Ge$_{0.14}$" a fat band touches the Fermi level at the P *k*-point with contributions from the Ni-$d_{xz,yz}$ and "P/Ge"-p_z orbitals. The band structures of CaFe$_2$Si$_2$ and CaRh$_2$Si$_2$ show no touching or crossing of bands at the P *k*-point, a clear band gap is observed along the X → P path.

The strength of the interatomic bonds within the CaT_2Si$_2$ compounds has been investigated using Crystal Orbital Hamilton Population (COHP) and integrated COHP (iCOHP) calculations. The COHPs and iCOHPs of the covalent bonds *T*–*T*, *T*–Si and Si–Si are plotted in Figure A20 (Appendix) for CaFe$_2$Si$_2$ (a-c) and CaRh$_2$Si$_2$ (d-f). In Table 3.18 a list of interatomic distances and the corresponding iCOHP values for the covalent bonds are given.

Table 3.18 Interatomic distances (*d*) for CaFe$_2$Si$_2$ and CaRh$_2$Si$_2$ and selected integrated Crystal Orbital Hamilton Populations (–iCOHP) values at E$_F$.

		***d* / Å**	**iCOHP / eV**			***d* / Å**	**iCOHP / eV**
CaFe$_2$Si$_2$							
Ca	–Ca	3.938(1)	-	Si	–Fe	2.343(2)	2.71
	–Fe	3.219(1)	-		–Si	2.555(9)	1.98
	–Si	3.064(2)	0.65	Fe	–Fe	2.785(1)	1.17
CaRh$_2$Si$_2$							
Ca	–Ca	4.069(2)	-	Si	–Rh	2.378(1)	2.68
	–Rh	3.220(1)	-		–Si	2.529(8)	2.10
	–Si	3.143(2)	0.65	Rh	–Rh	2.878(1)	1.02

The iCOHP values at E$_F$ for CaFe$_2$Si$_2$ and CaRh$_2$Si$_2$ reflect the observations made for the bond lengths in the structure. In CaFe$_2$Si$_2$ the distance between the Si atoms of two adjacent [TSi$_{4/4}$] layers is slightly longer than in CaRh$_2$Si$_2$, while the distances between the Fe–Si atoms and Fe–Fe atoms within the layer are shorter compared to Rh–Si and Rh–Rh. The iCOHP gives higher values for Fe–Si and Fe–Fe (2.71 eV and 1.17 eV, respectively) than for Rh–Si and Rh–Rh (2.68 eV and 1.02 eV, respectively). The shorter Si–Si distance in $CaRh_2Si_2$ gives a higher iCOHP value (2.10 eV) than that of $CaFe_2Si_2$ (1.98 eV).

Comparison of the iCOHP values for $SrCo_2Si_2$ and $CaCo_2Si_2$ (Table 3.19) shows that the value for Si–Si for the Sr-compound, which has no bonding between the Si–Si atoms, is twice as large for $SrCo_2Si_2$ than for $CaCo_2Si_2$ (collapsed modification with covalent Si–Si bonds). The iCOHP value for Co–Si and Co–Co are slightly larger in $SrCo_2Si_2$ (2.80 eV and 0.99 eV, respectively) than that of $CaCo_2Si_2$ (2.73 eV and 0.94 eV, respectively). The Co–Co iCOHP values for $AeCo_2Si_2$ (Ae = Ca, Sr) are in both cases smaller than the Fe–Fe and Rh–Rh ones for $CaFe_2Si_2$ and $CaRh_2Si_2$ whereas the Co–Si values are slightly larger than in the Fe- and Rh-silicides. The three CaT_2Si_2 (T = Fe, Co, Rh) compounds, which all contain covalent bonds between the tetrahedral layers, have Si–Si iCOHP values of 1.82 - 2.10 eV while for $SrCo_2Si_2$ it is only 0.93 eV. This reflects the observation that weaker [$TSi_{4/4}$] interlayer interactions strengthen the intralayer interactions.

Table 3.19 Selected interatomic distances (*d*) and integrated Crystal Orbital Hamilton Populations (–iCOHP) values at E_F for $CaCo_2Si_2$ and $SrCo_2Si_2$.[7, 12]

		***d* / Å**	**iCOHP / eV**			***d* / Å**	**iCOHP / eV**
$CaCo_2Si_2$				$SrCo_2Si_2$			
Co	–Co	2.77	0.99	Co	–Co	2.81	0.94
	–Si	2.29	2.73		–Si	2.30	2.80
Si	–Si	2.58	1.82	Si	–Si	2.90	0.93

Additional information about the bonding situation in the compounds is obtained from Electron Localization Function (ELF) analyses (Figure 3.28). For both compounds a bisynaptic valence basin ($\eta > 0.72$) can be observed between the Si atoms along the *c*-direction (Figure 3.28a, b). The basins are denoted with ①. Similar basins for localized bonds have been described in $CaCo_2Si_2$[12] and $CaNi_2Ge_2$.[68] In $SrCo_2Si_2$[7] no bisynaptic valence basin is observed along the *c*-direction due to the elongated Si–Si distance. Monotactic (non-bonding) ELF domains between the Si atoms of adjacent layers are found in $SrCo_2Si_2$ which are orientated towards each other indicating only very weak bonding interactions.

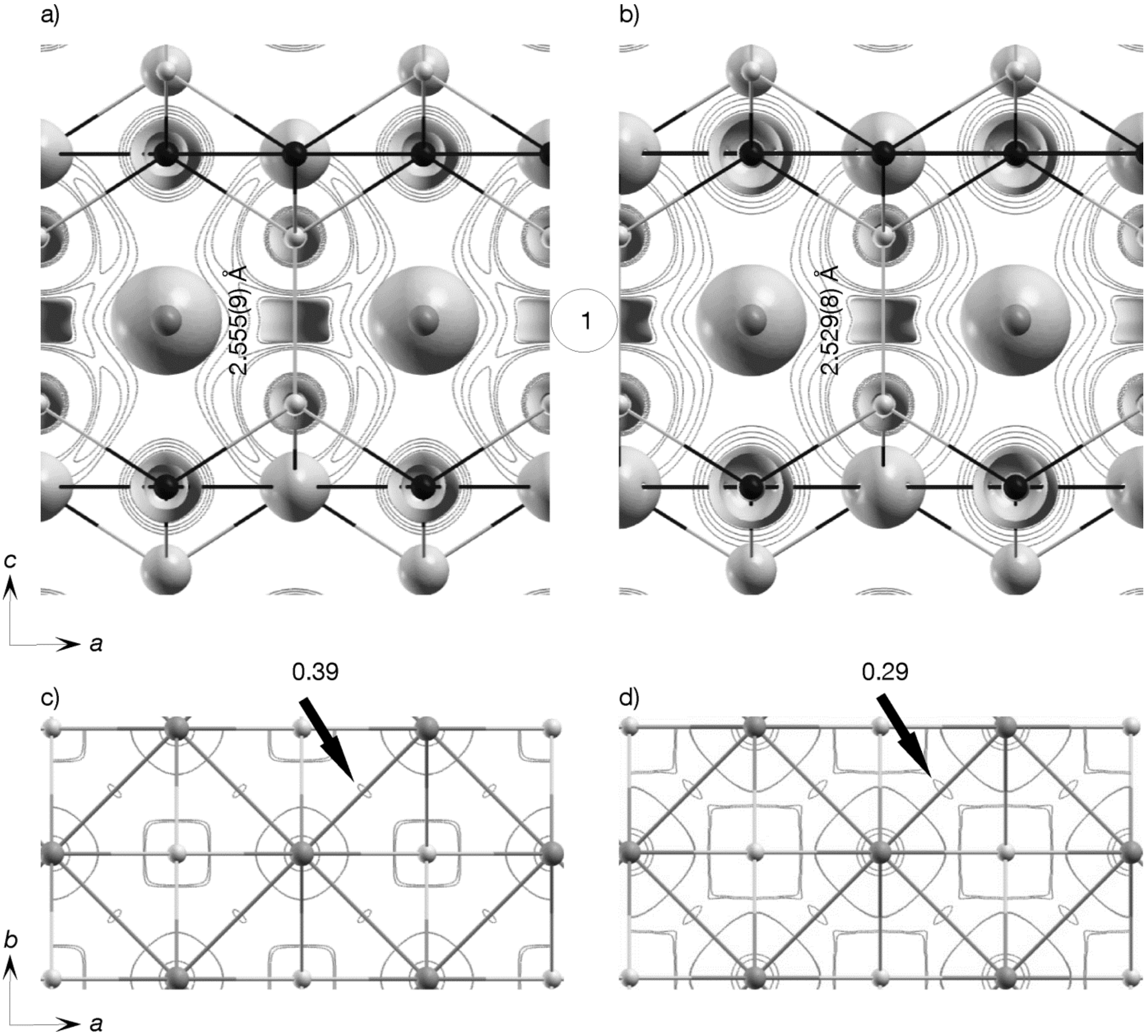

Figure 3.28 ELF representation of $CaFe_2Si_2$ (a,c) and $CaRh_2Si_2$ (b,d) calculated from the all electron density. a, c) 3D plot with bonding ELF domains located between the Si atoms (denoted ①) along the *c*-direction; b, d) contour line diagram in the *ab*-plane at the *T* square planar layer. Only the region $\eta = 0.39 - 0.40$ ($CaFe_2Si_2$, c) and $\eta = 0.285 - 0.29$ ($CaRh_2Si_2$, d) are displayed for clarity reasons.

The contour line diagrams in the *ab*-plane show the weak interactions between the Fe–Fe atoms (Figure 3.28c) with an ELF attractor at $\eta = 0.39$ and between the Rh–Rh atoms (Figure 3.28d) with an ELF attractor at $\eta = 0.29$ (indicated with the arrows in both figures). Similar results were obtained for isostructural LaT_2Ge_2 (T = Mn - Co) compounds.[71] The ELF attractors indicate interactions between the $d_{x^2-y^2}$ orbitals of the Fe or Rh atoms in the *ab*-plane.

3.5. References

[1] Z. Ban, M. Sikirica, *Acta Cryst.* **1965**, *18*, 594-599.

[2] *FindIt, ICSD Database, Version 1.7.0*, FIZ Karlsruhe, Germany, **2010**.

[3] P. Villars, K. Cenzual, *Pearson's Crystal Data: Crystal Structure Database for Inorganic Compounds (on CD-ROM)*, ASM International @, Materials Park, Ohio, USA, **2007/8**.

[4] R. Hoffmann, C. Zheng, *J. Phys. Chem.* **1985**, *89*, 4175-4181.

[5] G. Venturini, B. Malaman, *J. Alloy. Compd.* **1996**, *235*, 201-209.

[6] O. S. Zarechnyuk, P. I. Kripyakevich, E. I. Gladyshevskii, *Krystallografiya* **1964**, *9*, 835-838.

[7] V. Hlukhyy, A. V. Hoffmann, T. F. Fässler, *J. Solid State Chem.* **2013**, *203*, 232–239.

[8] A. V. Hoffmann, *Masterthesis*, Uppsala University **2010**.

[9] A. Mewis, *Z. Naturforsch.* **1980**, *35b*, 141-145.

[10] A. Mewis, A. Distler, *Z. Naturforsch., B: J. Chem. Sci.* **1980**, *35*, 391-393.

[11] H. Schlenger, H. Jacobs, R. Juza, *Z. Anorg. Allg. Chem.* **1971**, *385*, 177-201.

[12] L. Siggelkow, V. Hlukhyy, T. F. Fässler, *Z. Anorg. Allg. Chem.* **2010**, *636*, 378-384.

[13] P. Klüfers, A. Mewis, *Z. Naturforsch. B.* **1978**, *33*, 151-155.

[14] R. J. Cava, H. Takagi, B. Batlogg, H. W. Zandbergen, J. J. Krajewski, W. F. Peck Jr, R. B. van Dover, R. J. Felder, T. Siegrist, K. Mizuhashi, J. O. Lee, H. Eisaki, S. A. Carter, S. Uchida, *Nature* **1994**, *367*, 146-148.

[15] R. J. Cava, H. Takagi, H. W. Zandbergen, J. J. Krajewski, W. F. Peck Jr, T. Siegrist, B. Batlogg, R. B. van Dover, R. J. Felder, K. Mizuhashi, J. O. Lee, H. Eisaki, S. Uchida, *Nature* **1994**, *367*, 252-253.

[16] R. J. Cava, H. W. Zandbergen, B. Batlogg, H. Eisaki, H. Takagi, J. J. Krajewski, W. F. Peck Jr, E. M. Gyorgy, S. Uchida, *Nature* **1994**, *327*, 245-247.

[17] T. Siegrist, H. W. Zandbergen, R. J. Cava, J. J. Krajewski, W. F. Peck Jr, *Nature* **1994**, *367*, 254-256.

[18] D. Kasinathan, A. Ormeci, K. Koch, U. Burkhardt, W. Schnelle, A. Leithe-Jasper, H. Rosner, *New Journal of Physics* **2009**, *11*, 025023.

[19] M. Rotter, M. Pangerl, M. Tegel, D. Johrendt, *Angew. Chem. Int. Ed.* **2008**, *47*, 7949-7952.

[20] M. Rotter, M. Tegel, D. Johrendt, *Phys. Rev. Lett.* **2008**, *101*, 107006.

[21] F. Ronning, N. Kurita, E. D. Bauer, B. L. Scott, T. Park, T. Klimczuk, R. Movshovich, J. D. Thompson, *J.Phys.: Condens. Matter* **2008**, *20*, 342202.

[22] T. Mine, H. Yanagi, T. Kamiya, Y. Kamihara, M. Hirano, H. Hosono, *Solid State Commn.* **2008**, *147*, 111.

[23] F. Ronning, T. Klimczuk, E. D. Bauer, H. Volz, J. D. Thompson, *J. Phys.: Cond. Matt* **2008**, *20*, 322201.

[24] C. D. Yang, H. C. Hsu, W. Y. Tseng, H. C. Chen, H. C. Ku, M. N. Ou, Y. Y. Chen, Y. Y. Hsu, *J. Phys.: Conf. Ser.* **2011**, *273*, 012089.

[25] F. Ronning, E. D. Bauer, T. Park, S.-H. Baek, H. Sakai, J. D. Thompson, *Phys. Rev. B.* **2009**, *79*, 134507.

[26] V. Keimes, D. Johrendt, A. Mewis, C. Huhnt, W. Schlabitz, *Z. anorg. allg. Chem.* **1997**, *623*, 1699-1704.

[27] A. S. Sefat, M. A. McGuire, R. Jin, B. C. Sales, D. Mandrus, F. Ronning, E. D. Bauer, Y. Mozharivskyi, *Phys. Rev. B* **2009**, *79*, 094508.

[28] A. S. Sefat, D. J. Singh, R. Jin, M. A. McGuire, B. C. Sales, F. Ronning, D. Mandrus, *Physica C* **2009**, *469*, 350-354.

[29] D. Hirai, F. von Rohr, R. J. Cava, *Phys. Rev. B* **2012**, *86*, 100505(R).

[30] Y. Mizuguchi, Y. Hara, K. Deguchi, S. Tsuda, T. Yamaguchi, K. Takeda, H. Kotegawa, H. Tou, Y. Takano, *Supercond. Sci. Technol.* **2010**, *23*, 054013.

[31] H. Fujii, A. Sato, *J. Alloy. Compd.* **2009**, *487*, 198-201.

[32] M. Tegel, *HConvert*, 0.8ed., Ludwig Maximilians Universität, München, **2011**.

[33] A. Coelho, *TOPAS-Academic*, 4.1ed., Coelho Software, Brisbane, **2007**.

[34] J. Rodriguez-Carvajal, *FullProf. 2k*, 5.4ed., Laboratoire Leon Brillouin (CEA-CNRS), France, **2014**.

[35] L. Pauling, B. Kamb, *PNAS* **1986**, *83*, 3569-3571.

[36] W. Dörrscheidt, N. Niess, H. Schäfer, *Z. Naturforsch., B: J. Chem. Sci.* **1976**, *31*, 890-891.

[37] V. Hlukhyy, A. Senyshyn, D. Trots, T. F. Fässler, *HASYLAB Ann. Rep.* **2007**, *1*, 1021.

[38] A. F. Holleman, N. Wiberg, *Lehrbuch der Anorganischen Chemie* **2007**, *102. Ed.*

[39] C.-H. Lee, A. Iyo, H. Eisaki, H. Kito, M. T. Fernandez-Diaz, T. Ito, K. Kihou, H. Matsuhata, M. Braden, K. Yamada, *J. Phys. Soc. Jpn.* **2008**, *77*, 083704.

[40] V. Keimes, A. Hellmann, D. Johrendt, A. Mewis, *Z. Anorg. Allg. Chem.* **1998**, *624*, 830-836.

[41] W. K. Hofmann, W. Jeitschko, *J. Solid State Chem.* **1986**, *51*, 152-158.

[42] R. J. Goetsch, V. K. Anand, A. Pandey, D. C. Johnston, *Phys. Rev. B* **2012**, *85*, 054517.

[43] M. Tinkham, *Introduction to Superconductivity*, 2 ed., Dover Publications INC, Mineola, New York, **2004**.

[44] J. W. Wang, I. A. Chen, T. L. Hung, Y. B. You, H. C. Ku, Y. Y. Hsu, J. C. Ho, Y. Y. Chen, *Phys. Rev. B* **2012**, *85*, 024538.

[45] T. L. Hung, I. A. Chen, C. H. Huang, C. Y. Lin, C. W. Chen, Y. B. You, S. T. Jian, M. C. Yang, Y. Y. Hsu, J. C. Ho, Y. Y. Chen, H. C. Ku, *J. Low Temp Phys* **2013**, *171*, 148-155.

[46] N. H. Sung, J. S. Rhyee, B. K. Cho, *Phys. Rev. B* **2011**, *83*, 094511.

[47] I. R. Shein, A. L. Ivanovskii, *Phys. Rev. B* **2009**, *79*, 054510.

[48] T. Yildirim, *Phys. Rev. Lett.* **2009**, *102*, 037003.

[49] I. R. Shein, A. L. Ivanovskii, *JETP Letters* **2008**, *88*, 107-110.

[50] A. Leithe-Jasper, W. Schnelle, C. Geibel, H. Rosner, *Phys. Rev. Lett.* **2008**, *101*, 207004.

[51] P. E. Blöchl, O. Jepsen, O. K. Andersen, *Phys. Rev. B* **1994**, *49*, 16223.

[52] E. Z. Kuchinskii, M. Sadovskii, *JETP Letters* **2010**, *91*, 729-733.

[53] *WinTools*, Bruker, Berlin, **1997**.

[54] B. Cordero, V. Gomez, A. E. Platero-Prats, M. Reves, J. Echeverria, E. Cremades, F. Barragan, S. Alvare, *Dalton Trans.* **2008**, 2832-2838.

[55] J. R. Van Wazer, *Phosphorous and its Compounds Band 1*, Interscience, New York, **1958**.

[56] M. Rotter, C. Hieke, D. Johrendt, *Phys. Rev. B* **2010**, *82*, 014513.

[57] A. Palenzona, S. Cirafici, F. Canepa, *J. Less Comm. Met.* **1987**, *135*, 185-194.

[58] C. Kranenberg, D. Johrendt, A. Mewis, R. Pottgen, G. Kotzyba, H. Trill, B. D. Mosel, *J. Solid State Chem.* **2002**, *167*, 107-112.

[59] N. May, H. Schäfer, *Z. Naturforsch.* **1972**, *27*, 864-865.

[60] B. Eisenmann, N. May, W. Mueller, H. Schaefer, A. Weiss, J. Winter, G. Ziegleder, *Z. Naturforsch.* **1970**, *25*, 1350-1352.

[61] G. Wu, H. Chen, T. Wu, Y. L. Xie, Y. J. Yan, R. H. Liu, X. F. Wang, J. J. Ying, Chen, X.H., *J. Phys.: Condens. Matter* **2008**, *20*, 422201.

[62] V. B. Zinth, *Dissertation* **2012**, *Ludwig-Maximilians-Universität München*.

[63] N. Ni, S. Nandi, A. Kreyssig, A. I. Goldman, E. D. Mun, S. L. Bud'ko, P. C. Canfield, *Phys. Rev. B* **2008**, *78*, 014523.

[64] P. C. Canfield, S. L. Bud'ko, N. Ni, A. Kreyssig, A. I. Goldman, R. J. McQueeney, M. S. Torikachvili, D. N. Argyriou, G. Luke, W. Yu, *Physica C* **2009**, *469*, 404-412.

[65] Y. Qi, L. Wang, Z. Gao, D. Wang, X. Zhang, C. Wang, C. Yao, Y. Ma, *New J. Phys.* **2011**, *13*, 033020.

[66] Z. Gao, Y. Qi, L. Wang, D. Wang, X. Zhang, C. Yao, C. Wang, Y. Ma, *EPL* **2011**, *95*, 67002.

[67] J. R. Jeffries, N. P. Butch, K. Kirshenbaum, S. R. Saha, S. T. Weir, Y. K. Vohra, J. Paglione, *Phys. Rev. B* **2012**, *85*, 184501.

[68] V. Hlukhyy, N. Chumalo, V. Zaremba, T. F. Fässler, *Z. Anorg. Allg. Chem.* **2008**, *634*, 1249-1255.

[69] I. R. Shein, A. L. Ivanovskii, *Physica B* **2010**, *405*, 3213-3216.

[70] Y. Singh, Y. Lee, S. Nandi, A. Kreyssig, A. Ellern, S. Das, R. Nath, B. N. Harmon, A. I. Goldman, D. C. Johnston, *Phys. Rev. B* **2008**, *78*, 104512.

[71] M. Kohout, F. R. Wagner, Y. Grin, ***Theor. Chem. Acc.*** **2002**, *108*, 150-156.

4. Intermetallic CaCoSi phase

4.1. Introduction

Intermetallic compounds containing edge-sharing *TE*$_4$ (*T* = transition metals, *E* = 3rd - 6th main group elements) tetrahedral layers have been known for decades. The ternary compounds with CeFeSi[1, 2] (alternatively anti-PbFCl) structure type (space group *P*4/*nmm*, No. 129) contain two-dimensional polyanionic [*TE*]$^{n-}$ layers. A number of compounds with rare earth metals (*RE*), alkaline metals (*A*) and alkaline earth metals (*Ae*) as cations have been reported.[3, 4] The polyanionic [*TE*] units commonly contain the transition metals (*T*) Mn, Fe, Co, Ni and tetrel or pnictide elements (*E*). Mg*T*Ge compounds (*T* = Mn, Fe, Co)[5-7] all crystallize in the CeFeSi structure type while ternary *Ae*NiGe compounds (*Ae* = Mg, Ca, Sr, Ba) show structural variations for the different alkaline earth metals: depending on the cation the polyanionic [NiGe] networks decrease in dimensionality with increasing cation size. The ternary phase CaMnSi is the only compound besides CaCoSi in the Ca*T*Si (*T* = Mn - Ni) row known so far,[5] it has the CeFeSi structure type. In the system *Ae*CoSi (*Ae* = Mg - Ba) CaCoSi is the first member reported so no trend of dimensionality within this system can be made.

Magnetism in these compounds varies and depends on the composition. For example, the *RE*CoSi phases (*RE* = La - Sm, Gd, Tb) show different magnetic properties. Whereas Pauli-paramagnetism is reported for La, Curie-Weiss paramagnetism for Ce and Pr and antiferromagnetism for Nd, Sm, Gd and Tb,[8] the iron pnictide compounds LiFeAs, NaFeAs and LiFeP show superconducting behavior with critical temperatures (T_c) of 18 K,[9] 12 K[10] and 6 K,[11] respectively. The cations in *RE*CoSi compounds have a strong magnetic moment and are responsible for the observed magnetism. In the iron-pnictide compounds the alkaline metals do not have a very strong magnetic moment and the magnetism of the tetrahedral layers that leads to superconductivity is dominant.

The electronic structure for compounds with CeFeSi structure type is dominated by the transition metal-d states which are mainly located at and below the Fermi level, the compounds exhibit metallic character. The structural motif of the tetrahedral layer forms the shape of the DOS below the Fermi level. The magnetic properties are governed by the electronic structure at the Fermi level. The elemental composition can shift the conduction band towards higher or lower energy which gives rise to the different physical properties.

4.2. Results and discussion

In this chapter the results of the chemical bonding analysis from electronic structure calculations of CaCoSi will be discussed.

The compound crystallizes in the CeFeSi structure type (space group *P*4/*nmm*) with $a = 3.977(1)$ Å and $c = 7.089(5)$ Å. Synthesis results and detailed crystal structure description has been given in the Master-thesis[12] in 2010 and a corresponding publication.[13] Figure 4.1 shows the crystal structure.

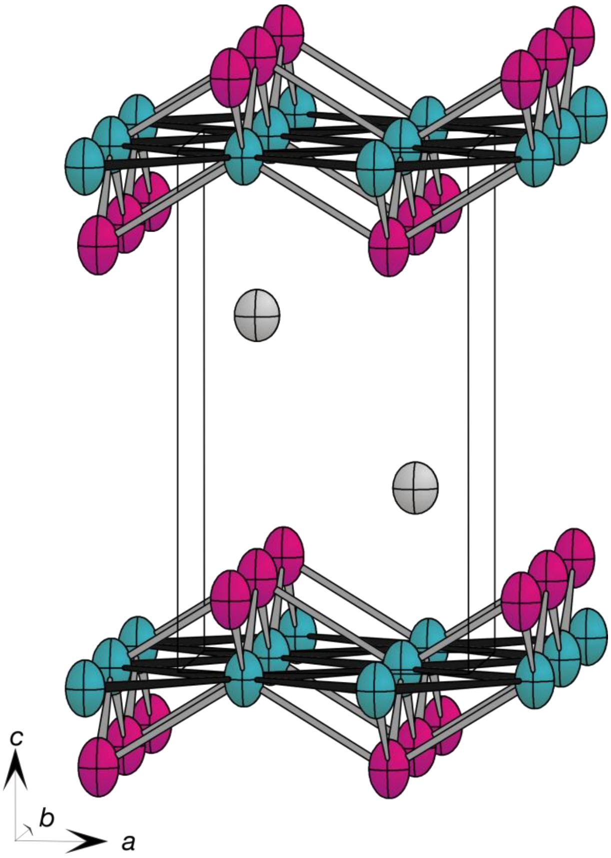

Figure 4.1 Crystal structure of CaCoSi (Ca atoms light gray, Co atoms teal, Si atoms magenta ellipsoids, respectively). Atoms are represented as atomic displacement ellipsoids with a 90 % possibility. Co–Si bonds are light gray; Co–Co bonds are dark gray.

The input data for the theoretical calculations were taken from single crystal refinement. Atomic *x*, *y*, *z* coordinates were set as ¼, ¼, 0.6751 for Ca; ¾, ¼, 0 for Co and ¼, ¼, 0.1714 for Si. The muffin-tin radii for the atoms were calculated as 3.902 a.u. = 2.065 Å for Ca, 2.439 a.u. = 1.291 Å for Co and 2.539 a.u. = for Si. The *k*-space was quadrupled from 8 8 4 to 32 32 16 for a more accurate description. The total DOS including iDOS and pDOS for Co-d, Si-s, Si-p and Ca-d and the band structure including fat bands for the Si-s, Si-p and Co-d were calculated for a more detailed analysis of the individual contributions. Bands are described along the relevant Brillouin-zones[14] (given in Figure A21, Appendix) for the *P*4/*nmm* space group with *k*-paths: Γ = (0,0,0), X = (0,0.5,0), M = (0.5,0.5,0), Z = (0,0,0.5), R = (0,0.5,0.5) and A = (0.5,0.5,0.5). Topological ELF analysis was used to explain the bonding peculiarities within the structure.

The DOS analysis reveals two separated blocks for CaCoSi (see Figure 4.2a) which are separated by an energy gap of approximately 2.3 eV. The block located at lower energies between −10.5 eV and −7.8 eV is dominated by Si-s orbitals. The total DOS and Si-s DOS show a sharp peak around −8 eV.

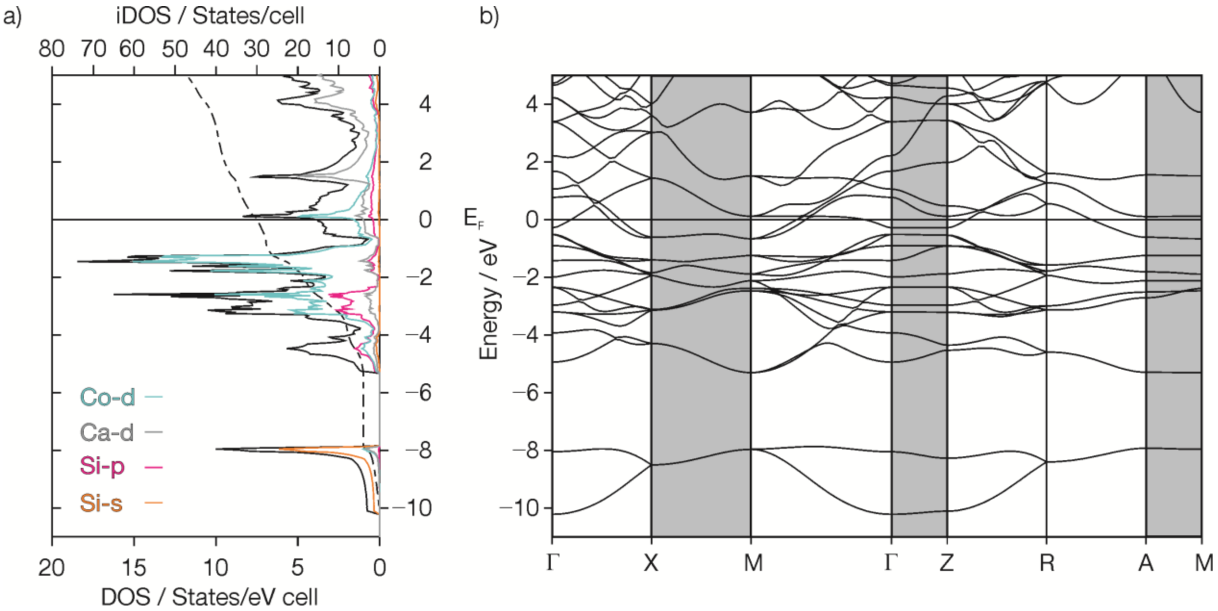

Figure 4.2 DOS and band structure of CaCoSi: a) DOS (black) including iDOS (dashed line) and pDOS contributions of Co–d (turquois), Ca–d (gray), Si–p (magenta) and Si–s (orange); b) total band structure, *k*-paths parallel to the *c*-direction are highlighted gray, path parallel to *ab*-plane are white.

It was reported for the *Ae*NiGe compounds (*Ae* = Mg - Ba)[15] that the shape of the DOS curve in that region is related to the coordination of the Ge atoms and their bonding situation. In *Ae*NiGe (*Ae* = Ca, Sr and Ba) the Ge atoms have lone pairs and sharp peaks in the DOS are observed for all three compounds. In MgNiGe the Ge atoms are coordinated by four Ni atoms with strong bonding interactions (no lone pairs) and the DOS has a flat curve progression at low energies. The observed sharp DOS peak for CaCoSi therefore indicates lone pairs at the Si atoms. This corresponds to the crystal structure observations where the Co–Si tetrahedral layers are shifted in the *a*,*b*-direction with respect to each other and therefore the lone pairs of the Si-atoms point towards the adjacent Ca-atom layer (see Figure 4.1 and Figure 4.4). Small contributions also come from Si-p and Co-d orbitals.

The second block lies at energies above –5.5 eV. Main contributions in this part of the DOS are of Si-p and Co-d orbitals with only small contributions of the Si-s and Ca-d orbitals. The curve progression of the Si-p and Co-d indicates covalent bonding interaction between neighboring Si- and Co-atoms in the tetrahedral layers. At –0.7 eV a local minimum can be seen followed by a peak located at approximately 0.1 eV. Co-d orbitals are dominant in this region and up to 2 eV. The Fermi level cuts through the shoulder of this peak. Minor contributions of Si-p and Ca-d are present as well. CaCoSi has metallic character due to the absence of a band gap at the Fermi level. The pseudo-gap at –0.5 eV has an iDOS value of 28 e^- per unit cell. Shifting E_F to that pseudo-gap would require a reduction of –2 in valence electrons. The compound CaFeSi, which would have 28 e^- per unit cell, has not been reported and it was not possible to synthesize it during this work.

A closer look at the individual contributions of the orbitals is obtained by band structure analysis. The total band structure without fat band contribution is shown in Figure 4.2b; the previously described blocks between –10.5 eV to –7.8 eV and –5.5 eV to 5 eV are clearly distinguishable. Multiple bands cross the Fermi level in the *a*,*b*-direction ($\Gamma \rightarrow$X, M $\rightarrow \Gamma$, Z $\rightarrow$R and R $\rightarrow$A path). No bands cross the Fermi level in the *c*-direction (X $\rightarrow$M, $\Gamma \rightarrow$Z and A $\rightarrow$M path) which is in accordance with the two dimensionality of the polyanionic [CoSi] substructure.

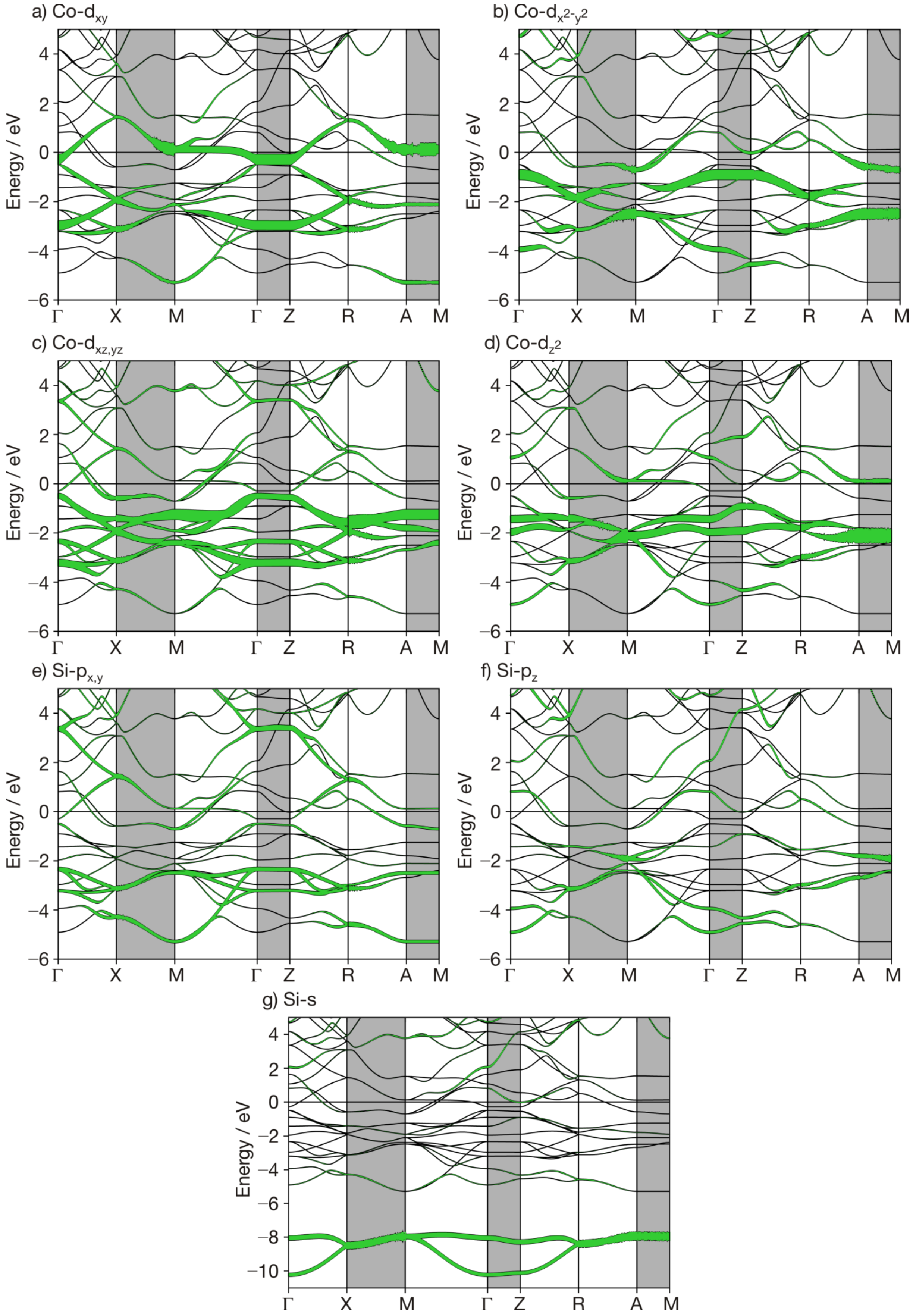

Figure 4.3 Band structure including fat band representation of CaCoSi orbitals: a) Co-d_{xy}, b) Co-d_{x2-y2}, c) Co-$d_{xz,yz}$, d) Co-d_{z2}, e) Si-$p_{x,y}$, f) Si-p_z, g) Si-s; *k*-paths parallel to the *c*-direction are highlighted gray, path parallel to *ab*-plane are white.

The Co-d_{xy} fat bands (Figure 4.3a) are most prominent at the Fermi level and responsible for the sharp peak at approximately 0.1 eV. The fat bands cut the Fermi level in the $\Gamma \rightarrow$ X, M $\rightarrow \Gamma$ and Z $\rightarrow$ R path. The Co-d_{x2-y2} orbitals (Figure 4.3b) show strong contributions along the M $\rightarrow \Gamma$ path which corresponds to the shortest Co–Co distance (2.812(1) Å) in the planar Co square net. These fat bands also cross the Fermi level along the M $\rightarrow \Gamma$ and R $\rightarrow$ A path. The Co-$d_{xz,yz}$ orbitals (Figure 4.3c) below the Fermi level are located in the region of −4 eV to −0.5 eV.

The Co-$d_{xz,yz}$ orbitals point towards the Si atoms in the tetrahedral layer and hybridization between these fat bands and the Si-$p_{x,y}$ fat bands (Figure 4.3c and e) is observed. The mixing indicates covalent interactions between Co atoms and Si atoms which is in agreement with the observed Co–Si distance of 2.330(2) Å within the layers. The observed $d_{\text{Co–Si}}$ is slightly shorter than the sum of covalent radii (2.41 Å).[16] The small contribution of Si-p orbitals at the Fermi level which was detected from pDOS analysis is reflected by the Si-p fat bands (Figure 4.3e). The fat bands cross the Fermi level exclusively in *k*-paths parallel to the *ab*-plane and mix mainly with the Co-$d_{x2-y2,xz,yz}$ orbitals. Co-d_{z2} fat bands (Figure 4.3d) have their main contributions between −2.5 eV and −1 eV, Si-s fat bands (Figure 4.3g) are mainly located in the low energy block between −10.5 eV and −7.8 eV.

The ELF representation gives a detailed picture of the bonding situation in real space. The 3D ELF plot (Figure 4.4a) shows clearly monotactic ELF domains (denoted by number 1) which represents the Si lone pairs ($\eta > 0.7$). These Si lone pairs are oriented along the *c*-direction towards the centers of the square nets occupied with Ca atoms. The character of the localized Si lone pair shows reminiscence to a p_z orbital. A closer look at the Co square net in the [110] plane is obtained by the contour line diagram shown in Figure 4.4b. The η region displayed is between 0.35 - 0.38 with two contour lines. A local ELF maximum can be observed between 0.37 - 0.38 indicated by the arrow. In combination with the experimentally obtained $d_{\text{Co–Co}}$ = 2.812(1) Å it can be concluded that weak bonding interactions within the square net exists. The Co–Co distance is similar to those found in *RE*CoSi (*RE* = La - Nd, Sm)[2, 8] and *Ae*Co_2Si_2 (*Ae* = Ca, Sr).[17, 18]

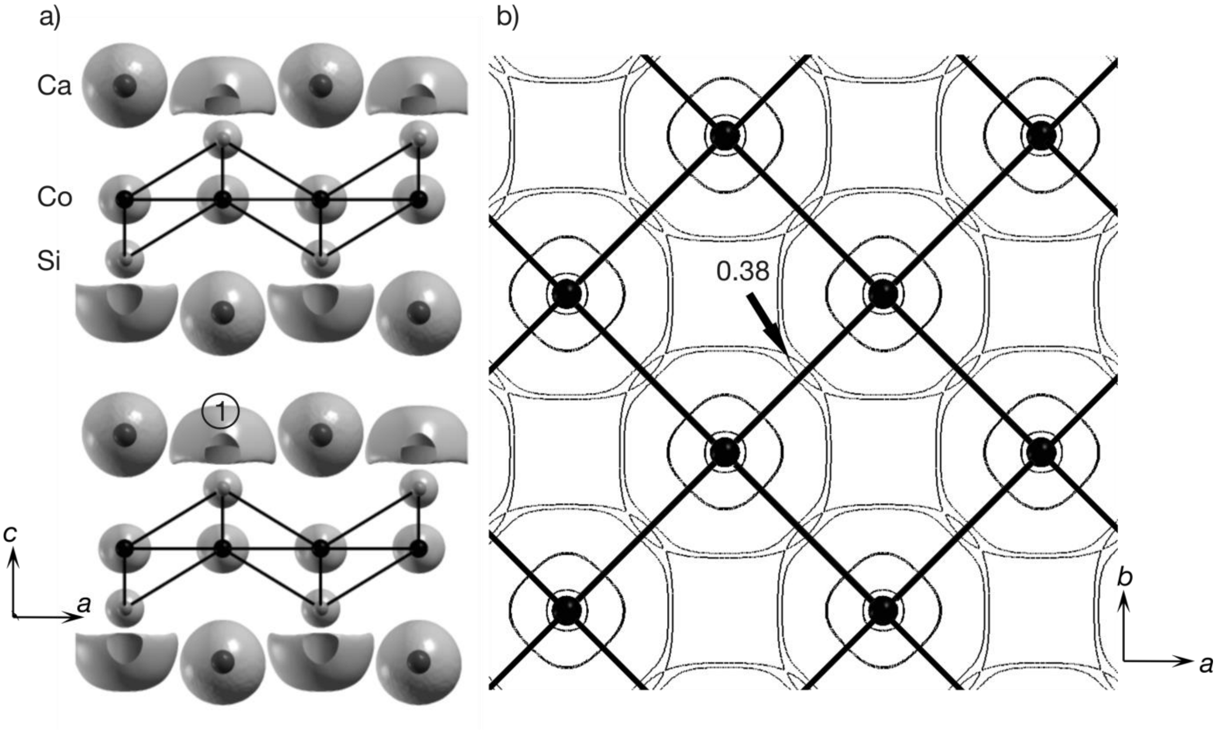

Figure 4.4 ELF representation of CaCoSi calculated from the all electron density. a) 3D plot with non-bonding ELF domains located at the Si atoms (denoted with number 1), the Si lone pairs are directed along the *c*-direction; b) contour line diagram in the *ab*-plane at the Co square planar layer. η region displayed between 0.35 and 0.38 with two contour lines of 0.2 steps.

Similar observations were reported for the isostructural CaNiGe compound.[6] DOS analysis of CaNiGe (see Figure 4.5) also reveals two blocks and no band gap at the Fermi level is observed indicating metallic character just like in CaCoSi. The low energy block is dominated by the Ge-s orbitals in CaNiGe as it is dominated by the Si-s orbitals in CaCoSi with a sharp peak of the pDOS.

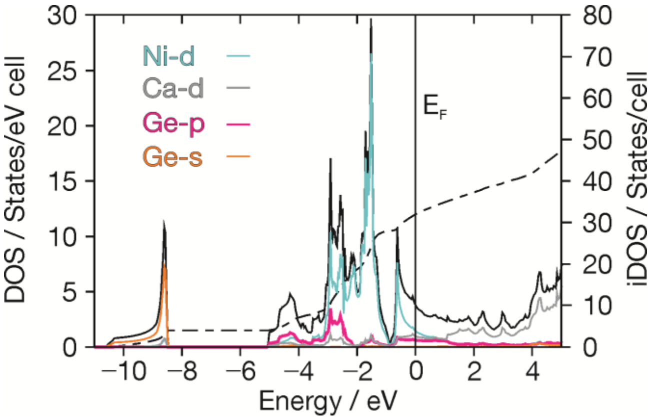

Figure 4.5 Total and partial DOS presentation of CaNiGe[6]: total DOS (solid black) including iDOS (black dashed) and the pDOS contributions of Ni–d (turquois), Ca–d (gray), Ge–p (magenta) and Ge–s (orange).

The region between –5.5 eV and 1 eV is dominated by the d-orbitals of Co/Ni in both cases with contributions of Ca-d and Si/Ge-p orbitals. In contrast to CaCoSi the pseudo-gap in CaNiGe is located at a lower energy (–1 eV compared to –0.7 eV). The shift of the Fermi level towards the pseudo-gap for CaCoSi is in accordance with the lower number of electrons in the anionic substructure. The DOS curve above the pseudo-gap displays big differences for CaCoSi in comparison with CaNiGe. The local maximum at 0.1 eV in CaCoSi is not observed in CaNiGe, the peak is shifted to energies below the Fermi level. The local peak at approximately 1.5 eV for CaCoSi is not observed in CaNiGe. The ELF analysis of CaNiGe shows localized Ge lone pairs directed towards the Ca atoms just like in CaCoSi.

No ELF attractors between the Ni atoms within the square Ni net were found in contrast to the CaCoSi compound. Both compounds can be formally written as $Ca^{2+}[TE]^{2-}$ (T = Co, Ni; E = Si, Ge) to emphasize the bonding within the tetrahedral layers.

Comparing CaCoSi with the isostructural rare earth compounds CeCoSi[19] and NdCoSi[20] shows remarkable differences for the electronic structure behavior at the Fermi level. The maximum of the Co-d pDOS is located at the Fermi level for the rare earth compounds whereas for CaCoSi the peak is shifted towards the valence band and is located at 0.1 eV. Extrapolating the iDOS value at the Co-d peak in CaCoSi gives a value of 32 e^- per unit cell which corresponds to the valence electron number of CeCoSi and NdCoSi. Reasons for the shift of the Co-d peak are the two-dimensionality of the structure and the higher oxidation state of the rare earth atoms (+3 compared to +2 for Ca) as well as steric effects. The additional electron of Ce and Nd affects the reduced oxidation state of Co, shifting the Fermi level to the local maximum.

In comparison with the intermetallic phases crystallizing in the $ThCr_2Si_2$ structure type, which has been described in Chapter 3, the 111 compounds (CeFeSi structure type) do not exhibit covalent interactions between the TE_4 tetrahedral layers along the c-direction and therefore cannot form 3D networks. Twice the amount of cations is present in 111 compounds compared to 122 compounds (see Figure 4.6) and the tetrahedral layers are shifted in the [100] direction. In CaCoSi the Si atoms of one layer point towards the Ca atoms and not to the Si atoms in the adjacent layer as is the case in $CaCo_2Si_2$.[18] So, even though both structure types contain similar tetrahedral layers, the shift of these layers in the 111 type structure prohibits covalent bonding interactions between layers.

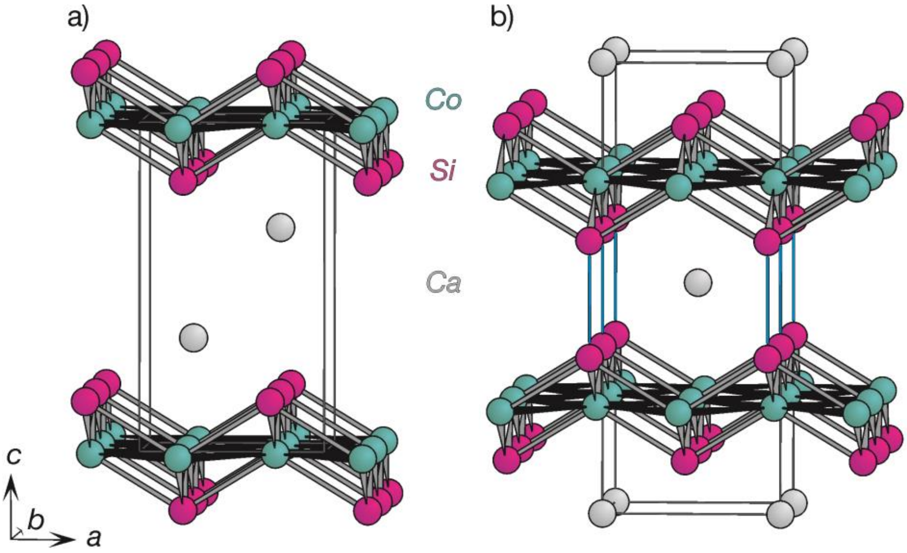

Figure 4.6 Structure model of a) CaCoSi (*P*4/*nmm*) and b) $CaCo_2Si_2$ (*I*4/*mmm*).[18] Ca atoms shown in light gray, Co atoms teal, Si atoms magenta spheres. Co–Si bonds are light gray; Co–Co bonds are black and the Si–Si bonds in $CaCo_2Si_2$ are blue.

In CaCoSi the Ca cations have a charge of 2+ which is counterbalanced by the 2D [CoSi] layers which therefore have a charge of 2−. The formal charge transfer for CaCoSi can be written as $Ca^{2+}[CoSi]^{2-}$. In $CaCo_2Si_2$ the ratio of Ca cations to [CoSi] layer is 1:2; the polyanionic substructure can be written as $[Co_2Si_2]^{2-}$ or alternatively as $[CoSi]^{-}$. The polyanionic layers are more electron-deficient in $CaCo_2Si_2$ and covalent Si–Si bonds along the *c*-axis appear between the 2D [CoSi] layers which results in the formation of a 3D $[CoSi]^{-}$ network. The Si–Si bond formation can be regarded as an oxidative coupling product of the 2D $[CoSi]^{2-}$ layers of CaCoSi.

4.3. References

[1] O. I. Bodak, E. I. Gladyshevskii, A. V. Kardash, E. E. Cherkashin, *Izv.Akad.Nauk, Neorg.Mater.* **1970**, *6*, 935-938.

[2] O. I. Bodak, E. I. Gladyshevskii, P. I. Kripyakevich, *J. Struct. Chem.* **1970**, *11*, 283-288.

[3] *FindIt ICSD Database*, 1.7.0ed., FIZ Karlsruhe, Germany, **2010**.

[4] P. Villars, K. Cenzual, *Pearson's Crystal Data: Crystal Structure Database for Inorganic Compounds (on CD-ROM)*, 1.0ed., ASM International, Materials Park, Ohio, Usa, **2007/8**.

[5] A. Dascoulidou, F. Schucht, W. Jung, H. U. Schuster, *Z. Anorg. Allg. Chem.* **1998**, *624*, 119-123.

[6] V. Hlukhyy, N. Chumaloa, V. Zaremba, T. F. Fässler, *Z. Anorg. Allg. Chem.* **2008**, *634*, 1249-1255.

[7] R. Welter, B. Malaman, G. Venturini, *Solid State Comm* **1998**, *108*, 933-938.

[8] R. Welter, G. Venturini, E. Ressouche, B. Malaman, *J. Alloys Compd.* **1994**, *210*, 279-286.

[9] J. H. Tapp, Z. Tang, B. Lv, K. Sasmal, B. Lorenz, P. C. W. Chu, A. M. Guloy, *Phys. Rev. B* **2008**, *78*, 060505.

[10] C. W. Chu, F. Chen, M. Gooch, A. M. Guloy, B. Lorenz, B. Lv, K. Sasmal, Z. J. Tang, J. H. Tapp, Y. Y. Xue, *Physica C* **2009**, *469*, 326–331.

[11] Z. Deng, X. C. Wang, Q. Q. Liu, S. J. Zhang, Y. X. Lv, J. L. Zhu, R. C. Yu, C. Q. Jin, *EPL* **2009**, *87*, 37004.

[12] A. V. Hoffmann, *Masterthesis*, Uppsala University **2010**.

[13] A. V. Hoffmann, V. Hlukhyy, T. F. Fässler, *Z. Anorg. Allg. Chem.* **2014**, *640*, 2882-2888.

[14] M. I. Aroyo, D. Orobengoa, G. de la Flor, E. S. Tasci, J. M. Perez-Mato, H. Wondratschek, *Acta Cryst.* **2014**, *A70*, 126-137.

[15] V. Hlukhyy, L. Siggelkow, T. F. Fässler, *Inorg. Chem.* **2013**, *52*, 6905-6915.

[16] L. Pauling, B. Kamb, *PANS* **1986**, *83*, 3569-3571.

[17] V. Hlukhyy, A. V. Hoffmann, T. F. Fässler, *J. Solid State Chem.* **2013**, *203*, 232–239.

[18] L. Siggelkow, V. Hlukhyy, T. F. Fässler, *Z. Anorg. Allg. Chem.* **2010**, *636*, 378-384.

[19] B. Chevalier, S. F. Matar, *Phys. Rev. B* **2004**, *70*, 174408.

[20] S. Tence, S. F. Matar, G. Andre, E. Gaudin, B. Chevalier, *Inorg. Chem.* **2010**, *49*, 4836-4842.

5. New compounds in the Ca–Fe–As phase system

5.1. Introduction

The ternary phase $CaFe_2As_2$ belongs to the family of iron-pnictide superconductors. The compound is not superconducting at normal pressure but superconductivity can be induced by applying pressure.[1] It is a parent compound for charged doped superconductors like $Ca_{1-x}Na_xFe_2As_2$ ($T_c = 20$ K),[2] $Ca_{1-x}La_xFe_2As_2$ ($T_c = 42.7$ K),[3] $Ca(Fe_{1-x}Co_x)_2As_2$ ($T_c = 20$ K)[4] and $Ca(Fe_{1-x}Rh_x)_2As_2$ ($T_c = 18$ K).[5]

In 2011 new iron-pnictide superconductors with the composition $(CaFe_{1-x}Pt_xAs)_{10}Pt_{4-y}As_8$ were reported.[6-8] Attempting to synthesize similar compounds containing Ca, Fe, As, Rh and Si (to ideally obtain $(CaFe_{1-x}Rh_xAs)_{10}Rh_{4-y}Si_8$ phases) was not successful but the samples contained new members of the Ca–Fe–As phase system which were subsequently further investigated.

In the ternary phase system Ca–Fe–As multiple binary Ca–As and Fe–As compounds have been reported in addition to three ternary compounds. Binary Ca-Fe compounds do not exists due to immiscibility in the system. The phase diagram of the Ca–Fe–As system is shown in Figure 5.1 including known compounds (black stars).

Six binary Ca–As compounds are so far reported: Ca_2As,[9] Ca_5As_3,[10] $Ca_{16}As_{11}$,[11] CaAs,[12] Ca_2As_3[13] and $CaAs_3$.[14] In the binary phase system the following trend is observed: with increasing As-content the number of covalent As–As bonds increases. Ca_2As and Ca_5As_3 are reported as intermetallic phases. The Ca-richest compound Ca_2As ($I4/mmm$ space group), has As atoms form a square pyramidal coordination around Ca atoms while Ca atoms in the first coordination sphere of As (3.33 Å) form quadratic square prism with capped faces. In Ca_5As_3 ($P6_3/mcm$ space group), the Ca atoms form a string of face-sharing octahedra along the *c*-direction, the As atoms cap the octahedral edges within the first coordination sphere of 3.36 Å. No covalent bonds are found in either compound.

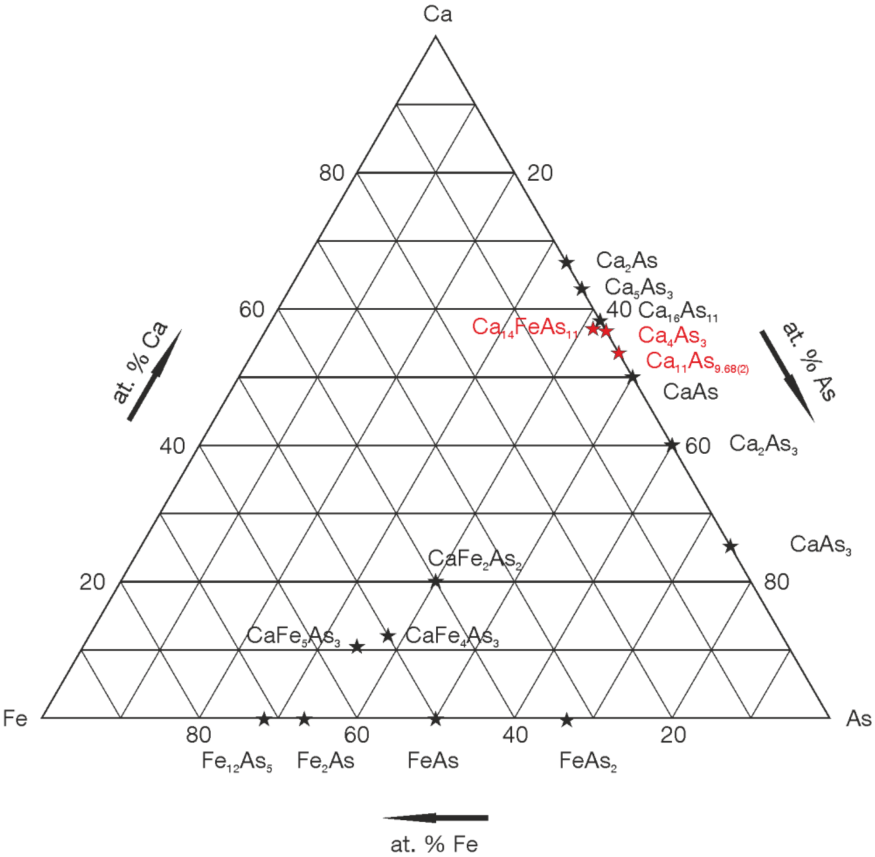
Ca
80
20
60
40
20
Ca_2As
Ca_5As_3
40
$Ca_{16}As_{11}$
$Ca_{14}FeAs_{11}$
Ca_4As_3
$Ca_{11}As_{9.68(2)}$
$CaAs$
60
Ca_2As_3
$CaAs_3$
80
at. % Ca
at. % As
$CaFe_2As_2$
$CaFe_5As_3$
$CaFe_4As_3$
Fe
As
80
60
40
20
$Fe_{12}As_5$
Fe_2As
$FeAs$
$FeAs_2$
at. % Fe

Figure 5.1 Ternary phase diagram of Ca–Fe–As. Known phases are marked with black stars, the new compounds are indicated by red stars.

The structures of the other four Ca–As compounds can be described with polyanionic substructures of covalent bonded As atoms and are Zintl phases. The polyarsenic substructure varies with the atomic-% of As in the compounds. Compounds that have at. % of Ca between 50 - 59.26 (CaAs, $Ca_{16}As_{11}$) all contain $[As_2]^{4-}$ dumbbells as a structure motif.[11, 12] Ca_2As_3 crystallizes in the monoclinic $P2/c$ space group and contains two types of As chains, $[As_4]^{6-}$ and $[As_8]^{10-}$.[13] $CaAs_3$ has the highest As-content of the binary phases, crystallizing in $P\overline{1}$ space group. The compound contains a two-dimensional $[As_3]^{2-}$ network as polyarsenic substructure with three bonded $[As]^0$ and two bonded $[As]^{1-}$ atoms in a ratio 1:2.[15]

The binary Fe–As system has four members: $Fe_{12}As_5$,[16] Fe_2As,[17] FeAs[18] and $FeAs_2$.[19] The Fe-richest compound $Fe_{12}As_5$ ($R3$ space group) contains square pyramids formed by As with an Fe atom in the center of the square plane, trigonal bipyramids of As atoms around an Fe atom and a trigonal bipyramid formed entirely by five Fe atoms.[16] Fe_2As (space group $P4/nmm$) contains layers of edge-shared $FeAs_4$ tetrahedra in the *ab*-plane. The layers are separated by Fe atoms in the *c*-direction which are connected to the As atoms of the tetrahedra.[17] The stoichiometric compound FeAs crystallizes in the *Pnma* space group, the Fe atoms are coordinated by six As atoms to form distorted octahedra. The octahedra share edges and form 3D networks.[18] The As-richest compound $FeAs_2$ crystallizes in the orthorhombic space group *Pnnm*. Fe in $FeAs_2$ is coordinated by six As atoms that form octahedra, in contrast to FeAs the octahedra share only vertices in $FeAs_2$ to form a 3D network.[19]

The three known ternary compounds $CaFe_2As_2$,[1] $CaFe_4As_3$[20] and $CaFe_5As_3$[21] all share the same structure motif of $FeAs_4$ tetrahedra (see Figure 5.2). The connectivity of the tetrahedra varies between the three compounds. The Ca-richest compound $CaFe_2As_2$, crystallizing in the tetragonal space group *I*4/*mmm*, contains 2D $FeAs_4$ layers with edge-shared tetrahedra in the *ab*-plane (Figure 5.2a).

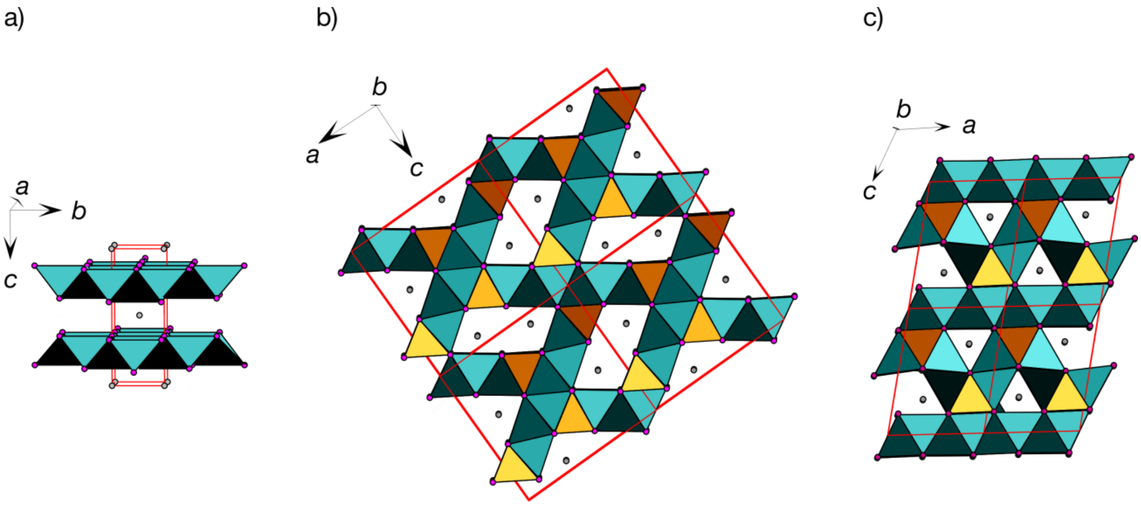

Figure 5.2 Structures of $CaFe_2As_2$ (a),[1] $CaFe_4As_3$ (b)[20] and $CaFe_5As_3$ (c).[21] Ca atoms shown in gray, Fe in teal, As in magenta; cell edges are red. Teal polyhedra represent $[FeAs_4]$ tetrahedral layers while orange polyhedra represent $[FeAs_5]$ square pyramids.

The layers are separated in the *c*-direction. Under pressure the layers move closer together and at some point become connected via As–As covalent bonds to form 3D $FeAs_4$ networks.[1] In $CaFe_4As_3$ (space group *Pnma*) the tetrahedral layers form a 3D network, however no covalent As–As bonds are present. Fe–As ribbons in the *ac*-plane form channels for two Ca atoms which lie in the *b*-direction (Figure 5.2b).[20] At the joints of the ribbons the Fe atoms are coordinated by five As atoms which form square pyramids (Figure 5.2b, orange polyhedra). The Fe-richest ternary compound $CaFe_5As_3$ (space group $P2_1/m$) displays the same structure motifs as $CaFe_4As_3$, the tetrahedral layers are closer packed and only one Ca atom is located in the channels (Figure 5.2c).[21] The distances $d_{\text{Fe–As}}$ for the tetrahedral coordinated Fe atom are between 2.38 Å and 2.50 Å for the ternary compounds. The angles within the tetrahedra (α) vary between 92.4 ° and 116.3 °. The distances between the Fe and the As atoms that form the square pyramid (orange coordination polyhedra in Figure 5.2) are 2.5 - 2.63 Å. They form the connection between the tetrahedral $FeAs_4$ layers.

The ternary phase system Ca–Fe–As shows a variety of different structure motifs depending on the composition of the compounds. Besides $FeAs_4$, similar structural motifs can be observed for multiple compounds; like the As–As dumbbells in calcium-arsenides and the ternary compound $CaFe_2As_2$ (under pressure),[1] the octahedral coordination of As by six Ca atoms in Ca_5As_3 or Fe by six As atoms in FeAs and $FeAs_2$.

5.2. Intermetallic $Ca_{14}FeAs_{11}$ phase

Intermetallic compounds with structure type $Ca_{14}AlSb_{11}$ have been first described by Cordier *et al*. in 1984.[22] Since then a number of new compounds with this structure type have been reported. The group of Prof. S. M. Kauzlarich has investigated this family of compounds for the past 20 years.[23-42] The interest in these complex phases is due to the variety of electronic and magnetic properties observed depending on the composition. $Ae_{14}TE_{11}$ compounds which display ferromagnetic (Ae = Ca, Sr, Ba, Eu, Yb; T = Mn; E = Sb, Bi),[27, 28, 37, 39] antiferromagnetic ($Ba_{14}MnBi_{11}$)[39] or paramagnetic behavior following Curie-Weiss law (T = Mn, E = As, P)[36, 41, 42] at lower temperatures as well as narrow gap semiconductors (T = Al, Ga; E = Sb, As)[23, 33, 42] have been reported. The magnetic ordering in the Mn compounds occurs via long-range interactions, the distance between the magnetic centers is approximately 10 Å.[40] The $Eu_{14}MnE_{11}$ compounds (E = Sb, Bi) are more complex concerning their magnetic behavior since two magnetic sites (Eu and Mn) are present.[28] The magnetic moments of the compounds couple ferromagnetical via interactions between the Mn site and the Eu sites below 100 K, a second magnetic transition is observed below 15 K attributed to the antiferromagnetic ordering of the Eu spins.

Of high interest are the two compounds $Eu_{14}MnSb_{11}$ and $Yb_{14}MnSb_{11}$. The Eu compound shows a giant magnetoresistance (GMR sometimes also called colossal magnetoresistance, CMR) at the ferromagnetic-paramagnetic phase transition.[26] The behavior is associated with a transition from a low-temperature metallic ferromagnetic phase to a high-temperature semiconducting paramagnetic phase.[34] Below the second magnetic transition a large negative magnetoresistance is observed. To investigate this effect further Kauzlarich *et al*. have prepared pseudo-ternary compounds $Eu_{14-x}Ae_xMnSb_{11}$ (Ae = Ca, Ba).[34, 37] The investigation revealed that the second magnetic ordering in $Eu_{14}MnSb_{11}$ is more likely ferrimagnetic and arises from multiple magnetic sublattices. The T_C (Curie transition temperature) of $Eu_{14}MnSb_{11}$ is enhanced by Eu–Mn exchange interactions. With increasing Ca content T_C of the compound increases but the second magnetic transition occurs at lower temperatures, the antiferromagnetic ordering is partially suppressed. Both the Ca-doped and the Ba-doped compounds still display GMR behavior.

$Yb_{14}MnSb_{11}$ became of high interest when Kauzlarich *et al*. discovered that the compound has higher efficiency and figure of merit as a thermoelectric material than p-$Si_{1-x}Ge_x$ thermoelectrica.[24] By substituting Mn with Zn in $Yb_{14}MnSb_{11}$ the performance of the material was even further enhanced.[25]

5.2.1. Synthesis of $Ca_{14}FeAs_{11}$

The compound $Ca_{14}FeAs_{11}$ was first obtained as a side product in a sample that contained Ca, Fe, As, Rh and Si. Single crystals could be isolated from the sample and the structure was solved with single crystal refinement. Reproduction of the ternary $Ca_{14}FeAs_{11}$ compound was subsequently tried using the three elements Ca, Fe and As and the nominal starting composition 14:1:11 (Ca:Fe:As). Attempts made from the pure elements did not contain the ternary $Ca_{14}FeAs_{11}$ phase but resulted in the ternary $CaFe_2As_2$ phase and binary Ca–As phases. Therefore a two-step method with FeAs as a precursor was used in the synthesis. FeAs was prepared from pure elements with 1:1 (0.225 g Fe: 0.300 g As) nominal composition heated in a closed Nb ampoule sealed in a silica glass tube using a muffle furnace (temperature program see Figure 5.3a). Powder X-ray diffraction pattern showed the FeAs phase (see Figure A22, Appendix), which was subsequently ground to fine powders. The ternary samples were prepared by using Ca ingots, FeAs powder and As pieces; different ratios of 14:1+x:11−x (Ca:FeAs:As) with varying x values between 0 - 1 (see Table 5.1) were used in an attempt to reproduce the compound.

Table 5.1 Masses of Ca, FeAs and As used for the synthesize of $Ca_{14}Fe_{1+x}As_{11}$ samples.

Nominal composition, *x*	**Ca / g**	**FeAs / g**	**As / g**	**Total mass / g**
0	0.215	0.050	0.288	0.553
0.1	0.196	0.050	0.259	0.505
0.5	0.199	0.067	0.242	0.508
1	0.187	0.087	0.225	0.499

Silica glass tubes were used as the reaction containers and the thermal treatment took place in a muffle furnace (temperature program given in Figure 5.3b)

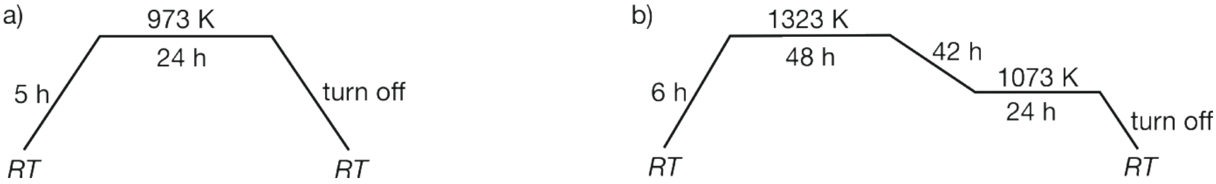

Figure 5.3 Temperature program for: a) FeAs precursors; b) $Ca_{14}FeAs_{11}$ samples.

The resulting products were composed of $Ca_{11}As_{10-x}$ (Chapter 5.3.2.2) as main phase with $Ca_{14}FeAs_{11}$ as side phase (see Figure A23, Appendix). In some cases the binary CaAs was also present. Single crystals (metallic black-blue luster, pyramidal shape) of $Ca_{14}FeAs_{11}$ with good quality were isolated. The crystals could be distinguished from crystal of the binary $Ca_{11}As_{10-x}$ phase (plate-like shaped crystals of metallic luster) by shape and color. The compound is highly air and moisture sensitive. Single crystal measurements were performed on a *Xcalibur3* (Oxford) diffractometer under N_2 flow at 150 K.

5.2.2. Results and discussion

The ternary compound $Ca_{14}FeAs_{11}$ has been successfully synthesized for the first time. It is the first iron containing representative of $Ca_{14}AlSb_{11}$ type structure[22] and the first reported compound with isolated $FeAs_4$ tetrahedra.

5.2.2.1. Crystal Structure

The cell parameters for $Ca_{14}FeAs_{11}$ could be determined from single crystal X-ray diffraction analysis. $Ca_{14}FeAs_{11}$ crystallizes in the tetragonal space group $I4_1/acd$ ($Z = 8$) with $a = 15.627(1)$ Å, $c = 20.978(1)$ Å and a volume of 5122.8(2) Å^3. The unit cell of the ternary compound is shown in Figure 5.4, the refinement details are given in Table 5.2, Table 5.3, Table A19 and Table A20 (Appendix).

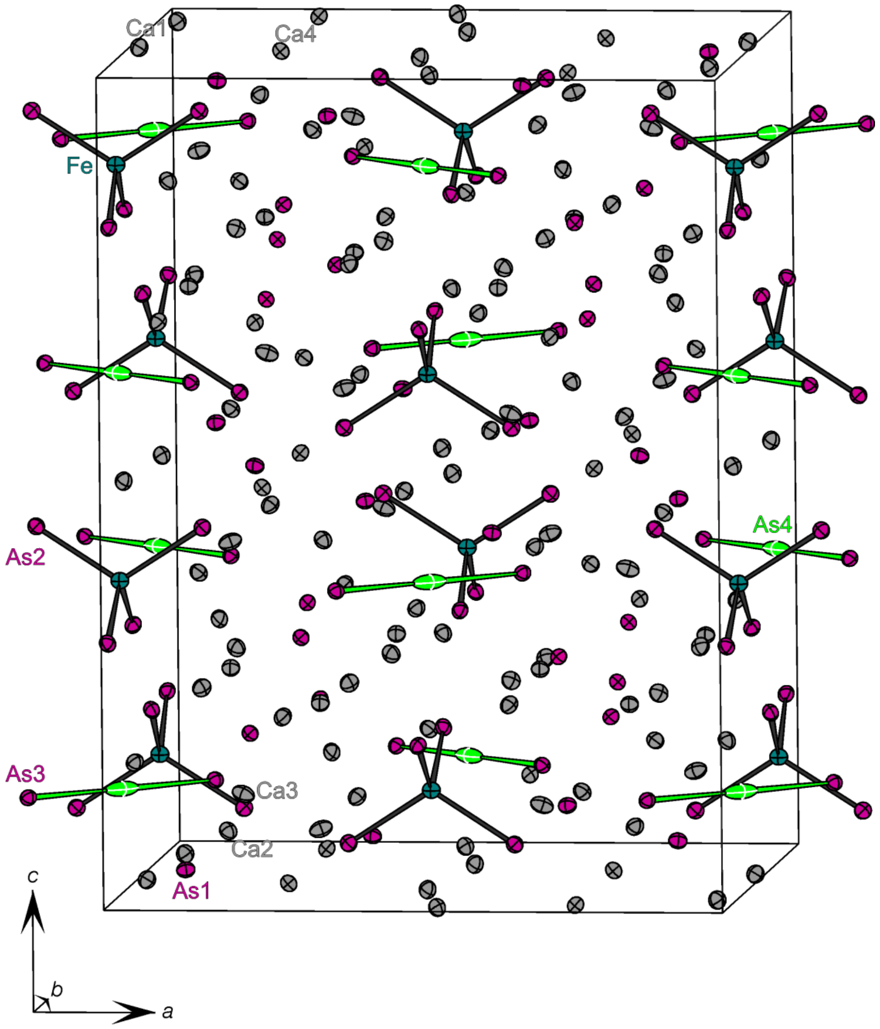

Figure 5.4 Crystal structure of $Ca_{14}FeAs_{11}$ (space group $I4_1/acd$, $Z = 8$). The atoms are represented as atomic displacement ellipsoid with 75 % probability level; Ca = gray, Fe = teal, As = magenta and green (non-split position for the central As4 atom in the $[As_3]^{7-}$ unit). Covalent bonds between Fe–As shown in dark gray, As–As in green.

The unit cell contains isolated $FeAs_4$ tetrahedra, $[As_3]$ units and isolated As and Ca atoms. In total there are 112 Ca atoms, 8 $[As_3]$ units, 8 $[FeAs_4]$ units and 32 isolated As atoms for $Z = 8$.

The Ca cations have the charge 2+ and the isolated As anions 3−. The As atoms that are covalently bond to the Fe atoms in the tetrahedra have a formal charge of 3−, the Fe atoms in the tetrahedra can have the formal charge of 3+ which would give a $[FeAs_4]^{9-}$ unit or can be 2+ resulting in $[FeAs_4]^{10-}$ unit. There are 224 positive charges from the Ca^{2+} cations, 96 negative charges from the isolated As^{3-} anions and 72 negative charges for the $[FeAs_4]^{9-}$ tetrahedra (in case of Fe^{3+}). The remaining 56 negative charges come from the eight $[As_3]$ units resulting in $[As_3]^{7-}$ entities. The formal charge for the unit can be explained with an As–As dumbbell where each As has a formal charge of 2− ($[As_2]^{4-}$) and an isolated As anion with 3−. In that case the compound could be explained according to Zintl-Klemm concept.

However, it is also possible that the Fe atoms have an oxidation state of +2 and the tetrahedra could be $[FeAs_4]^{10-}$ units, which would lead to 80 negative charges from the tetrahedra in the unit cell. In that case the compound cannot be described with the Zintl-Klemm concept; other positions would have to variate from the "ideal" charge.

Table 5.2 Crystal data, measurement details and structure parameter for single crystal refinement of $Ca_{14}FeAs_{11}$, collected at 150 K.

Empirical formula		**$Ca_{14}FeAs_{11}$**
Diffractometer		*Oxford Xcalibur3*
Detector distance	/ mm	50
Formula weight	/ g·mol^{-1}	1441.09
Space group, *Z*		$I4_1/acd$, 8
Unit cell dimensions	/ Å	$a = 15.627(1)$
		$c = 20.978(1)$
	/ Å^3	$V = 5122.8(2)$
Absorption coefficient	/ mm^{-1}	17.486
Crystal size	/ mm	0.02 × 0.1 × 0.07
Absorption correction		semi-empirical
Calculated density	/ g·cm^{-3}	3.373
$F(000)$		5352
θ range	/ °	3.07 to 32.88
Range in *hkl*		± 23, $-23 < k < 19$, ± 31
Reflections collected		45417
Independent reflections		2344 ($R_{int} = 0.0740$)
Reflections with $I \geq 2\sigma(I)$		1604 ($R_\sigma = 0.0423$)
Data/Parameters		2344/64
GOF on F^2		0.923
Final *R* indices [$I \geq 2\sigma(I)$]		$R_1 = 0.0345$
		$wR_2 = 0.0748$
R indices (all data)		$R_1 = 0.0578$
		$wR_2 = 0.0835$
Largest diff. peak and hole	/ e Å^{-3}	1.475, −1.553

Table 5.3 Atomic coordinates and isotropic equivalent displacement parameters /Å^2 × 10^3 (space group $I4_1/acd$, $Z = 8$, split atom model).

Atom	**Occupancy**	**Wyckoff position**	***x***	***y***	***z***	**U_{eq} / Å^2 × 10^3**
Ca1	1	32*g*	0.0234(1)	0.3779(1)	0.0052(1)	11.5(2)
Ca2	1	32*g*	0.0433(1)	0.0734(1)	0.1714(1)	11.1(2)
Ca3	1	32*g*	0.3434(1)	0.0704(1)	0.0928(1)	13.0(2)
Ca4	1	16*e*	0.3531(1)	0	¼	10.3(2)
Fe	1	8*a*	0	¼	⅜	11.2(2)
As1	1	32*g*	0.1300(1)	0.0257(1)	0.0468(1)	10.1(1)
As2	1	32*g*	0.3653(1)	0.2541(1)	0.0606(1)	10.0(1)
As3	1	16*f*	0.1344(1)	0.3844(1)	⅛	9.4(2)
As4	0.5	16*f*	0.0088(2)	0.2588(2)	⅛	11.3(7)

Fe is coordinated by As2 atoms that form the tetrahedron, the $FeAs_4$ unit is shown in Figure 5.5a. The distance $d_{Fe–As}$ = 2.503(1) Å is longer than the sum of covalent radii for Fe and As (2.45 Å).[43] The ionic radius for Fe^{3+} (CN = 4, hs) is 0.63 Å and 2.10 Å for As^{3-} (CN = 6),[44] the sum of the ionic radii is 2.73 Å which is 0.23 Å longer than $d_{Fe–As}$ (2.503(1) Å) in the $FeAs_4$ unit of $Ca_{14}FeAs_{11}$. The tetrahedra angles are α = 106.95(2) ° and β = 114.64(2) °, which deviates from the ideal tetrahedral angle of 109.4 °. The discrete $FeAs_4$ tetrahedron is more distorted in comparison to the tetrahedral angles of 109.4 ° and 109.5 ° (α and β, respectively) which are found in the uncollapsed $CaFe_2As_2$ modification (ambient pressure) where the tetrahedra share common edges in the *ab*-plane. The tetrahedral angles in $Ca_{14}FeAs_{11}$ are less distorted as in collapsed structure of $CaFe_2As_2$ (under pressure) were the $FeAs_4$ tetrahedra form a 3D network and the angles change to 119 ° and 105 °.[1]

The isolated TE_4 units show distortion in all reported compounds; the tetrahedra are flattened along the *c*-axis. The highest distortion is observed for the Mn compounds and is attributed to a d^4 *Jahn-Teller* distortion. In most of these compounds the *T* element has the oxidation state +3 according to the Zintl-Klemm concept, the oxidation state +3 has been confirmed by magnetic susceptibility and transport measurements.[23, 26, 33, 41, 42, 45, 46] Kauzlarich *et al*. have shown that $Ca_{14}MnP_{11}$ displays a paramagnetic moment most consistent with an oxidation state of +2 on the Mn site and the tetrahedra show less distortion in this case.[36]

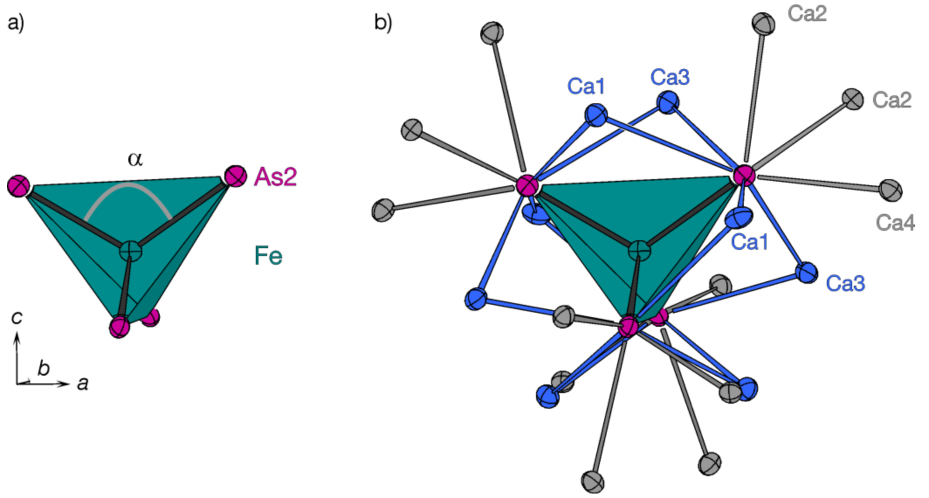

Figure 5.5 $FeAs_4$ tetrahedron structure motif in $Ca_{14}FeAs_{11}$: a) isolated tetrahedron with the angle α indicated by the gray curve; b) tetrahedron coordinated by Ca ($d_{As–Ca}$ < 3.505 Å). The atoms are represented as atomic displacement ellipsoid with 75 % probability level. The terminal Ca atoms are represented in gray, the bridging Ca atoms in blue.

Each As atom of the $FeAs_4$ unit in $Ca_{14}FeAs_{11}$ is coordinated to three terminal Ca atoms (Ca2, Ca4) and four bridging Ca atoms (Ca1, Ca3) within the first coordination sphere. The two bridging Ca atoms coordinate to the other As atoms of the tetrahedra (see Figure 5.5b). As a result the $FeAs_4$ unit is surrounded by 20 Ca atoms, the distances between the As atoms and the surrounding Ca atoms are listed in Table 5.4.

A further structure motif in $Ca_{14}FeAs_{11}$ is a trimeric $[As_3]^{7-}$ unit. The unit is formed by the As3 and As4 atoms, where As3 are the terminal atoms and As4 is located in the center of the linear unit (Figure 5.6). The trimeric unit lies between adjacent $FeAs_4$ tetrahedra in the *ab*-plane (see Figure 5.4). In $Ca_{14}AlSb_{11}$ the central Al atoms (here As4) is reported to lie on the special atomic position at 0, ¼, ⅛ (Wyckoff position 8*b*) for the *I*4₁/*acd* space group, the corresponding site symmetry is 222.[22] Using this structure model results in a $[As_3]^{7-}$ unit with equivalent distances $d_{As3–As4}$ of 2.970(1) Å between the three As atoms for $Ca_{14}FeAs_{11}$. The $[As_3]^{7-}$ is isoelectronic to the linear $[I_3]^-$, a *Jahn-Teller* distortion for $[As_3]^{7-}$ is not expected, in analogy to triiodide.[47]

The refinement shows a noticeable elongation of the As4 atomic displacement ellipsoid towards the adjacent As atoms (Figure 5.6a) which was already observed in the isostructural $Ca_{14}GaAs_{11}$ compound by Kauzlarich *et al.*.[33] The isostructural phosphides all showed noticeable elongation of the anisotropic displacement parameters for the central position as well.[36, 40, 45, 46]

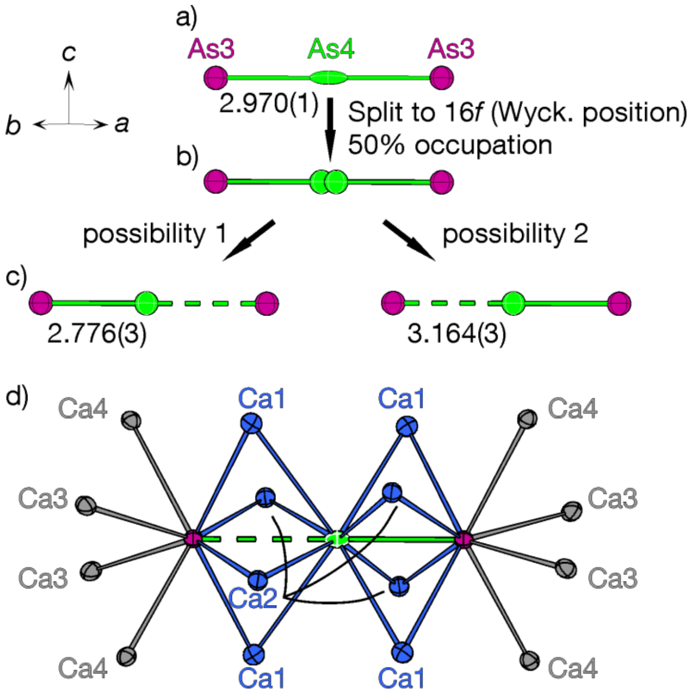

Figure 5.6 $[As_3]^{7-}$ unit with the As3 atoms shown in magenta and As4 atoms in green, the atoms are represented as atomic displacement ellipsoid with 75 % probability level. a) The unit with As4 lying on Wyckoff position 8*b* with 100 % occupancy, with equivalent As3–As4 distances. b) As4 split into two atoms each with 50 % occupancy. c) The two possible $[As_3]^{7-}$ motifs with a shorter (solid) and longer (dashed) As3–As4 distance. d) Coordination of Ca around the $[As_3]^{7-}$ unit, terminal Ca atoms are represented in gray, the bridging Ca atoms in blue.

The elongation has been interpreted as a statistical distortion of the structure motif and the authors described the $[P_3]^{7-}$ unit alternatively in terms of $[P_2]^{4-}$ dumbbells coordinated linearly to isolated P^{3-} atoms. The atomic position for As4 in the $Ca_{14}FeAs_{11}$ structure is therefore split into 2 positions which are each occupied 50 % (as shown in Figure 5.6b, green As atoms).

The resulting atomic position is shifted by 0.0088(2) in the *x* and *y* direction (see Table 5.3 As4 50 % occ.) and the Wyckoff position is adjusted to 16*f*. This split leads to two different distances within the unit (Figure 5.6c), a shorter $d_{As3–As4}$ of 2.776(3) Å (solid line) for the dumbbells and a longer $d_{As3–As4}$ of 3.164(3) Å (dashed line). The split of the atomic position results in acceptable atomic displacement ellipsoids for the structure. The shorter As3–As4 bond (2.776(3) Å) is longer than covalent As bonds in α-As (2.44 Å)[43] and in binary Ca–As compounds (2.47 Å - 2.57 Å)[12, 13] and somewhat shorter than that observed for the collapsed $CaFe_2As_2$ phase (2.86 Å).[1] The Van der Waals radius of As–As is 1.85 Å,[48] the $d_{As3–As4}$ of 3.164(3) Å (dashed line in Figure 5.6c) is shorter than the Van der Waals distance (3.70 Å) and weak bonding interactions result. The $[As_3]^{7-}$ unit is surrounded by 16

Ca atoms within the first coordination sphere. Four Ca atoms (Ca1, Ca2) bridge the As–As bonds (see Figure 5.6d). The other eight Ca atoms (Ca3, Ca4) are terminally coordinated to the As3 atoms (four on each side). The atomic distances are listed in Table 5.4.

Table 5.4 Atomic distances (*d*) within the first coordination sphere including their multiplicity for the individual structural units of $Ca_{14}FeAs_{11}$, space group *I*4_1/*acd*, *Z* = 8 (split atom model).

Atom1	**Atom2**	***d* / Å**	**Atom1**	**Atom2**	***d* / Å**	**Atom1**	**Atom2**	***d* / Å**
Isolated As^{3-}			$[As_3]^{7-}$ unit			$FeAs_4$ unit		
As1	–Ca4	2.920(1); ×1	As3	–Ca3	3.004(2); ×2	Fe1	–As2	2.503(1); ×4
	–Ca1	2.964(1); ×1		–Ca4	3.190(1); ×2	As2	–Ca1	2.945(1); ×1
	–Ca2	2.996(1); ×1		–As4	2.776(3); ×1		–Ca3	2.969(1); ×1
	–Ca2	3.037(1); ×1		–As4	3.164(3); ×1		–Ca2	3.063(1); ×1
	–Ca3	3.039(1); ×1		–Ca2	3.016(1); ×2		–Ca2	3.082(1); ×1
	–Ca1	3.050(1); ×1		–Ca1	3.055(1); ×2		–Ca4	3.138(1); ×1
	–Ca3	3.071(1); ×1	As4(16*f*)	–Ca2	2.914(3); ×2		–Ca3	3.207(1); ×1
	–Ca3	3.541(2); ×1		–Ca2	3.104(3); ×2		–Ca1	3.502(1); ×1
				–Ca1	3.135(2); ×2			
				–Ca1	3.356(17); ×2			

The isolated As^{3-} anions (As1) are coordinated by eight Ca^{2+} cations in form of a distorted trigonal prism with two caped faces (Figure 5.7). The trigonal prismatic coordination of Ca around As is also observed in binary Ca–As phase, for example Ca_2As_3.

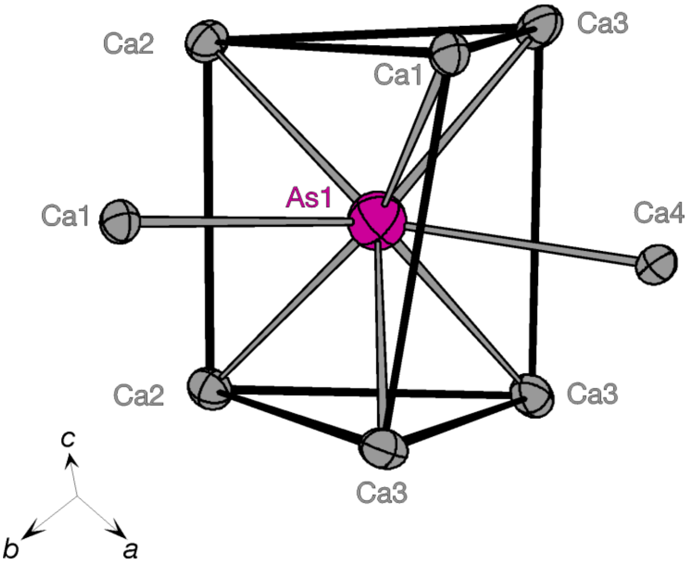

Figure 5.7 Coordination of As1 atoms. The atoms are depicted as atomic displacement ellipsoids with 75 % probability level. Ca–As bonds are shown in gray, Ca–Ca contacts in black (non-covalent and only for visible clarification).

A number of compounds crystallizing in the $Ca_{14}AlSb_{11}$ structure type have been reported in the past 30 years (Table 5.5). For the reported $Ae_{14}TE_{11}$ compounds (Ae = Ca, Sr, Ba Yb; T = Al, Mn, Zn, Ga and E = pnictides) the main-group element Al and the transition metal Mn have been most prominent for the T position.[22, 23, 27, 28, 35, 37-39, 41, 42]

For the first reported compound $Ca_{14}AlSb_{11}$ no sign of positional distortion for the centering Sb atom of the linear $[Sb_3]^{7-}$ unit was reported.[22] For the isostructural compounds $Ae_{14}AlSb_{11}$ (Ae = Sr and Ba) an increase of the U_{ii} and U_{12} values for the central atom of the $[Sb_3]^{7-}$ unit was noticeable.[23] The observed disordering for the central atom of the trimeric unit is the highest for P compounds.[36, 42, 46] It is not as pronounced in the As compounds.[33, 42] In $Ca_{14}FeAs_{11}$ the As–As distance is 0.388(3) Å shorter for the dumbbell than that of the distance to the neighboring As atom. In the isostructural arsenides $Ca_{14}MnAs_{11}$ and $Sr_{14}MnAs_{11}$ the deviation is 0.58 Å and 0.7 Å,[42] respectively.

Comparing the analogs $Ca_{14}MnP_{11}$,[36] $Ca_{14}MnAs_{11}$[42] and $Ca_{14}MnSb_{11}$[42] shows that cell parameters increase for the heavier pnictides (see Table 5.5). The P-compound was measured at a temperature of 90 K, the As- and Sb-compounds at 130 K which also partially influences the structure parameters. The *a*-axis increases from 15.33 Å for the phosphide to 15.71 Å for the arsenide to 16.69 Å for the antimonide. Analogously, the *c*-axis goes from 20.76 Å over 21.14 Å to 22.27 Å, respectively. Exchanging Mn in $Ca_{14}MnAs_{11}$ with Fe results in a slight decrease of the cell parameters (the single crystals were measured at 130 K and 150 K, respectively). The lattice parameter *a* decreases minimally from 15.71 Å to 15.627(1) Å whereas *c* decreases from 21.14 Å to 20.978(1) Å (Mn and Fe, respectively). The observed changes in unit cell parameters are due to the smaller covalent radius (1.37 Å for Mn and 1.24 Å for Fe, respectively).[43] A comparison of the ionic radii is problematic since the oxidation state of Fe is not conclusively determined; if the oxidation state +3 is assumed, the ionic radii of Fe and Mn are approximately the same for CN = 6 with ls or hs electronic configuration (0.72 Å).[44] The unit cell parameters for the Fe compound lie between those of $Ca_{14}MnP_{11}$ and $Ca_{14}MnAs_{11}$. Besides the influences on the unit cell parameters the exchange of Mn for Fe also drastically affects the $[TAs_4]$ tetrahedron (Figure 5.5).

The distance between the transition metal and the 4 surrounding As atoms decreases from 2.60 Å in $Ca_{14}MnAs_{11}$ to 2.503(1) Å in $Ca_{14}FeAs_{11}$ which is equal to the difference (0.13 Å) between the covalent radii of Mn and Fe. The tetrahedra are slightly less distorted with angles of $\alpha = 107.5$ ° and $\beta = 114.4$ ° ($Ca_{14}MnAs_{11}$) compared to $\alpha = 106.95(2)$ ° and $\beta = 114.64(2)$ ° ($Ca_{14}FeAs_{11}$). It has been stated in the literature that the high distortion of the tetrahedra in the Mn compounds (Mn^{3+}) is due to *Jahn-Teller* distortion of the Mn d^4 atoms.[28, 39-42]

Table 5.5 Crystallographic parameters of $Ae_{14}TE_{11}$ compounds (space group $I4_1/acd$, Z = 8) from single crystal measurements: unit cell parameters, d_{T-E} = distance between the T atom and the E atom in the tetrahedra, d_{E-E} = distance between the two E atoms forming the $[E_3]^{7-}$ unit (central E atom on the 8*b* Wyckoff position with 100 % occupancy, non-split atom model).

Compound	***a* / Å**	***c* / Å**	***V* / Å^3**	***c*/*a***	**d_{T-E}/ Å**	**d_{E-E} / Å**	**$T_{measurement}$ / K**	**Ref**
$Ca_{14}AlSb_{11}$	16.68	22.42	6236	1.35	2.72	3.20	Not stated	[22]
$Sr_{14}AlSb_{11}$	17.50	23.48	7185	1.34	2.83	3.30	130	[23]
$Ba_{14}AlSb_{11}$	18.29	24.22	8105	1.32	2.80	3.37	130	[23]
$Ca_{14}MnP_{11}$	15.33	20.76	4875	1.35	2.54	2.93	90	[36]
$Ca_{14}MnAs_{11}$	15.71	21.14	5220	1.35	2.60	3.10	130	[42]
$Sr_{14}MnAs_{11}$	16.58	22.17	6091	1.34	2.68	3.01	130	[42]
$Ca_{14}MnSb_{11}$	16.69	22.27	6201	1.33	2.76	3.22	130	[42]
$Sr_{14}MnSb_{11}$	17.51	23.32	7151	1.33	2.84	3.31	130	[42]
$Ba_{14}MnSb_{11}$	18.39	24.07	8144	1.31	2.87	3.42	130	[42]
$Yb_{14}MnSb_{11}$	16.62	21.95	6059	1.32	2.75	3.20	143	[27]
$Ca_{14}MnBi_{11}$	17.00	22.42	6481	1.32	2.81	3.34	130	[39]
$Sr_{14}MnBi_{11}$	17.82	23.40	7427	1.31	2.89	3.43	130	[39]
$Ba_{14}MnBi_{11}$	18.63	24.34	8450	1.31	2.94	3.50	130	[39]
$Yb_{14}MnBi_{11}$	17.00	22.26	6433	1.31	2.80	3.34	143	[27]
$Yb_{14}ZnSb_{11}$	16.56	21.86	5996	1.32	2.73	3.18	90	[30]
$Ca_{14}GaAs_{11}$	15.62	21.14	5157	1.35	2.55	2.96	130	[33]

The isostructural compound $Ca_{14}GaAs_{11}$ (measured at 130 K) shows only slight changes for the unit cell parameters compared to $Ca_{14}FeAs_{11}$, the covalent radius of Ga is similar to that of Fe (1.26 Å and 1.24 Å, respectively).[43] The ionic radii for Ga^{3+} and Fe^{3+} are 0.47 Å and 0.49 Å (CN = 4).[49] The *a* lattice parameter is almost identical for both compounds (15.627(1) Å and 15.62 Å for Fe- and Ga- containing compound, respectively), the *c* lattice parameter is 0.16 Å larger for the Ga-compound (20.978(1) Å to 21.14 Å, respectively). In $Ca_{14}FeAs_{11}$ the Fe–As distance is 0.05 Å shorter (2.503(1) Å) as the Ga–As distance of 2.55 Å in $Ca_{14}GaAs_{11}$, which is in accordance with the covalent radii of Fe and Ga. The tetrahedra are less distorted in $Ca_{14}GaAs_{11}$ than in the Fe compound: $\alpha = 107.8$ ° and $\beta = 113.0$ °. The size of the coordinating cations around the tetrahedra unit affects the interatomic distances within the TE_4 motif (as well as for the other structural motifs). Comparing $Yb_{14}MnSb_{11}$[27] with $Ca_{14}MnSb_{11}$, $Sr_{14}MnSb_{11}$ and $Ba_{14}MnSb_{11}$,[42] it can be observed that d_{Mn-Sb} increases steadily with the ionic size of the cation. The same trend holds for the isostructural Bi compounds.[27, 39]

Comparing the distances (d_{As-As}) between the As atoms of the $[As_3]^{7-}$ trimer in the non-split atom model (Figure 5.6a) with the previously reported $Ca_{14}TAs_{11}$ compounds show that $Ca_{14}GaAs_{11}$[33] and $Ca_{14}FeAs_{11}$ have similar values of 2.96 Å and 2.970(1) Å (non-split atom model). In $Ca_{14}MnAs_{11}$[42] that distance is 0.13 Å longer (3.10 Å). The distance d_{As-As} (bonding) and d_{As-As} (non-bonding) in the split atom model are 2.776(3) Å and 3.164(3) Å ($Ca_{14}FeAs_{11}$). For $Ca_{14}MnAs_{11}$ the values for the split atom model are given as 2.73 Å for the bonding distance and 3.31 Å for the non-bonding. The similarity of this distance for the Fe and Ga compound (non-split atom model) is expected due to the similar unit cell parameters. A large difference for the Mn compound (split atom model) is observed. Since the $[As_3]^{7-}$ unit lies in the *ab*-plane the variation can be explained with the larger *a* lattice parameter of $Ca_{14}MnAs_{11}$. The distances within the $[As_3]^{7-}$ unit for $Sr_{14}MnAs_{11}$ (split atom model) are longer in comparison to $Ca_{14}MnAs_{11}$, it is 2.75 Å for the bonding and 3.45 Å for the non-bonding As–As distance. The heavier homologue Sr enlarges the unit cell parameters which lead to an elongation of the distances within the structural motifs. The distance of the bonding As atoms, d_{As-As}, is slightly longer in $Ca_{14}FeAs_{11}$ (2.776(3) Å) than in $Sr_{14}MnAs_{11}$ (2.75 Å). The distance to the adjacent As atom of the trimeric unit is however shorter in $Ca_{14}FeAs_{11}$ (3.164(3) Å) than in $Sr_{14}MnAs_{11}$ (3.45 Å). The Sr-compound was measured at lower temperature (130 K) and the weaker interaction of the As dumbbell with the adjacent As atom can explain the slightly stronger As–As bonding in the dumbbells. The same is observed in $LaTAsO$ compounds (T = Mn, Fe) where two-dimensional $[TAs_4]$ layers are present.[50, 51]

The oxidation state of the Fe in the tetrahedra could be +2 or +3 resulting in $[FeAs_4]^{9-}$ or $[FeAs_4]^{10-}$ units. Fe^{3+} has d^5 configuration, the tetrahedra are expected to show no *Jahn-Teller* distortion but ideal tetrahedral coordination in that case. If Fe has the oxidation state +2 the configuration would be d^6 which is expected to show a distortion for tetrahedra. However, if Fe has the oxidation state +3 the compound could be explained with the Zintl rule. The tetrahedra in $Ca_{14}FeAs_{11}$ show weak distortion. Distorted FeE_4 tetrahedra with Fe^{3+} do exist in certain compounds: for example, the compound Na_5FeS_4 contains isolated FeS_4 tetrahedra with the angles between 106.6 ° and 113.1 °.[52]

Part of the sample was used to perform Mössbauer spectroscopy to conclusively determine the oxidation state of Fe. Unfortunately, the Fe content of the ternary compound is rather low. In addition the sample also contained the binary $Ca_{11}As_{10-x}$ phase as main phase decreasing the total Fe content within the sample even more. The measurements were unsuccessful and the question of the Fe oxidation state is still unclear.

5.2.2.2. Differential Scanning Calorimetry

To investigate the thermal stability of $Ca_{14}FeAs_{11}$ 50 mg (powder) of the sample was sealed into a Nb ampoule and differential scanning calorimetry (DSC) measurement was performed. The ampoule was heated to 1000 °C and cooled back down. The ramping temperature was set to 5 °C/min (see Figure A24, Appendix). No strong endothermic or exothermic signals were observed in either of the two cycles performed. A broad bump at approximately 800 °C in the heating curves and approximately 500 °C in the cooling curves can be observed. What causes the bump is not known. A powder X-ray diffraction measurement showed the same two phases $Ca_{11}As_{10-x}$ and $Ca_{14}FeAs_{11}$ to be present after the DSC measurement (see Figure A25, Appendix). Brown *et al*. reported that $Yb_{14}MnSb_{11}$ shows no sign of melting up to 1200 K while a small loss of Zn in $Yb_{14}ZnSb_{11}$ was observed to happen when the compound is heated above 800 K.[25]

5.2.2.3. Electronic structure of $Ca_{14}FeAs_{11}$

In order to analyze the electronic structure of $Ca_{14}FeAs_{11}$ total and partial DOS were calculated. The theoretical DOS calculations were performed for two models. For one model (tetragonal space group $I4_1/acd$) the structural parameters obtained from single crystal refinement were used where the central As position (As4) of the $[As_3]^{7-}$ unit was not split (further referred to as non-split atom model). The input data is listed in Table A21 (Appendix). Since the TB-LMTO-ASA program allows only calculations with full occupied atomic sites, a symmetry reduction was performed for the second model. The As4 atom lies on a special position where all the glide planes of the $I4_1/acd$ space group cut through. In order to lift the restrictions the tetragonal space group $P4_3$ was chosen (further referred to as split atom model). Due to the symmetry reduction 22 individual As atomic positions, 2 Fe atomic positions and 28 Ca atomic positions are present. As a result the $[As_3]^{7-}$ unit can be described according to Figure 5.6c with a non-split atom model and full atomic occupancy. The atomic parameters of all positions used for the calculations are listed in Table A22 (Appendix).

The total and partial DOS for both models are presented in Figure 5.8. The partial DOS for Fe-d (turquois), Ca-d (gray), As-s,p ($FeAs_4$ unit, magenta) and As-s,p (As_3 unit, green) are presented. The total DOS (black curves) show 5 separate blocks divided by gaps for both models. The first block at the lower energies lies between −12 eV and −9.5 eV followed by a gap of approximately 5 eV. The main contribution in this block comes from the As-s,p orbitals of the $FeAs_4$ and the As_3 unit (the As-s orbitals are the most dominant contributor, the corresponding pDOS is not shown). At approximately −9.5 eV minor contribution of the Ca-d orbitals is observed. The second block is located between −4.5 eV and −0.5 eV. All presented pDOS have contributions in this block. The shapes of the Fe-d orbitals are similar to that of the As-s,p orbitals of the $FeAs_4$ unit indicating hybridization of these orbitals. The strong interactions of the orbitals correspond to the covalent bonds between Fe and As within the isolated tetrahedra. The same is observed in the Fe-d and As-s,p pDOS of $CaFe_2As_2$ ($ThCr_2Si_2$ structure type) with [FeAs] tetrahedral layers.[53] Interestingly, the contributions of the Ca-d orbitals in $Ca_{14}FeAs_{11}$ are rather pronounced and show a similar shape.

Around the Fermi level, between −0.5 eV and 0.6 eV, main contributions are attributed to Fe-d orbitals with input from As-s,p orbitals of the $FeAs_4$ unit and Ca-d orbitals. At the Fermi level the DOS shows a local maximum. The presence of DOS contributions at the Fermi level indicates metallic behavior for the compound. Since all contributions come from Fe-d and As-s,p orbitals belonging to the $FeAs_4$ unit, the Ca-d contributions in this block come most likely from the Ca atoms coordinating the tetrahedra.

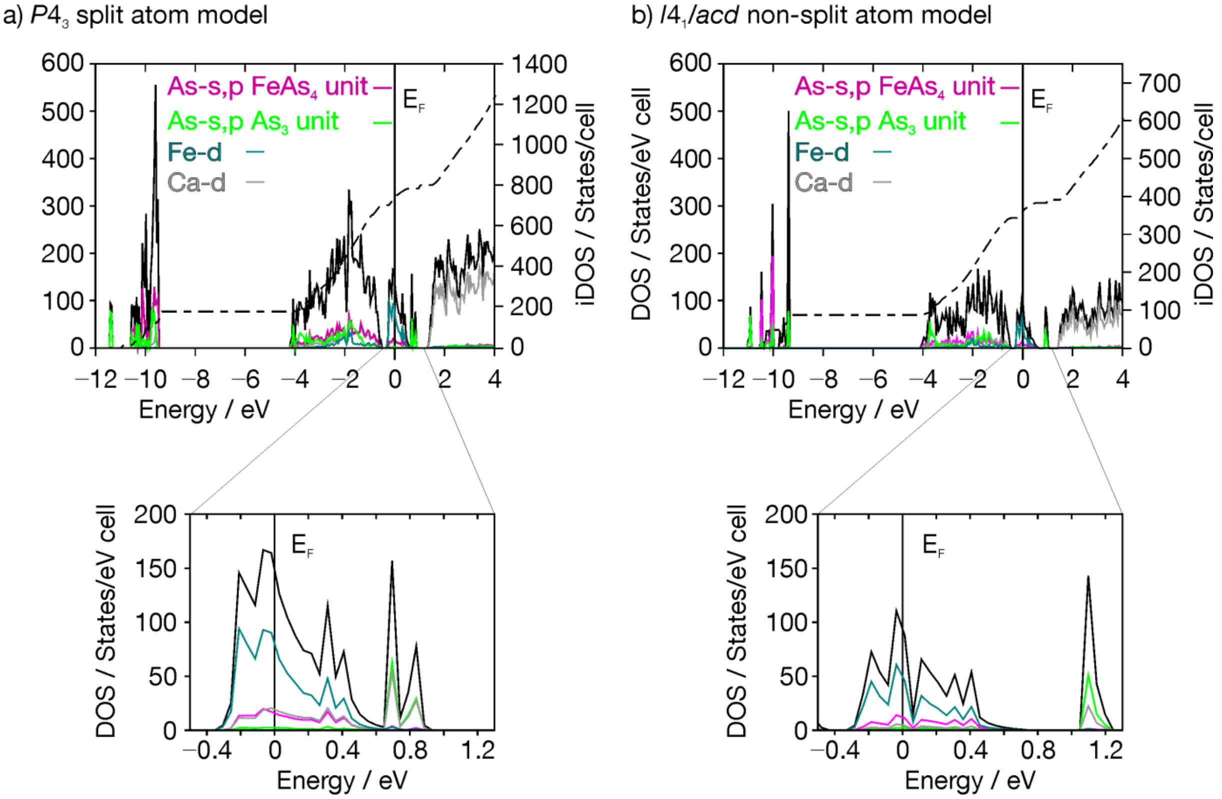
a) *P*4$_3$ split atom model

b) *I*4$_1$/*acd* non-split atom model

Figure 5.8 DOS and partial DOS of Ca$_{14}$FeAs$_{11}$: a) split atom model (space group $P4_3$); b) non-split atom model (space group $I4_1/acd$). Total DOS (black) including pDOS of Fe–d (turquois), As–s,p tetrahedra (magenta), As–s,p As3 unit (green) and Ca-d (gray). The DOS region between –0.5 eV and 1.3 eV are magnified in the bottom graphs.

Above 0.9 eV the main contributions come from the Ca-d orbitals. Next to the block present at the Fermi level a local maximum is observed. The Ca-d and As-s,p orbitals (from the As$_3$ unit) contribute to the peak. The non-split atom model shows one peak at approximately 1 eV while the split atom model shows two peaks between approximately 0.8 eV and 1 eV. The pDOS show similar shapes indicating interactions between the As atoms of the As$_3$ unit and the coordinating Ca atoms. Comparing the two models (Figure 5.8a and b) the overall curve progression is similar, the main difference is that the sharp peaks observed for the split atom model (Figure 5.8a) often show the expected splitting of the peaks in the non-split atom model (Figure 5.8b). A noticeable difference for both models is observed around 1 eV.

In addition the band structure, including fat bands of Fe-d orbitals, and the Crystal Orbital Hamilton Population (COHP) for the Fe–As bond are investigated. The calculations could only be performed with the high symmetry non-split atom model. The work space needed and computational requirements for the split atom model with lower symmetry were too demanding to perform the calculations. The overall similarities of the two DOS models show that the non-split atom model can be used as an acceptable approximation for the band and COHP calculations. However, the COHP for the As–As distances in the As_3 unit is not calculate since the non-split atom model contains an average bond length within that unit which does not represents the real situation. Also the fat bands for the As atoms of the $FeAs_4$ tetrahedra could not be calculated during this work.

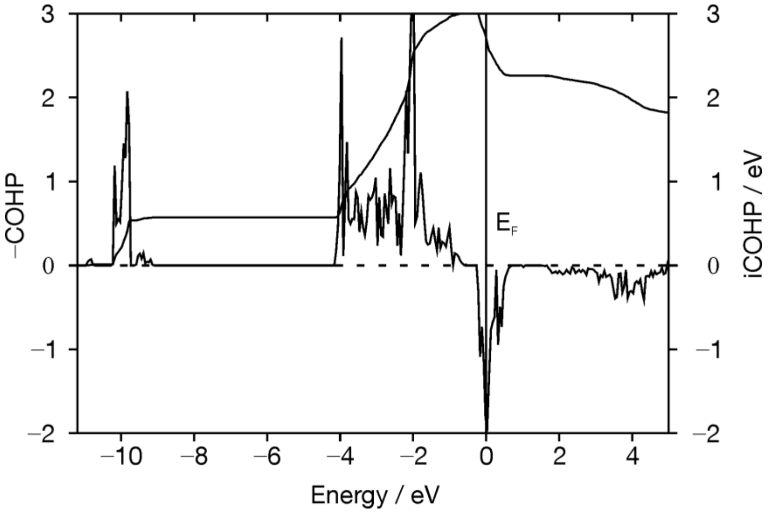

Figure 5.9 COHP and iCOPH of the Fe–As bond (2.503(1) Å) in $Ca_{14}FeAs_{11}$ (non-split atom model).

The COHP for the Fe–As bond (2.503 Å) including the iCOHP is shown in Figure 5.9. At energies below −9 eV the bonding states of the As-s orbitals are present, the iCOHP value is low for the block. Between approximately −4.2 eV and −0.4 eV a second block of bonding states is present. From DOS the states present are contributions from As-p and Fe-d orbitals. The block of peaks observed in DOS around the Fermi level (−0.4 eV and 0.8 eV) shows an anti-bonding character. The iCOHP at the Fermi level has a value of 2.66 eV which confirms the covalent bonding interaction within the isolated $FeAs_4$ tetrahedron.

Fe-d orbitals in a tetrahedral environment are split into e_g with 2 degenerated states at lower energies and t_{2g} with 3 degenerated states at higher energies. The e_g states are d_{xy} and d_{z2} and the t_2g states are d_{x2y2}, d_{xz} and d_{yz} in the coordination system used for this calculation. To determine if the e_g states and the t_{2g} states in $Ca_{14}FeAs_{11}$ are of bonding or anti-bonding character and where the states are located, the fat bands for the 5 Fe-d orbitals have been calculated.

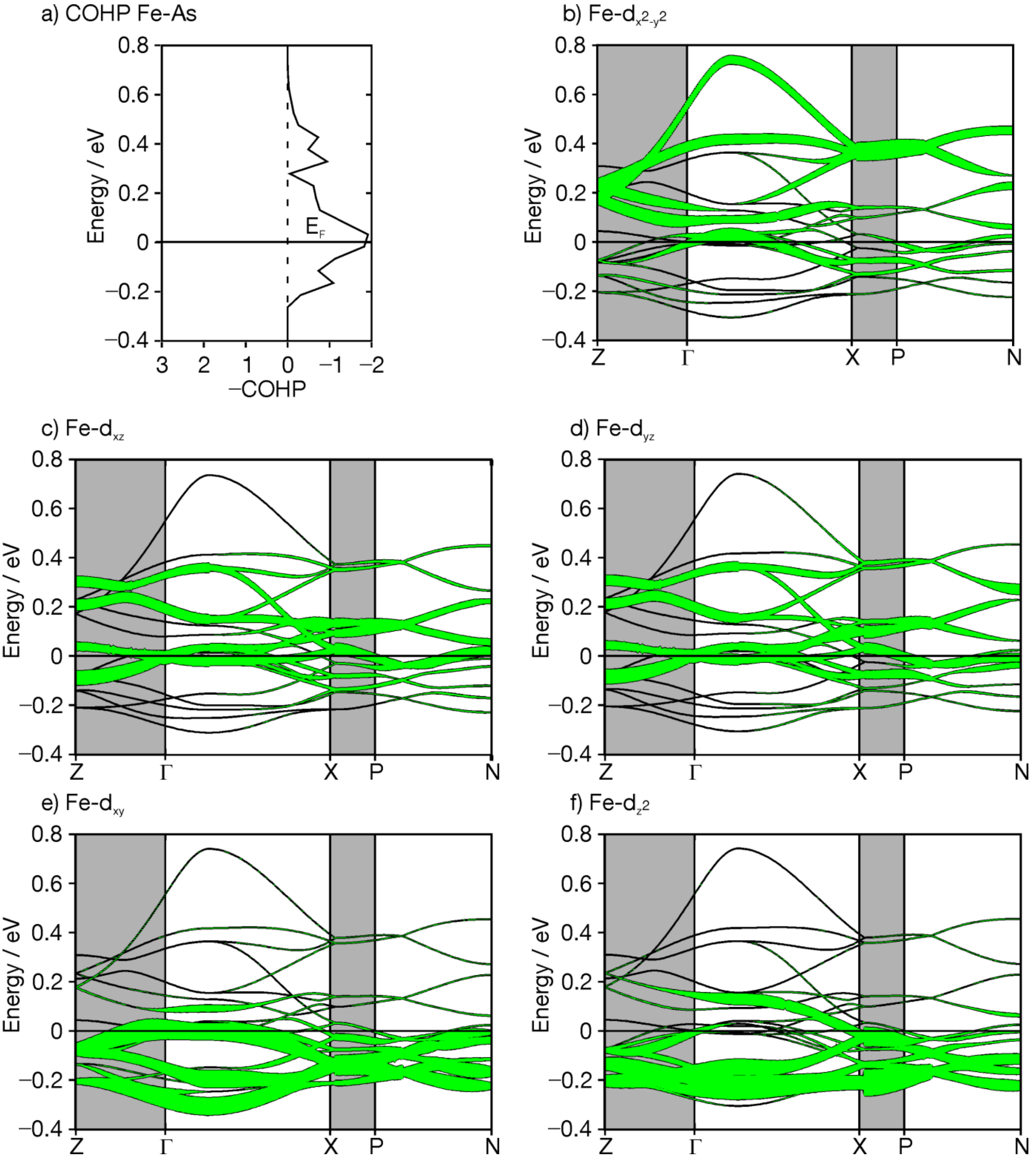

Figure 5.10 Electronic structure for $Ca_{14}FeAs_{11}$ (non-split atom model). a) COHP for Fe–As bond (d_{Fe-As} = 2.503 Å); fat bands for b) Fe-d_{x2-y2}, c) Fe-d_{xz}, d) Fe-d_{yz}, e) Fe-d_{xy} and f) Fe-d_{z2}. *k*-paths parallel to the *c*-direction are highlighted gray, path parallel to *ab*-plane are white.

The representation for the Fe-d fat bands for $Ca_{14}FeAs_{11}$ between –0.4 eV and 0.8 eV are depicted in Figure 5.10(b-f). The anti-bonding COHP region between –0.4 eV and 0.8 eV also shows fat band contribution from the Fe-d orbitals. For the tetragonal space group *I*4$_1$/*acd* the Γ *k*-point lies in the origin of the Brillouin zone, therefore the fat band distribution of the Fe-d orbitals at Γ is compared. A clear distinction between the different Fe-d orbitals can be made. Fe-d_{xy} and Fe-d_{z^2} has fat band contributions mainly located below the Fermi level. The Fe-d_{xz}, Fe-d_{yz} and

Fe-d_{x2-y2} fat band contributions are above the Fermi level. At the Fermi level all Fe-d orbitals show contributions. This distribution of the Fe-d fat bands reflects the expected e_g and t_{2g} states for Fe in a tetrahedral environments. However, Fe-d_{x2-y2} lies in the higher energy t_{2g} state while Fe-d_{xy} lays in the lower energy e_g state. It can be explained by a 45 ° rotation of the unit cell around the *c*-axis for the non-split atom model.

In conclusion the Fe-d states responsible for the Fe–As interactions all show anti-bonding character and are positioned around the Fermi level. A separation into e_g and t_{2g} states is observed in accordance with the ligand field theory.

5.3. New binary Ca–As phases

Two new phases in the binary phase system Ca–As could be synthesized and characterized as part of this work. The new compounds Ca_4As_3 and $Ca_{11}As_{9.68(2)}$ were first observed as a side phase in a sample containing the elements Ca, Fe, Rh, Si and As. The phases could be identified from refinement of single crystals found in that sample. The binary phases were subsequently tried to be synthesized from the pure elements. The binary phase Ca_4As_3 crystallizes in space group *Pbam* (Z = 8) with Ba_4P_3 structure type,[54] the binary phase $Ca_{11}As_{9.68(2)}$ crystallizes in the space group *I*4/*mmm* (Z = 4) with $Ho_{11}Ge_{10}$ structure type.[55]

5.3.1. Syntheses of the binary phases

5.3.1.1. Ca_4As_3

Attempts to synthesize the compound from the pure elements Ca and As in the nominal compositions $Ca_{4+x}As_3$ (x = 0, 0.05 and 0.1, see Table 5.6) were made. The elements were sealed in silica glass tubes (non-graphitized and graphitized) and syntheses took place in a muffle furnace. The ampoules were heated up to 1173 K for 48 h and slowly cooled down to 973 K. After 24 h the furnace was switched of.

Table 5.6 Masses of Ca and As used for the samples of $Ca_{4+x}As_3$.

Nominal composition, *x*	**Ca / g**	**As / g**	**Total mass / g**
0	0.183	0.256	0.439
0.05	0.210	0.290	0.500
0.1	0.304	0.417	0.721

The samples contained mainly CaAs and $Ca_{11}As_{10}$ with only small amounts of Ca_4As_3 as side phase (see Figure A26, Appendix). This is most likely due to the close compositions of the three phases. No good quality single crystals could be isolated from the samples made from Ca and As in any of the nominal starting compositions.

Single crystals of Ca_4As_3 were isolated from the previously mentioned batch containing Ca, Fe, Rh, Si and As. A sample with the nominal composition of 12:10:10:4:8 (Ca:Fe:As:Rh:Si) was prepared. The initial goal was to synthesize a $(CaFeAs)_{10}Rh_{4-y}Si_8$ compound analog to the reported $(CaFeAs)_{10}Pt_{4-y}As_8$ compounds with 2D $[Fe_{1-x}Pt_xAs]$ and $[Pt_{4-y}As_8]$ layers in 2011.[6, 56] Ca was provided in excess (20 at. %) since losses of alkaline earth metal in previous reactions were often observed.

First a Rh–Si precursor was prepared from pure elements in a 1:2 (0.453 g Rh: 0.247 g Si) ratio. The elements were sealed in a Ta ampoule and thermally treated in the induction furnace (temperature program given in Figure 5.11a). The resulting powder contained RhSi and Si. The Rh–Si precursor was intended to help with the formation of a $[Rh_{4-y}Si_8]$ layer analogous to the reported $[Pt_{4-y}As_8]$ ones.

The sample was then prepared from the elements and the “Rh–Si” precursor and thermally treated in a sealed Ta ampoule using a resistance furnace (temperature program given in Figure 5.11b).

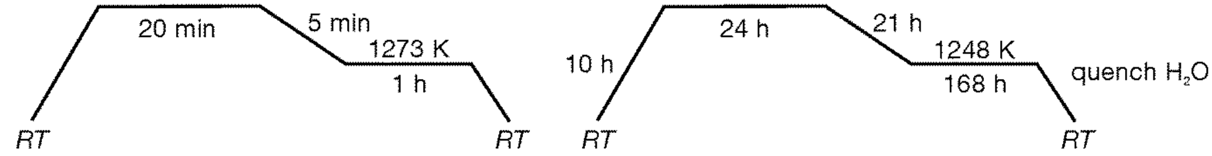

Figure 5.11 Temperature program for measured single crystals of Ca_4As_3: a) Rh-Si precursor heating cycle; b) heating cycle for the sample with nominal composition “$Ca_{12}(RhSi_2)_4(Fe_2As_2)_5$”.

Single crystals of good quality (needles, metallic luster) were measured on a *Xcalibur3* (Oxford) diffractometer under N_2 flow at 150 K. The Ca_4As_3 compound is air and moisture sensitive.

5.3.1.2. $Ca_{11}As_{9.68(2)}$

Reproduction of the compound was attempted with preparation from pure elements. Ca ingots and As pieces were placed in a silica glass ampoule which was sealed and thermally treated in a muffle furnace. After heating the ampoule was opened in a glove box. Different stoichiometric compositions were tested in order to increase phase purity. Samples with a starting ratio of 11:10 (0.259 g Ca: 0.441 g As) resulted in a mixture of CaAs as main phase and $Ca_{11}As_{10-x}$ as side phase. Samples prepared in graphitized silica glass ampoules, to prevent reaction of Ca with the ampoule, did not result in phase purity either. The corresponding temperature program is shown in Figure 5.12.

The fraction of $Ca_{11}As_{10-x}$ phase in the product was increased by giving 20 at. % Ca in excess (nominal $Ca_{13.2}As_{10}$; 0.183 g Ca and 0.256 g As) and annealing (sample ground and pelletized between the heating cycles) of the sample (see Figure A27, Appendix). The powder diffraction pattern indicated mainly $Ca_{11}As_{10-x}$ phase, additional reflections which are present in the pattern do not belong to the CaAs phase but to an unidentified phase.

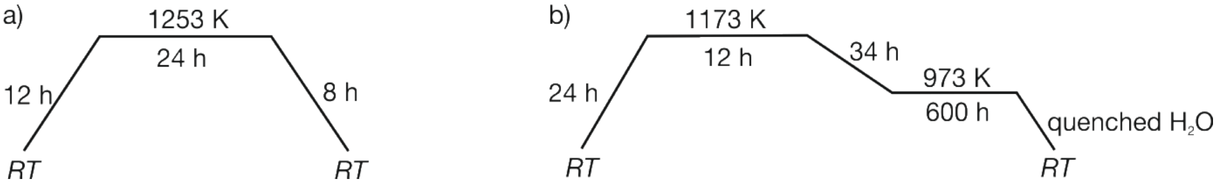

Figure 5.12 Temperature program for the $Ca_{11}As_{10}$ compound: a) short heating cycle; b) long heating cycle.

Good quality single crystals (plate shape, metallic luster) could be isolated from the sample made with $Ca_{14}Fe_{1.1}As_{11}$ (Chapter 5.2.1) and were measured on a *Xcalibur3* (Oxford) diffractometer under N_2 flow at 150 K. Crystal quality in binary Ca–As samples was not very good. The $Ca_{11}As_{10-x}$ phase is air and moisture sensitive.

5.3.2. Results and discussion

5.3.2.1. Crystal structure of Ca_4As_3

The structure of Ca_4As_3 was obtained using single crystal X-ray diffraction method. The refinement details are given in Table 5.7, Table 5.8 and Table A23 (Appendix). The compound crystallizes in the orthorhombic *Pbam* space group (Z = 8) with lattice parameters a = 11.514(1) Å, b = 12.058(1) Å and c = 10.343(1) Å. It is isostructural to Ba_4P_3 and Sr_4As_3. The results described in this subchapter can also be found in the corresponding publication.[57] The structure type contains six individual Ca positions and five As position.

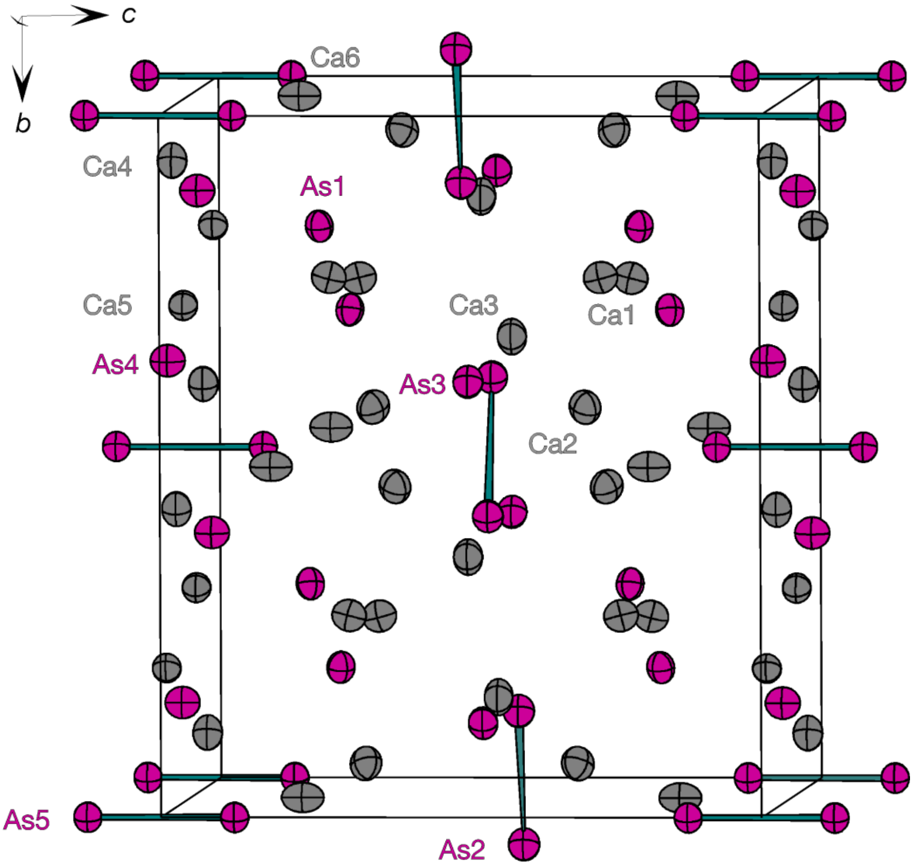

Figure 5.13 Unit cell of Ca_4As_3 with space group *Pbam*, Z = 8. The atoms are represented as atomic displacement ellipsoids with 90 % probability level, As depicted in magenta, Ca depicted as gray. The covalent As–As bonds are shown in green.

Two individual As positions (As2 and As5) have covalent bonding interactions in form of As–As dumbbells. The other As atoms are isolated and only coordinated by Ca atoms. The unit cell is shown in Figure 5.13.

The compound can be explained with the Zintl-Klemm concept: 32 Ca^{2+} cations are counterbalanced by 16 isolated As^{3-} anions and 4 $[As_2]^{4-}$ dumbbells (two As2–As2 dumbbells and two As5–As5 dumbbells) per unit cell.

The dumbbells formed by the As2 anions lie in the *ab*-plane with a bond distance $d_{As2-As2}$ of 2.507(1) Å. The second type of dumbbells are made by the As5 anions, $d_{As5-As5}$ is 2.528(1) Å and lie along the *c*-direction.

Table 5.7 Crystal data and measurement details for single crystal refinement of Ca_4As_3, collected at 150 K.

Empirical formula		**Ca_4As_3**
Diffractometer		*Oxford Xcalibur3*
Detector distance	/ mm	50
Formula weight	/ g·mol^{-1}	385.08
Space group, *Z*		*Pbam*, 8
Unit cell dimensions	/ Å	a = 11.514(1)
		b = 12.058(1)
		c = 10.343(1)
	/ Å^3	V = 1435.9(1)
Absorption coefficient	/ mm^{-1}	16.614
Crystal size	/ mm	0.08 × 0.4 × 0.01
Absorption correction		multi-scan
Calculated density	/ g·cm^{-3}	3.563
F(000)		1432
θ range	/ °	3.38 to 29.99
Range in *hkl*		± 16, ± 16, $-13 < l < 14$
Reflections collected		23960
Independent reflections		2207 (R_{int} = 0.1329)
Reflections with $I \geq 2\sigma(I)$		1202 (R_σ = 0.1293)
Data/Parameters		2207/75
GOF on F^2		0.705
Final R indices [$I \geq 2\sigma(I)$]		R_1 = 0.0309
		wR_2 = 0.0448
R indices (all data)		R_1 = 0.0739
		wR_2 = 0.0481
Largest diff. peak and hole	/ e Å^{-3}	1.534, −1.161

Both dumbbell distances are similar to covalent single bonds observed in pure As and binary Ca–As compounds (2.44 - 2.57 Å).[12, 13, 43] Eight Ca cations coordinate the As anions of the dumbbells in both cases. Six Ca cations form a distorted trigonal prism while two Ca cations cap two of the faces, the third face is capped by the bonded As atom (Figure 5.14b and e). The interatomic distances for the coordination spheres are listed in Table 5.9.

Two of the isolated As^{3-} anions (As1 and As3) are also coordinated by Ca atoms in form of distorted trigonal prism. For As1 only two faces of the prism are capped (Figure 5.14a) while As3 has three faces capped by Ca atoms (Figure 5.14c). The coordination in form of trigonal prism with capped faces around As anions is also observed in Ca_2As_3 and $Ca_{14}FeAs_{11}$.

Table 5.8 Wyckoff positions, atomic coordinates and isotropic equivalent displacement parameters /Å^2 × 10^3 (space group *Pbam*, *Z* = 8).

Atom	**Wyckoff position**	***x***	***y***	***z***	***U*$_{eq}$ / Å^2 × 10^3**
Ca1	8*i*	0.0941(1)	0.2354(1)	0.2734(1)	11.4(3)
Ca2	8*i*	0.3232(1)	0.4330(1)	0.3233(1)	12.5(3)
Ca3	4*h*	0.3750(2)	0.1360(2)	½	13.5(4)
Ca4	4*g*	0.2257(1)	0.0767(2)	0	11.3(4)
Ca5	4*g*	0.3997(2)	0.2931(1)	0	10.6(4)
Ca6	4*g*	0	½	0.1853(2)	13.1(4)
As1	8*i*	0.3372(1)	0.1763(1)	0.2334(1)	9.8(2)
As2	4*h*	0.0388(1)	0.0971(1)	½	11.6(2)
As3	4*h*	0.1352(1)	0.3864(1)	½	10.8(2)
As4	4*g*	0.1402(1)	0.3569(1)	0	12.1(2)
As5	4*e*	0	0	0.1222(1)	9.3(2)

The two trigonal prisms around As2 share the tetragonal face with the As dumbbell in the center. The double prisms are oriented along the *ab*-plane. The same face sharing of two trigonal prisms around As5 is observed, they are oriented along the *c*-direction. The trigonal prisms around As1 and As3 are connected by common edges.

The only As anion that has a different coordination is As4 with the highest number of Ca cations (10) in the sphere that result in 14 faces (Figure 5.14d). The coordination sphere can be described as an icosahedron that has two adjacent corners removed. Four Ca cations form a distorted tetragonal base, five Ca cations form a distorted pentagon which is capped by the last Ca cation.

The coordination around the Ca cations is formed by six or seven As atoms and eight - ten different Ca atoms. Distorted octahedra are formed by six As atoms around Ca1, Ca4, Ca5 and Ca6 (Figure 5.15a, d - f). For Ca4 and Ca5 one edge is formed by an As5 dumbbell (green bond).

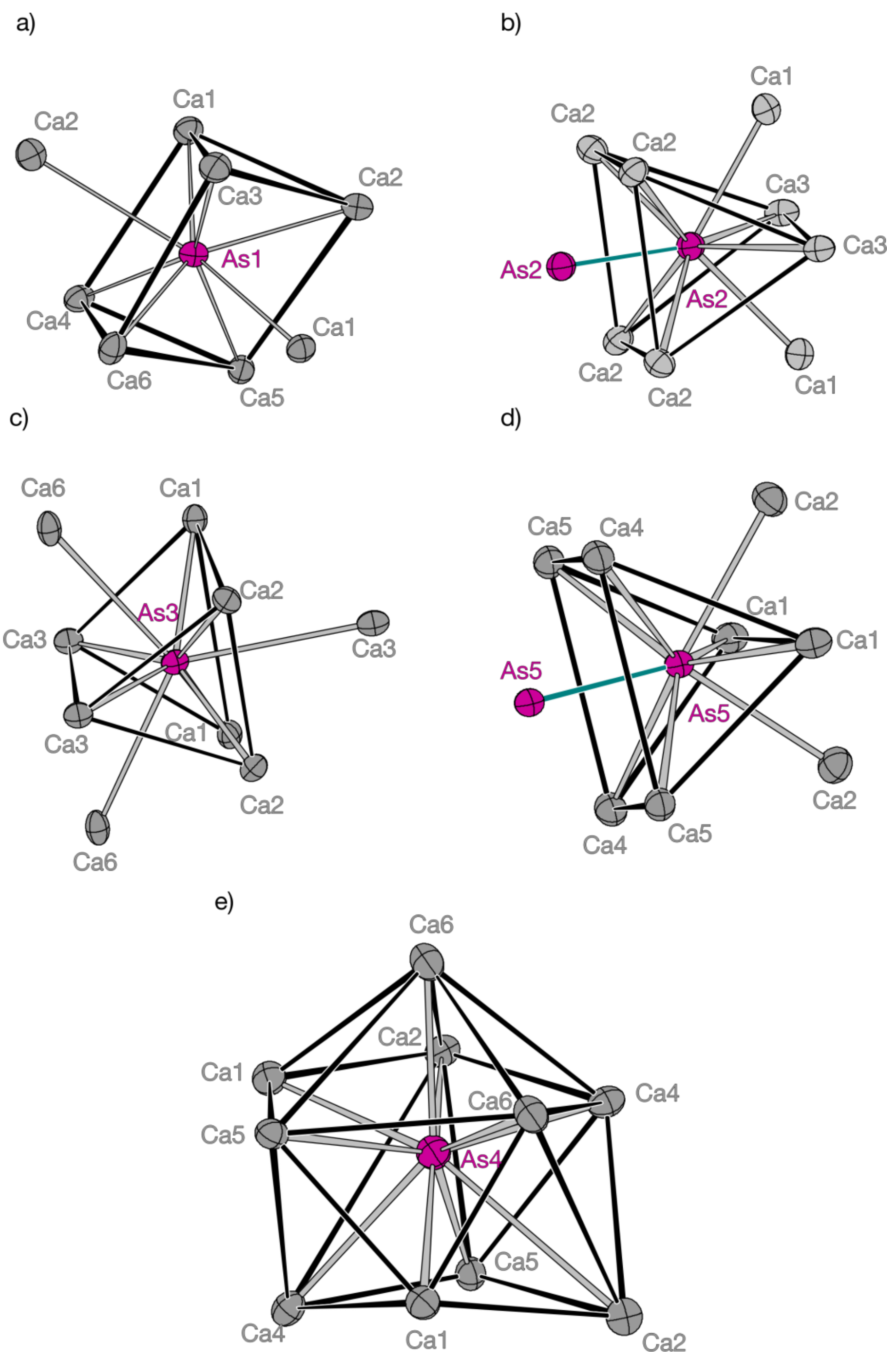
a)
Ca2
Ca1
Ca3
Ca2
As1
Ca4
Ca1
Ca6
Ca5
b)
Ca1
Ca2
Ca2
Ca3
Ca3
As2
As2
Ca2
Ca2
Ca1
c)
Ca6
Ca1
Ca2
As3
Ca3
Ca3
Ca1
Ca3
Ca2
Ca6
d)
Ca2
Ca5
Ca4
Ca1
Ca1
As5
As5
Ca2
Ca4
Ca5
e)
Ca6
Ca2
Ca1
Ca6
Ca4
Ca5
As4
Ca5
Ca4
Ca1
Ca2

Figure 5.14 Coordination of the Ca^{2+} cations around the As positions in Ca$_4$As$_3$ atoms are represented as atomic displacement ellipsoids with 90 % probability level. The covalent As–As bonds are depicted in green, the non-bonding distances Ca–As (gray) and Ca–Ca (black) are for visible help.

The faces of the octahedral are capped by Ca cations, the number of capping cations depends on the maximum $d_{\text{Ca–Ca}}$ chosen. In most cases $d_{\text{Ca–Ca}}$ is larger than 3.5 Å, however a rather short distance of 3.289(2) Å is observed between Ca4 and Ca5. Those are the two Ca positions that are coordinated by the As5 dumbbells (Figure 5.15d and e). The distorted As octahedra around Ca4 and Ca5 share a common face (As1–As1–As4) in the *ab*-plane.

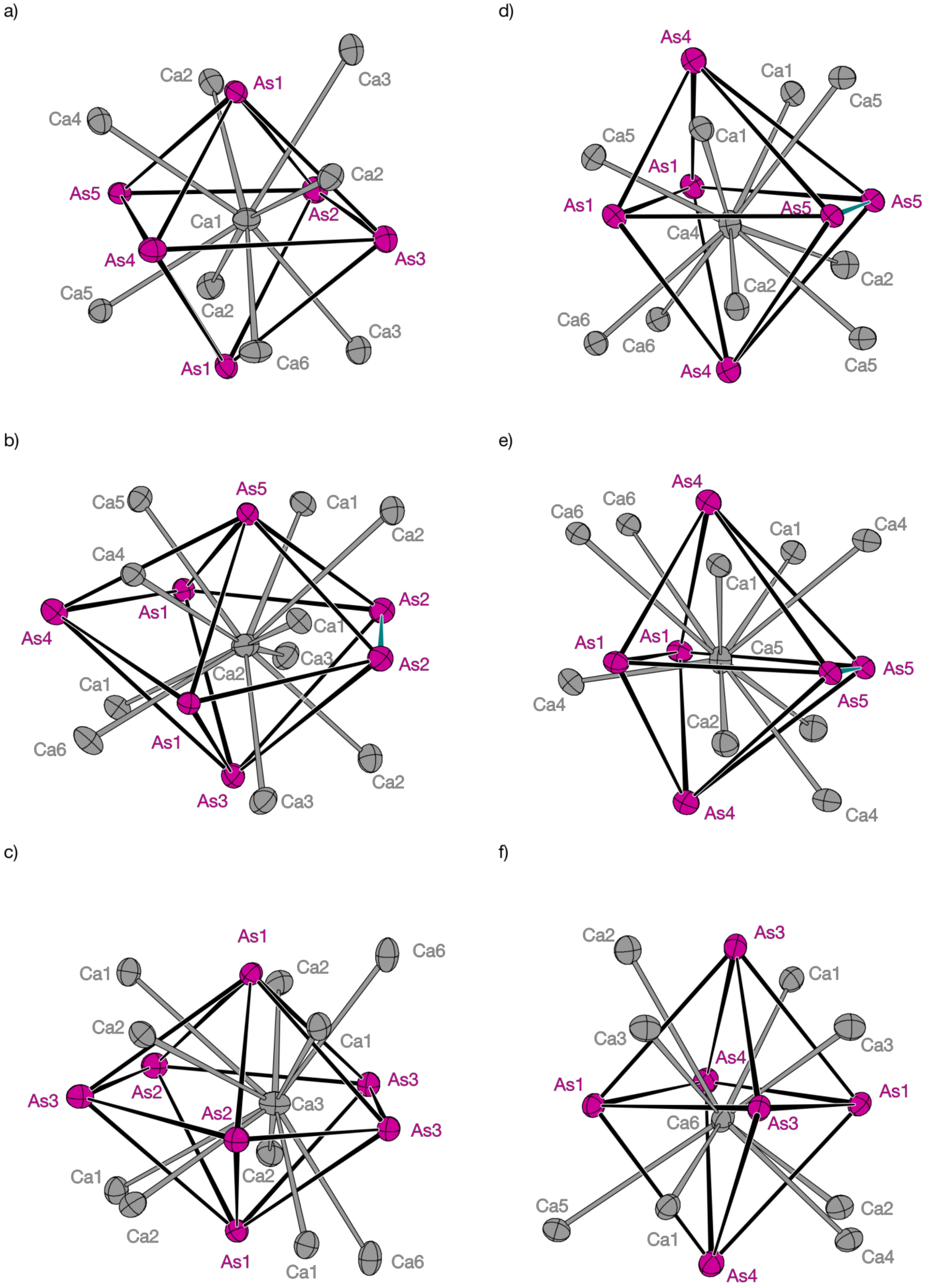
a)
Ca2
As1
Ca3
Ca4
As5
Ca2
As2
Ca1
As4
As3
Ca5
Ca2
Ca3
As1
Ca6
d)
As4
Ca1
Ca5
Ca5
Ca1
As1
As1
As5
As5
Ca4
Ca2
Ca2
Ca6
Ca6
Ca5
As4
b)
Ca5
As5
Ca1
Ca2
Ca4
As2
As1
As4
Ca1
Ca3
As2
Ca2
Ca1
Ca6
As1
Ca2
As3
Ca3
e)
As4
Ca6
Ca6
Ca1
Ca4
Ca1
As1
As1
Ca5
As5
Ca4
As5
Ca2
As4
Ca4
c)
As1
Ca6
Ca1
Ca2
Ca2
Ca1
As3
As3
As2
Ca3
As2
As3
Ca1
Ca2
Ca2
As1
Ca1
Ca6
f)
Ca2
As3
Ca1
Ca3
Ca3
As4
As1
As1
Ca6
As3
Ca5
Ca2
Ca1
Ca4
As4

Figure 5.15 Coordination of the As anions and Ca^{2+} cations around the Ca positions in Ca_4As_3 atoms are represented as atomic displacement ellipsoids with 90 % probability level. The covalent As–As bonds are depicted in green, the non-bonding distances Ca–As (gray) and Ca–Ca (black) are for visible help.

Ca2 and Ca3 are surrounded by seven As atoms (Figure 5.15b, c). In both cases the coordination polyhedron resembles a distorted pentagonal bipyramide. For Ca2 one edge of the pentagon is an As2 dumbbell. Each of the trigonal faces is capped by Ca atoms.

Table 5.9 Atomic distances (*d*) within the first coordination sphere including their multiplicity for the individual structural units of Ca_4As_3; space group *Pbam*, *Z* = 8. The homoatomic distances $d_{Ca–Ca}$ for the coordination of Ca not individually given, they are between 3.289(2) Å and 4.380(2) Å.

Atom1	**Atom2**	***d* / Å**	**Atom1**	**Atom2**	***d* / Å**
As1	–Ca3	2.834(1); ×1	Ca1	–As1	2.918(1); ×1
	–Ca6	2.878(1); ×1		–As2	2.946(1); ×1
	–Ca5	2.886(1); ×1		–As3	3.006(1); ×1
	–Ca1	2.918(1); ×1		–As1	3.171(1); ×1
	–Ca4	2.986(1); ×1		–As4	3.339(1); ×1
	–Ca1	3.171(1); ×1		–As5	3.416(1); ×1
	–Ca2	3.236(2); ×1			
	–Ca2	3.589(1); ×1	Ca2	–As3	2.888(1); ×1
				–As5	3.020(1); ×1
As2	–As2	2.507(1); ×1		–As2	3.104(1); ×1
	–Ca1	2.946(1); ×2		–As2	3.128(1); ×1
	–Ca2	3.104(1); ×2		–As1	3.236(1); ×1
	–Ca2	3.128(2); ×2		–As1	3.589(1); ×1
	–Ca3	3.730(2); ×1		–As4	4.057(1); ×1
	–Ca3	3.899(2); ×1			
			Ca3	–As1	2.834(1); ×2
As3	–Ca2	2.888(1); ×2		–As3	3.009(2); ×1
	–Ca1	3.006(1); ×2		–As3	3.012(2); ×1
	–Ca3	3.009(2); ×1		–As2	3.730(2); ×1
	–Ca3	3.012(2); ×1		–As2	3.899(2); ×1
	–Ca6	3.860(2); ×2		–As3	4.091(2); ×1
	–Ca3	4.091(2); ×1			
			Ca4	–As1	2.986(1); ×2
As4	–Ca6	3.042(1); ×2		–As5	3.035(2); ×2
	–Ca4	3.067(2); ×1		–As4	3.067(2); ×1
	–Ca5	3.085(2); ×1		–As4	3.519(2); ×1
	–Ca1	3.229(1); ×2			
	–Ca5	3.308(2); ×1	Ca5	–As1	2.886(1); ×2
	–Ca4	3.519(2); ×1		–As5	3.026(2); ×2
	–Ca2	4.057(1); ×2		–As4	3.085(2); ×1
				–As4	3.308(2); ×1
As5	–As5	2.528(1); ×1			
	–Ca2	3.020(2); ×2	Ca6	–As1	2.878(1); ×2
	–Ca5	3.026(2); ×2		–As4	3.042(1); ×2
	–Ca4	3.035(2); ×2		–As3	3.860(2); ×2
	–Ca1	3.416(2); ×2			

Comparison of Ca_4As_3 with the isostructural Sr_4As_3 and Ba_4P_3 show that the lattice parameters increase in accordance with the cation size.[49] The lattice parameters are approximately 6 % larger in Sr_4As_3 (a = 12.19 Å, b = 12.78 Å, c = 10.96 Å).[58] The distances in the As–As dumbbells are 2.52 Å and 2.55 Å which is slightly longer than observed in dumbbells of Ca_4As_3 (2.507(1) Å and 2.528(1) Å, respectively). The lattice parameters for Ba_4P_3 are further increased because of the bigger Ba.[54] The distances in the dumbbells are however shorter than in the As compounds due to the smaller covalent radius of P: $d_{P–P}$ are 2.25 Å and 2.32 Å.

5.3.2.2. $Ca_{11}As_{9.68(2)}$ crystal structure

Lattice parameters for $Ca_{11}As_{9.68(2)}$ could be determined from single crystal X-ray diffraction measurements: a = 11.253(1) Å, c = 16.235(1) Å with V = 2055.9(1) $Å^3$ from single crystal refinement (measurement at 150 K). Refinement data from single crystal measurement are given in Table 5.10 and Table 5.11 as well as Table A24 (non-split atom model) and Table A25 (split atom model) (Appendix). The refinement gave a composition of $Ca_{11}As_{9.68(2)}$ for the measured single crystal. The unit cell contains isolated As^{3-} atoms, As dumbbells $[As_2]^{4-}$ and $[As_4]^{4-}$ square units as structure motifs. The As atomic positions in the square unit have defects which results in the composition of Ca:As = 11:9.68(2) . The crystal structure of $Ca_{11}As_{9.68(2)}$ (non-split atom model) is shown in Figure 5.16.

The unit cell contains 44 Ca cations (formal charge 2+) leading to 88 positive charges. 16 isolated As anions (formal charge 3–) give 48 negative charges, in addition eight As–As dumbbells ($[As_2]^{4-}$) provide 32 negative charges. The remaining eight negative charges come from the two $[As_4]$ units ($[As_4]^{4-}$), in that case the compound could be described according to the Zintl-Klemm concept.

It has been reported for other $Ae_{11}E_{10}$ compounds (Ae = Ca-Ba, Eu and Yb; E = Sb, Bi) that the atomic position of the As anions in the square (here As5) show rather large anisotropic displacement parameters.[55, 59-61] The adjacent cations (here Ca4) that lie in the same *ab*-plane also show larger anisotropic displacement parameters with an elongation directed towards the anions of the square. The displacement parameters for the two atomic positions (8*h* Wyckoff position) are two or three times larger than for other atomic positions.[59-62] Clark *et al.*[62] proposed that the 8*h* position of the anion is not fully occupied in $Yb_{11}Sb_{10}$ and that the real composition deviates from 11:10. They stated that a reduction of the occupancy leads to better temperature factors but the *R* values increases. The position of the anion in the $[As_4]$ square of $Ca_{11}As_{9.68(2)}$ is not fully occupied but shows a deficiency of approximately 16 at. % resulting in the composition $Ca_{11}As_{9.68(2)}$.

Table 5.10 Crystal data and measurement details for single crystal refinement of $Ca_{11}As_{9.68(2)}$ in the split model, collected at 150 K.

Empirical formula		**$Ca_{11}As_{9.68(2)}$**
Diffractometer		*Oxford Xcalibur3*
Detector distance	/ mm	50
Formula weight	/ g·mol^{-1}	1136.77
Space group, *Z*		*I*4/*mmm*, 4
Unit cell dimensions	/ Å	a = 11.253(1)
		c = 16.235(1)
	/ Å^3	V = 2055.9(1)
Absorption coefficient	/ mm^{-1}	18.420
Crystal size	/ mm	0.2 × 0.12 × 0.03
Absorption correction		semi-empirical
Calculated density	/ g·cm^{-3}	3.673
F(000)		2094
θ range	/ °	3.59 to 29.99
Range in *hkl*		± 15, ± 15, ± 22
Reflections collected		17976
Independent reflections		900 (R_{int} = 0.0696)
Reflections with $I \geq 2\sigma(I)$		718 (R_{σ} = 0.0263)
Data/Parameters		900/49
GOF on F^2		1.200
Final *R* indices [$I \geq 2\sigma(I)$]		R_1 = 0.0373
		wR_2 = 0.0989
R indices (all data)		R_1 = 0.0466
		wR_2 = 0.1013
Largest diff. peak and hole	/ e Å^{-3}	2.642, –3.101

Another suggestion was that the structure type of these compounds might be a distorted version of $Ho_{11}Ge_{10}$. Taylor *et al.* indexed the $Eu_{11}As_{10}$ compound in orthorhombic symmetry with the lattice parameters a = 11.26 Å, b = 11.72 Å and c = 17.39 Å. The exact space group was not determined and no atomic coordinates were provided.[63] The orthorhombic structure was also proposed for $Ba_{11}Sb_{10}$ of Emmerling *et al.*.[64] They reported $Ba_{11}Sb_{10}$ to crystallizes in the *Immm* space group with a = 12.65 Å, b = 13.16 Å, c = 19.47 Å. The symmetry reduction results in the split of the $[Sb_4]^{4-}$ squares (d_{Sb-Sb} = 3.05 Å) into two Sb dumbbells with shorter distances (2.78 Å) along the *a*-direction, the dumbbells are not electron precise but given as $[Sb_2]^{3-}$. In $Ca_{11}As_{9.68(2)}$ the distortion on the 8*h* position for As5 and Ca4 (Table 5.11) is rather large, the anisotropic displacement parameters is five times higher than the others. A reduction in symmetry to the orthorhombic *Immm* space group, like in $Ba_{11}Sb_{10}$, did not solve the problem.

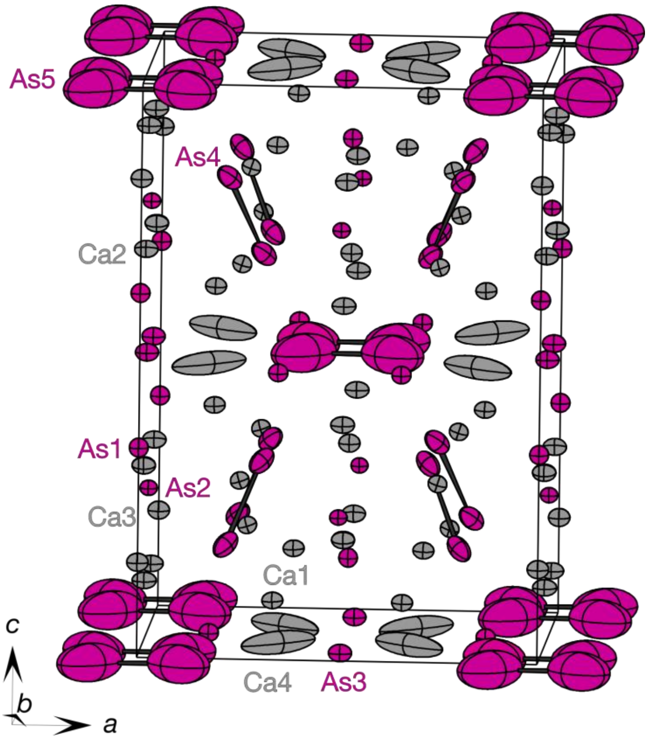

Figure 5.16 Structure of $Ca_{11}As_{9.68(2)}$ in space group *I*4/*mmm* with $Z = 4$ in the non-split atom model. Ca depicted in gray and As depicted in magenta as atomic displacement ellipsoids with 90 % probability level. The covalent As–As bonds are shown in black.

The crystal data was therefore refined in the tetragonal *I*4/*mmm* space group but the 8*h* Wyckoff position of As5 and Ca4 were split into two positions: As5A and As5B, Ca4A and Ca4B, respectively (see Table 5.11). The occupancy for Ca4A and Ca4B was refined to 0.5 each while for As5A it is 0.39(2) and for As5B it is 0.45(2). The effect of the split on the 8*h* Wyckoff positions is shown separately in Figure 5.18. The discussion of the structure details is done in regard to the split atom model unless specifically stated otherwise.

The As dumbbells (As4 atoms) lie in the *ac*-direction, $d_{As–As}$ is 2.621(2) Å long (split atom model, Figure 5.17).

Table 5.11 Wyckoff positions, atomic coordinates and isotropic equivalent displacement parameters / Å^2 × 10^3 (space group $I4/mmm$, Z = 4, split atom model).

Atom	**Occupancy**	**Wyckoff position**	***x***	***y***	***z***	$\boldsymbol{U_{eq}}$ **/ Å^2 × 10^3**
Ca1	1	16*n*	0.3376(1)	0	0.1036(1)	13.3(3)
Ca2	1	16*n*	0.2529(1)	0	0.3116(1)	12.6(3)
Ca3	1	4*e*	0	0	0.1656(2)	13.0(5)
Ca4A	0.5	8*h*	0.3596(4)	0.3596(4)	0	23(1)
Ca4B	0.5	8*h*	0.3082(5)	0.3082(5)	0	30(1)
As1	1	4*e*	0	0	0.3655(1)	11.3(3)
As2	1	4*d*	0	½	¼	8.8(3)
As3	1	8*j*	0.1542(1)	½	0	12.7(2)
As4	1	16*m*	0.2082(1)	0.2082(1)	0.1805(1)	18.3(2)
As5A	0.39(2)	8*h*	0.1366(7)	0.1366(7)	0	69(3)
As5B	0.45(2)	8*h*	0.0955(5)	0.0955(5)	0	59(2)

The covalent $d_{\mathrm{As-As}}$ is larger than those found in other binary Ca–As compounds (CaAs: 2.49 Å,[12] Ca_2As_3: 2.47 Å - 2.57 Å[13]) and smaller than the observed dumbbell distance in $Ca_{14}TAs_{11}$ (2.776(3) Å and 2.73 Å for T = Fe and Mn,[42] respectively).

The dumbbells point towards the As atoms of the As_4 squares, the distance $d_{\mathrm{As4-As5A}}$ is non-bonding with a value of 3.144(3) Å (Figure 5.17b), $d_{\mathrm{As4-As5B}}$ is approximately 0.3 Å longer (3.436(3) Å). If the center of each As_4 square is regarded as one point, six units would resemble the corners of an octahedron and the As dumbbells would represent the edges. The "octahedra" share edges and span a 3D network (see Figure A28, Appendix). The dumbbell is coordinated by twelve Ca atoms ($d_{\mathrm{As-Ca}} > 3.4$ Å), four Ca2 atoms bridge the As–As covalent bond resulting in a "Ca_4As_2" octahedron (Figure 5.17b), similar to that of $Ca_{14}FeAs_{11}$ compound (Figure 5.6).

Four Ca atoms (2× Ca1, Ca3 and Ca4B) are terminally coordinated to each As4 atoms building a distorted square (Figure 5.17b). The same coordination around the As–As dumbbell in the $[As_3]^{7-}$ unit is observed in $Ca_{14}FeAs_{11}$ (see Chapter 5.2.2.1). In $Ca_{11}As_{9.68(2)}$ a string of vertex-sharing octahedra along the c-direction results.

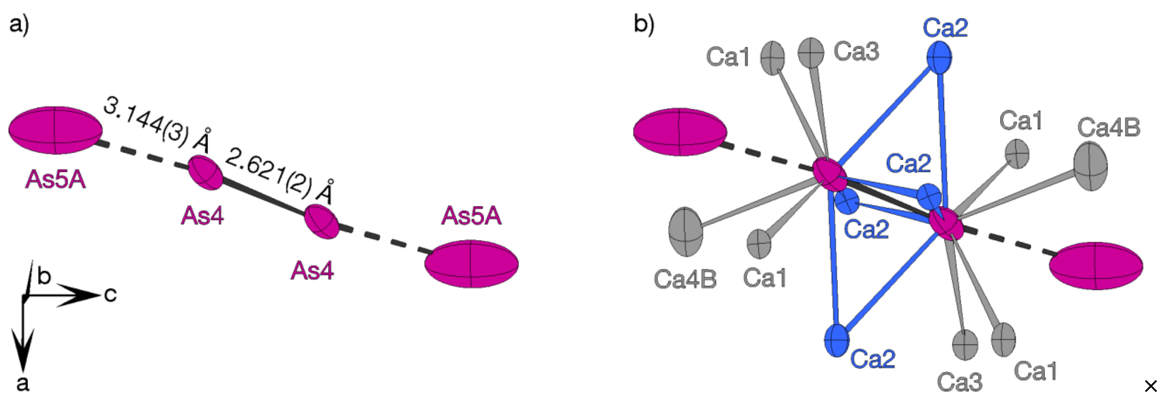

Figure 5.17 The dumbbell structure motif in $Ca_{11}As_{9.68(2)}$ (split atom model); atoms depicted as atomic displacement ellipsoids with 90 % probability level. a) As dumbbell with the As–As covalent bond shown in black including the coordination of the adjacent As5A anions (dashed black lines); b) coordination of Ca cations (gray, terminal coordinated and blue, bridging) around the dumbbell.

The other structure motif is the As_4 squares. As was mentioned previously the anions of the squares show large anisotropic displacement parameters. The squares are found in the plane with $z = 0$ and ½. Between four squares in one plane lie the Ca4 atoms which also resemble a square (without covalent bonds). The Ca atoms show elongation of the thermal displacement parameters in the [110] direction pointing towards the As atoms of the squares. The splitting of the Ca4 position into a Ca4A and Ca4B position, each with 50 % occupation, leads to a reduction of the atomic displacement ellipsoids (Figure 5.18), the anisotropic displacement parameters are still enlarged. The situation for the As_4 squares (As5 atomic position) is more complex.

Table 5.12 Atomic distances (*d*) within the first coordination sphere including their multiplicity for the individual structural units of $Ca_{11}As_{9.68(2)}$ split model; space group *I*4/*mmm*, *Z* = 4.

Atom1	**Atom2**	***d* / Å**	**Atom1**	**Atom2**	***d* / Å**	**Atom1**	**Atom2**	***d* / Å**
Isolated As^{3-}			$[As_3]^{4-}$ dumbbells			$[As_4]^{4-}$ unit		
As1	–Ca2	2.977(2); ×4	As4	–As4	2.621(2); ×1	As5A	–As5B	2.652(13); ×2
	–Ca4A	3.125(5); ×4		–Ca1	3.028(1); ×2		–Ca4B	2.730(13); ×1
	–Ca3	3.245(3); ×1		–Ca2	3.206(2); ×4		–Ca1	3.210(2); ×4
As2	–Ca2	2.955(2); ×4		–Ca3	3.323(1); ×1		–Ca3	3.458(7); ×2
	–Ca1	2.999(2); ×4		–Ca4B	3.333(4); ×1		–Ca4A	3.548(12); ×1
As3	–Ca4B	2.768(1); ×2		–As5A	3.144(3); ×1	As5B	–As5A	2.652(13); ×2
	–Ca4A	2.800(2); ×2					–Ca3	3.088(4); ×2
	–Ca1	3.030(1); ×4					–Ca1	3.377(3); ×4
	–Ca2	3.233(1); ×2					–Ca4B	3.385(11); ×1

In Figure 5.18 the different models (non-split and split atom) are shown. The large atomic displacement ellipsoids for the non-split atom model and the adjacent

Ca atoms are represented in Figure 5.18a. The equivalent distances $d_{As–As}$ is 2.499(14) Å within the square. The value is similar to typical bond lengths for covalent As–As single bonds (2.4 – 2.58 Å).[12, 13, 43, 65] As was previously mentioned the atomic position of As5 is not 100 % occupied but shows a deficiency of 16 at. %. Statistically, approximately every 6th ring has one As position unoccupied resulting in two anions with a charge of 2− and one anion with a charge of 1− leading to a $[As_3]^{5-}$ unit. Averaging the two possible units including their probabilities gives a formal charge of approximately 4.2− for the squares. The compound therefore cannot be described according to Zintl-Klemm concept.

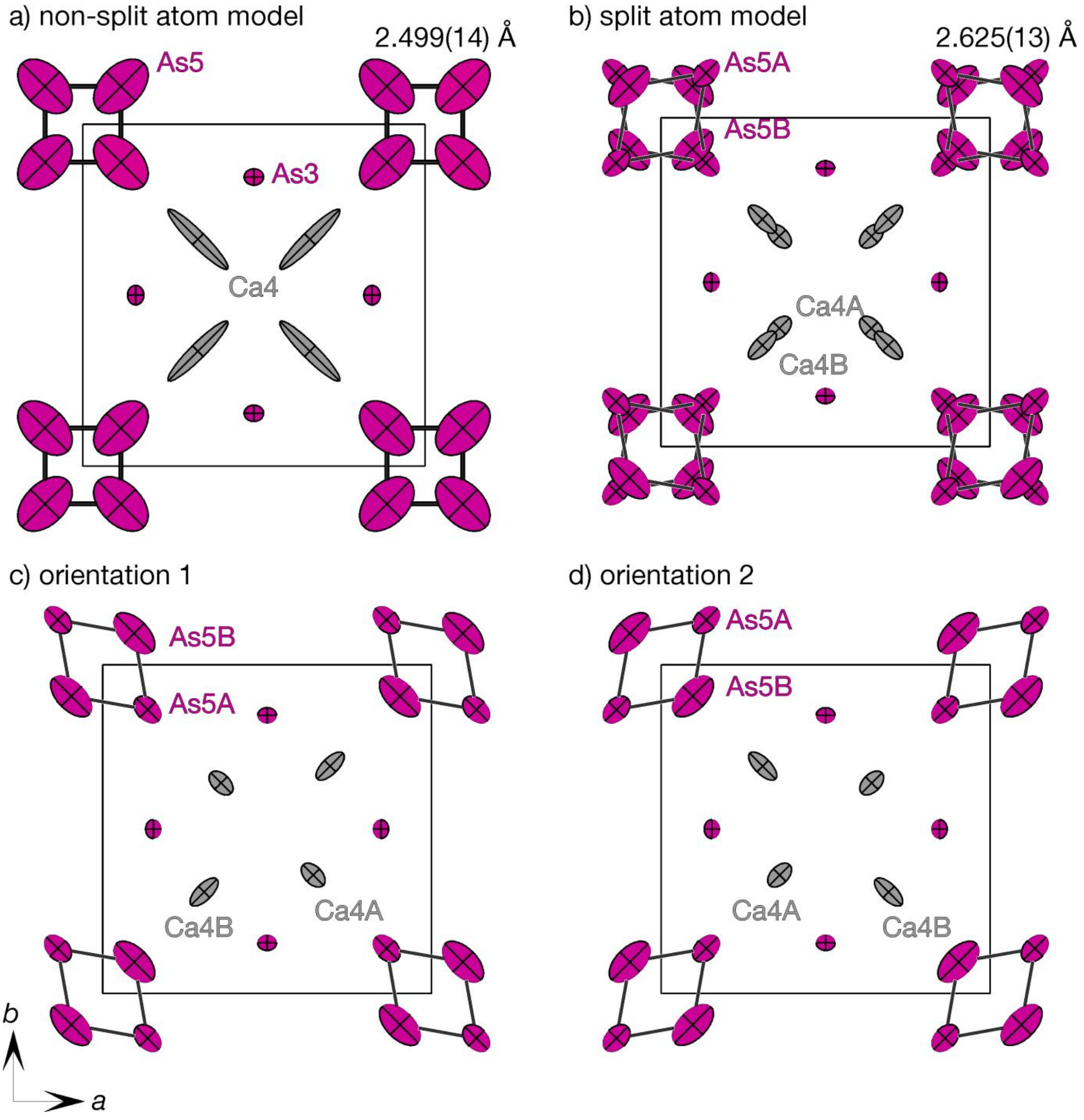
a) non-split atom model
2.499(14) Å
As5
As3
Ca4
b) split atom model
2.625(13) Å
As5A
As5B
Ca4A
Ca4B
c) orientation 1
As5B
As5A
Ca4B
Ca4A
d) orientation 2
As5A
As5B
Ca4A
Ca4B
b
a

Figure 5.18 Structure motif of the As_4 unit, view along the *ab*-plane, atoms depicted as atomic displacement ellipsoids with 90 % probability level. a) non-split atom model; b) split atom model with the position As5 and Ca4 split into two atomic positions; c) and d) possible orientation of the As_4 rhombi.

The splitting of the As5 position into an As5A and an As5B atomic position with different occupancies: 0.39(2) for As5A and 0.45(2) for As5B, averaging the As_4 unit to have 0.84(2) occupancy. The split As5A position has the elongation of the atomic displacement ellipsoids oriented along the *c*-direction [001] while the As5B position has the atomic displacement ellipsoid oriented along [110]. As a result As_4 units formed by two As5A atoms and two As5B atoms result (Figure 5.18b). The squares (non-split model) are now rhombi with longer distances between the As atoms in the As_4 unit. $d_{As–As}$ is 2.63(1) Å which is approximately 0.12 Å longer than in the non-split atom model, the diagonals of the square are 3.53(1) Å. In the split model a shorter and a longer diagonal is found. The shorter d_1 between the As5B atoms is 3.04(1) Å while the diagonal d_2 between the As5A atoms is 4.35(1) Å which leads to d_2/d_1 = 1.43. Two possible orientations of the rhombi are represented in Figure 5.18c and d.

The isolated As^{3-} atoms in $Ca_{11}As_{9.68(2)}$ (As1, As2 and As3) are only coordinated by Ca atoms within the first coordination sphere. As1 is coordinated by nine Ca atoms, four Ca2 and four Ca4A (2.977(2) Å and 3.125(5) Å for $d_{As1–Ca2}$ and $d_{As1–Ca4A}$, respectively) form a distorted square anti-prism around As1 with one Ca3 atom ($d_{As1–Ca3}$ = 3.243(3) Å) capping the square formed by the Ca2 atoms. The coordination polyhedron is a distorted mono-capped square anti-prism (Figure 5.19a).

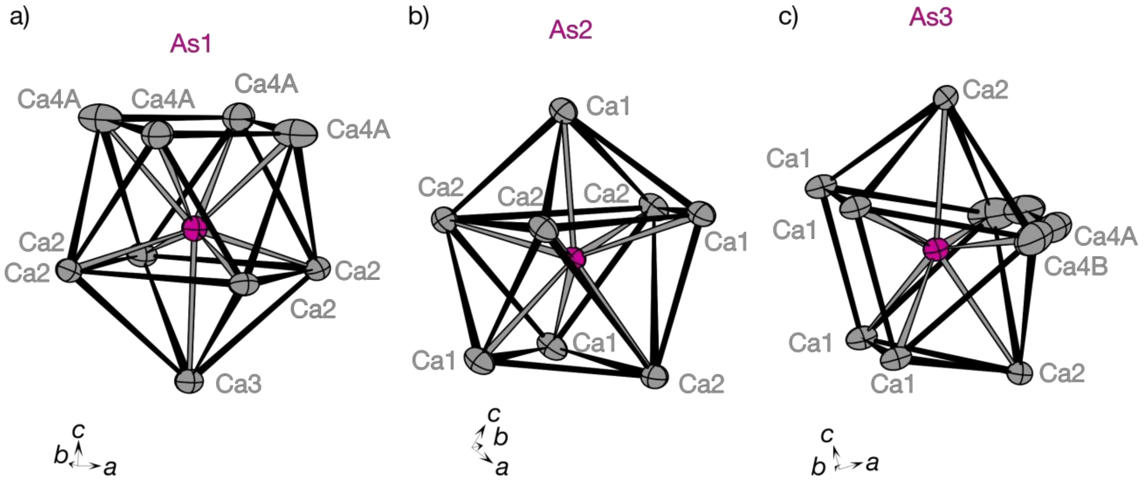

Figure 5.19 Coordination around the isolated As^{3-} anions in $Ca_{11}As_{9.68(2)}$ atoms depicted as atomic displacement ellipsoids with 90 % probability level. a) Ca^{2+} cations around As1; b) Ca^{2+} cations around As2; c) Ca^{2+} cations around As3. The contacts are non-bonding and only for visible help, As–Ca in gray and Ca–Ca in black.

As2 is coordinated by eight Ca atoms (Figure 5.19b), four Ca2 atoms ($d_{As2–Ca2}$ = 2.955(2) Å) and four Ca1 atoms ($d_{As2–Ca1}$ = 2.999(2) Å). As3 is coordinated by ten Ca (totally eight) atoms in the split atom model (Ca4A, Ca4B, Ca1 and Ca2). In the literature the coordination of this *E* position is reported to be build up by eight *Ae* atoms (*Ae* = Ca, *E* = Sb and Bi).[59] The same is observed for $Ca_{11}As_{9.68(2)}$ in the non-split atom model. In case of eight coordinating Ca atoms around the As3 atom the coordination polyhedron (Figure 5.19c) is equal for As2 and As3. The additional two Ca atoms coordinating As3 are therefore a result of the splitting of the Ca4 atom. The distances $d_{As\text{–}Ca}$ for the split Ca4B and Ca4A position differ by 0.032 Å.

A comparison of $Ca_{11}As_{9.68(2)}$ with the isostructural heavier homologues $Ca_{11}Sb_{10}$ and $Ca_{11}Bi_{10}$ shows an increase of the lattice parameter in correspondence with the increasing atomic radius of the anions (1.15 Å, 1.45 Å and 1.60 Å; As, Sb and Bi, respectively).[66] The lattice parameters increase from 11.253(1) Å and 16.235(1) Å (*a* and *c*) in $Ca_{11}As_{9.68(2)}$ to 11.94 Å and 17.40 Å in $Ca_{11}Sb_{10}$ and 12.22 Å and 17.79 Å in $Ca_{11}Bi_{10}$.[59] The covalent bonds within the structures increase from 2.50 - 2.62 Å in $Ca_{11}As_{9.68(2)}$ (non-split atom model) to 2.95 - 3.00 Å in $Ca_{11}Sb_{10}$ and 3.15 - 3.20 Å in $Ca_{11}Bi_{10}$ (first distance for *E*–*E* dumbbells, second one for E_4 squares).

So far, compounds with $Ho_{11}Ge_{10}$ structure type have been reported with *E* atoms from the main groups 3 - 5 (*E* = Ga, Ge, As, Sb, Bi),[55, 59, 61-64] however in some cases only the lattice parameters obtained from powder data were reported. The distortion for the E_4 squares has been only observed for compounds with *E* = 5th main group (single crystal data). The compounds have 72 eV/cell unit valence electrons which is 1 electron less than $Ho_{11}Ge_{10}$ (73 eV/cell unit). The lower valence electron count seems to destabilize the structure so that partial deficiencies on *E* atomic positions occurs and a deviation from the ideal composition 11:10 or a lowering of the symmetry results. If the observed distortion is connected exclusively to anions of main group 5 elements or to the number of valence electrons in the unit cell can therefore not be conclusively said. It will take more research into the compounds with the $Ho_{11}Ge_{10}$ structure type to determine if the composition, the structure distortion or maybe both are inconsistent depending on the elements included.

5.4. Comparison of the new compounds within the Ca–As–Fe system

The three new compounds show common structural motifs with the previously reported binary and ternary compounds in the Ca–As–Fe phase system. All new compounds contain covalent bonded As dumbbells in their structure.

The only binary Ca–As phases with As dumbbells reported up to now were CaAs (50 at. % Ca) and $Ca_{16}As_{11}$ (59.26 at. % Ca).[11, 12] In Ca_2As_3, with 60 at. % Ca, the As atoms already form 4 and 8 membered chains.[13] A clear trend for the binary Ca–As compounds, with a Ca content between 50 at. % and 59.26 at. %, is observed. In CaAs all As atoms form dumbbells and the compound is a Zintl phase with 2 Ca^{2+} cations and one $[As_2]^{4-}$ anion. The coordination around each As anion can be described as a distorted trigonal anti-prism with a mono capped face by the covalent bonded As atom.[12]

Ca_4As_3 (57.1 at. % Ca) contains two different dumbbells, each of them is coordinated by eight Ca atoms forming distorted trigonal anti-prism with two capped faces, while the third face is capped by the covalent bonded As atoms. Distorted trigonal anti-prims are also observed for two of the three isolated As^{3-} atoms.

$Ca_{11}As_{9.68(2)}$ with a Ca content of 53.2 at. % contains As–As dumbbells. The Ca coordination around the dumbbell atoms increases and forms distorted tetragonal anti-prism with one face capped by the adjacent dumbbell atom. As it was mentioned in Chapter 5.3.2.2, the compound also contains an As_4 unit. However, the unit shows a high degree of distortion and is not fully occupied. In $Ba_{11}Sb_{10}$ the symmetry was reduced and an orthorhombic space group (*Immm*) with two Sb dumbbells instead of a Sb_4 ring is reported. The coordination of Ca around the As anions in the As_4 unit ($Ca_{11}As_{9.68(2)}$) also represents a distorted trigonal square anti-prism. One face of the anti-prism is capped by a Ca atom, the other two faces are capped by the bonding As atoms of the As_4 unit.[64]

The structure of the ternary compound $Ca_{14}FeAs_{11}$ combines the structural motifs observed in binary Ca–As phases on the one hand and in binary Fe–As phases as well as in ternary Ca–Fe–As phases on the other.[12, 17, 20, 21, 67] $FeAs_4$ tetrahedra are observed for Fe_2As and all ternary Ca–Fe–As compounds. In the previously reported phases the tetrahedra are always connected by edges, while $Ca_{14}FeAs_{11}$ contains only isolated $FeAs_4$ tetrahedra. In addition, the As–As dumbbells observed for binary Ca–As phases are found. The dumbbell atoms are coordinated by eight Ca atoms forming a distorted square anti-prism that has one square face capped by covalent bond As atom of the dumbbell. The Ca content in $Ca_{14}FeAs_{11}$ is approximately 53.8 at. % which falls into the range where As dumbbells are observed in binary Ca–As compounds. The coordination around the dumbbells is similar in all cases.

5.5. References

[1] P. C. Canfield, S. L. Bud'ko, N. Ni, A. Kreyssig, A. I. Goldman, R. J. McQueeney, M. S. Torikachvili, D. N. Argyriou, G. Luke, W. Yu, *Physica C* **2009**, *469*, 404-412.

[2] G. Wu, H. Chen, T. Wu, Y. L. Xie, Y. J. Yan, R. H. Liu, X. F. Wang, J. J. Ying, X. H. Chen, *J. Phys.: Cond. Matt* **2008**, *20*, 422201.

[3] Z. Gao, Y. Qi, L. Wang, D. Wang, X. Zhang, C. Yao, C. Wang, Y. Ma, *EPL* **2011**, *95*, 67002.

[4] L. Harnagea, S. Singh, G. Friemel, N. Leps, D. Bombor, M. Abdel-Hafiez, A. U. B. Wolter, C. Hess, R. Klingeler, G. Behr, S. Wurmehl, B. Büchner, *Phys. Rev. B.* **2011**, *83*, 094523.

[5] Y. Qi, L. Wang, Z. Gao, D. Wang, X. Zhang, C. Wang, C. Yao, Y. Ma, *New J. Phys.* **2011**, *13*, 033020.

[6] C. Löhnert, T. Strürzer, M. Tegel, R. Frankovsky, G. Friederichs, D. Johrendt, *Angew. Chem. Int. Ed.* **2011**, *50*, 9195 –9199.

[7] N. Ni, J. M. Allred, B. C. Chan, R. J. Cava, *PNAS* **2011**, *108*, 1019-1026.

[8] M. Nohara, S. Kakiya, K. Kudo, Y. Nishikubo, K. Oku, E. Nishibori, H. Sawa, T. Yamamoto, T. Nozaka, *J. Phys. Soc. Jpn* **2011**, *80*, 093704.

[9] A. Hütz, G. Nagorsen, *Z. Metallkd.* **1974**, *65*, 618.

[10] A. Hütz, G. Nagorsen, *Z. Metallkd.* **1975**, *66*, 314.

[11] E. A. Leon-Escamilla, W. M. Hurng, E. S. Peterson, J. D. Corbett, *Inorg. Chem.* **1997**, *36*, 703-710.

[12] A. Iandelli, E. Franceschi, *J. Less-Common Met.* **1973**, *30*, 211-216.

[13] K. Deller, B. Eisenmann, *Z. Naturforsch., B: J. Chem. Sci.* **1976**, *31*, 1023-1027.

[14] J. F. Brice, A. Courtois, J. Protas, J. Aubry, *J. Solid State Chem.* **1976**, *17*, 393-397.

[15] W. Bauhofer, M. Wittmann, H. G. von Schnering, *J. Phys. Chem. Solids* **1981**, *42*, 623-714.

[16] S. Maaref, R. Maddar, P. Chaudouet, R. Fruchart, J. P. Senateur, M. T. Averbuch-Pouchot, M. Bacmann, M. Durif, P. Wolfers, *Materials Research Bulletin* **1983**, *18*, 473-480.

[17] M. Elander, G. Haegg, A. Westgren, *Arkiv för Kemi, Mineralogi och Geologi B* **1935**, *12*, 1-6.

[18] K. Selte, A. Kjekshus, *Acta Chemica Scandinavica* **1969**, *23*, 2047-2054.

[19] M. J. Bürger, *Zeit. für Kristallographie, Kristallgeometrie, Kristallphysik, Kristallchemie* **1932**, *82*, 165-187.

[20] I. Todorov, D. Y. Chung, C. D. Malliakas, Q. Li, T. Bakas, A. Douvalis, G. Trimarchi, K. Gray, J. F. Mitchell, A. J. Freeman, M. G. Kanatzidis, *J. Am. Chem. Soc.* **2009**, *131*, 5405-5407.

[21] T. Stürzer, C. Hieke, C. Löhnert, F. Nitsche, J. Stahl, C. Maak, R. Pobel, D. Johrendt, *Inorg. Chem.* **2014**, *53*, 6235-6240.

[22] G. Cordier, H. Schäfer, M. Stelter, *Z. Anorg. Allg. Chem.* **1984**, *519*, 183-188.

[23] S. L. Brock, L. J. Weston, M. M. Olmstead, S. M. Kauzlarich, *J. Solid State Chem.* **1993**, *107*, 513-523.

[24] S. R. Brown, S. M. Kauzlarich, F. Gascoin, G. F. Snyder, *Chem. Mater.* **2006**, *18*, 1873-1877.

[25] S. R. Brown, E. S. Toberer, T. Ikeda, C. A. Cox, F. Gascoin, S. M. Kauzlarich, G. F. Snyder, *Chem. Mater.* **2008**, *20*, 3412-3419.

[26] J. Y. Chan, S. M. Kauzlarich, *Chem. Mater.* **1997**, *9*, 3132-3135.

[27] J. Y. Chan, M. M. Olmstead, S. M. Kauzlarich, D. J. Webb, *Chem. Mater.* **1998**, *10*, 3583-3588.

[28] J. Y. Chan, M. E. Wang, A. Rehr, S. M. Kauzlarich, *Chem. Mater.* **1997**, *9*, 2131-2138.

[29] C. A. Cox, E. S. Toberer, A. A. Levchenko, S. R. Brown, G. F. Snyder, A. Navrotsky, S. M. Kauzlarich, *Chem. Mater.* **2009**, *21*, 1354-1360.

[30] A. P. Holm, T. C. Ozawa, S. M. Kauzlarich, S. A. Morton, G. D. Waddill, J. G. Tobin, *J. Solid State Chem.* **2005**, *178*, 262-269.

[31] S. Kastbjerg, C. A. Uvarov, S. M. Kauzlarich, E. Nishibori, M. A. Spackman, B. Brummerstedt-Iversen, *Chem. Mater.* **2011**, *23*, 3723-3730.

[32] S. M. Kauzlarich, T. Y. Kuromoto, *Croat. Chim. Acta* **1991**, *64*, 343.

[33] S. M. Kauzlarich, M. M. Thomas, D. A. Odink, M. M. Olmstead, *J. Am. Chem. Soc* **1991**, *113*, 7205-7208.

[34] H. Kim, J. Y. Chan, M. M. Olmstead, P. Klavins, D. J. Webb, S. M. Kauzlarich, *Chem. Mater.* **2002**, *14*, 206-216.

[35] H. Kim, Q. Huang, J. W. Lynn, S. M. Kauzlarich, *J. Solid State Chem.* **2002**, *168*, 162-168.

[36] H. Kim, S. M. Kauzlarich, *J. Solid State Chem.* **2005**, *178*, 1935-1939.

[37] H. Kim, P. Klavins, S. M. Kauzlarich, *Chem. Mater.* **2002**, *14*, 2308-2316.

[38] H. Kim, M. M. Olmstead, P. Klavins, D. J. Webb, S. M. Kauzlarich, *Chem. Mater.* **2002**, *14*, 3382-3390.

[39] T. Y. Kuromoto, S. M. Kauzlarich, D. J. Webb, *Chem. Mater.* **1992**, *4*, 435-440.

[40] A. C. Payne, M. M. Olmstead, S. M. Kauzlarich, D. J. Webb, *Chem. Mater.* **2001**, *13*, 1398-1406.

[41] E. Ratal, P. Bruins, C. J. Hernandez, S. M. Kauzlarich, M. P. Augustine, *Chem. Mater.* **2002**, *14*, 2468-2475.

[42] A. Rehr, T. Y. Kuromoto, S. M. Kauzlarich, J. Del Castillo, D. J. Webb, *Chem. Mater.* **1994**, *6*, 93-99.

[43] A. F. Holleman, N. Wiberg, *Lehrbuch der Anorganischen Chemie* **2007**, *102. Ed.*

[44] J. Huheey, E. Keiter, R. Keiter, *Anorganische Chemie, Vol. 3*, Walter de Gruyter, Berlin, New York, **2003**.

[45] W. Carrillo-Cabrera, M. Somer, K. Peter, H. G. von Schnering, *Chem. Ber.* **1996**, *129*, 1015-10232.

[46] J. T. Vaughey, J. D. Corbett, *Chem. Mater.* **1996**, *8*, 671-675.

[47] G. A. Landrum, N. Goldberg, R. Hoffmann, *J. Chem. Soc., Dalton Trans* **1997**, 3605-3613.

[48] U. Müller, *Anorganische Strukturchemie, Vol. 5. Auflage*, B.G. Teubner Verlag/ GWV Fachverlage GmbH, Wiesbaden, **2006**.

[49] R. D. Shannon, *Acta Crystallogr. Sect. A* **1976**, *32*, 751-767.

[50] N. Emery, E. J. Wildman, J. M. S. Skakle, R. I. Smith, A. N. Fitch, A. C. Mclaughlin, *Phys. Rev. B* **2011**, *83*, 144429.

[51] T. Nomura, S. W. Kim, Y. Kamihara, M. Hirano, P. V. Sushko, K. Kato, M. Takata, A. L. Shluger, H. Hosono, *Supercond. Sci. Technol.* **2008**, *21*, 125028.

[52] K. O. Klepp, W. Bronger, *Z. Anorg. Allg. Chem.* **1986**, *532*, 23-30.

[53] T. Yildirim, *Phys. Rev. Lett.* **2009**, *102*, 037003.

[54] C. Hadenfeldt, H.-U. Terschüren, W. Hönle, L. Schröder, H. G. Von Schnering, *Z. Anorg. Allg. Chem.* **1993**, *619*, 843-848.

[55] G. S. Smith, Q. Johnson, A. G. Tharp, *Acta. Crystallogr.* **1967**, *23*, 640-644.

[56] N. Ni, J. M. Allred, B. C. Chan, R. J. Cava, *Proc Natl Acad Sci U S A* **2011**, *108*, E1019.

[57] A. V. Hoffmann, V. Hlukhyy, T. F. Fässler, *Acta Cryst. E* **2015**, *71*, 1548-1550.

[58] M. Somer, W. Carrillo-Cabrera, K. Peters, H. G. von Schnering, *Z. Kristallogr.* **1995**, *210*, 876.

[59] K. Deller, B. Eisenmann, *Z. Naturforsch.* **1976**, *31b*, 29-34.

[60] G. Derrien, M. Tillard-Charbonnel, A. Manteghetti, L. Monconduit, C. Belin, *J. Solid State Chem* **2002**, *164*, 169-175.

[61] R. Schmelczer, D. Schwarzenbach, F. Hulliger, *Z. Naturforsch.* **1979**, *34b*, 1213-1217.

[62] H. L. Clark, H. D. Simpson, H. Steinfink, *Inorg. Chem.* **1970**, *9*, 1962-1964.

[63] J. B. Taylor, L. D. Calvert, Z. Utsunomiya, Y. Wang, J. G. Despault, *J. Less Common Met.* **1978**, *57*, 39-51.

[64] F. Emmerling, N. Längin, F. Pickhard, M. Wendorff, C. Röhr, *Z. Naturforsch.* **2004**, *59b*, 7-16.

[65] P. Verdier, P. L'Haridon, M. Maunaye, Y. Laurent, *Acta. Crystallogr.* **1976**, *B32*, 726-728.

[66] E. Clementi, D. L. Raimondi, W. P. Reinhardt, *J. Chem. Phys* **1967**, *47*, 1300-1306.

[67] F. Ronning, T. Klimczuk, E. D. Bauer, H. Volz, J. D. Thompson, *J. Phys.: Cond. Matt* **2008**, *20*, 322201.

6. Summary and Outlook

Superconductivity in iron-arsenide and related compounds with $ThCr_2Si_2$ type structure (122 phases) has been extensively researched in recent years. The mechanism for superconductivity in 122 iron-pnictide and Ni-based compounds seems to be of different nature and more information is needed to understand the influence of the variations. In both cases the superconducting temperature T_c can be influenced by charge doping via partial substitution.

The motivation for this work was to extent the chemical compounds and to study their properties. The phase systems *Ae*–*T*–*E* (*Ae* = Ca, Sr, Ba; *T* = Fe, Co, Ni, Rh; *E* = Si, Ge, P, As) with focus on 122 phases were investigated for new compounds. The effects of charge doping were investigated for multiple 122 solid solutions, in analogy to known superconducting iron-pnictides ones.

The investigation of the Ni- and Fe-based 122 compounds done in this work provides detailed information on structural and physical properties as well as about the electronic structure of new members of this family. During the research new ternary compounds in the Ca–Fe–As phase system were also successfully synthesized and characterized.

The samples were prepared using high-temperature syntheses employing arc-, resistance- or induction-furnace. To investigate the influence of the starting materials in respect to sample purity and crystal quality, combinations of pure elements or precursors were tested during the preparation of the compounds.

It was observed that the use of precursors in the preparation of the ternary and pseudo-ternary compounds helps to reduce the appearance of side products. For the two solid solution series $SrNi_2(E_{1-x}Ge_x)_2$ (*E* = P, As) the best results were obtained by using ternary $SrNi_2E_2$ (*E* = P, As, Ge) precursors as starting materials. Binary *TE* (*T* = Fe, Rh; *E* = Si, Ge, P) precursors were used for the preparation of ternary CaT_2Si_2 compounds (*T* = Fe, Rh) and $BaFe_2(P_{0.930(6)}Ge_{0.070(6)})_2$.

The ternary $Ca_{14}FeAs_{11}$ phase was obtained from a reaction made with Ca, Fe, As, Rh and Si. $Ca_{14}FeAs_{11}$ is the first reported compound containing $FeAs_{4/4}$ tetrahedra and was also synthesized from binary FeAs precursor together with elemental Ca and As. The presented binary phases Ca_4As_3 and $Ca_{11}As_{9.68(2)}$, which were obtained as side products during a reaction of Ca, Fe, As, Rh and Si, could also be prepared from the elements.

The solid solutions $SrNi_2(P_{1-x}Ge_x)_2$ and $Ca(Fe_{1-x}Rh_x)_2Si_2$ and the pseudo-ternary compound $BaFe_2(P_{0.930(6)}Ge_{0.070(6)})_2$ are representatives of the 122 family. The solid solution $SrNi_2(P_{1-x}Ge_x)_2$ was synthesized in the whole substitution range; the results for x_{nom} = 0.15, 0.25, 0.40, 0.55, 0.70 and 0.85 are presented. The structural phase transition of the ternary $SrNi_2P_2$ phase at 320 K from LT orthorhombic modification (*Immm*) to HT tetragonal (*I*4/*mmm*) was successfully suppressed upon substitution of P with Ge at. % of approximately 11 and more. The pseudo-ternary compounds crystallize all in the tetragonal space group *I*4/*mmm* at room-temperature and adapt to the so-called uncollapsed structure that means with no covalent *E*–*E* bonds between the tetrahedral layers along the *c*-direction. Low temperature powder and single crystal X-ray diffraction measurements for the samples with x_{exp} = 0.110(3) and 0.212(3) did not show any indication of a structural phase transition to an orthorhombic modification or to the collapsed $ThCr_2Si_2$ structure type as is observed for $SrNi_2P_2$ and $SrNi_2(P_{1-x}As_x)_2$ ($x < 0.25$). The effect on the superconducting transition temperature (T_c), which is 1.4 K for $SrNi_2P_2$ (orthorhombic modification) and 0.87 K for $SrNi_2Ge_2$, upon partial P/Ge substitution was investigated employing magnetic measurements down to 1.8 K. The pseudo-ternary $SrNi_2(P_{1-x}Ge_x)_2$ compounds with a *x*-value of 0.110(3) and 0.212(3) exhibit superconducting behavior with a T_c of 3 K and 2.4 K, respectively, which is in both cases higher than the T_c for the parent compounds. Conductivity measurements for the sample $SrNi_2(P_{1-x}Ge_x)_2$ with x_{exp} = 0.110(3) confirmed superconductivity below 3 K and a $\Delta C/T_c$ value of 2.2 mJ/mol K^2 was obtained resulting in a $\Delta C/T_c\gamma$ value of ≈ 0.2. The samples with substitution values higher than 25 at. % Ge did not show superconducting behavior above 1.8 K but are expected to be superconductors at lower temperature. Further investigations below 1.8 K are needed to confirm the superconductivity in $SrNi_2(P_{1-x}Ge_x)_2$ phases with higher Ge content. The chemical bonding situations in the ternary superconductor $SrNi_2P_2$ (orthorhombic modification) and a theoretical model of the pseudo-ternary superconductor $SrNi_2(P_{1-x}Ge_x)_2$ (x = 0.14, tetragonal unit cell parameters at 130 K) are discussed. The effects of the structural deviation are analyzed; the separation of the tetrahedral layers positively affects T_c.

Substitution of As in the superconducting $SrNi_2As_2$ compound (T_c = 0.67 K) with Ge (T_c of 0.87 K for $SrNi_2Ge_2$), both belonging to uncollapsed structure type, was tested. No conclusive prove of successful substitution could be obtained. Only the sample with a small nominal amount of Ge (x_{nom} = 0.10) indicated small deviation in the unit cell parameters (powder data) from the reported values for pure $SrNi_2As_2$. However, all tested crystals did not show any Ge substitution. Only binary or ternary phases were observed in the other samples of $SrNi_2(As_{1-x}Ge_x)_2$.

The solid solution $BaFe_2(P_{1-x}Ge_x)_2$, analogue to $SrNi_2(P_{1-x}Ge_x)_2$ and the previously reported $BaNi_2(P_{1-x}Ge_x)_2$, was investigated. $BaFe_2P_2$ belongs to the uncollapsed 122 structure type and does not show superconducting behavior. Attempts to synthesize the ternary $BaFe_2Ge_2$ phase, which has not been reported so far, demand further study for the working synthesis methods have not been found yet. Only a small percentage of P substitution with Ge (7.0(6) at. %) could be determined from X-ray diffraction and EDX analysis of a single crystal. Lattice parameters and interatomic distance $d_{P/Ge–P/Ge}$ show non-covalent bonding between the tetrahedral layers in the *c*-direction, as reported for the ternary $BaFe_2P_2$ compound. Magnetic measurement of the impure sample did not show any indication of superconductivity above 1.8 K.

The $Ca(Fe_{1-x}Rh_x)_2Si_2$ solid solution was investigated for x = 0, 0.66(3), 1. All phases show collapsed $ThCr_2Si_2$ type structure with covalent Si–Si bonds in the *c*-direction. No superconducting behavior was observed for any of the samples. Electron structure calculations for the ternary CaT_2Si_2 compounds (T = Fe, Rh) are presented. Substitution of Fe with Rh did not result in superconductivity, in contrast to reports of the analogue $Ca(Fe_{1-x}Rh_x)_2As_2$ solid solution. However, the superconducting phases have uncollapsed modification in the As-based solid solution.

In addition chemical modification of the CeFeSi structure type, analogue to the reported superconductors LiFeAs, NaFeAs and LiFeP were investigated for *AeTE* (*Ae* = Ca, Sr, Ba; *T* = Fe, Co, Ni; *E* = Si, Ge, P, As). No new phases belonging to this family were found in frame of this study. The investigation of CaCoSi, which was already successfully synthesized and characterized during the Master-Thesis, is extended by theoretical calculations regarding the electronic structure and chemical bonding situation of the compound. CaCoSi is the first reported *Ae*CoSi (*Ae* = alkaline earth metal) compound. The calculations indicate metallic behavior for the compound. Unlike the LiFeAs and NaFeAs compounds, which have one valence electron less, CaCoSi does not display superconducting behavior.

During this work three new compounds within the Ca–Fe–As system were also successfully crystallized. The ternary $Ca_{14}FeAs_{11}$ phase crystallizes in the $Ca_{14}AlSb_{11}$ structure type. Members of this family are of interest because of their thermoelectric properties. The superconducting iron-arsenic compounds all contain tetrahedra which are connected via edges forming two-dimensional substructures. In $Ca_{14}FeAs_{11}$ the tetrahedra are separated by isolated Ca-, As-atoms and $[As_3]$ units. The previously reported structural disordering for the linear $[E_3]^{7-}$ unit (E = P, As) is also observed in $Ca_{14}FeAs_{11}$. This can be solved by describing the $[E_3]^{7-}$ unit as an E_2 dumbbell linearly coordinated by an isolated E anion. Theoretical calculations performed for two theoretical models (non-split and split atom model) of $Ca_{14}FeAs_{11}$ both indicate metallic behavior for the compound.

Two new binary Ca–As phases, which were synthesized and characterized in this work, are presented: Ca_4As_3 and $Ca_{11}As_{9.68(2)}$. Both compounds contain As–As dumbbells as a structure motif in addition to isolated Ca and As atoms. Ca_4As_3 is isostructural to Ba_4P_3 and Sr_4As_3, the compound can be described by the Zintl-Klemm concept containing two sorts of As–As dumbbells as well as isolated Ca and As atoms. $Ca_{11}As_{9.68(2)}$ is structurally related to the compounds with $Ho_{11}Ge_{10}$ structure type. Refinement of the single crystal data revealed noticeable enlargement of the atomic displacement ellipsoids for the As atoms in the $[As_4]$ unit; similar observations have been reported for other representatives of this structure type. The As atomic position in this unit shows a deficiency of 16 %. The refinement did not indicate a structural transition to an orthorhombic phase which was reported for $Ba_{11}Sb_{10}$.

The Ni-based 122 compounds have T_c values below 5 K but no type of charge doping or applied pressure is necessary to support superconductivity in contrast to iron-pnictide 122 superconductors. The higher electron concentration in the Ni-compounds compared to their Fe counterparts changes the electronic structure which supports superconductivity in the ternary Ni-compounds but only at low temperatures. The influences of charge doping on the superconducting temperature T_c in Ni-compounds has been investigated for $BaNi_2(P_{1-x}Ge_x)_2$, $BaNi_2(As_{1-x}P_x)_2$ and $Sr(Pd_{1-x}Ni_x)_2Ge_2$. The solid solution $SrNi_2(P_{1-x}Ge_x)_2$ expands the family of Ni-based 122 superconductors. As was already observed for other superconducting solid solutions, tuning the electronic structure influences the T_c value of the $SrNi_2(P_{1-x}Ge_x)_2$ compounds. In this aspect a reinvestigation of the solid solutions $SrNi_2(P_{1-x}As_x)_2$, $(Sr_{1-x}Ca_x)Ni_2P_2$ and $Sr(Ni_{1-x}T_x)P_2$ (T = Co, Cu) in respect to their possible superconductivity would be of interest. The determination of the substitution effects on the T_c of $SrNi_2P_2$ based solid solutions and a comparison with the results obtained for $SrNi_2(P_{1-x}Ge_x)_2$ are therefore essential. The theory behind high-temperature superconductors is an ongoing topic of research.

Appendix

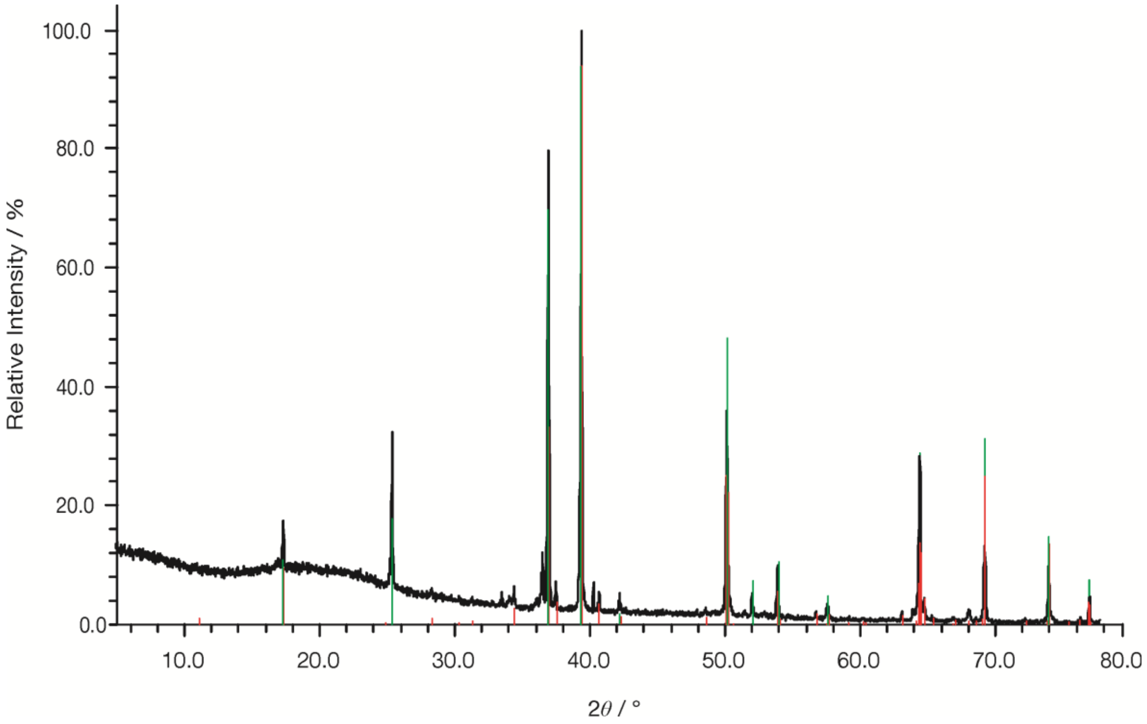

Figure A1 X-ray powder diffraction pattern of $SrNi_2P_2$ sample (Cu-$K_{\alpha1}$, measurement range 5 - 78 ° 2θ, 0.01 ° step size, 20 sec/step, Si as external standard). Theoretically calculated pattern of $SrNi_2P_2$ with HT-*I*4/*mmm* (green lines) and LT-*Immm* (red lines) modification shown in the bottom.

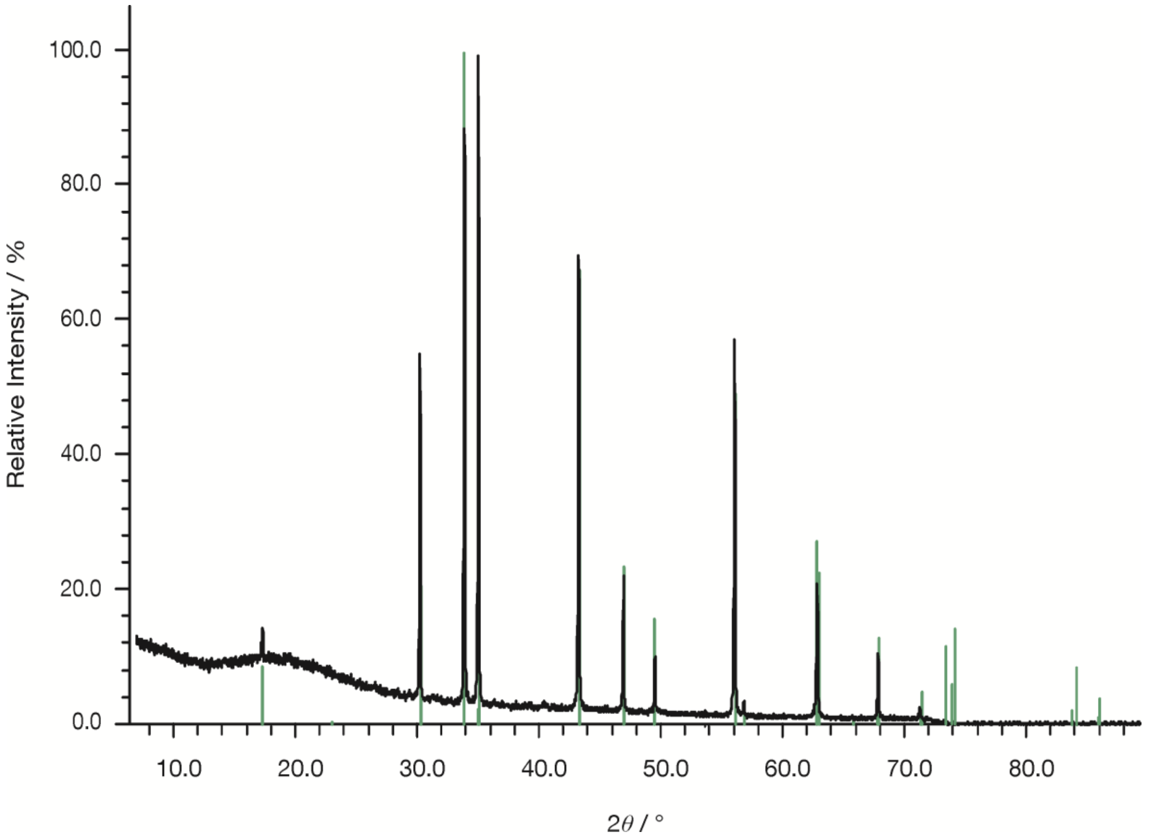

Figure A2 X-ray powder diffraction pattern of $SrNi_2Ge_2$ sample (Cu-$K_{\alpha1}$, measurement range 5 - 90 ° 2θ, 0.01 ° step size, 20 sec/step, Si as external standard). Theoretically calculated pattern of $SrNi_2Ge_2$ with $ThCr_2Si_2$ type structure (green lines) shown in the bottom.

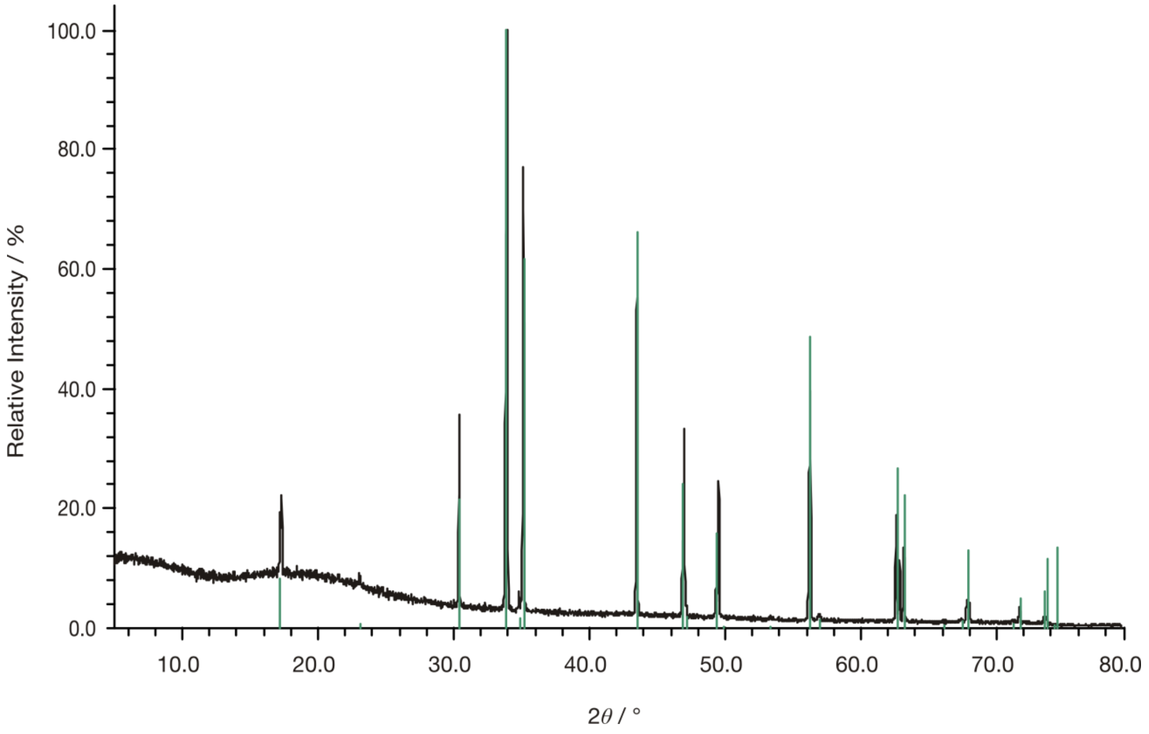

Figure A3 X-ray powder diffraction pattern of $SrNi_2As_2$ sample (Cu-$K_{\alpha1}$, measurement range 5 - 80 ° 2θ, 0.01 ° step size, 20 sec/step, Si as external standard). Theoretically calculated pattern of $SrNi_2As_2$ with $ThCr_2Si_2$ type structure (green lines) shown in the bottom.

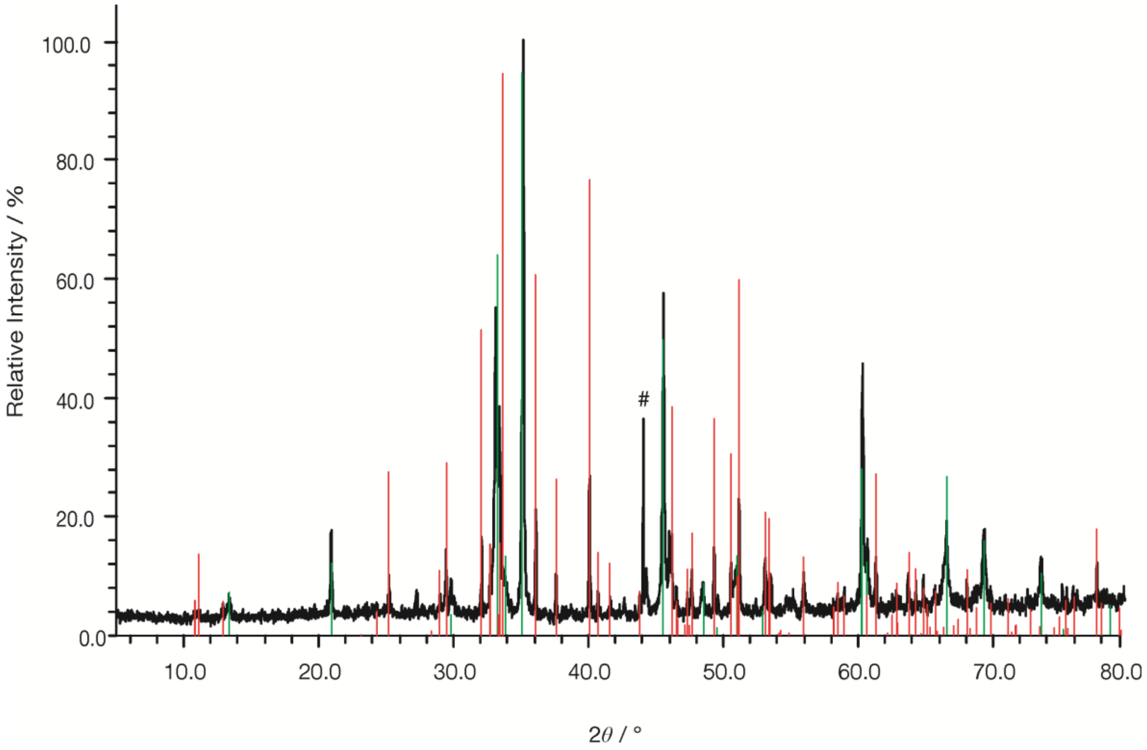

Figure A4 X-ray powder diffraction pattern of $SrNi_2(P_{1-x}Ge_x)_2$ sample with x_{nom} = 0.80 from NiP and NiGe precursors , (Cu-$K_{\alpha 1}$, measurement range 5 - 80 ° 2θ, 0.01 ° step size, 20 sec/step, Si as external standard). Theoretically calculated pattern of $SrNi_2(P_{1-x}Ge_x)_2$ in $ThCr_2Si_2$ type structure (green lines; a = 4.01 Å; c = 10.23 Å) and $SrNi_5(P_{3-x}Ge_x)$ space group *Cmcm* (red lines; a = 3.64 Å, b = 11.59 Å, c = 11.81 Å) shown in the bottom. The reflection marked with # belongs to cubic diamond used as standard.

Table A1 EDX results (values given in at. %, including standard deviation) for measured single crystals of $SrNi_2(P_{1-x}Ge_x)_2$ solid solution.

Composition	**Sr**	**Ni**	**P**	**Ge**	x_{EDX}
$SrNi_2(P_{0.855(6)}Ge_{0.145(6)})_2$	21(3)	39(7)	34(6)	5(3)	0.85
$SrNi_2(P_{0.747(7)}Ge_{0.253(7)})_2$	21(4)	40(7)	30(5)	10(3)	0.75
$SrNi_2(P_{0.580(13)}Ge_{0.420(13)})_2$	22(3)	38(7)	23(4)	16(5)	0.59
$SrNi_2(P_{0.452(7)}Ge_{0.548(7)})_2$	24(4)	32(7)	20(5)	25(9)	0.44
$SrNi_2(P_{0.348(8)}Ge_{0.652(8)})_2$	20(3)	41(8)	14(3)	26(8)	0.35

Table A2 Wyckoff positions, atomic coordinates and isotropic equivalent displacement parameters / Å^2 × 10^3 for $SrNi_2(P_{1-x}Ge_x)_2$ solid solution (space group *I*4/*mmm*, *Z* = 2) obtained from Rietveld refinements on powder patterns. Standard deviations are given in brackets.

Compound	**Atom**	**Wyckoff position**	***x***	***y***	***z***	U_{eq} **/ Å^2 × 10^3**
$SrNi_2(P_{0.89}Ge_{0.11})_2$	Sr	2*a*	0	0	0	24(1)
	Ni	4*d*	0	½	¼	28(1)
	P/Ge	4*e*	0	0	0.3608(2)	31(1)
$SrNi_2(P_{0.79}Ge_{0.21})_2$	Sr	2*a*	0	0	0	10(1)
	Ni	4*d*	0	½	¼	36(1)
	P/Ge	4*e*	0	0	0.3574(2)	2(1)
$SrNi_2(P_{0.56}Ge_{0.44})_2$	Sr	2*a*	0	0	0	8(1)
	Ni	4*d*	0	½	¼	20(1)
	P/Ge	4*e*	0	0	0.3590(2)	13(1)
$SrNi_2(P_{0.45}Ge_{0.55})_2$	Sr	2*a*	0	0	0	9(1)
	Ni	4*d*	0	½	¼	25(1)
	P/Ge	4*e*	0	0	0.3592(3)	10(1)
$SrNi_2(P_{0.33}Ge_{0.67})_2$	Sr	2*a*	0	0	0	8(1)
	Ni	4*d*	0	½	¼	19(1)
	P/Ge	4*e*	0	0	0.3599(2)	5(1)
$SrNi_2(P_{0.12}Ge_{0.88})_2$	Sr	2*a*	0	0	0	4(1)
	Ni	4*d*	0	½	¼	14(1)
	P/Ge	4*e*	0	0	0.3608(2)	10(1)

Table A3 Anisotropic displacement parameters (*Uij* / Å^2) for $SrNi_2(P_{0.86(1)}Ge_{0.14(1)})_2$ from single crystal refinement measured at 293 K.

Atom	U_{11}	U_{22}	U_{33}	U_{12}	U_{13}	U_{23}
Sr	0.0156(4)	0.0156(4)	0.0137(6)	0.000	0.000	0.000
Ni	0.0188(4)	0.0188(4)	0.0219(6)	0.000	0.000	0.000
P/Ge	0.0128(7)	0.0128(7)	0.0332(12)	0.000	0.000	0.000

Table A4 Anisotropic displacement parameters (U_{ij} / Å^2) for $SrNi_2(P_{0.86(1)}Ge_{0.14(1)})_2$ from single crystal refinement measured at 130 K.

Atom	U_{11}	U_{22}	U_{33}	U_{12}	U_{13}	U_{23}
Sr	0.0086(3)	0.0086(3)	0.0082(4)	0.000	0.000	0.000
Ni	0.0123(4)	0.0123(4)	0.0106(5)	0.000	0.000	0.000
P/Ge	0.0075(5)	0.0075(5)	0.0163(8)	0.000	0.000	0.000

Table A5 Anisotropic displacement parameters (U_{ij} / Å^2) for $SrNi_2(P_{0.76(1)}Ge_{0.24(1)})_2$ from single crystal refinement measured at 293 K.

Atom	U_{11}	U_{22}	U_{33}	U_{12}	U_{13}	U_{23}
Sr	0.0144(4)	0.0144(4)	0.0102(5)	0.000	0.000	0.000
Ni	0.0198(4)	0.0198(4)	0.0147(6)	0.000	0.000	0.000
P/Ge	0.0113(6)	0.0113(6)	0.0262(11)	0.000	0.000	0.000

Table A6 Anisotropic displacement parameters (U_{ij} / Å^2) for $SrNi_2(P_{0.76(1)}Ge_{0.24(1)})_2$ from single crystal refinement measured at 130 K.

Atom	U_{11}	U_{22}	U_{33}	U_{12}	U_{13}	U_{23}
Sr	0.0113(5)	0.0113(5)	0.0094(7)	0.000	0.000	0.000
Ni	0.0158(5)	0.0158(5)	0.0118(7)	0.000	0.000	0.000
P/Ge	0.0082(7)	0.0082(7)	0.0210(12)	0.000	0.000	0.000

Table A7 Anisotropic displacement parameters (U_{ij} / Å^2) for $SrNi_2(P_{0.56(2)}Ge_{0.44(2)})_2$ from single crystal refinement measured at 293 K.

Atom	U_{11}	U_{22}	U_{33}	U_{12}	U_{13}	U_{23}
Sr	0.0080(7)	0.0080(7)	0.0118(8)	0.000	0.000	0.000
Ni	0.0182(8)	0.0182(8)	0.0164(9)	0.000	0.000	0.000
P/Ge	0.0083(9)	0.0083(9)	0.0257(14)	0.000	0.000	0.000

Table A8 Anisotropic displacement parameters (U_{ij} / Å^2) for $SrNi_2(P_{0.45(1)}Ge_{0.55(1)})_2$ from single crystal refinement measured at 293 K.

Atom	U_{11}	U_{22}	U_{33}	U_{12}	U_{13}	U_{23}
Sr	0.0104(3)	0.0104(3)	0.0093(3)	0.000	0.000	0.000
Ni	0.0223(3)	0.0223(3)	0.0128(3)	0.000	0.000	0.000
P/Ge	0.0100(3)	0.0100(3)	0.0216(5)	0.000	0.000	0.000

Table A9 Anisotropic displacement parameters (U_{ij} / Å^2) for $SrNi_2(P_{0.35(1)}Ge_{0.65(1)})_2$ from single crystal refinement measured at 293 K.

Atom	U_{11}	U_{22}	U_{33}	U_{12}	U_{13}	U_{23}
Sr	0.0096(2)	0.0096(2)	0.0076(3)	0.000	0.000	0.000
Ni	0.0215(3)	0.0215(3)	0.0103(3)	0.000	0.000	0.000
P/Ge	0.0095(3)	0.0095(3)	0.0195(4)	0.000	0.000	0.000

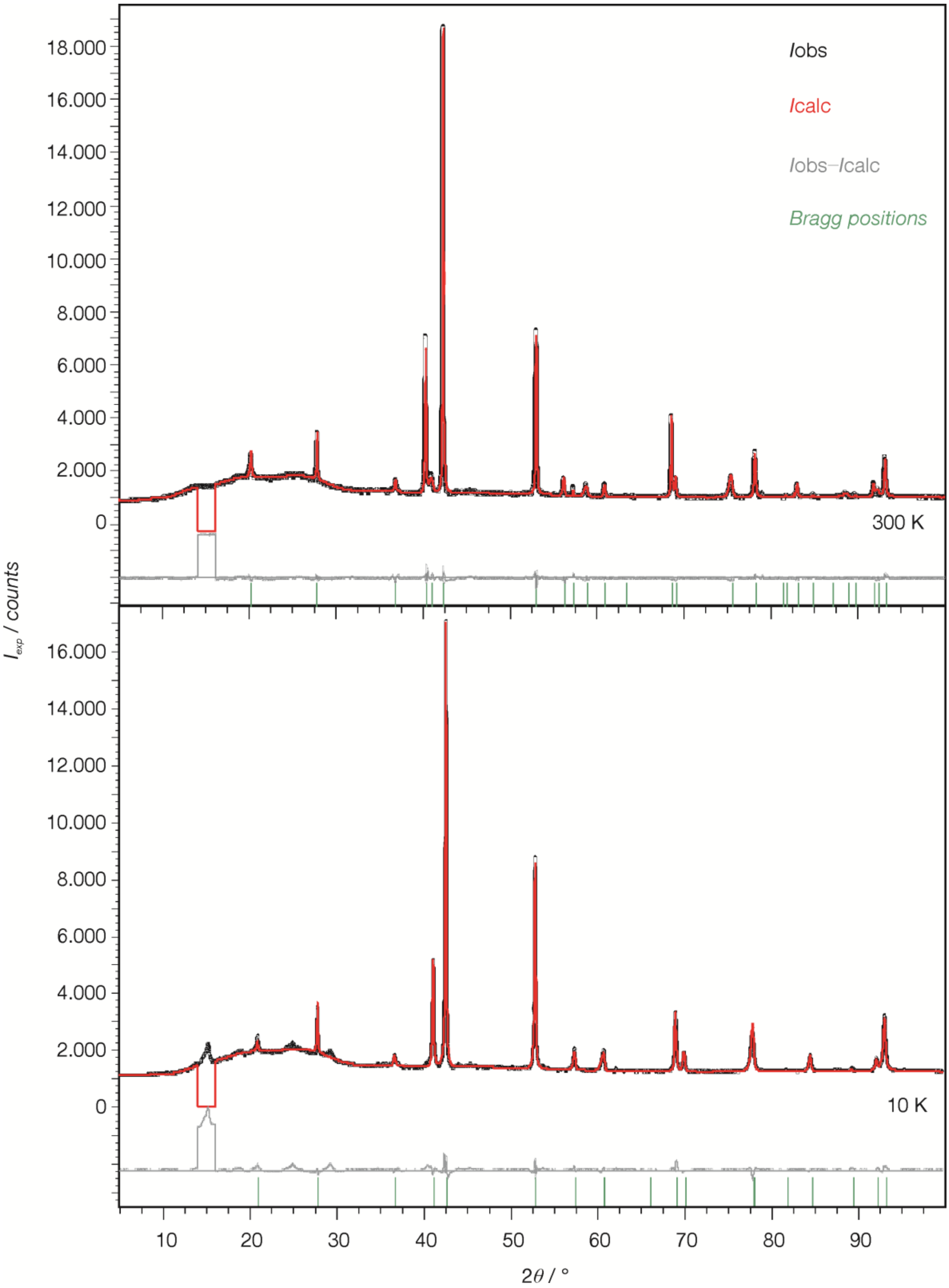

Figure A5 Rietveld refinement (TOPAS) of $SrNi_2(P_{1-x}Ge_x)_2$ (x_{exp} = 0.110(3)) for powder X-ray data collected on Huber Imaging Plate Guinier Diffractometer G670 (Co-$K_{\alpha1}$, measurement range 6 - 100 ° 2θ, 0.005 ° step size, measurement time 30 min, Si as external standard) at 300 K and 10 K. Refinement parameters: 300 K - GOF = 0.815, R_p = 0.0143, R_{wp} = 0.0209, R_{Bragg} = 0.0141; 10 K - GOF = 1.015, R_p = 0.0173, R_{wp} = 0.0271, R_{Bragg} = 0.0131. Excluded region between 14 - 16 ° 2θ is due to instrumental artifact.

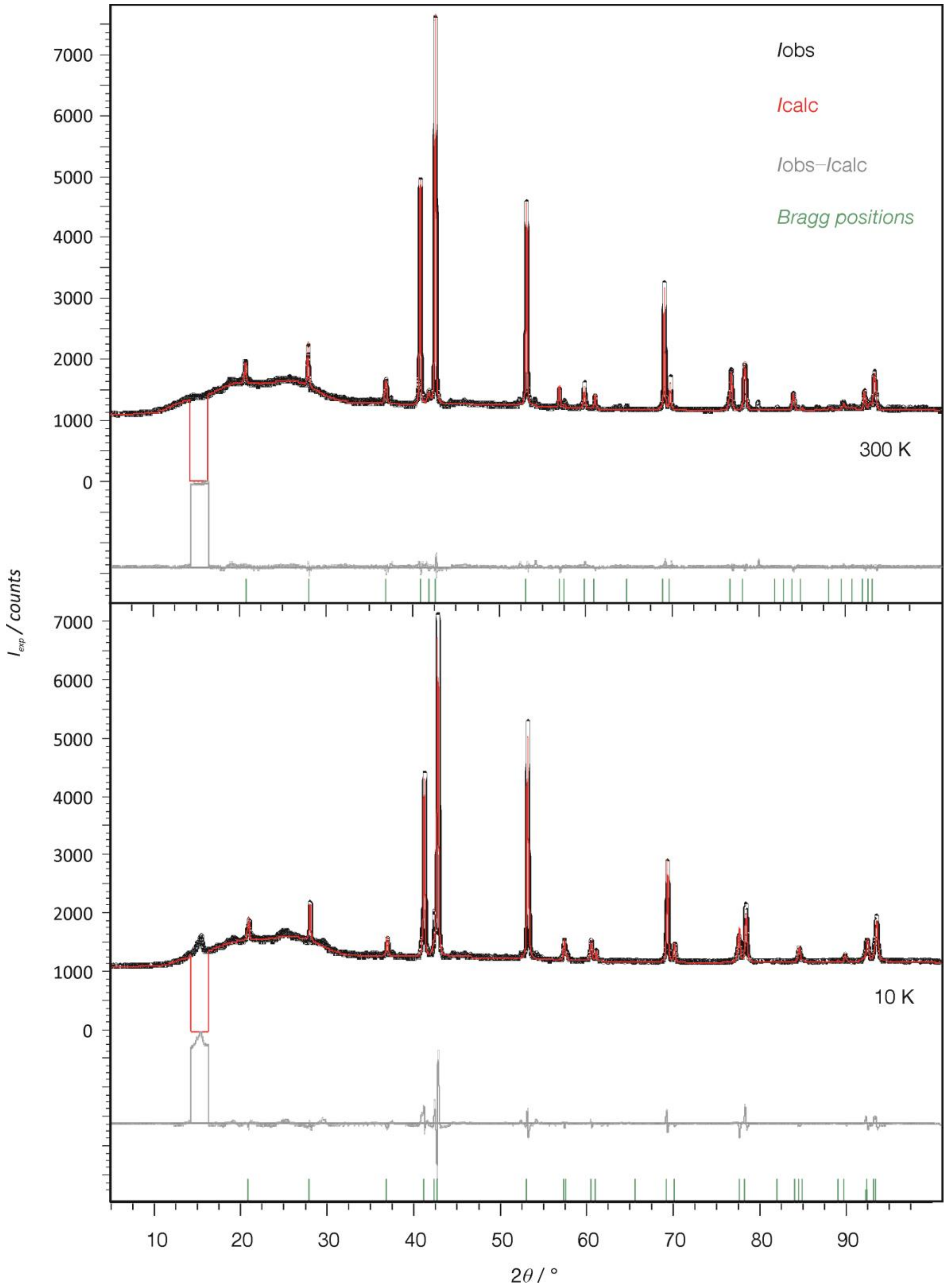

Figure A6 Rietveld refinement (TOPAS) of $SrNi_2(P_{1-x}Ge_x)_2$ ($x_{exp} = 0.212(3)$) for powder X-ray data collected on Huber Imaging Plate Guinier Diffractometer G670 (Co-$K_{\alpha1}$, measurement range 6 - 100 ° 2θ, 0.005 ° step size, measurement time 30 min, Si as external standard) at 300 K and 10 K. Refinement parameters: 300 K - GOF = 0.493, R_p = 0.0099, R_{wp} = 0.0137, R_{Bragg} = 0.0076; 10 K - GOF = 0.995, R_p = 0.0139, R_{wp} = 0.0275, R_{Bragg} = 0.0158. Excluded region between 14 - 16 ° 2θ is due to instrumental artifact.

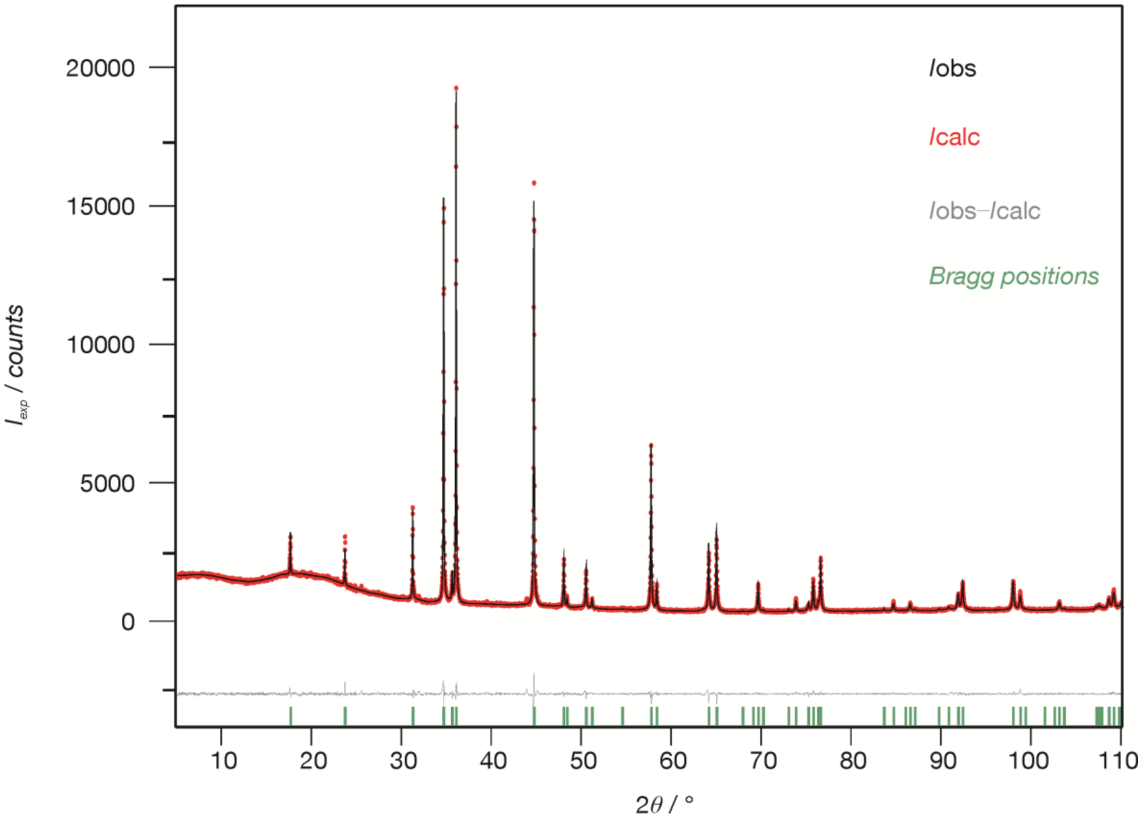

Figure A7 Rietveld refinement (FullProf) of $SrNi_2(P_{1-x}Ge_x)_2$ (x_{exp} = 0.436(2)) for powder X-ray data collected on Stoe Stadi P (Cu-$K_{\alpha 1}$, measurement range 5 - 110 ° 2θ, 0.015 ° step size, measurement time 5 hours, Si as external standard) at 300 K. Refinement parameters: GOF = 1.1, R_p = 0.138, R_{wp} = 0.113, R_{Bragg} = 1.99.

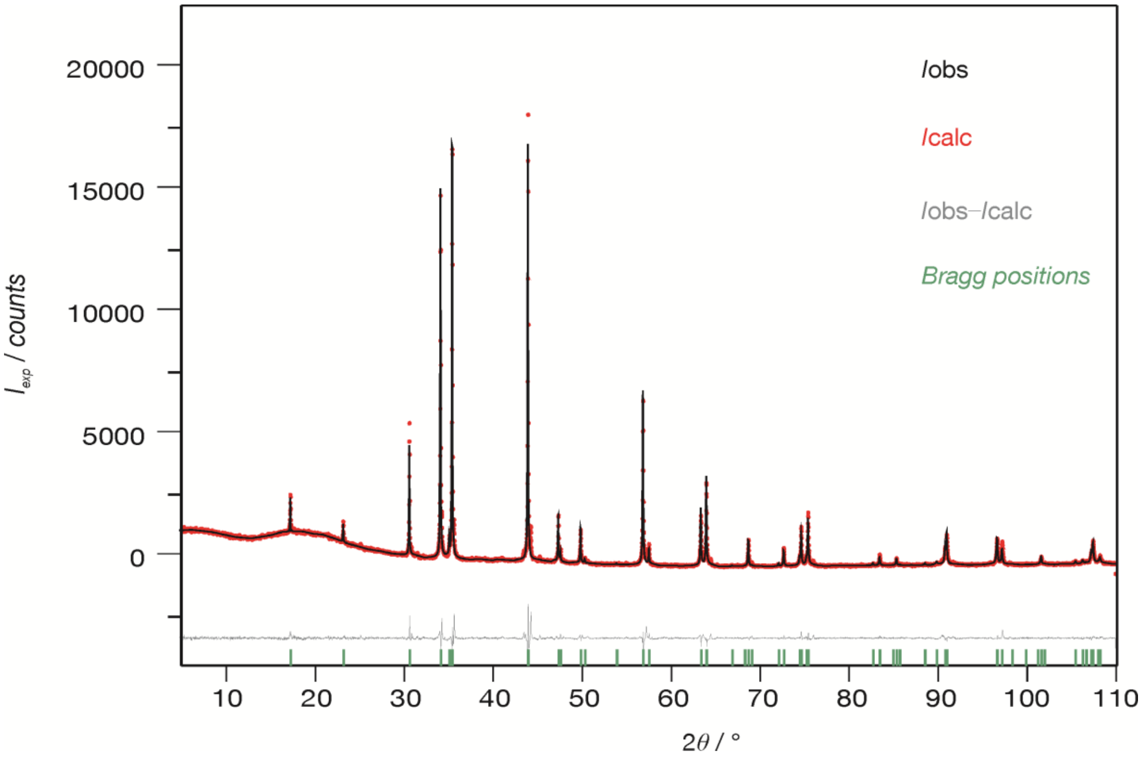

Figure A8 Rietveld refinement (FullProf) of $SrNi_2(P_{1-x}Ge_x)_2$ (x_{exp} = 0.547(2)) for powder X-ray data collected on Stoe Stadi P (Cu-$K_{\alpha1}$, measurement range 5 - 110 ° 2θ, 0.015 ° step size, measurement time 5 hours, Si as external standard) at 300 K. Refinement parameters: GOF = 1.8, R_p = 0.205, R_{wp} = 0.181, R_{Bragg} = 3.86.

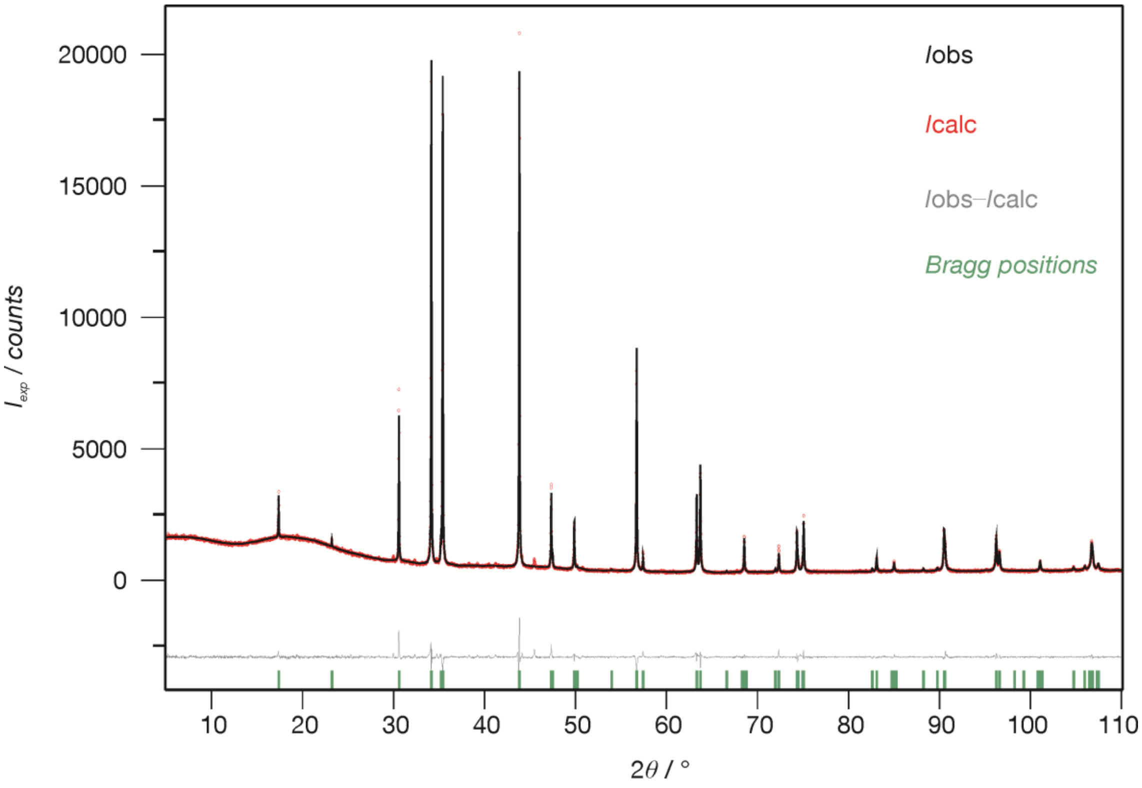

Figure A9 Rietveld refinement (FullProf) of $SrNi_2(P_{1-x}Ge_x)_2$ (x_{exp} = 0.671(2)) for powder X-ray data collected on Stoe Stadi P (Cu-$K_{\alpha1}$, measurement range 5 - 110 ° 2θ, 0.015 ° step size, measurement time 5 hours, Si as external standard) at 300 K. Refinement parameters: GOF = 1.4, R_p = 0.158, R_{wp} = 0.125, R_{Bragg} = 4.34.

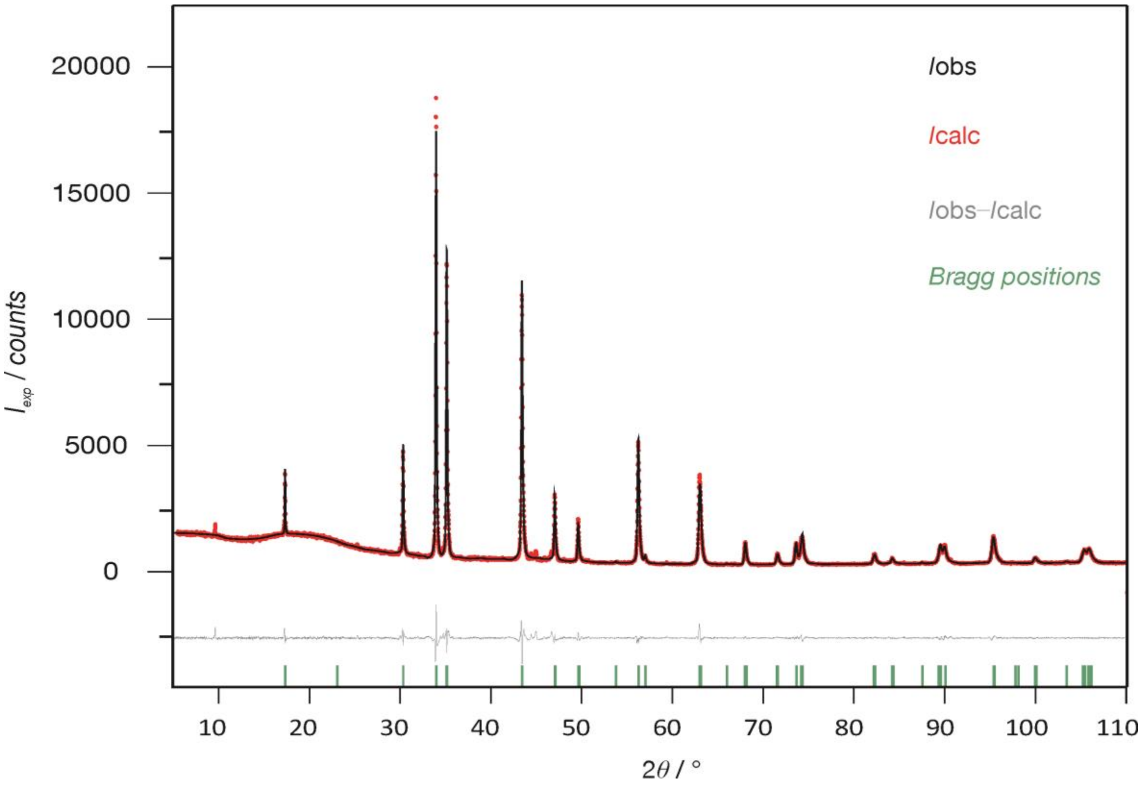

Figure A10 Rietveld refinement (FullProf) of $SrNi_2(P_{1-x}Ge_x)_2$ (x_{exp} = 0.884(1)) for powder X-ray data collected on Stoe Stadi P (Cu-$K_{\alpha 1}$, measurement range 5 - 110 ° 2θ, 0.015 ° step size, measurement time 5 hours, Si as external standard) at 300 K. Refinement parameters: GOF = 1.4, R_p = 0.133, R_{wp} = 0.119, R_{Bragg} = 1.89.

Table A10 $SrNi_2(P_{0.890(3)}Ge_{0.110(3)})_2$ lattice parameters obtained from powder data at varying temperatures.

$T_{measurement}$ / K	a / Å	c / Å	V / Å^3
300	4.0119(1)	10.220(1)	164.50(1)
290	4.0119(1)	10.208(1)	164.30(1)
280	4.0121(1)	10.195(1)	164.11(1)
270	4.0124(1)	10.181(1)	163.92(1)
260	4.0126(1)	10.168(1)	163.72(1)
250	4.0134(1)	10.150(1)	163.49(1)
240	4.0144(1)	10.124(1)	163.15(1)
230	4.0159(1)	10.093(1)	162.78(1)
220	4.0180(1)	10.058(1)	162.38(1)
210	4.0195(1)	10.028(1)	162.01(1)
200	4.0203(1)	10.006(1)	161.73(1)
190	4.0208(1)	9.991(1)	161.51(1)
180	4.0210(1)	9.976(1)	161.29(1)
170	4.0212(1)	9.962(1)	161.09(1)
160	4.0215(1)	9.949(1)	160.90(1)
150	4.0215(1)	9.937(1)	160.71(1)
140	4.0217(1)	9.927(1)	160.55(1)
130	4.0217(1)	9.917(1)	160.40(1)
120	4.0216(1)	9.909(1)	160.26(1)
110	4.0215(1)	9.901(1)	160.13(1)
100	4.0214(1)	9.893(1)	159.99(1)
90	4.0212(1)	9.886(1)	159.86(1)
80	4.0209(1)	9.879(1)	159.72(1)
70	4.0210(1)	9.872(1)	159.61(1)
60	4.0210(1)	9.866(1)	159.52(1)
50	4.0211(1)	9.860(1)	159.43(1)
40	4.0214(1)	9.853(1)	159.34(1)
30	4.0215(1)	9.851(1)	159.31(1)
20	4.0214(1)	9.851(1)	159.30(1)
10	4.0214(1)	9.849(1)	159.27(1)

Table A11 $SrNi_2(P_{0.788(3)}Ge_{0.212(3)})_2$ lattice parameters obtained from powder data at varying temperatures.

***T*measurement / K**	***a* / Å**	***c* / Å**	***V* / Å^3**
300	4.0448(1)	10.121(1)	165.58(1)
290	4.0446(1)	10.115(1)	165.48(1)
280	4.0444(1)	10.109(1)	165.36(1)
270	4.0439(1)	10.105(1)	165.24(1)
260	4.0434(1)	10.098(1)	165.09(1)
250	4.0432(1)	10.091(1)	164.96(1)
240	4.0430(1)	10.084(1)	164.83(1)
230	4.0425(1)	10.079(1)	164.71(1)
220	4.0421(1)	10.074(1)	164.59(1)
210	4.0415(1)	10.068(1)	164.45(1)
200	4.0416(1)	10.061(1)	164.34(1)
190	4.0411(1)	10.056(1)	164.22(1)
180	4.0403(1)	10.054(1)	164.12(1)
170	4.0407(1)	10.044(1)	163.99(1)
160	4.0408(1)	10.040(1)	163.93(1)
150	4.0404(1)	10.034(1)	163.80(1)
140	4.0400(1)	10.030(1)	163.70(1)
130	4.0396(1)	10.024(1)	163.58(1)
120	4.0391(1)	10.019(1)	163.46(1)
110	4.0389(1)	10.017(1)	163.40(1)
100	4.0386(1)	10.013(1)	163.32(1)
90	4.0385(1)	10.010(1)	163.25(1)
80	4.0380(1)	10.006(1)	163.14(1)
70	4.0378(1)	10.002(1)	163.07(1)
60	4.0376(1)	9.999(1)	163.00(1)
50	4.0377(1)	9.995(1)	162.95(1)
40	4.0377(1)	9.990(1)	162.87(1)
30	4.0376(1)	9.987(1)	162.81(1)
20	4.0376(1)	9.985(1)	162.79(1)
10	4.0376(1)	9.984(1)	162.76(1)

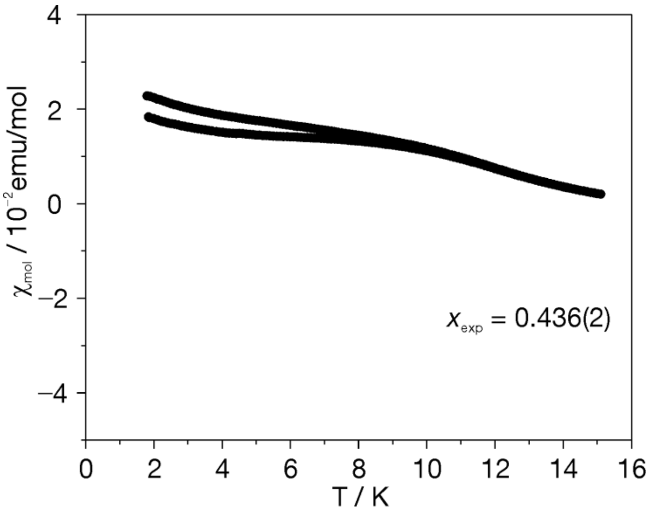

Figure A11 Zero field cooled-field cooled (zfc-fc) measurement for the sample $SrNi_2(P_{1-x}Ge_x)_2$ with x_{exp} = 0.436(2) and an applied field of 15 Oe.

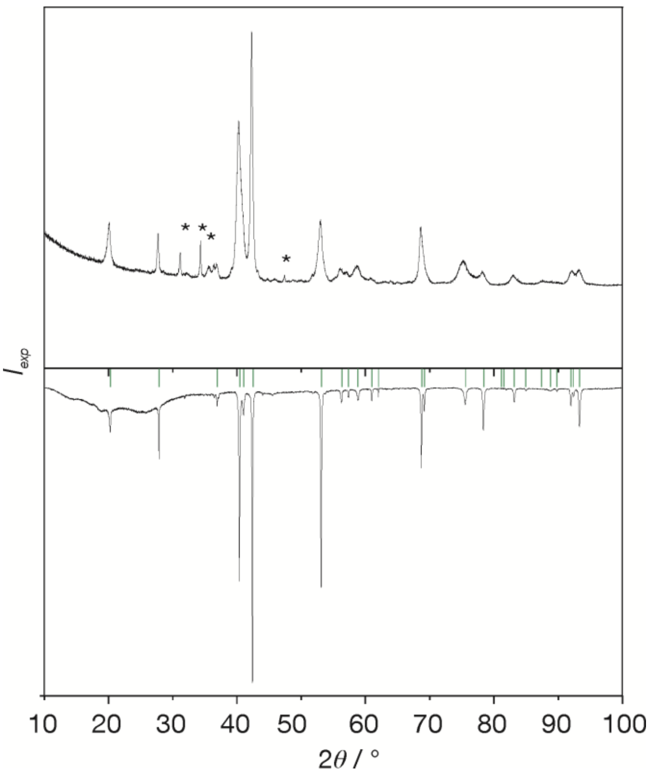

Figure A12 $SrNi_2(P_{1-x}Ge_x)_2$ (x_{nom} = 0.15) powder X-ray pattern (Co-$K_{\alpha1}$, measurement range 10 - 100 ° 2θ, at 300 K) of powder (top) after thermal pressure treatment (2 h at 973 K and 630 MPa). The theoretical Bragg positions (green) for the 122 phase calculated from the powder X-ray of x_{exp} = 0.110(3) (bottom).

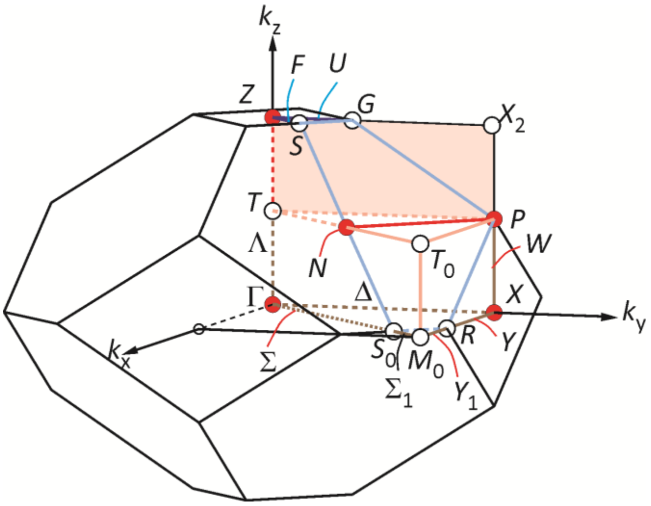
k_z
F
U
Z
G
X_2
S
T
P
W
Λ
N
T_0
Γ
Δ
X
k_y
R
Y
k_x
Σ
S_0
M_0
Σ_1
Y_1

Figure A13 Brillouin zone for space group *I*4/*mmm*.

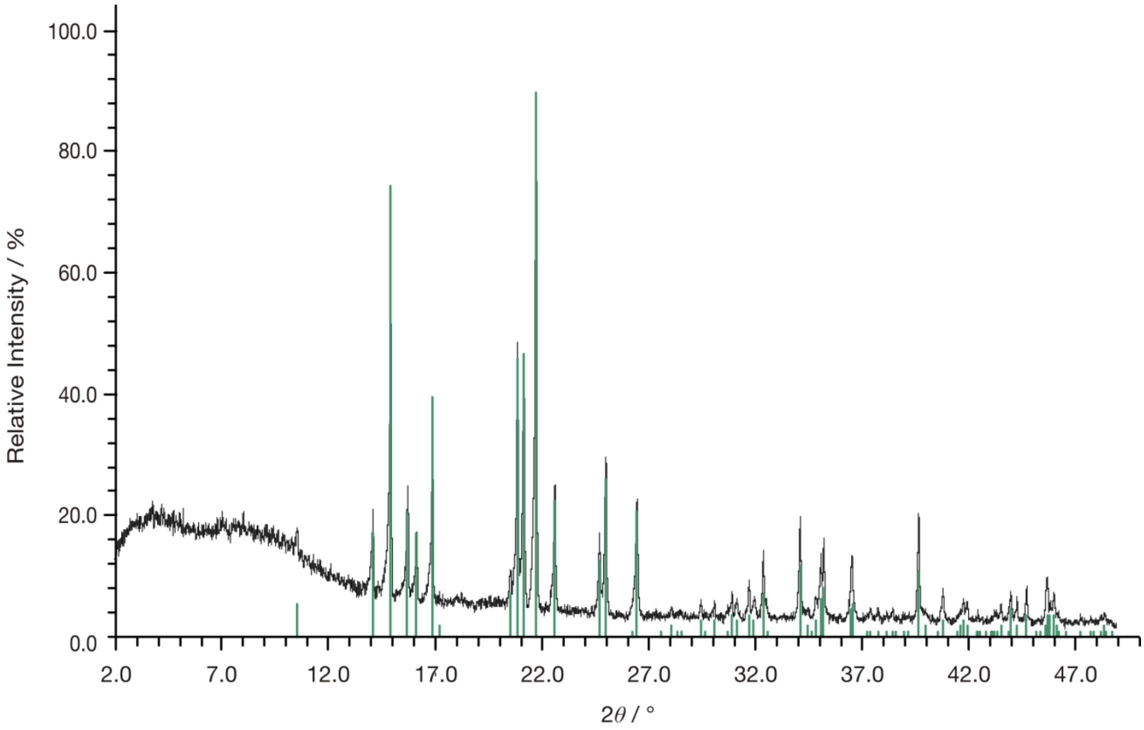

Figure A14 X-ray powder diffraction pattern of FeP sample (Mo-$K_{\alpha1}$, measurement range 2 - 50 ° 2θ, 0.015 ° step size, 25 sec/step). Theoretical calculated pattern of FeP (green lines) shown in the bottom.

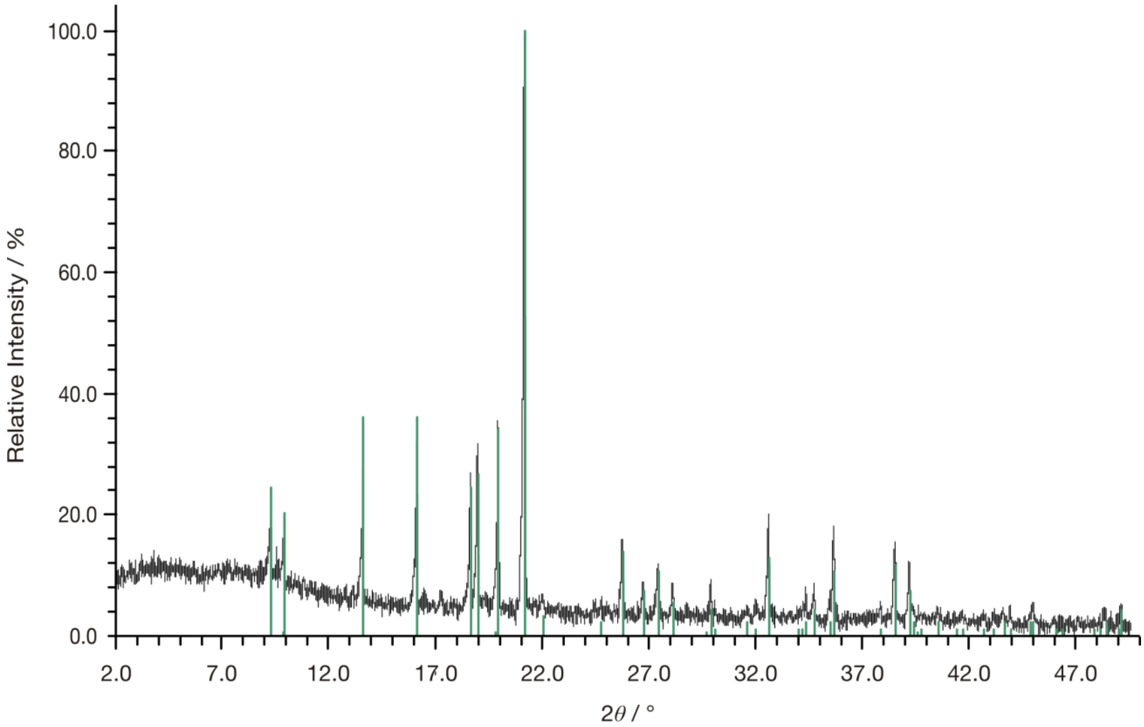

Figure A15 X-ray powder diffraction pattern of FeGe sample (Mo-$K_{\alpha 1}$, measurement range 2 - 50 ° 2*θ*, 0.015 ° step size, 25 sec/step). Theoretical calculated pattern of FeGe (green lines) shown in the bottom.

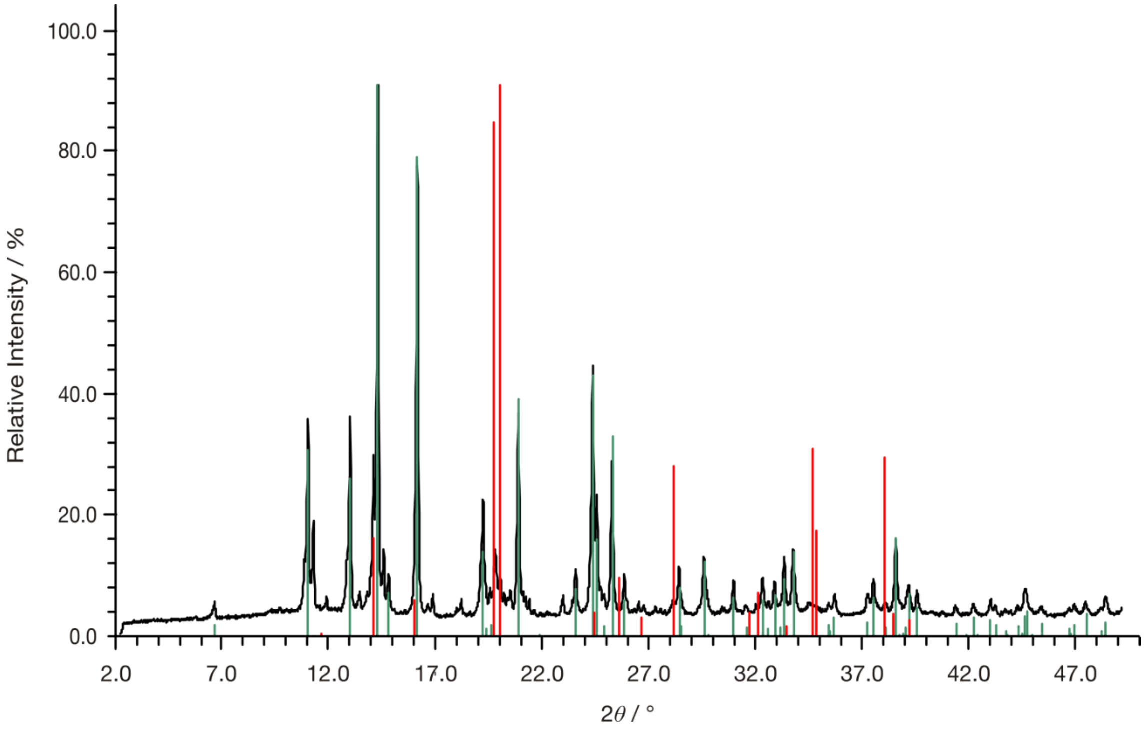

Figure A16 X-ray powder diffraction pattern of $BaFe_2(P_{1-x}Ge_x)_2$ sample with x_{nom} = 0.30 (Mo-$K_{\alpha 1}$, measurement range 2 - 50 ° 2*θ*, 0.015 ° step size, 45 sec/step). Theoretical calculated pattern of $BaFe_2(P_{1-x}Ge_x)_2$ with $ThCr_2Si_2$ structure (*a* = 3.857 Å, *c* = 12.464 Å; green lines) and $Fe_{1.67}Ge_1$ (red lines) shown in the bottom.

Table A12 EDX results (values given in at. %, including standard deviation) for measured single crystal of $BaFe_2(P_{1-x}Ge_x)_2$.

Composition	**Ba**	**Fe**	**P**	**Ge**	x_{EDX}
$BaFe_2(P_{0.930(6)}Ge_{0.070(6)})_2$	24(3)	43(5)	31(3)	3(1)	0.92

Table A13 Anisotropic displacement parameters (U_{ij} / Å^2) for $BaFe_2(P_{0.930(6)}Ge_{0.070(6)})_2$ measured at 293 K.

Atom	U_{11}	U_{22}	U_{33}	U_{12}	U_{13}	U_{23}
Ba	0.0104(2)	0.0104(2)	0.0135(3)	0.000	0.000	0.000
Fe	0.0080(3)	0.0080(3)	0.0146(5)	0.000	0.000	0.000
P/Ge	0.0080(5)	0.0080(5)	0.0152(9)	0.000	0.000	0.000

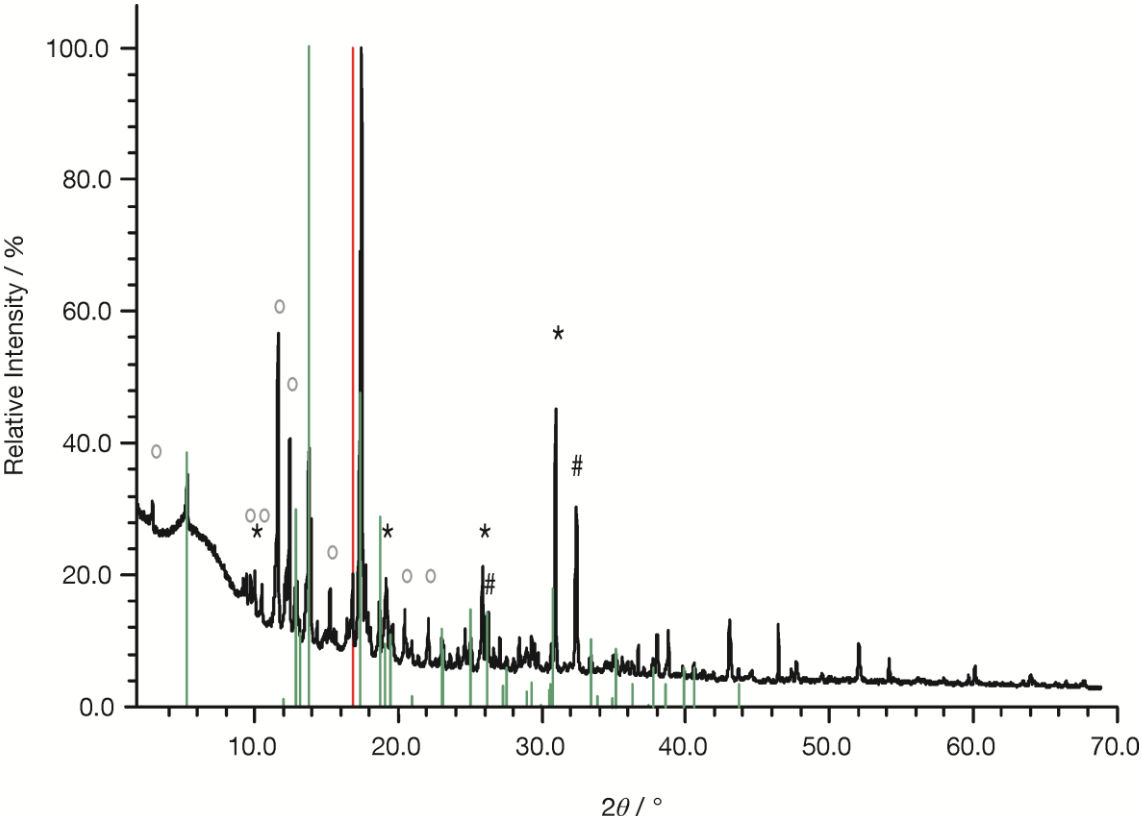

Figure A17 X-ray powder diffraction pattern of $CaFe_2Si_2$ sample (Mo-K$_{\alpha1}$, measurement range 2 - 70 ° 2θ, 0.015 ° step size, 25 sec/step). Theoretical calculated pattern of $CaFe_2Si_2$ with $ThCr_2Si_2$-type structure (green lines) shown in the bottom. The reflections marked with red line at 19.8 ° and 33.65 ° belong to cubic diamond which was used as an internal standard. Reflections marked with ^{0} belong to Ca_5Si_3, reflections marked with * belong to FeSi and reflections marked with # belong to Fe_3Si.

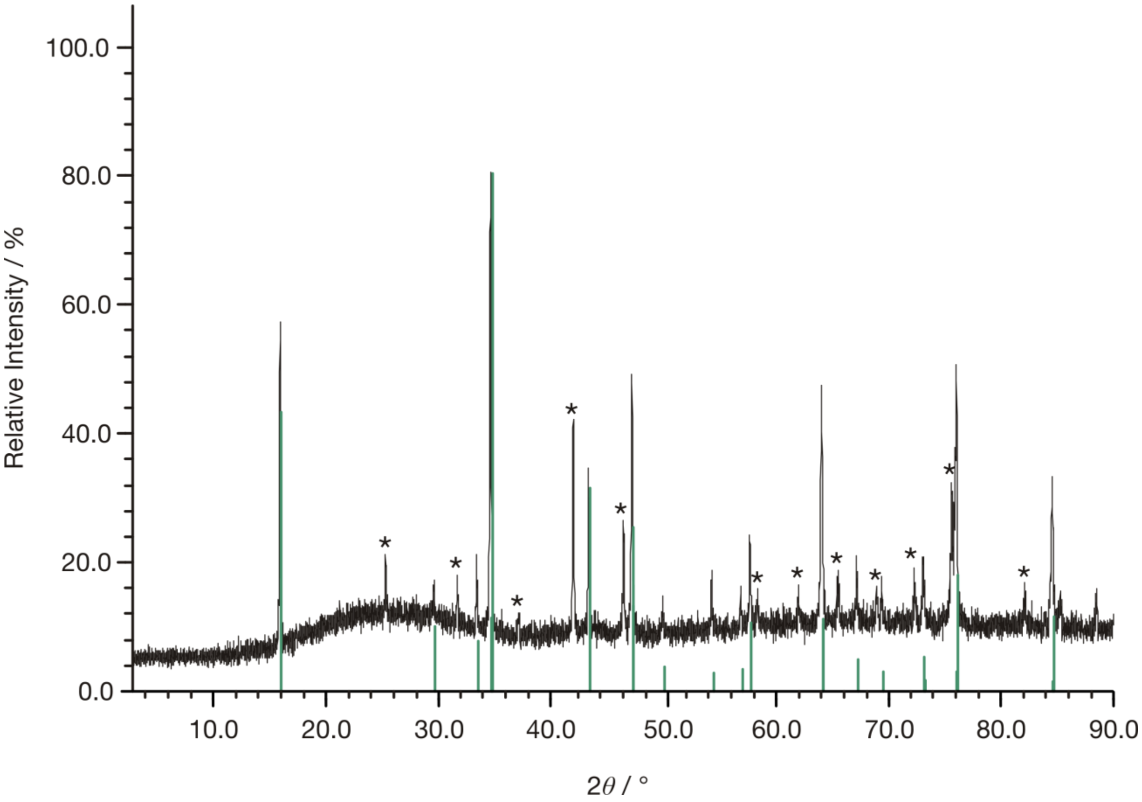

Figure A18 X-ray powder diffraction pattern of $CaRh_2Si_2$ sample), (Cu-$K_{\alpha 1}$, measurement range 2 - 90 ° 2θ, 0.01 ° step size, 40 sec/step, Si as external standard). Theoretically calculated pattern of $CaRh_2Si_2$ with $ThCr_2Si_2$ type structure (green lines) shown in the bottom. Reflections marked with * belong to RhSi.

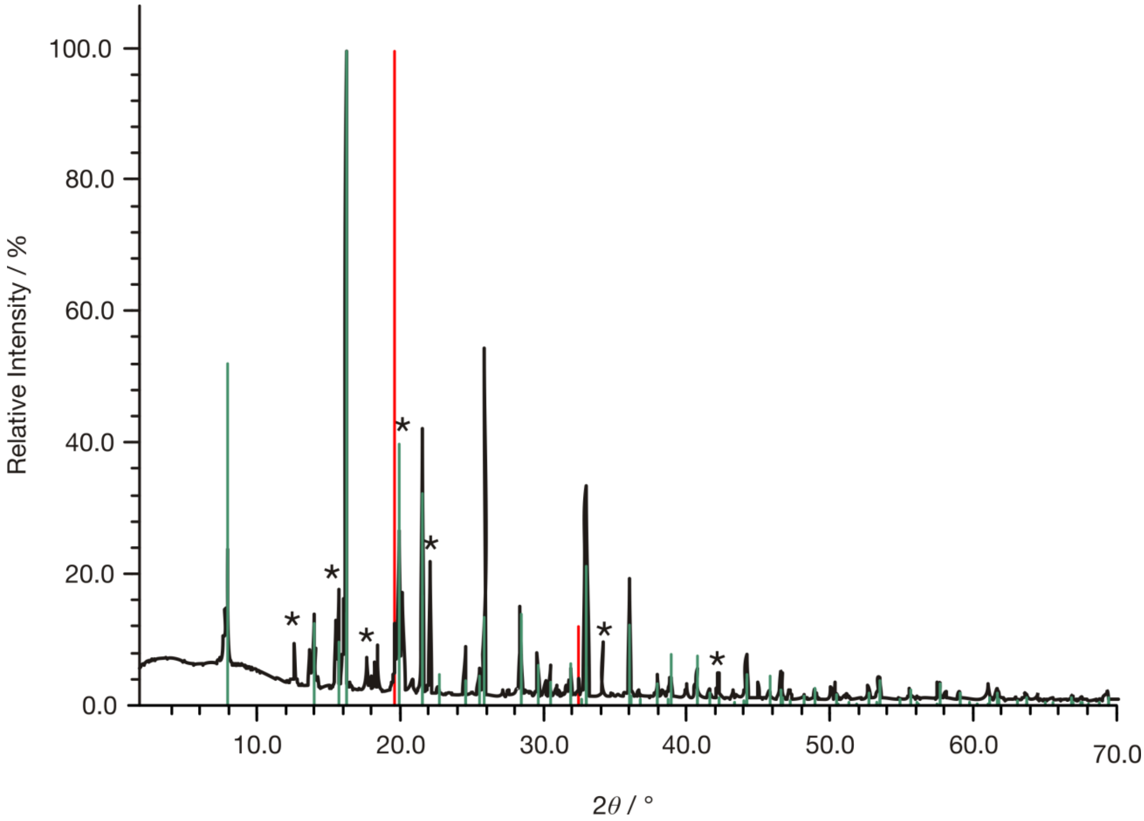

Figure A19 X-ray powder diffraction pattern of $CaFeRhSi_2$ sample (nominal composition), (Mo-$K_{\alpha 1}$, measurement range 2 - 78 ° 2θ, 0.015 ° step size, 25 sec/step). Theoretically calculated pattern of $Ca(Fe_{0.34(3)}Rh_{0.66(3)})_2Si_2$ with $ThCr_2Si_2$ type structure (green lines) shown in the bottom. The reflex marked with the red line at 19.8 ° and 33.65 ° belong to cubic diamond which was used as an internal standard. Reflections marked with * belong to FeSi.

Table A14 EDX results (values given in at. %, including standard deviation) for measured single crystals of $Ca(Fe_{1-x}Rh_x)_2Si_2$ solid solution.

Composition	**Ca**	**Fe**	**Rh**	**Si**	x_{EDX}
$CaFe_2Si_2$	21(2)	42(4)	-	38(3)	1
$Ca(Fe_{0.34(3)}Rh_{0.66(3)})_2Si_2$	19(2)	12(2)	30(4)	39(4)	0.29
$CaRh_2Si_2$	20(2)	-	42(4)	38(4)	0

Table A15 Wyckoff positions, atomic coordinates and isotropic equivalent displacement parameters / Å^2 × 10^3 for $Ca(Rh_{1-x}Fe_x)_2Si_2$ solid solution (space group *I*4/*mmm*, *Z* = 2). Standard deviations are given in brackets.

Atom	**Wyckoff position**	***x***	***y***	***z***	***U*$_{eq}$ / Å^2 × 10^3**
Ca	*2a*	0	0	0	12(1)
Rh	*4d*	0	½	¼	9(1)
Si	*4e*	0	0	0.3733(4)	12(1)
Ca	*2a*	0	0	0	8(1)
$Rh_{0.66(3)}/Fe_{0.34(3)}$	*4d*	0	½	¼	5(1)
Si	*4e*	0	0	0.3716(4)	7(1)
Ca	*2a*	0	0	0	19(1)
Fe	*4d*	0	½	¼	17(1)
Si	*4e*	0	0	0.3746(4)	18(2)

Table A16 Anisotropic displacement parameters (U_{ij} / Å^2) for $CaFe_2Si_2$ measured at 293 K.

Atom	***U*$_{11}$**	***U*$_{22}$**	***U*$_{33}$**	***U*$_{12}$**	***U*$_{13}$**	***U*$_{23}$**
Ca	0.0141(13)	0.0141(13)	0.029(2)	0.000	0.000	0.000
Fe	0.0127(8)	0.0127(8)	0.0264(11)	0.000	0.000	0.000
Si	0.0139(12)	0.0139(12)	0.027(2)	0.000	0.000	0.000

Table A17 Anisotropic displacement parameters (U_{ij} / Å^2) for $Ca(Fe_{0.34(3)}Rh_{0.66(3)})_2Si_2$ measured at 293 K.

Atom	***U*$_{11}$**	***U*$_{22}$**	***U*$_{33}$**	***U*$_{12}$**	***U*$_{13}$**	***U*$_{23}$**
Ca	0.0086(13)	0.0086(13)	0.0079(16)	0.000	0.000	0.000
Fe/Rh	0.0047(5)	0.0047(5)	0.0060(6)	0.000	0.000	0.000
Si	0.0064(12)	0.0064(12)	0.0081(15)	0.000	0.000	0.000

Table A18 Anisotropic displacement parameters (U_{ij} / Å^2) for $CaRh_2Si_2$ measured at 293 K.

Atom	***U*$_{11}$**	***U*$_{22}$**	***U*$_{33}$**	***U*$_{12}$**	***U*$_{13}$**	***U*$_{23}$**
Ca	0.0112(12)	0.0112(12)	0.0146(16)	0.000	0.000	0.000
Rh	0.0074(4)	0.0074(4)	0.0126(5)	0.000	0.000	0.000
Si	0.0101(12)	0.0101(12)	0.0155(17)	0.000	0.000	0.000

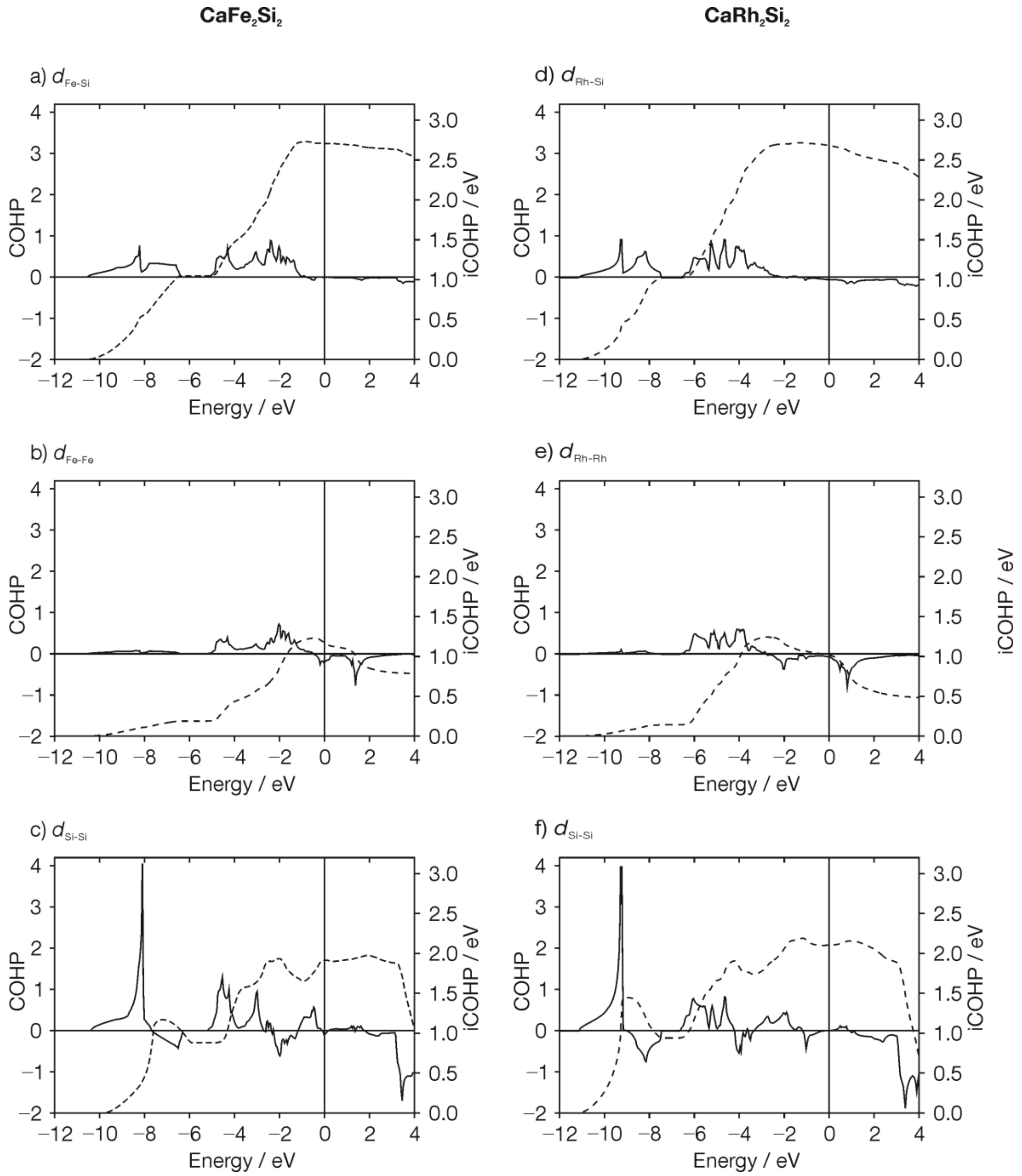

Figure A20 COHP curves (solid lines) including iCOHP (dashed lines) for selected interatomic distances of CaFe$_2$Si$_2$ (a-c) and CaRh$_2$Si$_2$ (d-f). a) $d_{\text{Fe–Si}}$ = 2.343 Å, b) $d_{\text{Fe–Fe}}$ = 2.785 Å, c) $d_{\text{Si–Si}}$ = 2.555 Å, d) $d_{\text{Rh–Si}}$ = 2.378 Å, e) $d_{\text{Rh–Rh}}$ = 2.878 Å and e) $d_{\text{Si–Si}}$ = 2.529 Å.

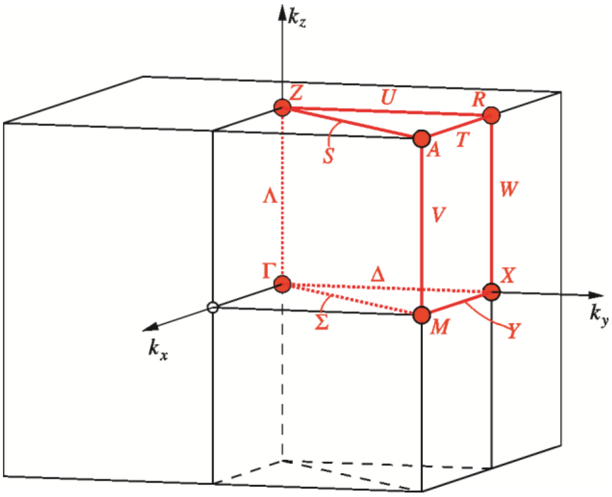

Figure A21 Brillouin zone for space group *P*4/*nmm*.

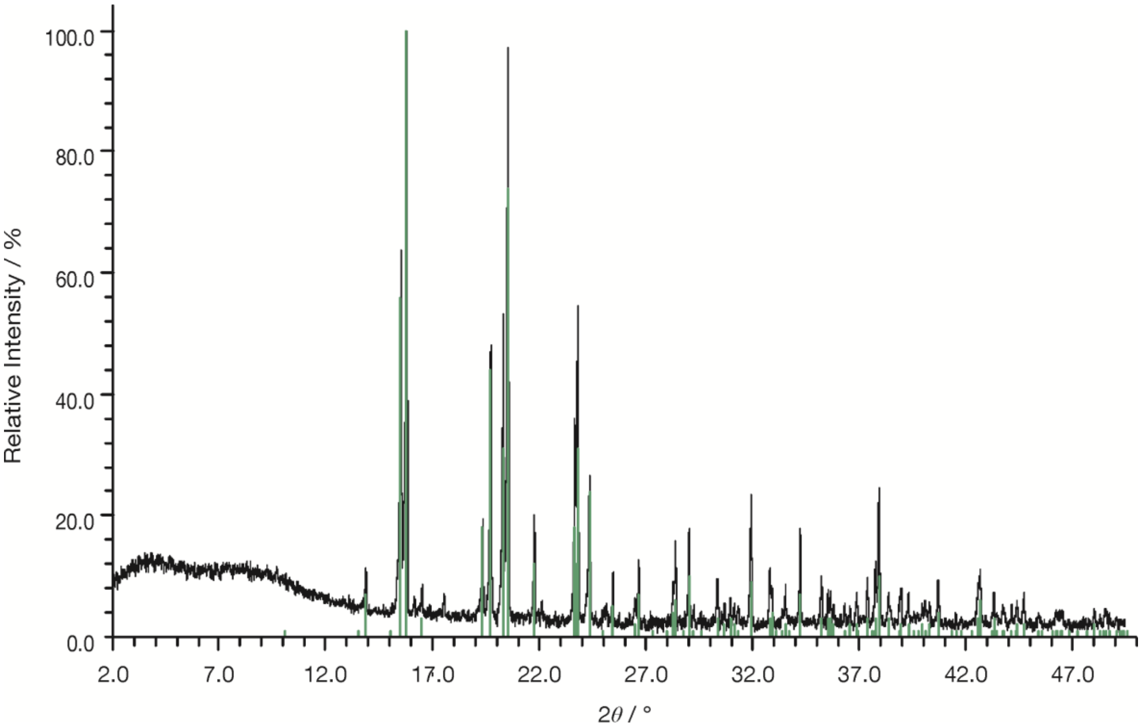

Figure A22 X-ray powder diffraction pattern of FeAs sample, (Mo-$K_{\alpha 1}$, measurement range 2 - 50 ° 2θ, 0.01 ° step size, 20 sec/step, Si as external standard). Theoretically calculated pattern of FeAs (green lines) shown in the bottom.

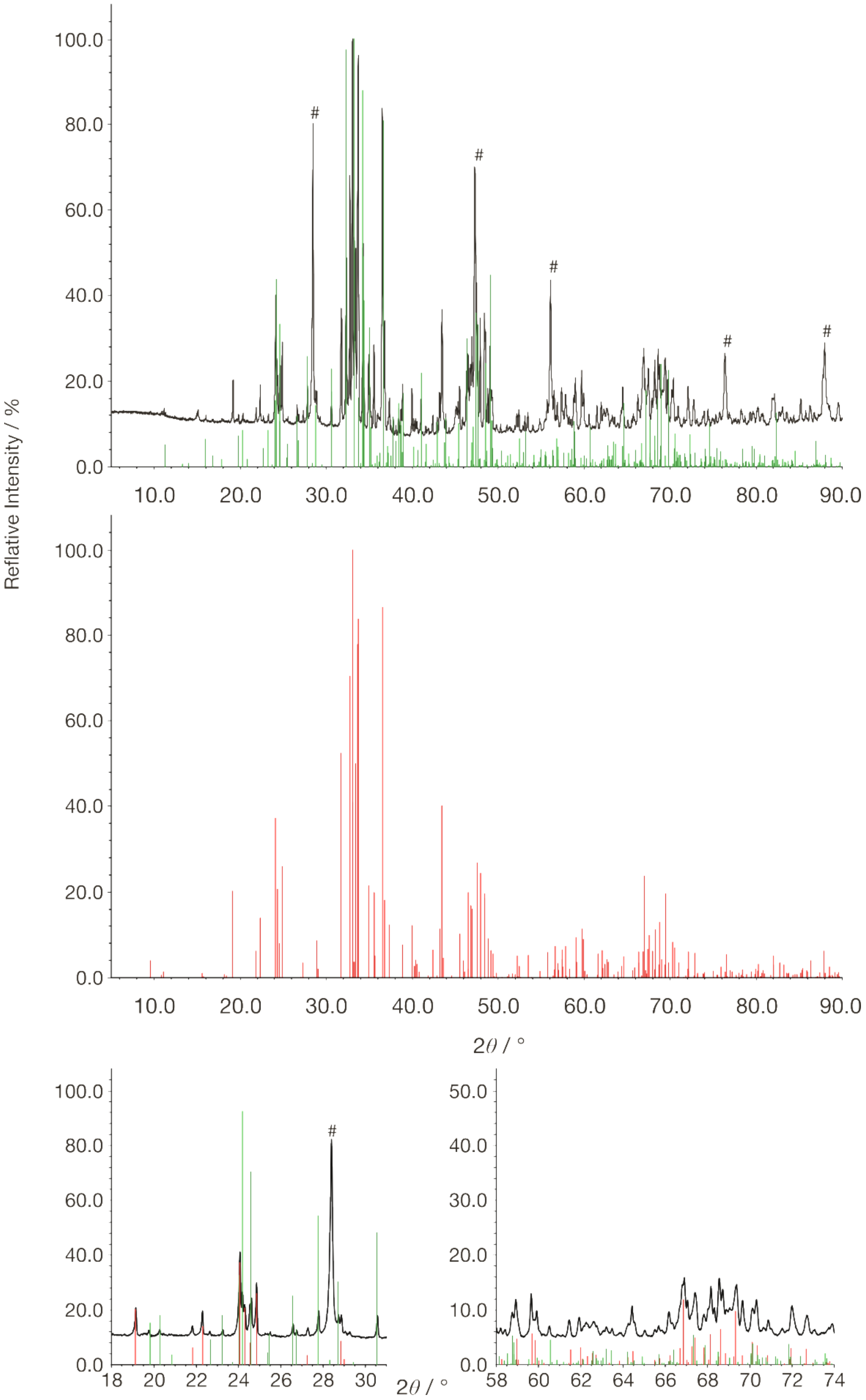

Figure A23 X-ray powder diffraction pattern of $Ca_{14}FeAs_{11}$ sample, (Cu-$K_{\alpha1}$, measurement range 5 - 90 ° 2θ, 0.01 ° step size, 45 sec/step). Theoretically calculated pattern of $Ca_{14}FeAs_{11}$ (green lines); $Ca_{11}As_{9.68}$ model (red lines, middle) and details between 18 - 31 ° 2θ & 58 - 74 ° 2θ shown in the bottom. Reflections marked with # belong to Si used as standard.

Table A19 Anisotropic displacement parameters (U_{ij} / Å^2) for $Ca_{14}FeAs_{11}$ measured at 150 K (non-split atom model).

Atom	**U_{11}**	**U_{22}**	**U_{33}**	**U_{12}**	**U_{13}**	**U_{23}**
Ca1	0.0106(4)	0.0120(4)	0.0120(3)	−0.0010(3)	0.0004(3)	0.0017(3)
Ca2	0.0108(4)	0.0112(4)	0.0111(3)	−0.0015(3)	0.0015(3)	−0.0005(3)
Ca3	0.0186(4)	0.0100(4)	0.0106(3)	0.0009(3)	0.0033(3)	0.0022(3)
Ca4	0.0114(5)	0.0096(5)	0.0099(5)	0.0012(4)	0.000	0.000
Fe	0.0119(4)	0.0119(4)	0.0099(5)	0.000	0.000	0.000
As1	0.0122(2)	0.0091(2)	0.00902(18)	−0.00068(14)	0.00058(15)	0.00073(15)
As2	0.0104(2)	0.0094(2)	0.01039(19)	0.00103(14)	0.00008(14)	−0.00101(16)
As3	0.00962(18)	0.00962(18)	0.0092(2)	0.00046(14)	−0.00046(14)	0.0005(2)
As4	0.0357(4)	0.0357(4)	0.0082(4)	0.000	0.000	0.0277(5)

Table A20 Anisotropic displacement parameters (U_{ij} / Å^2) for $Ca_{14}FeAs_{11}$ measured at 150 K (split atom model).

Atom	**U_{11}**	**U_{22}**	**U_{33}**	**U_{12}**	**U_{13}**	**U_{23}**
Ca1	0.0105(4)	0.0119(4)	0.0120(3)	−0.0010(3)	0.0003(3)	0.0016(3)
Ca2	0.0108(4)	0.0113(4)	0.0111(3)	−0.0015(3)	0.0015(3)	−0.0005(3)
Ca3	0.0186(4)	0.0100(4)	0.0105(3)	0.0009(3)	0.0033(3)	0.0020(3)
Ca4	0.0113(5)	0.0096(5)	0.0099(5)	0.0012(4)	0.000	0.000
Fe	0.0118(4)	0.0118(4)	0.0100(5)	0.000	0.000	0.000
As1	0.0122(2)	0.0091(2)	0.00897(18)	−0.00068(14)	0.00057(15)	0.00071(15)
As2	0.0103(2)	0.0093(2)	0.01038(19)	0.00104(14)	0.00009(14)	−0.00102(15)
As3	0.00952(17)	0.00952(17	0.0092(2)	0.00044(14)	−0.00044(14)	0.0004(2)
As4	0.0127(11)	0.0127(11)	0.0086(4)	−0.0003(5)	0.0003(5)	0.0042(11)

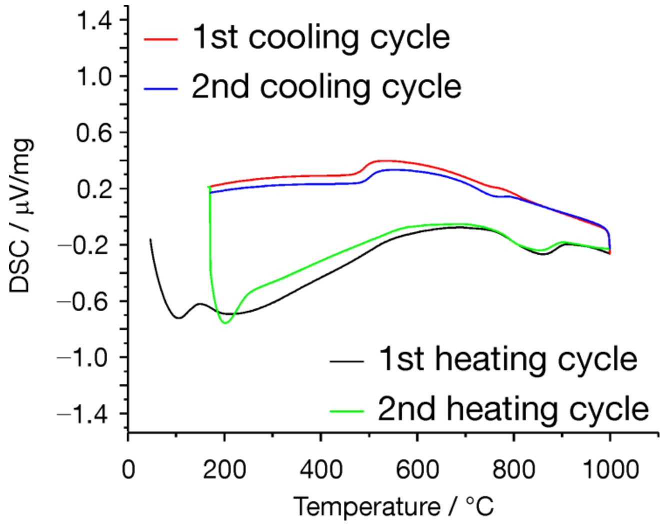

Figure A24 DSC curves for $Ca_{14}FeAs_{11}$ sample.

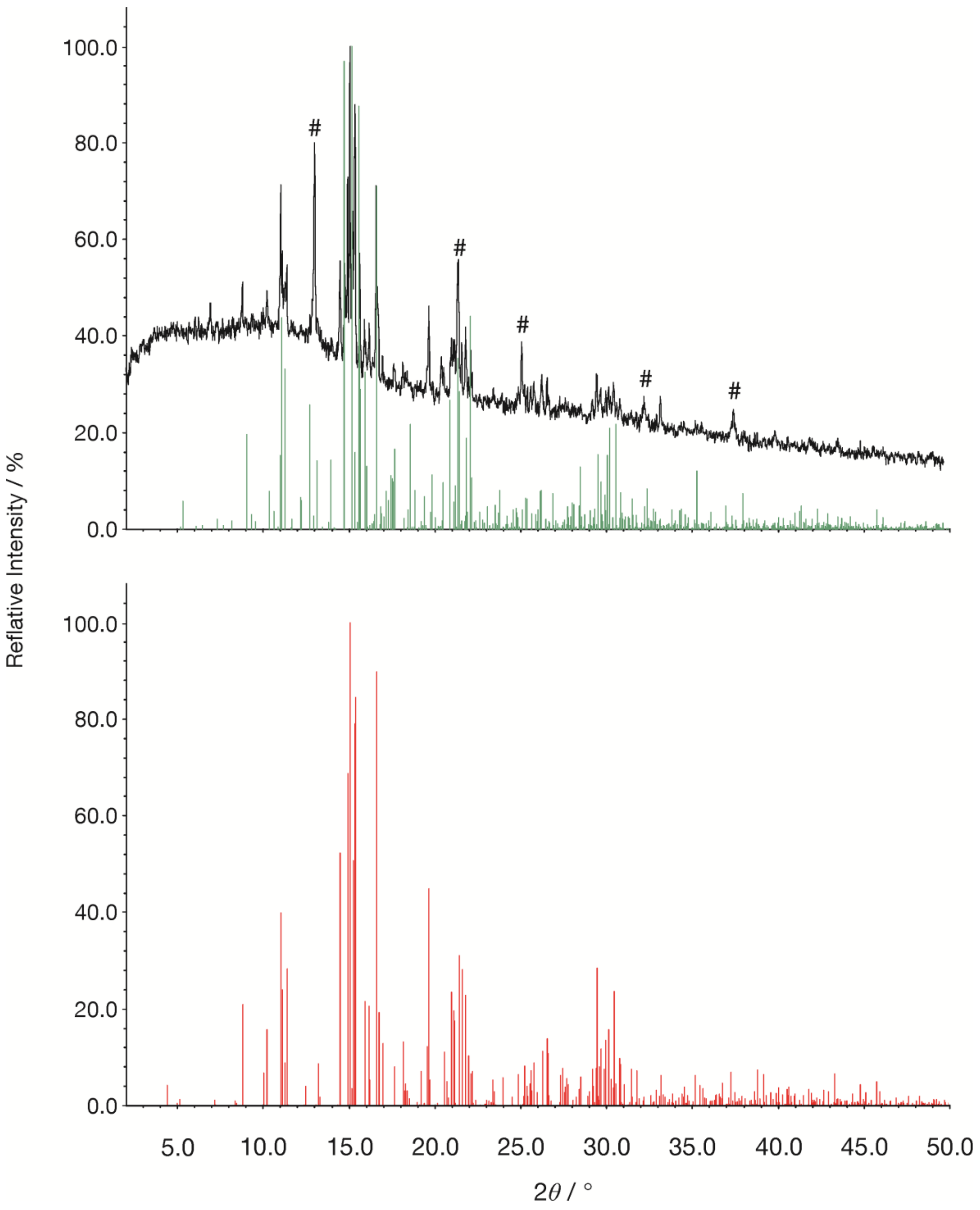

Figure A25 X-ray powder diffraction pattern of $Ca_{14}FeAs_{11}$ sample after DSC measurement, (Mo-$K_{\alpha1}$, measurement range 2 - 50 ° 2θ, 0.01 ° step size, 45 sec/step). Theoretically calculated pattern of $Ca_{14}FeAs_{11}$ (green lines); $Ca_{11}As_{9.68}$ model (red lines) shown in the bottom, reflections marked with # belong to Si.

Table A21 Input data for computational calculations for the tetragonal model non-split of the $[As_3]^{7-}$ units: space group, lattice parameters and atomic parameters obtained from single crystal data.

Space group	**Lattice parameters**	**Atom**	***x***	***y***	***z***
$I4_1/acd$	a = 15.627 Å	Ca1	0.02344	0.37785	0.00522
No. 142	c = 20.978 Å	Ca2	0.04333	0.07339	0.17140
Origin choice 2		Ca3	0.34344	0.07035	0.09278
tetragonal		Ca4	0.35305	0	¼
Z = 8		Fe	0	¼	0.37500
		As1	0.13000	0.02566	0.04680
		As2	0.36525	0.25405	0.06057
		As3	0.13438	0.38438	0.12500
		As4	0	0.25000	0.12500

Table A22 Input data for the computational calculations for $Ca_{14}FeAs_{11}$ with symmetry reduction to accommodate the split model of the $[As_3]^{7-}$ units: space group and atomic parameters chosen by symmetry reduction. Lattice parameters taken from single crystal refinement.

Space group	**Lattice parameters**	**Atom**	***x***	***y***	***z***
$P4_3$	a = 15.627 Å	Ca1	0.50	0.40	0.24
	c = 20.978 Å	Ca2	0	0.10	0.238
		Ca3	0.23	0.12	0.24
		Ca4	0.27	0.38	0.24
		Ca5	0.73	0.88	0.24
		Ca6	0.77	0.62	0.24
		Ca7	0.93	0.29	0.16
		Ca8	0.57	1.21	0.16
		Ca9	0.71	1.07	0.146
		Ca10	0.79	0.43	0.067
		Ca11	0.41	1.07	0.146
		Ca12	0.50	0.90	0.238
		Ca13	1.00	0.60	0.238
		Ca14	0.07	−0.21	0.16
		Ca15	0.43	0.71	0.16
		Ca16	0.73	0.38	0.233
		Ca17	0.77	1.21	0.23
		Ca18	0.43	0.41	0.082
		Ca19	0.07	0.09	0.081

Table A22 continued	**Atom**	***x***	***y***	***z***
	Ca20	0.23	0.62	0.023
	Ca21	0.27	−0.12	0.23
	Ca22	0.21	−0.07	0.07
	Ca23	0.29	0.57	0.07
	Ca24	0.93	0.59	0.081
	Ca25	0.91	0.43	0.33
	Ca26	0.59	0.57	0.146
	Ca27	−0.09	−0.07	0.15
	Ca28	0.09	0.43	0.15
	Fe1	0.75	0.75	0.114
	Fe2	0.25	0.25	0.144
	As1	0.75	0.259	0.114
	As2	0.75	0.741	0.364
	As3	0.385	0.246	0.178
	As4	0.115	0.246	0.178
	As5	0.12	−0.026	0.191
	As6	0.38	0.526	0.191
	As7	0.111	0.111	0.364
	As8	0.63	0.39	0.114
	As9	0.611	0.889	0.364
	As10	0.87	0.61	0.364
	As11	0.615	0.7541	0.178
	As12	0.885	0.7541	0.178
	As13	0.12	0.475	0.285
	As14	0.38	0.026	0.285
	As15	0.616	0.2459	0.299
	As16	0.116	0.2459	0.299
	As17	0.120	−0.026	0.285
	As18	0.620	0.526	0.285
	As19	0.25	0.385	0.05
	As20	0.25	0.115	0.05
	As21	0.88	0.475	0.191
	As22	0.62	1.026	0.191

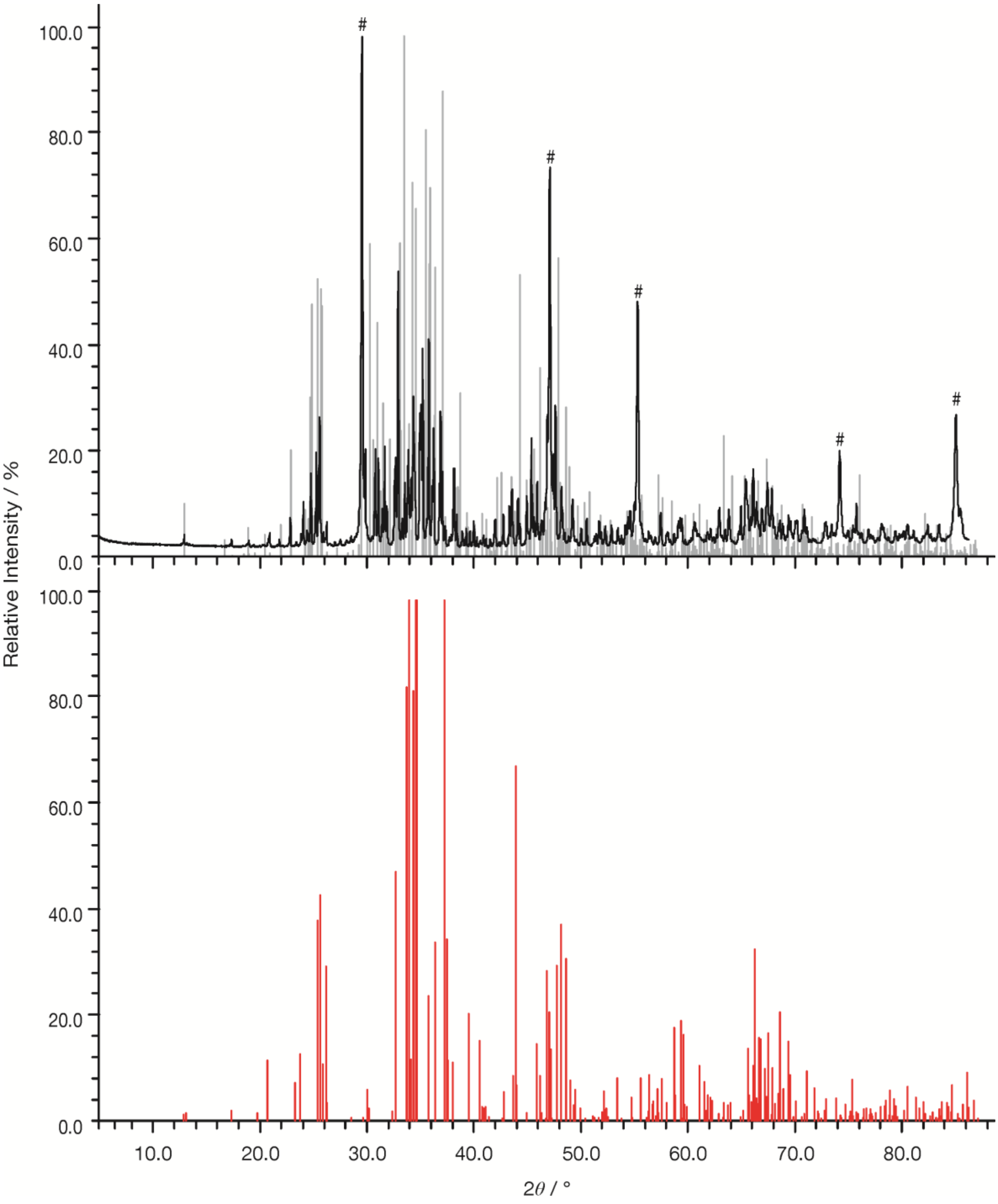

Figure A26 X-ray powder diffraction pattern of $Ca_{4+x}As_3$ sample (x = 0.05), (Cu-$K_{\alpha1}$, measurement range 2 - 90 ° 2θ, 0.01 ° step size, 45 sec/step). Theoretically calculated pattern of Ca_4As_3 (gray lines, top) and $Ca_{11}As_{9.68}$ (red lines, bottom) shown, reflections marked with # belong to Si.

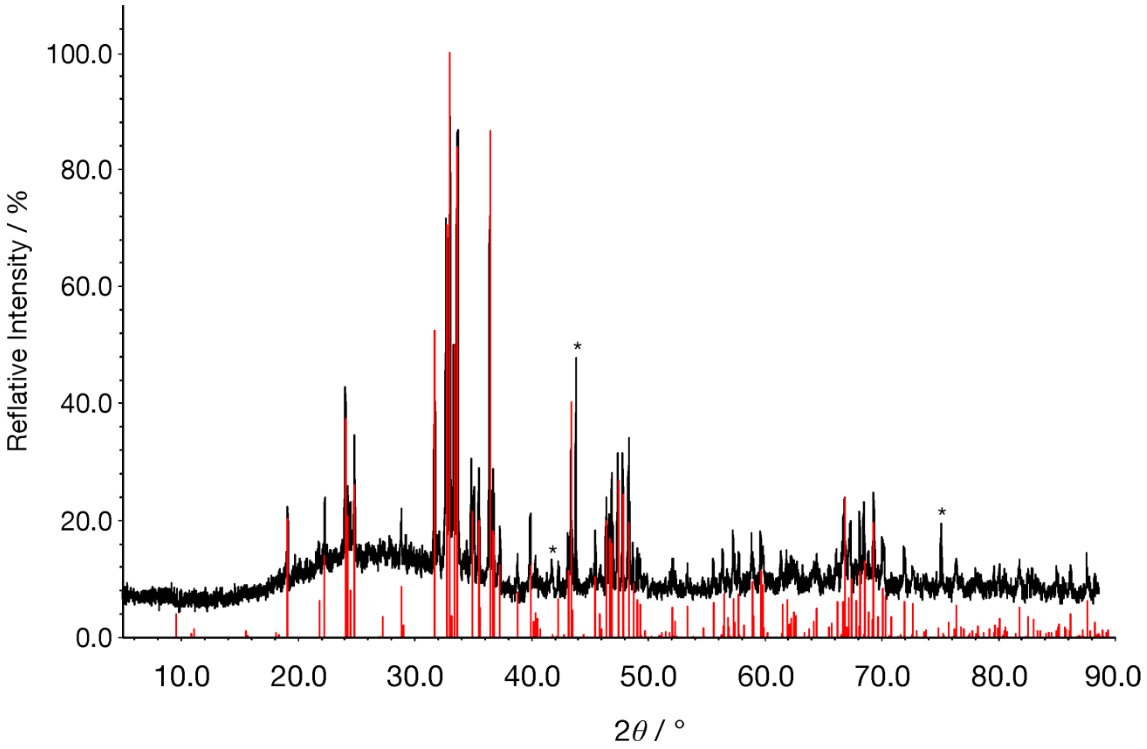

Figure A27 X-ray powder diffraction pattern of $Ca_{11+x}As_{10}$ sample (x = 2.2), (Cu-K$_{\alpha1}$, measurement range 5 - 90 ° 2θ, 0.01 ° step size, 45 sec/step). Theoretically calculated pattern of $Ca_{11}As_{9.68}$ (red lines) shown in the bottom, reflections marked with * belong to an unidentified phase.

Table A23 Anisotropic displacement parameters (U_{ij} / Å^2) for Ca_4As_3 measured at 150 K.

Atom	U_{11}	U_{22}	U_{33}	U_{12}	U_{13}	U_{23}
Ca1	0.0087(5)	0.0118(7)	0.0137(6)	0.0005(5)	0.0004(5)	0.0003(5)
Ca2	0.0122(6)	0.0135(6)	0.0117(6)	−0.0007(5)	0.0022(5)	0.0002(5)
Ca3	0.0154(9)	0.0155(9)	0.0097(9)	0.000	0.000	−0.0018(7)
Ca4	0.0095(9)	0.0143(9)	0.0100(9)	0.000	0.000	−0.0019(7)
Ca5	0.0125(9)	0.0100(9)	0.0094(9)	0.000	0.000	−0.0017(7)
Ca6	0.0081(8)	0.0103(9)	0.0211(10)	0.000	0.000	0.0001(7)
As1	0.0086(3)	0.0119(3)	0.0089(3)	0.0004(2)	−0.0005(3)	0.0009(3)
As2	0.0113(4)	0.0124(5)	0.0112(5)	0.000	0.000	−0.0005(4)
As3	0.0100(5)	0.0122(5)	0.0102(4)	0.000	0.000	−0.0020(4)
As4	0.0100(5)	0.0120(4)	0.0142(5)	0.000	0.000	0.0001(4)
As5	0.0080(4)	0.0107(5)	0.0090(4)	0.000	0.000	0.0009(4)

Table A24 Anisotropic displacement parameters (U_{ij} / Å^2) for $Ca_{11}As_{9.68(2)}$ measured at 150 K (non-split atom model).

Atom	U_{11}	U_{22}	U_{33}	U_{12}	U_{13}	U_{23}
Ca1	0.0137(12)	0.0182(12)	0.0083(10)	0.000	0.0002(9)	0.000
Ca2	0.0108(11)	0.0172(12)	0.0091(10)	0.000	0.0006(8)	0.000
Ca3	0.0144(14)	0.0144(14)	0.010(2)	0.000	0.000	0.000
Ca4	0.157(8)	0.157(8)	0.016(2)	0.000	0.000	0.147(8)
As1	0.0111(7)	0.0111(7)	0.0110(11)	0.000	0.000	0.000
As2	0.0094(7)	0.0094(7)	0.0072(9)	0.000	0.000	0.000
As3	0.0116(9)	0.0168(9)	0.0095(7)	0.000	0.000	0.000
As4	0.0178(5)	0.0178(5)	0.0185(6)	0.0065(4)	0.0065(4)	0.0074(5)

Table A25 Anisotropic displacement parameters (U_{ij} / Å^2) for $Ca_{11}As_{9.68(2)}$ measured at 150 K (split atom model).

Atom	U_{11}	U_{22}	U_{33}	U_{12}	U_{13}	U_{23}
Ca1	0.0133(6)	0.0179(7)	0.0088(6)	0.000	0.0004(5)	0.000
Ca2	0.0110(6)	0.0172(7)	0.0094(6)	0.000	0.0008(5)	0.000
Ca3	0.0144(8)	0.0144(8)	0.0100(12)	0.000	0.000	0.000
Ca4A	0.0265(15)	0.0265(15)	0.015(2)	0.000	0.000	0.012(2)
Ca4B	0.037(2)	0.037(2)	0.018(2)	0.000	0.000	0.025(3)
As1	0.0113(4)	0.0113(4)	0.0111(6)	0.000	0.000	0.000
As2	0.0097(4)	0.0097(4)	0.0072(5)	0.000	0.000	0.000
As3	0.0115(5)	0.0172(5)	0.0094(4)	0.000	0.000	0.000
As4	0.0183(3)	0.0183(3)	0.0185(4)	0.0065(2)	0.0065(2)	0.0076(3)
As5A	0.035(3)	0.035(3)	0.138(7)	0.000	0.000	0.013(2)
As5B	0.080(2)	0.080(2)	0.0112(17)	0.000	0.000	−0.043(3)

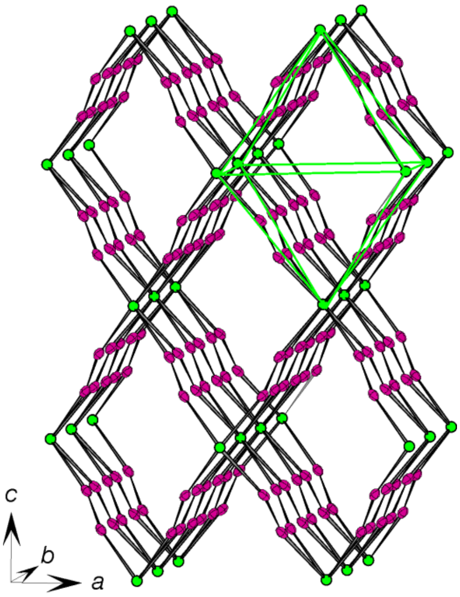

Figure A28 Model of $Ca_{11}As_{9.68(2)}$. Green spheres are dummy atoms lying in the center of the $As_{3.86}$ rings, the As–As dumbbells shown as represented as atomic displacement ellipsoids with 90 % probability level. The green lines indicate the theoretical octahedra formed by the "rings" and the As dumbbells.

List of Figures

Figure 1.1 Classes of the iron-pnictide superconductor family presented as models: a) 11 class, example FeSe superconductor; b) 111 class, example LiFeAs superconductor; c) 1111 class, example LaFePO superconductor; d) 122 class, example $BaFe_2As_2$ parent compound.... 5
Figure 1.2 Structure of $LuNi_2B_2C$ superconductor (T_c = 16.6 K) Lu = gray, Ni teal, B = magenta and represented as C = black spheres; bonds between Ni–Ni (dark gray), Ni–B (light gray lines) and B–C (blue lines) are included. 7
Figure 1.3 $BaFe_2As_2$ model in the low-temperature modification with space group *Fmmm*; Ba shown in gray, Fe in turquois and As in magenta. The orientations of the magnetic moments of Fe are presented as black arrows.[51] 8
Figure 2.1 Photographs of the different reaction containers used in this work: a) Nb/Ta ampoules closed by caps on one side (top) or on both sides (bottom); b) silica glass tubes of different diameter (top, bottom) and a graphitized example (middle). 18
Figure 2.2 Photograph of a silica glass tube attached to a quick fit molded inside a H_2/O_2 burner flame. 19
Figure 2.3 Mini Arc Melting Furnace installed inside a glove box. 20
Figure 2.4 Photograph of the resistance furnace: a) tubular furnace with the tubes protected by a metal cage; b) muffle furnace in extractor hood. 21
Figure 2.5 Photograph of the induction furnace with the sample chamber and pyrometer a) connected to the generator b) with the pyrometer control unit on top. 22
Figure 3.1 Model of the $ThCr_2Si_2$ structure type: Th as light gray, Cr as turquois and Si as magenta spheres. a) unit cell including the bonds, the interlayer distance $d_{E–E}$ (blue dashed line) is marked; b) polyanionic [$TE_{4/4}$] layer along [001] including tetrahedra. 33
Figure 3.2 Temperature program for $SrNi_2P_2$ precursor: a) first heating cycle; b) second heating cycle. 37
Figure 3.3 Temperature program for $SrNi_2(P_{1-x}Ge_x)_2$ samples: a) first heating cycle; b) second heating cycle. 39
Figure 3.4 Temperature program for: a) $SrNi_2As_2$ precursor; b) $SrNi_2(As_{1-x}Ge_x)_2$ samples. 41
Figure 3.5 Structure model of a) $SrNi_2E_2$ (E = Ge, P and As)[23, 26, 31] in ucT *I*4/*mmm* modification (HT $SrNi_2P_2$ above 320 K); b) $SrNi_2P_2$ in “partially collapsed” orthorhombic *Immm* modification (LT). The distance $d_{E–E}$ is 2.83 Å for E = Ge, As and 3.12 Å for E = P. 42
Figure 3.6 Dependence of composition (a) and lattice parameters (b) of mixed $SrNi_2(P_{1-x}Ge_x)_2$ and the ternary compounds (x = 0, 1 taken from literature; lattice parameters for HT $SrNi_2P_2$ *I*4/*mmm*, 373 K

measurement).[26, 31] Lines within the diagrams are for visible help. The standard deviation is within the size of the symbols used. 43

Figure 3.7 c/a ratio vs x_{exp} obtained from powder data refinement (room-temperature data, Table 3.7). 47

Figure 3.8 Powder X-ray patterns of phase pure samples of $SrNi_2(P_{1-x}Ge_x)_2$ between 45 - 110 ° 2θ, composition x_{exp} determined via Rietveld refinement. The theoretical reflection positions for the compound with $x_{exp} = 0.110(3)$ including their corresponding *hkl* values are shown in the bottom. The highlighted areas show examples of merging reflections. 48

Figure 3.9 Polyanionic substructure model of $ThCr_2Si_2$ including all the relevant structural parameters for the phase. 50

Figure 3.10 Trend of important structural parameter for $SrNi_2(P_{1-x}Ge_x)_2$ and ternary compounds (x = 0, 1 taken from literature).[26, 31] Dependency of a) interatomic distances $d_{Ni–Ni}$ (black symbols) and $d_{Ni–P/Ge}$ (gray symbols) within the tetrahedral layers and $d_{P/Ge–P/Ge}$ (blue symbols) between the layers; b) atomic coordinate $z_{P/Ge}$ (magenta symbols); the height of the P/Ge atoms above the plane of Ni atoms, $h_{Ni-P/Ge}$ (gray symbols), and the tetrahedral angle α (green symbols) from the experimental x values. Lines within the diagrams are for visible help. Standard deviation is smaller than the size of the symbols... 50

Figure 3.11 Lattice parameters at different temperature between 10 - 300 K (10 K steps) for $SrNi_2(P_{1-x}Ge_x)_2$: a) $x_{exp} = 0.110(3)$ and b) $x_{exp} = 0.212(3)$. ... 54

Figure 3.12 Zero field cooled-field cooled (zfc-fc) measurements for the samples of $SrNi_2(P_{1-x}Ge_x)_2$ solid solution with an applied field of 15 Oe. The compounds with $x_{exp} = 0.110(3)$ (red curve) and 0.212(3) (green curve) show superconducting behavior ($T_{c,onset}$ marked with arrows). 57

Figure 3.13 Field dependent magnetic measurements at 1.8 K for superconducting $SrNi_2(P_{1-x}Ge_x)_2$ solid solution (magnetization plotted): a) $x_{exp} = 0.110(3)$, H range 0 - 3000 Oe in 10 Oe steps; b) $x_{exp} = 0.212(3)$ H range 0 - 1000 Oe in 10 Oe steps. The upper critical field H_{c2} is shown in red and the lower critical field H_{c1} is shown in green, the zero line (black dashed) is shown as visual help. 58

Figure 3.14 Schematic representation for the magnetization curve in dependence of the field for a) type 1 and b) type 2 superconductors......................... 58

Figure 3.15 a) Electrical resistivity measurements of the $SrNi_2(P_{1-x}Ge_x)_2$ solid solution ($x_{nom} = 0.15$); upper insert shows a close up of the data between 6 - 10 K and bottom insert shows measurements at different applied currents I. b) Heat capacity measurements performed without an applied field (zf) and an applied field H = 30000 Oe, the fitted curve (blue) is used as reference; in the top the difference heat capacity is plotted including the entropy construction plot.................................... 60

Figure 3.16 DOS and partial DOS of $SrNi_2P_2$: a) *Immm* and b) ucT *I4/mmm*; the Fermi level for the pseudo-ternary compound is set at −0.1 eV corresponding to the composition $SrNi_2(P_{0.86}Ge_{0.14})_2$ according to a rigid band model. Total DOS (black) including pDOS of Ni-d (turquois, blue), P-p (magenta, brown) and P-s (orange, gray). 62

Figure 3.17 Band structure (a) and fat band representations (b-h) of "SrNi$_2$(P$_{0.86}$Ge$_{0.14}$)$_2$": a) all bands, b) "P/Ge"-s, c) Ni-d$_{xy}$, d) Ni-d$_{xz,yz}$, e) Ni-d$_x$2$_{-y}$2, f) Ni-d$_z$2, g) "P/Ge"-p$_{x,y}$ and h) "P/Ge"- p$_z$; *k*-paths parallel to the *c*-direction are highlighted gray, paths parallel to *ab*-plane are white. 64

Figure 3.18 ELF representation of a) SrNi$_2$P$_2$ (*Immm*) and b) "SrNi$_2$(P$_{0.86}$Ge$_{0.14}$)$_2$" (*I*4/*mmm*) calculated from the all electron density. 2D contour line diagram of the ELF ranging from η = 0.4 to η = 0.7 is included. 3D plot with bisynaptic ELF domains located between the P1 atoms of SrNi$_2$P$_2$ are denoted with ①, monotactic ELF domains located at the P2 atoms denoted with ②. 65

Figure 3.19 Powder X-Ray diffraction pattern for SrNi$_2$(As$_{1-x}$Ge$_x$)$_2$ samples: a) x_{nom} = 0.1, b) x_{nom} = 0.3, c) x_{nom} = 0.7 and d) x_{nom} = 0.9. Theoretical pattern from 122 phase (green), Ni$_{19}$Ge$_{12}$ phase (gray) and Sr$_2$As (red) included. Measurements performed on a Stoe Stadi P (Cu-K$_{\alpha 1}$, measurement range 5 - 85 ° 2θ, 0.1 ° step size, Si as external standard), reflections marked with # are of unknown origin. 66

Figure 3.20 Temperature program for FeP precursor: a) first heating cycle; b) second heating cycle. 68

Figure 3.21 Temperature program for BaFe(P$_{1-x}$Ge$_x$)$_2$ single crystals: a) first heating cycle; b) second heating cycle. 70

Figure 3.22 Temperature program for: a) CaFe$_2$Si$_2$; b) second heating cycle of CaRh$_2$Si$_2$. 74

Figure 3.23 Temperature program for the Ca(Fe$_{1-x}$Rh$_x$)$_2$Si$_2$ sample: a) first heating cycle; b) second heating cycle. 75

Figure 3.24 DOS and band structure of CaFe$_2$Si$_2$ (a,b; top) and CaRh$_2$Si$_2$ (c,d; bottom): a,c) DOS (black) including pDOS of *T*–d (turquois), Ca–d (gray), Si–p (magenta) and Si–s (orange); b,d) total band structure, *k*-paths parallel to the *c*-direction are highlighted gray, path parallel to *ab*-plane are white. 81

Figure 3.25 DOS including pDOS of CaFe$_2$Si$_2$ (a), SrCo$_2$Si$_2$ (b) and SrNi$_2$P$_2$ (c, HT modification of SrNi$_2$P$_2$, cell parameters from 373 K measurement)[26]: total DOS shown in black, *T*–d in turquois, *Ae*–d in gray, *E*–p in magenta and *E*–s in orange. 83

Figure 3.26 Band structure including fat band representation of CaFe$_2$Si$_2$ orbitals: a) Fe-d$_{xy}$; b) Fe- d$_x$2$_{-y}$2; c) Fe-d$_{xz,yz}$; d) Fe-d$_z$2; e) Si-p; f) Si-s. *k*-paths parallel to the *c*-direction are highlighted gray, paths parallel to *ab*-plane are white. 85

Figure 3.27 Band structure including fat band representation of CaRh$_2$Si$_2$ orbitals: a) Rh-d$_{xy}$; b) Rh-d$_x$2$_{-y}$2; c) Rh-d$_{xz,yz}$; d) Rh-d$_z$2; e) Si-p; f) Si-s. *k*-paths parallel to the *c*-direction are highlighted gray, paths parallel to *ab*-plane are white. 86

Figure 3.28 ELF representation of $CaFe_2Si_2$ (a,c) and $CaRh_2Si_2$ (b,d) calculated from the all electron density. a, c) 3D plot with bonding ELF domains located between the Si atoms (denoted ①) along the *c*-direction; b, d) contour line diagram in the *ab*-plane at the *T* square planar layer. Only the region $\eta = 0.39$ - 0.40 ($CaFe_2Si_2$, c) and $\eta = 0.285$ - 0.29 ($CaRh_2Si_2$, d) are displayed for clarity reasons. 89

Figure 4.1 Crystal structure of CaCoSi (Ca atoms light gray, Co atoms teal, Si atoms magenta ellipsoids, respectively). Atoms are represented as atomic displacement ellipsoids with a 90 % possibility. Co–Si bonds are light gray; Co–Co bonds are dark gray. 94

Figure 4.2 DOS and band structure of CaCoSi: a) DOS (black) including iDOS (dashed line) and pDOS contributions of Co–d (turquois), Ca–d (gray), Si–p (magenta) and Si–s (orange); b) total band structure, *k*-paths parallel to the *c*-direction are highlighted gray, path parallel to *ab*-plane are white. 95

Figure 4.3 Band structure including fat band representation of CaCoSi orbitals: a) Co-d_{xy}, b) Co-$d_{x}2_{-y}2$, c) Co-$d_{xz,yz}$, d) Co-$d_{z}2$, e) Si-$p_{x,y}$, f) Si-p_z, g) Si-s; *k*-paths parallel to the *c*-direction are highlighted gray, path parallel to *ab*-plane are white. 97

Figure 4.4 ELF representation of CaCoSi calculated from the all electron density. a) 3D plot with non-bonding ELF domains located at the Si atoms (denoted with number 1), the Si lone pairs are directed along the *c*-direction; b) contour line diagram in the *ab*-plane at the Co square planar layer. η region displayed between 0.35 and 0.38 with two contour lines of 0.2 steps. 99

Figure 4.5 Total and partial DOS presentation of CaNiGe[6]: total DOS (solid black) including iDOS (black dashed) and the pDOS contributions of Ni–d (turquois), Ca–d (gray), Ge–p (magenta) and Ge–s (orange). 99

Figure 4.6 Structure model of a) CaCoSi (*P*4/*nmm*) and b) $CaCo_2Si_2$ (*I*4/*mmm*).[18] Ca atoms shown in light gray, Co atoms teal, Si atoms magenta spheres. Co–Si bonds are light gray; Co–Co bonds are black and the Si–Si bonds in $CaCo_2Si_2$ are blue. 101

Figure 5.1 Ternary phase diagram of Ca–Fe–As. Known phases are marked with black stars, the new compounds are indicated by red stars. 104

Figure 5.2 Structures of $CaFe_2As_2$ (a),[1] $CaFe_4As_3$ (b)[20] and $CaFe_5As_3$ (c).[21] Ca atoms shown in gray, Fe in teal, As in magenta; cell edges are red. Teal polyhedra represent [$FeAs_4$] tetrahedral layers while orange polyhedra represent [$FeAs_5$] square pyramids. 105

Figure 5.3 Temperature program for: a) FeAs precursors; b) $Ca_{14}FeAs_{11}$ samples. 108

Figure 5.4 Crystal structure of $Ca_{14}FeAs_{11}$ (space group *I*4$_1$/*acd*, *Z* = 8). The atoms are represented as atomic displacement ellipsoid with 75 % probability level; Ca = gray, Fe = teal, As = magenta and green (non-split position for the central As4 atom in the $[As_3]^{7-}$ unit). Covalent bonds between Fe–As shown in dark gray, As–As in green. 109

Figure 5.5 $FeAs_4$ tetrahedron structure motif in $Ca_{14}FeAs_{11}$: a) isolated tetrahedron with the angle α indicated by the gray curve; b) tetrahedron coordinated by Ca ($d_{As–Ca} < 3.505$ Å). The atoms are represented as atomic displacement ellipsoid with 75 % probability level. The terminal Ca atoms are represented in gray, the bridging Ca atoms in blue. 112

Figure 5.6 $[As_3]^{7-}$ unit with the As3 atoms shown in magenta and As4 atoms in green, the atoms are represented as atomic displacement ellipsoid with 75 % probability level. a) The unit with As4 lying on Wyckoff position 8*b* with 100 % occupancy, with equivalent As3–As4 distances. b) As4 split into two atoms each with 50 % occupancy. c) The two possible $[As_3]^{7-}$ motifs with a shorter (solid) and longer (dashed) As3–As4 distance. d) Coordination of Ca around the $[As_3]^{7-}$ unit, terminal Ca atoms are represented in gray, the bridging Ca atoms in blue. 113

Figure 5.7 Coordination of As1 atoms. The atoms are depicted as atomic displacement ellipsoids with 75 % probability level. Ca–As bonds are shown in gray, Ca–Ca contacts in black (non-covalent and only for visible clarification). 114

Figure 5.8 DOS and partial DOS of $Ca_{14}FeAs_{11}$: a) split atom model (space group $P4_3$); b) non-split atom model (space group $I4_1/acd$). Total DOS (black) including pDOS of Fe–d (turquois), As–s,p tetrahedra (magenta), As–s,p As3 unit (green) and Ca-d (gray). The DOS region between −0.5 eV and 1.3 eV are magnified in the bottom graphs. 120

Figure 5.9 COHP and iCOPH of the Fe–As bond (2.503(1) Å) in $Ca_{14}FeAs_{11}$ (non-split atom model). 121

Figure 5.10 Electronic structure for $Ca_{14}FeAs_{11}$ (non-split atom model). a) COHP for Fe–As bond ($d_{Fe–As} = 2.503$ Å); fat bands for b) Fe-$d_{x^2-y^2}$, c) Fe-d_{xz}, d) Fe-d_{yz}, e) Fe-d_{xy} and f) Fe-d_{z^2}. *k*-paths parallel to the *c*-direction are highlighted gray, path parallel to *ab*-plane are white. 122

Figure 5.11 Temperature program for measured single crystals of Ca_4As_3: a) Rh-Si precursor heating cycle; b) heating cycle for the sample with nominal composition "$Ca_{12}(RhSi_2)_4(Fe_2As_2)_5$". 124

Figure 5.12 Temperature program for the $Ca_{11}As_{10}$ compound: a) short heating cycle; b) long heating cycle. 125

Figure 5.13 Unit cell of Ca_4As_3 with space group *Pbam*, $Z = 8$. The atoms are represented as atomic displacement ellipsoids with 90 % probability level, As depicted in magenta, Ca depicted as gray. The covalent As–As bonds are shown in green. 126

Figure 5.14 Coordination of the Ca^{2+} cations around the As positions in Ca_4As_3 atoms are represented as atomic displacement ellipsoids with 90 % probability level. The covalent As–As bonds are depicted in green, the non-bonding distances Ca–As (gray) and Ca–Ca (black) are for visible help.. 129

Figure 5.15 Coordination of the As anions and Ca^{2+} cations around the Ca positions in Ca_4As_3 atoms are represented as atomic displacement ellipsoids with 90 % probability level. The covalent As–As bonds are depicted in green, the non-bonding distances Ca–As (gray) and Ca–Ca (black) are for visible help. ... 130

Figure 5.16 Structure of $Ca_{11}As_{9.68(2)}$ in space group *I*4/*mmm* with *Z* = 4 in the non-split atom model. Ca depicted in gray and As depicted in magenta as atomic displacement ellipsoids with 90 % probability level. The covalent As–As bonds are shown in black. ... 134

Figure 5.17 The dumbbell structure motif in $Ca_{11}As_{9.68(2)}$ (split atom model); atoms depicted as atomic displacement ellipsoids with 90 % probability level. a) As dumbbell with the As–As covalent bond shown in black including the coordination of the adjacent As5A anions (dashed black lines); b) coordination of Ca cations (gray, terminal coordinated and blue, bridging) around the dumbbell. ... 136

Figure 5.18 Structure motif of the As_4 unit, view along the *ab*-plane, atoms depicted as atomic displacement ellipsoids with 90 % probability level. a) non-split atom model; b) split atom model with the position As5 and Ca4 split into two atomic positions; c) and d) possible orientation of the As_4 rhombi. ... 137

Figure 5.19 Coordination around the isolated As^{3-} anions in $Ca_{11}As_{9.68(2)}$ atoms depicted as atomic displacement ellipsoids with 90 % probability level. a) Ca^{2+} cations around As1; b) Ca^{2+} cations around As2; c) Ca^{2+} cations around As3. The contacts are non-bonding and only for visible help, As–Ca in gray and Ca–Ca in black. ... 138

Figure A1 X-ray powder diffraction pattern of $SrNi_2P_2$ sample (Cu-$K_{\alpha1}$, measurement range 5 - 78 ° 2θ, 0.01 ° step size, 20 sec/step, Si as external standard). Theoretically calculated pattern of $SrNi_2P_2$ with HT-*I*4/*mmm* (green lines) and LT-*Immm* (red lines) modification shown in the bottom. ... 151

Figure A2 X-ray powder diffraction pattern of $SrNi_2Ge_2$ sample (Cu-$K_{\alpha1}$, measurement range 5 - 90 ° 2θ, 0.01 ° step size, 20 sec/step, Si as external standard). Theoretically calculated pattern of $SrNi_2Ge_2$ with $ThCr_2Si_2$ type structure (green lines) shown in the bottom. ... 152

Figure A3 X-ray powder diffraction pattern of $SrNi_2As_2$ sample (Cu-$K_{\alpha1}$, measurement range 5 - 80 ° 2θ, 0.01 ° step size, 20 sec/step, Si as external standard). Theoretically calculated pattern of $SrNi_2As_2$ with $ThCr_2Si_2$ type structure (green lines) shown in the bottom. ... 152

Figure A4 X-ray powder diffraction pattern of $SrNi_2(P_{1-x}Ge_x)_2$ sample with x_{nom} = 0.80 from NiP and NiGe precursors , (Cu-$K_{\alpha1}$, measurement range 5 - 80 ° 2θ, 0.01 ° step size, 20 sec/step, Si as external standard). Theoretically calculated pattern of $SrNi_2(P_{1-x}Ge_x)_2$ in $ThCr_2Si_2$ type structure (green lines; *a* = 4.01 Å; *c* = 10.23 Å) and $SrNi_5(P_{3-x}Ge_x)$ space group *Cmcm* (red lines; *a* = 3.64 Å, *b* = 11.59 Å, *c* = 11.81 Å) shown in the bottom. The reflection marked with # belongs to cubic diamond used as standard. ... 153

Figure A5 Rietveld refinement (TOPAS) of $SrNi_2(P_{1-x}Ge_x)_2$ (x_{exp} = 0.110(3)) for powder X-ray data collected on Huber Imaging Plate Guinier Diffractometer G670 (Co-$K_{\alpha1}$, measurement range 6 - 100 ° 2θ, 0.005 ° step size, measurement time 30 min, Si as external standard) at 300 K and 10 K. Refinement parameters: 300 K - GOF = 0.815, R_p = 0.0143, R_{wp} = 0.0209, R_{Bragg} = 0.0141; 10 K - GOF = 1.015, R_p = 0.0173, R_{wp} = 0.0271, R_{Bragg} = 0.0131. Excluded region between 14 - 16 ° 2θ is due to instrumental artifact. 156

Figure A6 Rietveld refinement (TOPAS) of $SrNi_2(P_{1-x}Ge_x)_2$ (x_{exp} = 0.212(3)) for powder X-ray data collected on Huber Imaging Plate Guinier Diffractometer G670 (Co-$K_{\alpha1}$, measurement range 6 - 100 ° 2θ, 0.005 ° step size, measurement time 30 min, Si as external standard) at 300 K and 10 K. Refinement parameters: 300 K - GOF = 0.493, R_p = 0.0099, R_{wp} = 0.0137, R_{Bragg} = 0.0076; 10 K - GOF = 0.995, R_p = 0.0139, R_{wp} = 0.0275, R_{Bragg} = 0.0158. Excluded region between 14 - 16 ° 2θ is due to instrumental artifact. 157

Figure A7 Rietveld refinement (FullProf) of $SrNi_2(P_{1-x}Ge_x)_2$ (x_{exp} = 0.436(2)) for powder X-ray data collected on Stoe Stadi P (Cu-$K_{\alpha1}$, measurement range 5 - 110 ° 2θ, 0.015 ° step size, measurement time 5 hours, Si as external standard) at 300 K. Refinement parameters: GOF = 1.1, R_p = 0.138, R_{wp} = 0.113, R_{Bragg} = 1.99. 158

Figure A8 Rietveld refinement (FullProf) of $SrNi_2(P_{1-x}Ge_x)_2$ (x_{exp} = 0.547(2)) for powder X-ray data collected on Stoe Stadi P (Cu-$K_{\alpha1}$, measurement range 5 - 110 ° 2θ, 0.015 ° step size, measurement time 5 hours, Si as external standard) at 300 K. Refinement parameters: GOF = 1.8, R_p = 0.205, R_{wp} = 0.181, R_{Bragg} = 3.86. 159

Figure A9 Rietveld refinement (FullProf) of $SrNi_2(P_{1-x}Ge_x)_2$ (x_{exp} = 0.671(2)) for powder X-ray data collected on Stoe Stadi P (Cu-$K_{\alpha1}$, measurement range 5 - 110 ° 2θ, 0.015 ° step size, measurement time 5 hours, Si as external standard) at 300 K. Refinement parameters: GOF = 1.4, R_p = 0.158, R_{wp} = 0.125, R_{Bragg} = 4.34. 159

Figure A10 Rietveld refinement (FullProf) of $SrNi_2(P_{1-x}Ge_x)_2$ (x_{exp} = 0.884(1)) for powder X-ray data collected on Stoe Stadi P (Cu-$K_{\alpha1}$, measurement range 5 - 110 ° 2θ, 0.015 ° step size, measurement time 5 hours, Si as external standard) at 300 K. Refinement parameters: GOF = 1.4, R_p = 0.133, R_{wp} = 0.119, R_{Bragg} = 1.89. 160

Figure A11 Zero field cooled-field cooled (zfc-fc) measurement for the sample $SrNi_2(P_{1-x}Ge_x)_2$ with x_{exp} = 0.436(2) and an applied field of 15 Oe. ... 163

Figure A12 $SrNi_2(P_{1-x}Ge_x)_2$ (x_{nom} = 0.15) powder X-ray pattern (Co-$K_{\alpha1}$, measurement range 10 - 100 ° 2θ, at 300 K) of powder (top) after thermal pressure treatment (2 h at 973 K and 630 MPa). The theoretical Bragg positions (green) for the 122 phase calculated from the powder X-ray of x_{exp} = 0.110(3) (bottom). 163

Figure A13 Brillouin zone for space group *I*4/*mmm*. 164

Figure A14 X-ray powder diffraction pattern of FeP sample (Mo-$K_{\alpha1}$, measurement range 2 - 50 ° 2θ, 0.015 ° step size, 25 sec/step). Theoretical calculated pattern of FeP (green lines) shown in the bottom. 164
Figure A15 X-ray powder diffraction pattern of FeGe sample (Mo-$K_{\alpha1}$, measurement range 2 - 50 ° 2θ, 0.015 ° step size, 25 sec/step). Theoretical calculated pattern of FeGe (green lines) shown in the bottom. 165
Figure A16 X-ray powder diffraction pattern of $BaFe_2(P_{1-x}Ge_x)_2$ sample with x_{nom} = 0.30 (Mo-$K_{\alpha1}$, measurement range 2 - 50 ° 2θ, 0.015 ° step size, 45 sec/step). Theoretical calculated pattern of $BaFe_2(P_{1-x}Ge_x)_2$ with $ThCr_2Si_2$ structure (a = 3.857 Å, c = 12.464 Å; green lines) and $Fe_{1.67}Ge_1$ (red lines) shown in the bottom. 165
Figure A17 X-ray powder diffraction pattern of $CaFe_2Si_2$ sample (Mo-$K_{\alpha1}$, measurement range 2 - 70 ° 2θ, 0.015 ° step size, 25 sec/step). Theoretical calculated pattern of $CaFe_2Si_2$ with $ThCr_2Si_2$-type structure (green lines) shown in the bottom. The reflections marked with red line at 19.8 ° and 33.65 ° belong to cubic diamond which was used as an internal standard. Reflections marked with ^{0} belong to Ca_5Si_3, reflections marked with * belong to FeSi and reflections marked with # belong to Fe_3Si. 166
Figure A18 X-ray powder diffraction pattern of $CaRh_2Si_2$ sample), (Cu-$K_{\alpha1}$, measurement range 2 - 90 ° 2θ, 0.01 ° step size, 40 sec/step, Si as external standard). Theoretically calculated pattern of $CaRh_2Si_2$ with $ThCr_2Si_2$ type structure (green lines) shown in the bottom. Reflections marked with * belong to RhSi. 167
Figure A19 X-ray powder diffraction pattern of $CaFeRhSi_2$ sample (nominal composition), (Mo-$K_{\alpha1}$, measurement range 2 - 78 ° 2θ, 0.015 ° step size, 25 sec/step). Theoretically calculated pattern of $Ca(Fe_{0.34(3)}Rh_{0.66(3)})_2Si_2$ with $ThCr_2Si_2$ type structure (green lines) shown in the bottom. The reflex marked with the red line at 19.8 ° and 33.65 ° belong to cubic diamond which was used as an internal standard. Reflections marked with * belong to FeSi. 168
Figure A20 COHP curves (solid lines) including iCOHP (dashed lines) for selected interatomic distances of $CaFe_2Si_2$ (a-c) and $CaRh_2Si_2$ (d-f). a) $d_{Fe–Si}$ = 2.343 Å, b) $d_{Fe–Fe}$ = 2.785 Å, c) $d_{Si–Si}$ = 2.555 Å, d) $d_{Rh–Si}$ = 2.378 Å, e) $d_{Rh–Rh}$ = 2.878 Å and e) $d_{Si–Si}$ = 2.529 Å. 170
Figure A21 Brillouin zone for space group *P*4/*nmm*. 171
Figure A22 X-ray powder diffraction pattern of FeAs sample, (Mo-$K_{\alpha1}$, measurement range 2 - 50 ° 2θ, 0.01 ° step size, 20 sec/step, Si as external standard). Theoretically calculated pattern of FeAs (green lines) shown in the bottom. 171
Figure A23 X-ray powder diffraction pattern of $Ca_{14}FeAs_{11}$ sample, (Cu-$K_{\alpha1}$, measurement range 5 - 90 ° 2θ, 0.01 ° step size, 45 sec/step). Theoretically calculated pattern of $Ca_{14}FeAs_{11}$ (green lines); $Ca_{11}As_{9.68}$ model (red lines, middle) and details between 18 - 31 ° 2θ & 58 - 74 °

2θ shown in the bottom. Reflections marked with # belong to Si used as standard. 172

Figure A24 DSC curves for $Ca_{14}FeAs_{11}$ sample. 174

Figure A25 X-ray powder diffraction pattern of $Ca_{14}FeAs_{11}$ sample after DSC measurement, (Mo-$K_{\alpha1}$, measurement range 2 - 50 ° 2θ, 0.01 ° step size, 45 sec/step). Theoretically calculated pattern of $Ca_{14}FeAs_{11}$ (green lines); $Ca_{11}As_{9.68}$ model (red lines) shown in the bottom, reflections marked with # belong to Si. 175

Figure A26 X-ray powder diffraction pattern of $Ca_{4+x}As_{3}$ sample (x = 0.05), (Cu-$K_{\alpha1}$, measurement range 2 - 90 ° 2θ, 0.01 ° step size, 45 sec/step). Theoretically calculated pattern of Ca_4As_3 (gray lines, top) and $Ca_{11}As_{9.68}$ (red lines, bottom) shown, reflections marked with # belong to Si. 178

Figure A27 X-ray powder diffraction pattern of $Ca_{11+x}As_{10}$ sample (x = 2.2), (Cu-$K_{\alpha1}$, measurement range 5 - 90 ° 2θ, 0.01 ° step size, 45 sec/step). Theoretically calculated pattern of $Ca_{11}As_{9.68}$ (red lines) shown in the bottom, reflections marked with * belong to an unidentified phase. ... 179

Figure A28 Model of $Ca_{11}As_{9.68(2)}$. Green spheres are dummy atoms lying in the center of the $As_{3.86}$ rings, the As–As dumbbells shown as represented as atomic displacement ellipsoids with 90 % probability level. The green lines indicate the theoretical octahedra formed by the “rings” and the As dumbbells. 181

List of Tables

Table 2.1 Starting chemicals, source, shape and purity (atomic %). 17

Table 3.1 Masses of the $SrNi_2E_2$ (E = P, Ge) precursors used for the $SrNi_2(P_{1-x}Ge_x)_2$ samples described in this chapter. 39

Table 3.2 Masses of the $SrNi_2E_2$ (E = As, Ge) precursors used for the $SrNi_2(As_{1-x}Ge_x)_2$ samples described in this chapter. 40

Table 3.3 Crystal data and measurement details for single crystal refinement of $SrNi_2(P_{1-x}Ge_x)_2$ with $x_{nom} < 0.4$, collected at room-temperature (white column) and at 130 K (gray column)... 44

Table 3.4 Crystal data and measurement details for single crystal refinement of $SrNi_2(P_{1-x}Ge_x)_2$ with $x_{nom} < 0.4$, collected at room-temperature (white column) and at 130 K (gray column)... 45

Table 3.5 Crystallographic data of the Rietveld refinements for $SrNi_2(P_{1-x}Ge_x)_2$ solid solution (powder X-ray diffraction measurements at room-temperature). 45

Table 3.6 Crystal data and measurement details for single crystal refinement of $SrNi_2(P_{1-x}Ge_x)_2$ with $x_{nom} > 0.4$, collected at room-temperature........... 46

Table 3.7 Cell parameters, atomic coordinate $z_{P/Ge}$ and x values for $SrNi_2(P_{1-x}Ge_x)_2$ (space group $I4/mmm$, $Z = 2$) obtained from powder data (-p) and single crystal data (-sc) at room-temperature. Parameters for the ternary compounds (*) are taken from literature[26, 31] (parameters for the high-temperature $I4/mmm$ modification of $SrNi_2P_2$ measured at 373 K)... 47

Table 3.8 Selected atomic distances, height ($h_{Ni-P/Ge}$), angle (α) within the tetrahedral layer (parameters shown in Figure 3.9) and the temperature at which the data was collected for $SrNi_2(P_{1-x}Ge_x)_2$ solid solution. The gray highlighted values correspond to single crystal data while the non-highlighted values correspond to data from powder Rietveld refinement. 51

Table 3.9 Structural parameters of selected $AeNi_2E_2$ (Ae = Ca, Sr, Ba, La; E = P, As, Ge) compounds with $ThCr_2Si_2$ type structure. cT stands for collapsed, ucT for uncollapsed tetragonal modification. 55

Table 3.10 Masses of Ba, FeP and FeGe used for the different nominal compositions of the samples for $BaFe_2(P_{1-x}Ge_x)_2$ solid solution.......... 69

Table 3.11 Crystal data, measurement details and structure parameter for single crystal refinement of $BaFe_2(P_{0.930(6)}Ge_{0.070(6)})_2$, collected at room-temperature. Standard deviations are given in brackets...................... 71

Table 3.12 Wyckoff positions, atomic coordinates and isotropic equivalent displacement parameters / $Å^2 \times 10^3$ for $BaFe_2(P_{0.930(6)}Ge_{0.070(6)})_2$ (space group $I4/mmm$, $Z = 2$). Standard deviations are given in brackets. 72

Table 3.13 Interatomic distances (d) including their multiplicity (after semi-colon), height ($h_{Fe-P/Ge}$) and tetrahedral angle (α) for $BaFe_2(P_{0.930(6)}Ge_{0.070(6)})_2$ and $BaFe_2P_2$.[9] Standard deviations are given in brackets................. 72

Table 3.14 Masses of Ca and FeSi used for the different nominal compositions of the $CaFe_2Si_2$ samples.......... 74

Table 3.15 Crystal data, measurement details and structure parameter for single crystal refinement of $Ca(Fe_{1-x}Rh_x)_2Si_2$ for x_{exp} = 0, 0.66(3), 1; data collected at room-temperature. Standard deviations are given in brackets.......... 76

Table 3.16 Atomic distances (*d*) including their multiplicity (after semi-colon), height ($h_{T\text{–}Si}$) and angle (α) within the tetrahedral layer for $Ca(Fe_{1-x}Rh_x)_2Si_2$ solid solution. Standard deviations are given in brackets. 77

Table 3.17 Important structural parameters for related CaT_2E_2 (*T* = Fe, Co, Rh; *E* = Si, As) 122 compounds. 79

Table 3.18 Interatomic distances (*d*) for $CaFe_2Si_2$ and $CaRh_2Si_2$ and selected integrated Crystal Orbital Hamilton Populations (−iCOHP) values at E_F. 87

Table 3.19 Selected interatomic distances (*d*) and integrated Crystal Orbital Hamilton Populations (−iCOHP) values at E_F for $CaCo_2Si_2$ and $SrCo_2Si_2$.[7, 12].......... 88

Table 5.1 Masses of Ca, FeAs and As used for the synthesize of $Ca_{14}Fe_{1+x}As_{11}$ samples.......... 108

Table 5.2 Crystal data, measurement details and structure parameter for single crystal refinement of $Ca_{14}FeAs_{11}$, collected at 150 K.......... 110

Table 5.3 Atomic coordinates and isotropic equivalent displacement parameters /$Å^2 \times 10^3$ (space group *I*4$_1$/*acd*, *Z* = 8, split atom model). 111

Table 5.4 Atomic distances (*d*) within the first coordination sphere including their multiplicity for the individual structural units of $Ca_{14}FeAs_{11}$, space group *I*4$_1$/*acd*, *Z* = 8 (split atom model).......... 114

Table 5.5 Crystallographic parameters of $Ae_{14}TE_{11}$ compounds (space group *I*4$_1$/*acd*, Z = 8) from single crystal measurements: unit cell parameters, $d_{T\text{–}E}$ = distance between the *T* atom and the *E* atom in the tetrahedra, $d_{E\text{–}E}$ = distance between the two *E* atoms forming the $[E_3]^{7-}$ unit (central *E* atom on the 8*b* Wyckoff position with 100 % occupancy, non-split atom model). 116

Table 5.6 Masses of Ca and As used for the samples of $Ca_{4+x}As_3$. 124

Table 5.7 Crystal data and measurement details for single crystal refinement of Ca_4As_3, collected at 150 K.......... 127

Table 5.8 Wyckoff positions, atomic coordinates and isotropic equivalent displacement parameters /$Å^2 \times 10^3$ (space group *Pbam*, *Z* = 8)........ 128

Table 5.9 Atomic distances (*d*) within the first coordination sphere including their multiplicity for the individual structural units of Ca_4As_3; space group *Pbam*, *Z* = 8. The homoatomic distances $d_{Ca\text{–}Ca}$ for the coordination of Ca not individually given, they are between 3.289(2) Å and 4.380(2) Å. 131

Table 5.10 Crystal data and measurement details for single crystal refinement of $Ca_{11}As_{9.68(2)}$ in the split model, collected at 150 K. 133

Table 5.11 Wyckoff positions, atomic coordinates and isotropic equivalent displacement parameters / Å^2 × 10^3 (space group *I*4/*mmm*, *Z* = 4, split atom model). 135
Table 5.12 Atomic distances (*d*) within the first coordination sphere including their multiplicity for the individual structural units of $Ca_{11}As_{9.68(2)}$ split model; space group *I*4/*mmm*, *Z* = 4... 136

Table A1 EDX results (values given in at. %, including standard deviation) for measured single crystals of $SrNi_2(P_{1\text{-}x}Ge_x)_2$ solid solution................. 153
Table A2 Wyckoff positions, atomic coordinates and isotropic equivalent displacement parameters / Å^2 × 10^3 for $SrNi_2(P_{1\text{-}x}Ge_x)_2$ solid solution (space group *I*4/*mmm*, *Z* = 2) obtained from Rietveld refinements on powder patterns. Standard deviations are given in brackets. 154
Table A3 Anisotropic displacement parameters (*Uij* / Å^2) for $SrNi_2(P_{0.86(1)}Ge_{0.14(1)})_2$ from single crystal refinement measured at 293 K. 154
Table A4 Anisotropic displacement parameters (U_{ij} / Å^2) for $SrNi_2(P_{0.86(1)}Ge_{0.14(1)})_2$ from single crystal refinement measured at 130 K. 154
Table A5 Anisotropic displacement parameters (U_{ij} / Å^2) for $SrNi_2(P_{0.76(1)}Ge_{0.24(1)})_2$ from single crystal refinement measured at 293 K. 155
Table A6 Anisotropic displacement parameters (U_{ij} / Å^2) for $SrNi_2(P_{0.76(1)}Ge_{0.24(1)})_2$ from single crystal refinement measured at 130 K. 155
Table A7 Anisotropic displacement parameters (U_{ij} / Å^2) for $SrNi_2(P_{0.56(2)}Ge_{0.44(2)})_2$ from single crystal refinement measured at 293 K. 155
Table A8 Anisotropic displacement parameters (U_{ij} / Å^2) for $SrNi_2(P_{0.45(1)}Ge_{0.55(1)})_2$ from single crystal refinement measured at 293 K. 155
Table A9 Anisotropic displacement parameters (U_{ij} / Å^2) for $SrNi_2(P_{0.35(1)}Ge_{0.65(1)})_2$ from single crystal refinement measured at 293 K. 155
Table A10 $SrNi_2(P_{0.890(3)}Ge_{0.110(3)})_2$ lattice parameters obtained from powder data at varying temperatures... 161
Table A11 $SrNi_2(P_{0.788(3)}Ge_{0.212(3)})_2$ lattice parameters obtained from powder data at varying temperatures... 162
Table A12 EDX results (values given in at. %, including standard deviation) for measured single crystal of $BaFe_2(P_{1\text{-}x}Ge_x)_2$...................................... 166
Table A13 Anisotropic displacement parameters (U_{ij} / Å^2) for $BaFe_2(P_{0.930(6)}Ge_{0.070(6)})_2$ measured at 293 K.................................... 166
Table A14 EDX results (values given in at. %, including standard deviation) for measured single crystals of $Ca(Fe_{1\text{-}x}Rh_x)_2Si_2$ solid solution. 168
Table A15 Wyckoff positions, atomic coordinates and isotropic equivalent displacement parameters / Å^2 × 10^3 for $Ca(Rh_{1\text{-}x}Fe_x)_2Si_2$ solid solution (space group *I*4/*mmm*, *Z* = 2). Standard deviations are given in brackets.. 169
Table A16 Anisotropic displacement parameters (U_{ij} / Å^2) for $CaFe_2Si_2$ measured at 293 K.. 169

Table A17 Anisotropic displacement parameters (U_{ij} / Å^2) for $Ca(Fe_{0.34(3)}Rh_{0.66(3)})_2Si_2$ measured at 293 K. 169

Table A18 Anisotropic displacement parameters (U_{ij} / Å^2) for $CaRh_2Si_2$ measured at 293 K. 169

Table A19 Anisotropic displacement parameters (U_{ij} / Å^2) for $Ca_{14}FeAs_{11}$ measured at 150 K (non-split atom model). 173

Table A20 Anisotropic displacement parameters (U_{ij} / Å^2) for $Ca_{14}FeAs_{11}$ measured at 150 K (split atom model). 173

Table A21 Input data for computational calculations for the tetragonal model non-split of the $[As_3]^{7-}$ units: space group, lattice parameters and atomic parameters obtained from single crystal data. 176

Table A22 Input data for the computational calculations for $Ca_{14}FeAs_{11}$ with symmetry reduction to accommodate the split model of the $[As_3]^{7-}$ units: space group and atomic parameters chosen by symmetry reduction. Lattice parameters taken from single crystal refinement. 176

Table A23 Anisotropic displacement parameters (U_{ij} / Å^2) for Ca_4As_3 measured at 150 K. 179

Table A24 Anisotropic displacement parameters (U_{ij} / Å^2) for $Ca_{11}As_{9.68(2)}$ measured at 150 K (non-split atom model). 180

Table A25 Anisotropic displacement parameters (U_{ij} / Å^2) for $Ca_{11}As_{9.68(2)}$ measured at 150 K (split atom model). 180